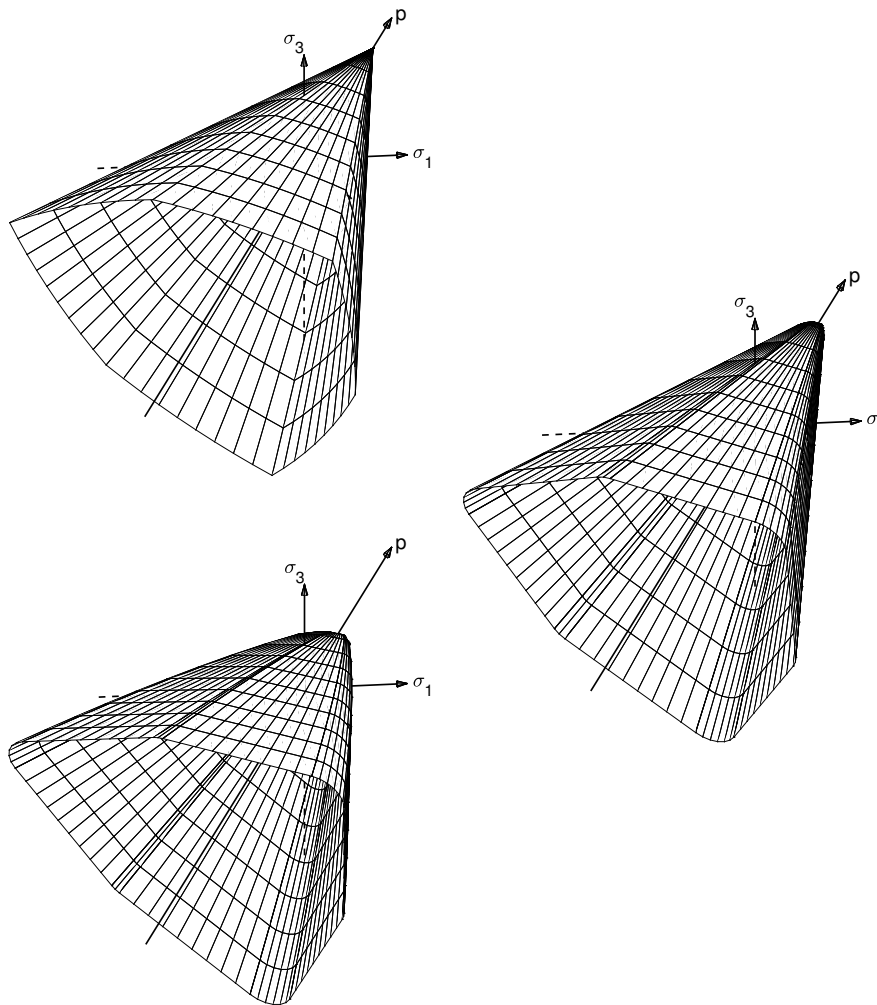

Elasto-Plastic Constitutive Modelling of Geotechnical Material

Investigation of the Intermediate Principle Stress Influence and
Exploration of the General Parametric Yield Surface Format



Johan Nielsen & Kenneth Sixhøj Jepsen

Aalborg University Esbjerg
Structural and Civil Engineering
Master Thesis



AALBORG UNIVERSITY
STUDENT REPORT

Title:

Elasto-Plastic Constitutive Modelling of
Geotechnical Material

Subtitle:

Investigation of the Intermediate Principle
Stress Influence and Exploration of the General
Parametric Yield Surface Format

Document type:

M.Sc. Thesis

Project period:

04/09/2018 to 07/06/2019

Authors:

Johan Nielsen
Kenneth Sixhøj Jepsen

Project supervisor:

Lars Damkilde

Total Pages: 51

Total Appendices: 4

Johan Nielsen
jniel13@student.aau.dk

Kenneth Sixhøj Jepsen
kjepse13@student.aau.dk

Abstract

In the matter of constitutive modelling of frictional material, two major models are the Mohr-Coulomb and the Drucker-Prager yield criteria. However, contradictions arise as the former neglects the intermediate principle stress and all stresses are of equal importance in the latter. Evidently both statements cannot be true and the actual material behaviour is somewhere in between. The Mohr-Coulomb model is in general a better limit stress representation for frictional soil, however, especially conservative in plane strain calculations, where it to some extent has become the norm to increase the angle of friction with some empirical expression. Yield surfaces to better describe the actual material behaviour has been proposed in plenty, however, as more advanced models thrive in academia, these have failed to gain a widespread use by practitioners.

In this thesis, a concept of yield surfaces denoted the General Parametric Yield Surface Format, proposed by Lars Damkilde, is explored. Three novel yield surfaces, which encompasses several existing models are formulated and implemented in a numerical framework. When evaluating the numerical performance of a plasticity model, discrepancy, computation time and robustness are of interest, where the latter two are somewhat connected. The first proposed yield surface operates on four parameters, of which two can be omitted to obtain the Mohr-Coulomb model. This model has proven efficient, however, lacks robustness, especially in the analyses of three-dimensional systems. The second proposed yield surface is therefore developed as a smooth continuous approximation of the first model for a numerically robust implementation. It is formulated by employment of a new concept of local corner rounding, which, to the authors knowledge is not presented elsewhere in the literature. Furthermore, this model enables a smooth tension cut-off, and can serve as an optimised material fit, provided the existence of experimental data. The first two models are formulated with linear hydrostatic stress dependency, as a common simplification. A widely accepted formulation of the nonlinear hydrostatic stress dependency for common sands was proposed by Bolton, which is incorporated in the third yield surface formulation. The result of this is an advanced nonlinear model, which operates on the well-known parameters from Bolton, and constitutes the most optimized material calibration conducted in this thesis, and demonstrates the generality of the new yield surface concept.

The novel yield surface models are implemented in a computational framework, in MATLAB as well as a Fortran source code for use in Abaqus. The models are calibrated to data from true triaxial experiments and employed in a series of elasto-plastic finite element analysis of typical geotechnical problems, to investigate the influence of the intermediate principal stress and computational performance of the models. The simulation results reveals a vast unused potential in comparison with the Mohr-Coulomb criterion in plane strain conditions, and a considerable increase in general 3D as well. A notable increase in bearing capacity can be obtained if the model is calibrated with standard triaxial tests in both extension and compression, which is not a possibility with the Mohr-Coulomb model. The novel corner rounded model comes with a cost in computation time, however, it is found numerically robust, especially in three-dimensional analyses. It is therefore the recommended model by the authors, as robustness is a desired quality of the numerical implementation.

Preface

The present master thesis is the results of the one year masters program at Aalborg University Esbjerg, Department of civil engineering. The objective is to investigate possible material optimisation in the field of geomechanics, especially towards frictional soil. For this purpose, a new yield surface concept, proposed by Lars Damkilde, which encompasses a wide range of the existing plasticity models in the field, is explored and implemented in a numerical framework. No material experiments are conducted in coherence with this thesis, as the work relies solely on numerical analysis. The model calibrations are therefore conducted with experimental results from the existing literature.

Frequently used mathematical symbols are listed in the nomenclature, and less frequently used is described posterior to its first use. Vectors and matrices are denoted with lower and upper case boldface font, respectively. References to literature are marked in square brackets as [Author,year of publish], figures, tables and equations are referenced to by type followed by a number referring to (Chapter.Number). All figures in this thesis are composed by the authors.

The herein proposed constitutive models are implemented in a numerical framework and are available in MATLAB scripts and Fortran source code for use in Abaqus software. The source code is handed in along with the thesis, and can be acquired from the AAU web page or by correspondence to the authors.

In coherence with this thesis, two articles have been composed and submitted for possible publication:

- Nielsen J, Jepsen KS, Damkilde L. Parametric Transition from Mohr-Coulomb to Drucker-Prager by Implementation of the General Parametric Yield Surface Format. *International Journal for Numerical and Analytical Methods in Geomechanics*. Submitted 2019
- Jepsen KS, Nielsen J, Damkilde L. A Concept of Local Rounding Applied to a Multi-Surface Plasticity Model with Sharp Edges. *International Journal for Numerical Methods in Engineering*. Submitted 2019

These are attached in appendices C and D and considered as part of the content in the thesis. Therefore, the majority of their content is not documented within this report, to avoid unnecessary repetition, and results from the articles are incorporated in the conclusion in Chapter 6.

The following software are used in the presented numerical studies in this thesis:

- MATLAB R2017b by MathWorks, release September 2017
- Abaqus 2017 by Dassault Systemes Simulia , release 2017
- Intel Fortran 2013 by Intel, release 2013

Acknowledgements

This thesis is accomplished under competent supervision by professor Lars Damkilde, whom formulated the General Parametric Yield Surface Format and proposed the thesis topic. He has further contributed with feedback on the subjects of constitutive modelling, and provided motivation and guidance towards publication in scientific journals. A thanks to Sven Krabbenhøft for sharing his practical experience and wide knowledge in geomechanics, under some professional discussions. Furthermore, a thanks to associate professor Johan Clausen, for an introduction to geomechanical finite element analysis, and guidance in the implementation of a user-defined subroutine in the Abaqus software.

Contents

Title Page	I
Abstract	III
Preface	V
Nomenclature	IX
1 Introduction	1
2 Methodology	5
2.1 Stress Invariants and Their Geometrical Interpretations	5
2.2 The Yield Criterion and the Plastic Potential	7
2.3 Elasto-Plastic Finite Element Analysis	8
2.4 Elasto-Plastic Stress Strain Relation	10
2.5 Stress Update by Return Mapping	11
2.5.1 Accuracy of return mapping	12
2.5.2 General solution algorithm for the implicit return map	13
3 Constitutive Models in Geomechanics	15
3.1 No Hydrostatic Stress Dependency	15
3.1.1 The Tresca Criterion	15
3.2 Yield Surfaces with Linear Generators	15
3.2.1 The Mohr-Coulomb criterion	16
3.2.2 The Drucker-Prager criterion	16
3.3 Yield Surfaces with Nonlinear Generators	17
3.3.1 The Lade criterion	18
3.3.2 The Bolton criterion	18
3.3.3 The Hoek-Brown criterion	19
3.4 A Schematic Overview	20
4 The General Parametric Yield Surface Format	23
4.1 Transformation to Reference Coordinates	24
4.2 Discontinuous Deviatoric Trace	25
4.3 Continuous Deviatoric Trace	25
4.4 Formulation with Mohr-Coulomb Generators	27
4.5 Formulation with Bolton Generators	29
4.6 Overview of the New Models	31
5 Finite Element Analysis of Geomechanical Systems	33
5.1 Influence of The Intermediate Principle Stress	33
5.1.1 Calibration of surface parameters	33
5.1.2 Vertical concentric loading of strip footing	35
5.1.3 Vertical concentric loading of spread footing	38
5.1.4 Slope safety factor	41
5.2 Spread Footing Analysis with the GPYS-NC model	43
5.2.1 Calibration of surface parameters	43
5.2.2 Analysis of square spread footing	45
6 Conclusion	47
Bibliography	49

A	Finite Element Analysis of Geomechanical Systems	53
A.1	Data from True Triaxial Experiments	53
A.2	The GPYS-LD model as approximation of Mohr-Coulomb	54
A.3	Finite Elements	54
A.3.1	Linear Strain Triangle	54
A.3.2	Linear Strain Tetrahedron	55
B	Implementation in Abaqus software	57
B.1	Writing UMAT in Fortran Fixed form	57
B.2	Linking Abaqus and Fortran compiler	59
B.3	Preparing Abaqus CEA for UMAT analysis	61
C	Parametric Transition from Mohr-Coulomb to Drucker-Prager by Implementation of a General Parametric Yield Surface Format	63
D	A Concept of Local Rounding Applied to a Multi-Surface Plasticity Model with Sharp Edges	83

Nomenclature

Frequently used symbols throughout the report are listed here. Less frequently used or symbols used in a different context are defined where they are used. Matrices and vectors are denoted with upper- and lower-case boldface letters, respectively.

Latin Letters		Greek Letters	
f	Yield criterion	ν	Poisson's ratio
g	Plastic potential	γ	Mass density
e	Void ratio	φ	Static angle of friction
I_d	Relative density	ψ	Angle of dilatation
c	Cohesion	ε, γ	Normal strain and engineering shear strain
k	Friction parameter	σ	Stress
E	Modulus of elasticity	∇	Differential operator
p	Hydrostatic stress	Δ	Increment
\bar{r}	ρ_c -normalized deviatoric radius	$\Delta\lambda$	Plastic multiplier
x, y, z	Cartesian coordinates	μ	Slope of Mohr-Coulomb compressive generator
u, v, w	Displacement components	Ω	Domain (Element area/volume)
i, j	Counter variables	ρ	Stress deviator norm
		θ	Lode angle
		α	Meridional eccentricity parameter
		β	Curvature parameter

Matrices and Vectors		Acronyms	
ε	Strain vector	GPYS	General Parametric Yield Surface
σ	Stress vector	-LD	Linear discontinuous
\mathbf{f}	Load vector	-LC	Linear continuous
\mathbf{u}	Displacement vector	-NC	Nonlinear continuous
\bar{c}^*	ρ_c -normalized deviatoric centre of curvature	d.o.f.	Degrees of freedom
\mathbf{B}	Strain interpolation matrix		
\mathbf{D}	Elastic constitutive matrix		
\mathbf{D}^{ep}	Elasto-plastic constitutive matrix		
\mathbf{D}^{epc}	Consistent elasto-plastic constitutive matrix		
\mathbf{J}	Jacobian matrix		
\mathbf{K}	Stiffness matrix		
\mathbf{N}	Displacement Interpolation matrix		

1 | Introduction

Constitutive modelling of geotechnical materials engages in the design of structures or facilities, which include soil materials as a load-bearing element, such as structural foundations, retaining walls or freestanding slopes. Soil materials is roughly categorised as clays, sand, and rock masses, and often occurs as some combination of these. In this thesis, constitutive modelling of the frictional soil types, namely sands or rock masses, is the main consideration. Frictional soil is composed of macroscopic grains, and the ideal analysis would include the details of each grain in the soil skeleton. However, such a representation would require unrealistic computational power, and the tools from elasto-plastic continuum mechanics has proven a feasible compromise. An elasto-plastic constitutive model is composed of a yield criterion, a plastic potential (or flow rule) and a hardening law. The yield criterion is a limit on the domain of elastic stress states, the flow rule is a model for the plastic strains and the hardening law describes how the yield criterion changes during plastic straining. The latter two are not given much attention in this thesis.

Frictional soil is an anisotropic material with hydrostatic stress dependency, however, often simplified as homogeneous, isotropic and with linear hydrostatic stress dependency. Here, two of the major linear plasticity models in the field of geomechanics, are the Mohr-Coulomb, which dates back to 1773 [Coulomb, 1773] and the Drucker-Prager model [Drucker and Prager, 1951]. Principle stress representation often simplifies the mathematical expressions in plasticity modelling, and enables geometrical arguments, which can be utilised for efficient numerical implementations of elasto-plastic material models, see for instance [Clausen et al., 2005]. In principle stress space, the Mohr-Coulomb yield criterion shapes a hexagonal pyramid and the Drucker-Prager surface as a right circular cone, as depicted in Figure 1.1.

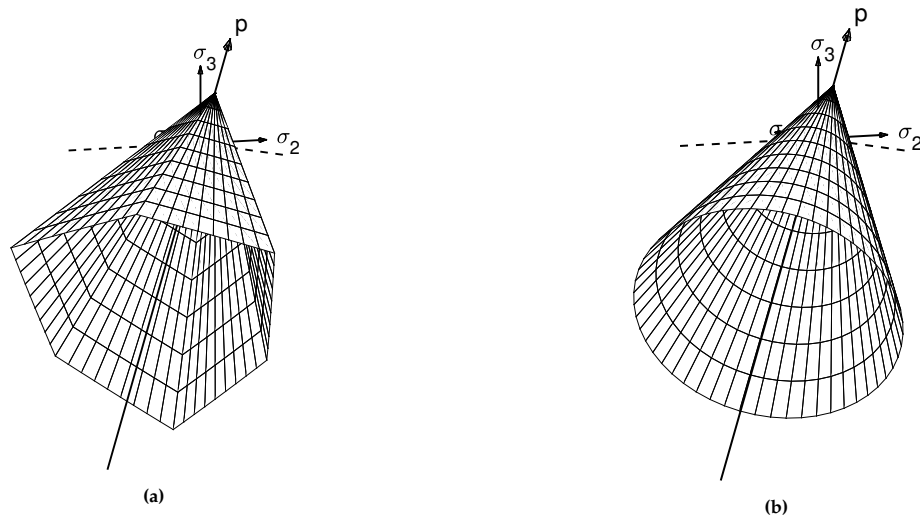


Figure 1.1: Yield surfaces in principle stress space (a) Mohr-Coulomb and (b) Drucker-Prager.

The Mohr-Coulomb and Drucker-Prager yield criteria stands out as two extrema, as the former neglects the intermediate principle stress and all stresses are of equal importance in the latter. The true material behaviour is evidently somewhere in-between, as supported by numerous experimental evidences [Bishop, 1966]. The popularity of the Drucker-Prager model mainly stems from its continuous shape as seen in Figure 1.1b, which renders it efficient and robust in numerical analysis. The Mohr-Coulomb model is in general a better limit stress representation of frictional soil than the Drucker-Prager model, however, not as robust in numerical analysis due to its sharp edges. As the intermediate principle stress is absent in the Mohr-Coulomb criterion, the question remains:

“What is the influence of the intermediate principle stress?”

Some knowledge of the intermediate principle stress influence can be obtained by considering the ϕb -plot in Figure 1.2. It shows the angle of friction with respect to the principle stress ratio, obtained from true triaxial tests performed by [Bønding, 1977]. The typical laboratory tests of soil materials is the standard cylindrical triaxial compression test, $b = 0$, where the intermediate principle stress cannot be analysed. However, as the more advanced true triaxial tests has been performed by researchers, it is found that the

lowest angle of friction is measured under triaxial compression, see for instance [Lade, 1977], [Bønding, 1977], [Reddy and Saxena, 1993], [Praagstrup, 2000], or [Wang and Lade, 2001]. Sands of different relative densities are considered in Figure 1.2, and the dependency on the principle stress ratio is in general more pronounced for dense sands. This is a general tendency, however, varies with different types of sand see for instance [Lade, 2006]. Yield surfaces to better describe the actual material behaviour has been proposed in plenty, see for instance [Matsuoka and Nakai, 1974], [Lade, 1977], [Hoek and Brown, 1980] to mention a few. Such models may be more accurate, however, the majority of the more complex criteria have failed to gain commercial use. An elaboration on some of these models are given in Chapter 3.

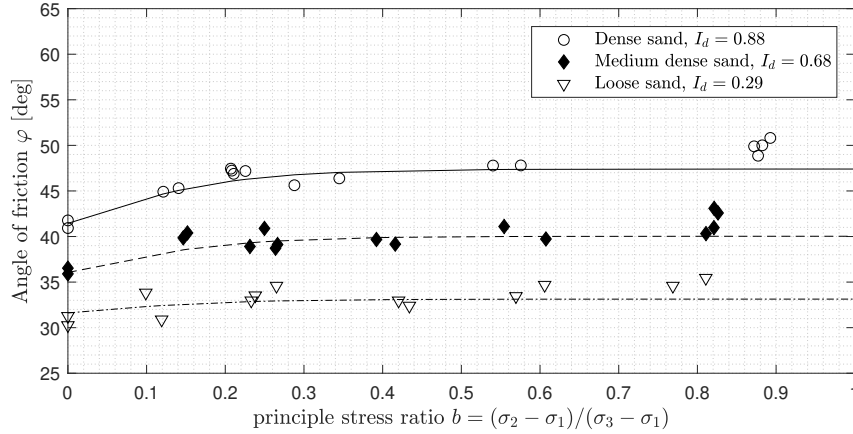


Figure 1.2: ϕb -plot of data from true triaxial tests performed by [Bønding, 1977], see Appendix A.1. The approximation lines are generated with $\phi = \phi_{tr}(1 + 0.163 \tanh(5b))$ as proposed by S. Krabbenhøft, for $\phi_{tr} = 41.40$, $\phi_{tr} = 36.00$ and $\phi_{tr} = 31.60$, respectively, included for illustrative purposes.

In conventional geotechnical calculations, an angle of friction and an internal cohesion are used to define the linear Mohr-Coulomb failure envelope as sketched in Figure 1.3a, first brought forth by [Coulomb, 1773], and later generalized by Mohr in 1883, see for instance [Ottosen and Ristinmaa, 2005, sec. 8.5]. This early linearisation has to some extent become the assumption of the actual material behaviour outside the world of academia. However, most frictional materials does not obey to a linear failure envelope, and more accurate material models operates with a secant, or an instantaneous angle of friction, as illustrated in Figure 1.3b. A widely accepted model which expresses the angle of friction as a function of the dilatancy, relative density and the hydrostatic stress level, was proposed by [Bolton, 1986]. Both the Mohr-Coulomb and Bolton failure criteria are elaborated in this thesis, and enters the formulations of the proposed yield surface concept in chapter 4.

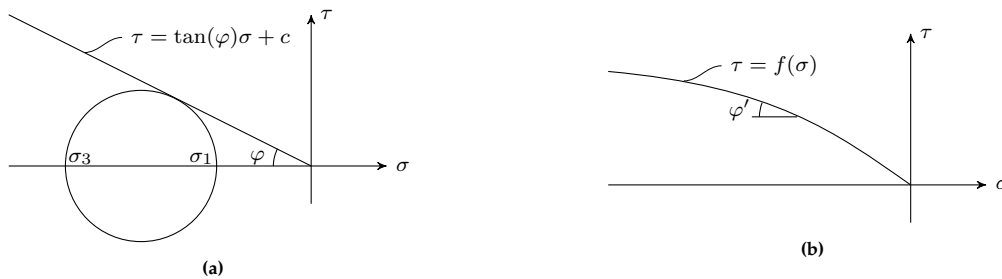


Figure 1.3: Failure envelopes in Mohr diagrams for (a) the linear Coulomb failure criterion and (b) the general nonlinear Mohr failure criterion.

From the early days in geotechnical engineering, some problems have been solved with empirical solutions, and some of a certain simplicity have been solved with analytical mathematics. In the past few decades, the finite element method has been implemented as a powerful tool in the engineering industry as computer technology has advanced. Limit loads of geomechanical systems can efficiently be found by use of upper and lower bound analysis in finite element context, as available in for instance the “Optum” software [Krabbenhøft et al., 2016c]. However, elasto-plastic analysis is a more general approach, and is conducted if the deformation under load is desired, or if response history affects the solution in for instance soil-structure interaction. The finite element method is a general mathematical method, which

enables the implementation of advanced material models in analysis. Other numerical tools, such as the finite difference method, is frequently used in geomechanics as well, see for instance [Martin, 2003]. Some more advanced methods for numerical analysis of soils are gaining ground in academia, for instance the particle finite element method see for instance [Zhang, 2014], which may be more suited for slip line or erosion problems etc. The latter two methods are not explored further in this thesis, as solely the finite element method is used. However, the constitutive models are not restricted to this method.

Project specification

The scope of this thesis is to investigate the intermediate principle stress influence for frictional soil, through numerical studies. For this purpose, a new yield surface concept, as proposed by professor Lars Damkilde, denoted the General Parametric Yield Surface (GPYS) Format, is explored. It can parametrically include the intermediate principle stress and are developed to encompass several of the existing models, and optimized material utilisation. A second topic in this thesis is the computational performance of multi-surface plasticity models, and a total of three new yield criteria are formulated based on the GPYS format. Prior to the numerical analyses, the proposed constitutive models are implemented in both a MATLAB and Fortran code as a user-defined subroutine for use with the the Abaqus software, intended for commercial use.

Several material specific constitutive models have been proposed, however, failed to gain a widespread use in the geotechnical community. Therefore, it is intended to formulate a yield surface, which encompasses some of the numerous existing models, at least their overall characteristics, whilst maintaining simplicity and familiarity in the parameters. The first proposed yield surface operates on four parameters, two of which are the well-known parameters of the Mohr-Coulomb model. It is intended as a general model, which in a simple manner can be used as the familiar Mohr-Coulomb or Drucker Prager model, whilst being capable of more advanced material calibrations as well. The implementation in numerical analysis of this model is efficient, however, the surface discontinuities leads to poor convergence. Therefore, the second proposed yield surface is a smooth continuous approximation of the first model, for improved robustness. It is based on a new concept of corner rounding, which mainly exploits vector calculus, opposed to trigonometric functions as the methods in the existing literature. Furthermore, it enables an even more advanced material calibration, with the optionality of a smooth tension cut-off. The third proposed yield surface is based on Bolton's formula, to accommodate nonlinear hydrostatic stress dependency. The result is an advanced nonlinear model, which operates on the well-known parameters from Bolton, and constitutes the most optimized material calibration conducted in this thesis. The model includes a smooth continuous tension cut-off as well, and it demonstrates the generality of the new yield surface concept. The first two plasticity models presented in this thesis are submitted for peer review in technical journals as well, these papers are attached in Appendices C and D.

Throughout this thesis, linearly elastic perfectly plastic material behaviour and associated flow is assumed, which does not compromise the appeal to the civil engineering practices, where these are common assumptions. The novel plasticity models are, however, not restricted to these assumptions and the mathematical expressions are given in a non-associated format for generality. The analyses are conducted to investigate the influence of optimised material fits, and the results are not design values as no statistical safety are incorporated etc. The set of experimental data, used in the studies, is naturally not transferable to other grading's and material types. The finite element analysis are conducted both in a program written by the authors in MATLAB script, and some are conducted in the Abaqus software through a user-defined subroutine with the novel constitutive model. The plasticity models are not restricted to soils, however, this is the sole group of materials analysed in this project.

2 | Methodology

Some of the fundamentals of continuum mechanics and the mathematical theory of plasticity are presented in this section. This includes a review of some stress invariants, followed by elasto-plastic constitutive modelling and some specifics towards the finite element method.

The materials considered in this thesis are assumed to act as linear elastic perfectly plastic. The principle of the stress strain relation under this assumption is sketched in Figure 2.1. The stress strain relation in the elastic stress range is linear and when a certain level of stress causes yielding, it cannot be exceeded, and additional strains are irreversible. Figure 2.1 is, however, a simple one-dimensional case, and elastic strains can occur during plastic loading in general 3D conditions. Soil is sometimes modelled with nonlinear elastic response, for instance by the elasticity modulus proposed by [Lade, 1977], however, the assumption of linear elasticity mainly affects the displacement results.

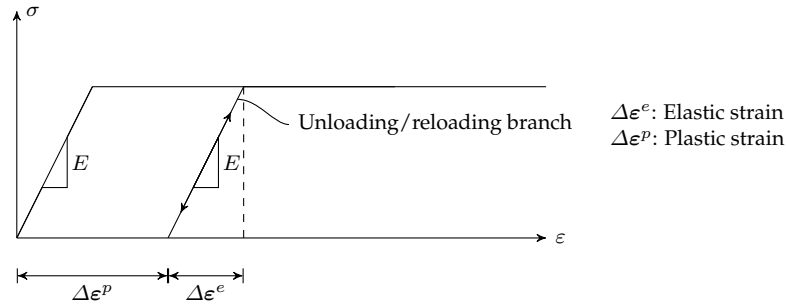


Figure 2.1: One-dimensional linearly elastic perfectly plastic stress strain curve.

2.1 Stress Invariants and Their Geometrical Interpretations

As a preliminary consideration in formulating and understanding the yield criteria discussed in subsequent sections, some of the important stress invariants and their geometrical interpretations are presented in this section. It can be shown that there exists a unique coordinate system, where the shear stresses are zero and the normal stresses are referred to as principal stresses. These are conveniently found from the symmetric eigenvalue problem of the stress matrix, see for instance [Ottosen and Ristinmaa, 2005, sec. 3.3],

$$([\sigma] - \lambda_i \mathbf{I}_3) \mathbf{v}_i = \mathbf{0}, \quad [\sigma] = \begin{bmatrix} \sigma_{11} & \sigma_{12} & \sigma_{13} \\ \sigma_{21} & \sigma_{22} & \sigma_{23} \\ \sigma_{31} & \sigma_{23} & \sigma_{33} \end{bmatrix}, \quad (2.1)$$

where the eigenvalues, λ_i , as mentioned yields the principal stresses, and the eigenvectors, \mathbf{v}_i , contains the direction cosines with the principal axis as

$$\mathbf{v}_i = \begin{Bmatrix} l_i \\ m_i \\ n_i \end{Bmatrix}.$$

The direction cosines between the reference coordinate system, xyz , and the local coordinate system, $x'y'z'$, can be used to establish the following transformation matrix, see fore instance [Cook et al., 2002, p. 274]

$$\mathbf{T}_\varepsilon = \begin{bmatrix} l_1^2 & m_1^2 & n_1^2 & l_1 m_1 & m_1 n_1 & n_1 l_1 \\ l_2^2 & m_2^2 & n_2^2 & l_2 m_2 & m_2 n_2 & n_2 l_2 \\ l_3^2 & m_3^2 & n_3^2 & l_3 m_3 & m_3 n_3 & n_3 l_3 \\ 2l_1 l_2 & 2m_1 m_2 & 2n_1 n_2 & l_1 m_2 + l_2 m_1 & m_1 n_2 + m_2 n_1 & n_1 l_2 + n_2 l_1 \\ 2l_2 l_3 & 2m_2 m_3 & 2n_2 n_3 & l_2 m_3 + l_3 m_2 & m_2 n_3 + m_3 n_2 & n_2 l_3 + n_3 l_2 \\ 2l_3 l_1 & 2m_3 m_1 & 2n_3 n_1 & l_3 m_1 + l_1 m_3 & m_3 n_1 + m_1 n_3 & n_3 l_1 + n_1 l_3 \end{bmatrix}, \quad (2.2)$$

where, l_i , m_i , and n_i , are direction cosines as illustrated in Figure 2.2. The following ordering of the stress and strain components are assumed by Equation (2.2)

$$\boldsymbol{\sigma} = [\sigma_{xx}; \sigma_{yy}; \sigma_{zz}; \tau_{xy}; \tau_{yz}; \tau_{xz}]^T.$$

The stresses, strains and the constitutive matrix can be transformed by the relations,

$$\boldsymbol{\varepsilon}' = \mathbf{T}_\varepsilon \boldsymbol{\varepsilon} \quad \wedge \quad \boldsymbol{\sigma}' = \mathbf{T}_\varepsilon^{-T} \boldsymbol{\sigma} \quad \wedge \quad \mathbf{D}' = \mathbf{T}_\varepsilon^T \mathbf{D} \mathbf{T}_\varepsilon,$$

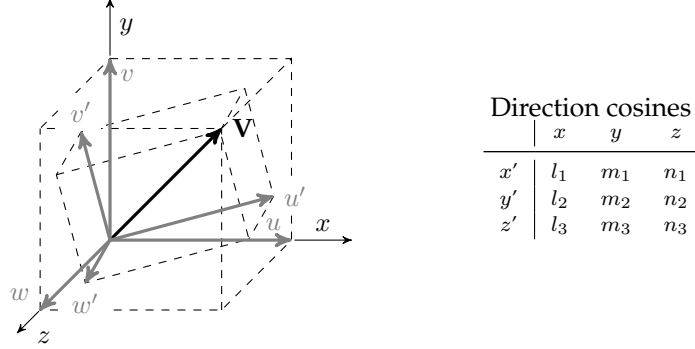


Figure 2.2: Illustration of the local and global components for describing the same vector \mathbf{V} , inspired by [Cook et al., 2002, p. 272].

The principal stresses, obtained from Equation (2.1) are invariants, and the general 6D stress state in xyz -space can be visualized as a point in the 3D principle stress space, enabling spatial geometry. To further exploit the geometrical interpretations, the stress matrix is conveniently decomposed into a deviator and a hydrostatic component as

$$\begin{bmatrix} \sigma_{11} & \sigma_{12} & \sigma_{13} \\ \sigma_{21} & \sigma_{22} & \sigma_{23} \\ \sigma_{31} & \sigma_{32} & \sigma_{33} \end{bmatrix} = \begin{bmatrix} s_{11} & s_{12} & s_{13} \\ s_{21} & s_{22} & s_{23} \\ s_{31} & s_{32} & s_{33} \end{bmatrix} + \begin{bmatrix} p & 0 & 0 \\ 0 & p & 0 \\ 0 & 0 & p \end{bmatrix},$$

where the hydrostatic stress, p , which also is an invariant, is given as

$$p = \frac{1}{3}(\sigma_{11} + \sigma_{22} + \sigma_{33}).$$

The decomposition of the stress state into a deviatoric and a hydrostatic part in principle stress space can conveniently be formulated as vector equation as

$$\begin{Bmatrix} \sigma_1 \\ \sigma_2 \\ \sigma_3 \end{Bmatrix} = \mathbf{p} + \mathbf{s} = \begin{Bmatrix} p \\ p \\ p \end{Bmatrix} + \begin{Bmatrix} s_1 \\ s_2 \\ s_3 \end{Bmatrix}, \quad (2.3)$$

as the deviatoric shear strains is definitively zero in principle stress space. Further stress invariants used in this thesis, in tensor notation,

$$\begin{aligned} I_1 &= \sigma_{ii} && \text{First invariant of the stress tensor} \\ I_2 &= \sigma_{ij}\sigma_{ji} && \text{Second invariant of the stress tensor} \\ I_3 &= \sigma_{ij}\sigma_{jk}\sigma_{ki} && \text{Third invariant of the stress tensor} \\ J_2 &= 1/2 s_{ij}s_{ji} && \text{Second invariant of the stress deviator} \\ J_3 &= 1/3 s_{ij}s_{jk}s_{ki} && \text{Third invariant of the stress deviator.} \end{aligned} \quad (2.4)$$

It is often advantageous to adopt the cylindrical Haigh-Westergaard coordinate system denoted $\xi\rho\theta$ in the principal stress space, as depicted in Figure 2.3. The normal vector along the space diagonal are given as, $\mathbf{n} = 1/\sqrt{3} [1; 1; 1]$, and the line defined by this vector is referred to as the hydrostatic axis, as $\sigma_1 = \sigma_2 = \sigma_3$ for all points on the line. The cylindrical coordinates are related to the stress invariants as, see for instance [Ottosen and Ristinmaa, 2005, sec 8.1]

$$\xi = \frac{I_1}{\sqrt{3}}, \quad \rho = \sqrt{2J_2}, \quad \cos 3\theta = \frac{3\sqrt{3}}{2} \frac{J_3}{J_2^{3/2}} \quad (2.5)$$

The principle stresses are recovered from the Haigh-Westergaard coordinates by the relation

$$\boldsymbol{\sigma}(\xi, \rho, \theta) = \frac{\xi}{\sqrt{3}} \begin{Bmatrix} 1 \\ 1 \\ 1 \end{Bmatrix} + \sqrt{2/3} \rho \begin{Bmatrix} \cos \theta \\ \cos 2\pi/3 - \theta \\ \cos 2\pi/3 + \theta \end{Bmatrix}. \quad (2.6)$$

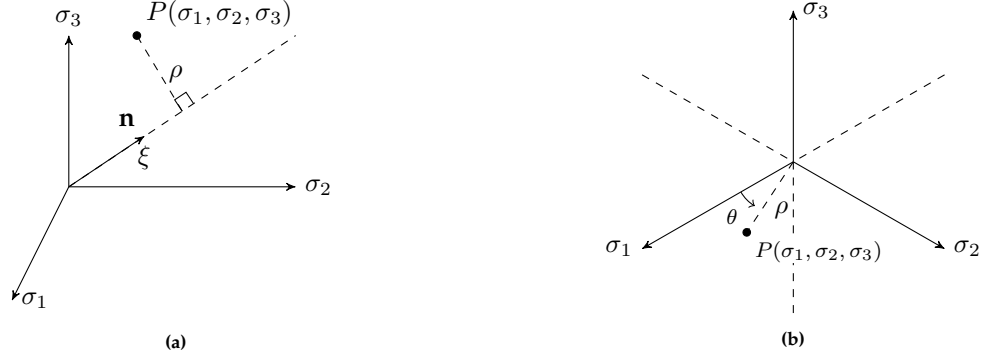


Figure 2.3: Illustration of cylindrical coordinates for a stress state in principal stress space (a) sideview of space diagonal and (b) view in the deviatoric plane.

2.2 The Yield Criterion and the Plastic Potential

In this sections, some of the fundamental assumptions for performing elasto-plastic analysis is presented. The term elasto-plastic, refers to the mechanism that a strain state is considered as composed of purely elastic and plastic components. A yield criterion, a plastic potential and a hardening law are usually adopted to model such material behaviour. Hardening of the material is not considered in this thesis and perfect plasticity is assumed in all the analysis. Therefore, the yield criterion and the plastic potential are introduced in this section. To evaluate whether plastic strains occur in a material point, a yield criterion, which fits the behaviour of the material, is needed. The yield criterion, f , is a function of the stresses and some strength parameters of the material, which defines the state as

$$\begin{aligned} f(\boldsymbol{\sigma}, \boldsymbol{\alpha}) &< 0 && \text{Elastic stress state,} \\ f(\boldsymbol{\sigma}, \boldsymbol{\alpha}) &= 0 && \text{Plastic stress state,} \\ f(\boldsymbol{\sigma}, \boldsymbol{\alpha}) &> 0 && \text{Inadmissible stress state,} \end{aligned} \quad (2.7)$$

where $\boldsymbol{\alpha}$ represents material parameters. The yield criterion can be depicted as a hypersurface in principle stress space, representing the failure surface when $f = 0$, and is often conveniently formulated through stress invariants. The yield criterion itself is an invariant as well, as it must yield the same value regardless of the coordinate system orientation. For isotropic materials, the trace in the deviatoric plane is of six-fold symmetry in the Lode angles $\theta = \{0, \pi/3, 2\pi/3, \pi/3, 4\pi/3, 5\pi/3\}$, as indicated in the sketch in Figure 2.4. For a thorough discussion on the yield criterion, see for instance [Ottosen and Ristinmaa, 2005]. As a note to isotropy, the behaviour of frictional soils may be more accurately presented by a cross-anisotropic model, see for instance [Praagstrup, 2000].

In nonlinear analysis, an incremental approach is used to accommodate nonlinearities. When a strain increment results in material yielding, and plastic strains occur, There is no longer a unique relation between the stress and strain increments. The strain increment is decomposed in a purely elastic and a purely plastic component as

$$d\boldsymbol{\varepsilon} = d\boldsymbol{\varepsilon}^e + d\boldsymbol{\varepsilon}^p. \quad (2.8)$$

The elastic part of the strain increment obeys Hooke's law, and the plastic part is described by the flow rule

$$d\boldsymbol{\varepsilon}^p = d\lambda \nabla g, \quad \nabla g = \frac{\partial g}{\partial \boldsymbol{\sigma}},$$

where, $d\lambda$, is called the plastic multiplier, and, g , is a scalar function called the plastic potential. As plastic strains are irreversible, the plastic multiplier is restricted to $d\lambda > 0$. In geomechanics, the dilative

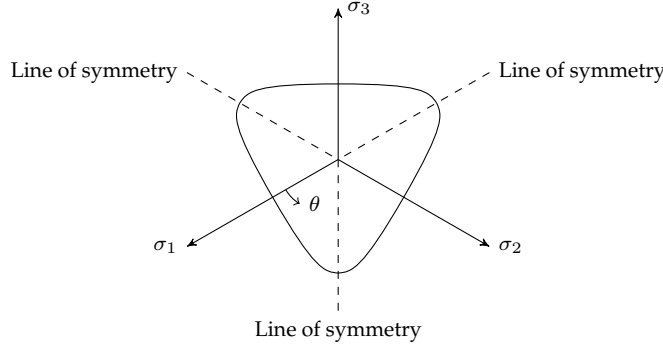


Figure 2.4: The deviatoric trace of some yield surface for an isotropic material.

behaviour of the material is a fundamental issue, that is, the change in volume during plastic straining. The plastic potential function dictates the dilative behaviour as the direction of plastic strain increments are derived by its gradient. In granular materials, the dilatation is often described by the angle of dilatation, ψ , which gives the inclination of the plastic potential with respect to volumetric strains. In soils, the angle of dilatation is typically well below the angle of friction, for instance $\psi \approx \varphi - 30$, however, associated flow, $\varphi = \psi$, is often assumed. The principle of the yield criterion (2.7) and associated and non-associated plasticity is sketched in Figure 2.5. A plastic potential with a significantly smaller inclination with the hydrostatic axis as sketched in Figure 2.5b is typical for soil materials.

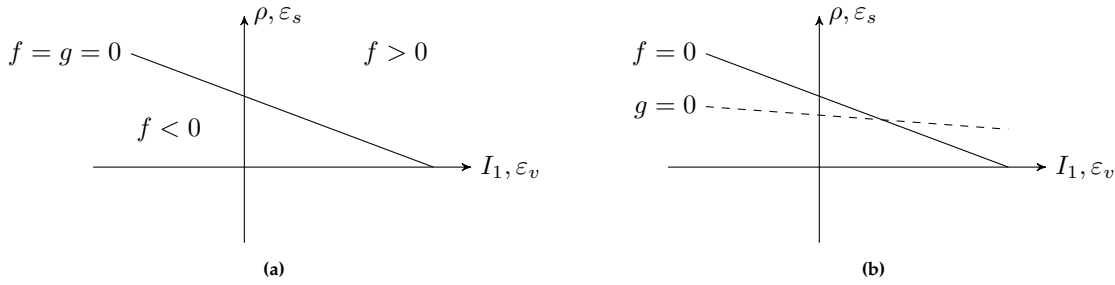


Figure 2.5: Yield surface and plastic potential meridians (a) associated plasticity $f = g$ and (b) non-associated plasticity $f \neq g$.

The angle of dilatation is zero during the ideal shear failure of frictional soils, which means, no volumetric straining during pure shear failure. As mentioned, the numerical analysis of non-associated materials, often fails due to numerical instability, to which a solution has been proposed, see for instance [Krabbenhoft et al., 2012]. To analyse non-associated materials, with an associated flow rule, the following modification of shear strength parameters was argued by [Davis et al., 1968]

$$\begin{aligned}\varphi_{ass} &= \frac{\cos \psi \sin \varphi}{1 - \sin \psi \sin \varphi}, \\ c_{ass} &= \frac{c \cos \psi \cos \varphi}{1 - \sin \psi \cos \varphi},\end{aligned}\quad (2.9)$$

where, φ , ψ and c , are the internal angle of friction, angle of dilatation and cohesion, respectively. The plastic potential surface must be convex as a direct consequence of positive plastic work. Therefore, as associated plasticity is considered in this thesis, the yield surface is restricted to convex shapes.

2.3 Elasto-Plastic Finite Element Analysis

In this section the overall tasks in an elasto-plastic finite element analysis is described. A linear quasi static finite element analysis solves the well known system of equations

$$\mathbf{K}\mathbf{u} = \mathbf{f},$$

where the force vector can be composed of various types of forces. In this thesis, these are body forces from the gravitational pull, the consistent nodal forces from surface traction and concentrated loads, which are given respectively by the expressions

$$\mathbf{f}_{\text{body}} = \int_{\Omega} \mathbf{N}^T \mathbf{b} \, d\Omega, \quad \mathbf{f}_c = \int_{\Omega} \mathbf{N}^T q \, d\Omega, \quad \mathbf{f}_n = \mathbf{N}^T P,$$

where, \mathbf{N} , \mathbf{b} , q , and P is the field interpolation matrix, the body force vector, a surface traction and a point force, respectively. The stiffness matrix \mathbf{K} is assembled in the usual manner by the element stiffness matrices, which are calculated with the integral

$$\mathbf{K}_{\text{element}} = \int_{\Omega} \mathbf{B}^T \mathbf{D} \mathbf{B} \, d\Omega, \quad (2.10)$$

where, \mathbf{B} and \mathbf{D} , is the strain interpolation matrix and the constitutive matrix, respectively. The stiffness matrix becomes non-linear when a material point in the element is subjected to yielding, as the constitutive matrix, \mathbf{D} , evidently changes. The Newton-Raphson scheme for conducting nonlinear finite element analysis, is described in the following. The approach in solving the nonlinear system equations is to increment the load, to obtain a displacement increment

$$\mathbf{K}_t \Delta \mathbf{u} = \Delta \mathbf{f}. \quad (2.11)$$

Index t on the system stiffness matrix indicates a tangent system matrix. The stresses in the system due to the displacement increment are then integrated to obtain a vector of internal forces. The internal forces in an element is found by [Cook et al., 2002, p. 412]

$$\mathbf{q} = \int_{\Omega} \mathbf{B}^T \boldsymbol{\sigma} \, d\Omega. \quad (2.12)$$

Equilibrium requires the external and internal forces to equate. however this will not be true with nonlinearities present, so a residual is calculated instead

$$\mathbf{r} = \mathbf{f} - \mathbf{q},$$

where, \mathbf{r} , is the global residual force vector. The global residual force vector is then used to calculate a correction in the displacement increment as

$$\mathbf{K}_t \delta \mathbf{u} = \mathbf{r}.$$

The displacement increment, $\Delta \mathbf{u}$, is then adjusted with, $\delta \mathbf{u}$. This procedure is continued until the residual becomes sufficiently small, and another global load increment is then added, see Table 2.1 for the full schematics of the Newton-Raphson procedure. Initial stresses and gravitational forces are calculated and checked for equilibrium prior to the Newton-Raphson algorithm, as it is a typical step in geotechnical analysis.

Table 2.1: Schematics of the Newton Raphson algorithm for nonlinear elasto-plastic finite element analysis.

Initialize, $\mathbf{u}_0 = \mathbf{0}$, $\mathbf{f}_0 = \mathbf{0}$ and $\mathbf{K}_{t,i}$.
Calculate \mathbf{f}_{body} , initial stresses, $\boldsymbol{\sigma}_1^0$ and ensure equilibrium, $\mathbf{f}_{\text{body}} - \mathbf{q}(\boldsymbol{\sigma}_1^0) = \mathbf{0}$
Global incrementation: $i = 1, 2, \dots$, number of loadsteps
$\Delta \mathbf{u}_i^1 = \mathbf{K}_t^{-1} \Delta \mathbf{f}_i$
Inner iterations: $j = 1, 2, \dots$
For all integration points, $\boldsymbol{\sigma}_i^j = \boldsymbol{\sigma}_i^{j-1} + \mathbf{D}_i^j \mathbf{B} \Delta \mathbf{u}_i^j$.
Check yield condition. If $f(\boldsymbol{\sigma}_i^j) \geq 0$, update $\boldsymbol{\sigma}_i^j$ and \mathbf{D}_i^j , in return algorithm subroutine.
Update tangent stiffness matrix, $\mathbf{K}_{t,i+1}^j = \mathbf{K}(\mathbf{D}_i^j)$.
Calculate residual, $\mathbf{r}^j = \mathbf{f}_{\text{body}} + \mathbf{f}_{i-1} + \Delta \mathbf{f} - \mathbf{q}(\boldsymbol{\sigma}_i^j)$.
Calculate displacement adjustment, $\delta \mathbf{u}^j = (\mathbf{K}_{t,i+1}^j)^{-1} \mathbf{r}^j$
Update displacement increment, $\Delta \mathbf{u}^j = \Delta \mathbf{u}^{j-1} + \delta \mathbf{u}^j$
End iterations when $\ \mathbf{r}^j\ < TOL \ \mathbf{f}_{i-1} + \Delta \mathbf{f}\ $
$\mathbf{u}_i = \mathbf{u}_{i-1} + \Delta \mathbf{u}^j$
$\mathbf{f}_i = \mathbf{f}_{i-1} + \Delta \mathbf{f}$
End of loadstep

One of the main tasks in the algorithm presented in Table 2.1 is to update the stresses and constitutive matrices at the Gauss integration points in all elements. This is done according to the procedures described in Sections 2.5 and 2.4, and in thorough detail for the proposed yield surface models in Appendix C and D. It can be advantageous for the convergence rate of the analysis to apply a forced displacement instead of an external load. This can easily be implemented by defining a forced displacement in a number of nodes and separating those from the unknown displacements as

$$\mathbf{K}_t(\mathbf{u}_{\text{unknown}} + \mathbf{u}_{\text{known}}) = \mathbf{f}_{\text{ext}} \quad \Leftrightarrow \quad \mathbf{K}_t \mathbf{u}_{\text{unknown}} = \mathbf{f}_{\text{ext}} - \mathbf{K}_t \mathbf{u}_{\text{known}}.$$

Thereby, the load increment, $\Delta \mathbf{f}$, depends on the stiffness of the finite element domain, \mathbf{K}_t , and naturally drops in magnitude, as the extend of plastic strains increase in the model. A task for the analyst is to determine the tolerance for accepting convergence, TOL . A decent value for this, is for instance $TOL = 5 \cdot 10^{-3}$, which is the default setting in Abaqus.

2.4 Elasto-Plastic Stress Strain Relation

In all the analysis conducted in this thesis, the materials are assumed to act homogeneous and isotropic. The linear elastic stress strain relation is given as, see for instance [Ottosen and Ristinmaa, 2005, sec. 4.6]

$$\boldsymbol{\sigma} = \mathbf{D}\boldsymbol{\varepsilon}$$

$$\begin{Bmatrix} \sigma_{xx} \\ \sigma_{yy} \\ \sigma_{zz} \\ \sigma_{xy} \\ \sigma_{yz} \\ \sigma_{zx} \end{Bmatrix} = \frac{E}{(1+\nu)(1-2\nu)} \begin{bmatrix} 1-\nu & \nu & \nu & 0 & 0 & 0 \\ \nu & 1-\nu & \nu & 0 & 0 & 0 \\ \nu & \nu & 1-\nu & 0 & 0 & 0 \\ 0 & 0 & 0 & \frac{1}{2}(1-2\nu) & 0 & 0 \\ 0 & 0 & 0 & 0 & \frac{1}{2}(1-2\nu) & 0 \\ 0 & 0 & 0 & 0 & 0 & \frac{1}{2}(1-2\nu) \end{bmatrix} \begin{Bmatrix} \varepsilon_{xx} \\ \varepsilon_{yy} \\ \varepsilon_{zz} \\ \gamma_{xy} \\ \gamma_{yz} \\ \gamma_{zx} \end{Bmatrix}, \quad (2.13)$$

where, ν , and E , are Poisson's ratio and the modulus of elasticity, respectively. In geomechanics, the mechanical systems under consideration can often be simplified from general 3D to either plain strain or axis symmetric conditions. In plain strain conditions, the model is considered planar, and the out of plain displacements are zero $\varepsilon_{zz} = \gamma_{yz} = \gamma_{zx} = 0$, and the stress strain relation is reduced to

$$\begin{Bmatrix} \sigma_{xx} \\ \sigma_{yy} \\ \sigma_{zz} \\ \sigma_{xy} \end{Bmatrix} = \frac{E}{(1+\nu)(1-2\nu)} \begin{bmatrix} 1-\nu & \nu & \nu & 0 \\ \nu & 1-\nu & \nu & 0 \\ \nu & \nu & 1-\nu & 0 \\ 0 & 0 & 0 & \frac{1}{2}(1-2\nu) \end{bmatrix} \begin{Bmatrix} \varepsilon_{xx} \\ \varepsilon_{yy} \\ \varepsilon_{zz} \\ \gamma_{xy} \end{Bmatrix}.$$

The strain interpolation matrix, as described in Appendix A.3, ensures $\varepsilon_{zz} = 0$, in the analysis. When yielding occurs in a material point, Hooke's law of Equation (2.13) is no longer applicable, and a relation between increments in stresses and strains are needed. A relation for the yield criterion with an infinitesimal stress increment is given as

$$f(\boldsymbol{\sigma} + d\boldsymbol{\sigma}) = f(\boldsymbol{\sigma}) + (\nabla f)^T d\boldsymbol{\sigma} = 0, \quad \nabla f = \frac{\partial f}{\partial \boldsymbol{\sigma}}.$$

As $f(\boldsymbol{\sigma}) = 0$ the second term is zero as well, this is referred to as the consistency condition

$$(\nabla f)^T d\boldsymbol{\sigma} = 0 \quad (2.14)$$

An infinitesimal stress increment during plastic loading can be expressed by Hooke's law and the flow rule as

$$d\boldsymbol{\sigma} = \mathbf{D}d\boldsymbol{\varepsilon}^e = \mathbf{D}(d\boldsymbol{\varepsilon} - d\lambda \nabla g) = \mathbf{D}(d\boldsymbol{\varepsilon} - d\lambda \nabla g). \quad (2.15)$$

Substituting Equation (2.15) into (2.14) and isolating the plastic multiplier yields

$$(\nabla f)^T (\mathbf{D}(d\boldsymbol{\varepsilon} - d\lambda \nabla g)) = 0 \quad \Leftrightarrow \quad d\lambda = \frac{(\nabla f)^T \mathbf{D}d\boldsymbol{\varepsilon}}{(\nabla f)^T \mathbf{D}\nabla g}. \quad (2.16)$$

The plastic multiplier inserted in (2.15) yields the elasto-plastic constitutive matrix, which relates infinitesimal stress and strain increments during plastic loading,

$$d\boldsymbol{\sigma} = \mathbf{D}^{ep} d\boldsymbol{\varepsilon} = \left(\mathbf{D} - \frac{\mathbf{D} \nabla g (\nabla f)^T \mathbf{D}}{(\nabla f)^T \mathbf{D} \nabla g} \right) d\boldsymbol{\varepsilon}, \quad (2.17)$$

which was first derived by [O. C. Zienkiewicz and King, 1969]. The elasto-plastic constitutive matrix does not conform with a finite increment analysis as conducted in a numerical framework, and leads to poor convergence rate if in the nonlinear finite element analysis. It is therefore modified to relate changes in finite increments as

$$d(\Delta\boldsymbol{\sigma}) = \mathbf{D}^{epc} d(\Delta\boldsymbol{\varepsilon}),$$

where, epc , denotes a consistent elasto-plastic quantity. To arrive at an expression for \mathbf{D}^{epc} , the stress update algorithm from Equation (2.21) is considered as

$$\mathbf{p} = -\Delta\boldsymbol{\sigma} + \mathbf{D}\Delta\boldsymbol{\varepsilon} - \Delta\lambda \mathbf{D} \nabla g = 0,$$

which is merely a finite increment formulation of Equation (2.15). Differentiation of \mathbf{p} gives,

$$\begin{aligned} d(\mathbf{p}) &= \left(\frac{\partial \mathbf{p}}{\partial \Delta\boldsymbol{\varepsilon}} \right)^T d(\Delta\boldsymbol{\varepsilon}) + \left(\frac{\partial \mathbf{p}}{\partial \Delta\boldsymbol{\sigma}} \right)^T d(\Delta\boldsymbol{\sigma}) + \left(\frac{\partial \mathbf{p}}{\partial \Delta\lambda} \right)^T d(\Delta\lambda) \\ &= \hat{\mathbf{D}} d(\Delta\boldsymbol{\varepsilon}) - \left(\mathbf{I} + \Delta\lambda \hat{\mathbf{D}} \nabla^2 g \right) d(\Delta\boldsymbol{\sigma}) - d(\Delta\lambda) \hat{\mathbf{D}} \nabla g = 0. \end{aligned}$$

Rearranging yields the relation between changes in finite stress and strain increments as

$$d(\Delta\boldsymbol{\sigma}) = (\mathbf{I} + \Delta\lambda \mathbf{D} \nabla^2 g)^{-1} \mathbf{D} (d(\Delta\boldsymbol{\varepsilon}) - d(\Delta\lambda) \nabla g) = \mathbf{D}^c d(\Delta\boldsymbol{\varepsilon}^e),$$

where the consistent constitutive matrix, \mathbf{D}^c , has been introduced. Insertion in Equation (2.17) yields the consistent tangent as

$$\mathbf{D}^{epc} = \mathbf{D}^c - \frac{\mathbf{D}^c \nabla g (\nabla f)^T \mathbf{D}^c}{(\nabla f)^T \mathbf{D}^c \nabla g}, \quad \mathbf{D}^c = (\mathbf{I} + \Delta\lambda \mathbf{D} \nabla^2 g)^{-1} \mathbf{D}. \quad (2.18)$$

This expression was first derived by [Simo and Taylor, 1984] and is described in the majority of literature on the subject since. Some further considerations of the consistent elasto-plastic constitutive matrix are made at singularities with multi-surface plasticity models, as described thoroughly in Appendix C.

2.5 Stress Update by Return Mapping

When a material point in the finite element model reaches a plastic stress state, Hooke's law no longer applies as a unique relation between stress and strain increments. Therefore, the stress increment needs to be calculated by other means. In this thesis, a conventional return mapping scheme is utilised for this purpose, see for instance [de Borst et al., 2012] for a thorough elaboration on this. All the calculations are carried out in principal stress representation, which enables geometrical arguments and interpretations of the steps in the return mapping algorithm.

Assuming the complete decomposition of strains into elastic and plastic components, gives an infinitesimal stress increment according to Hooke's law as

$$d\boldsymbol{\sigma} = \mathbf{D} d\boldsymbol{\varepsilon}^e = \mathbf{D} (d\boldsymbol{\varepsilon} - d\boldsymbol{\varepsilon}^p). \quad (2.19)$$

Integration over a finite increment yields

$$\Delta\boldsymbol{\sigma} = \Delta\boldsymbol{\sigma}^e - \Delta\boldsymbol{\sigma}^p = \mathbf{D} \boldsymbol{\varepsilon} - \int_{\lambda}^{\lambda+\Delta\lambda} \mathbf{D} \nabla g d\lambda, \quad (2.20)$$

where, $\Delta\boldsymbol{\sigma}^e$, is referred to as the elastic predictor, and, $\Delta\boldsymbol{\sigma}^p$, the plastic corrector. As the return path is unknown, the integral for the plastic corrector is approximated as a linear incrementation, where the gradient of the potential function is evaluated at the return point on the yield surface as

$$\Delta\boldsymbol{\sigma}^p \simeq \Delta\lambda \mathbf{D} \nabla g(\boldsymbol{\sigma}_C),$$

where subscript C denotes the return point on the yield surface, as indicated in the sketch in Figure 2.6. Inserting in Equation (2.20) and employing the yield criterion as an additional constrained equation yields the system of equations to be solved in the implicit return mapping scheme as

$$\begin{aligned}\sigma_C &= \sigma_B - \Delta\lambda \mathbf{D} \nabla g(\sigma_C) \\ f(\sigma_C) &= 0\end{aligned}\quad (2.21)$$

Utilising the expression for the plastic multiplier in Equation (2.16), and the notation from Figure 2.6, the plastic corrector is given as

$$\Delta\sigma^p = \Delta\lambda \mathbf{D} \nabla g(\sigma_C) = \frac{f(\sigma_B) \mathbf{D} \nabla g(\sigma_C)}{\nabla g_C^T \mathbf{D} \nabla f(\sigma_C)} = \sigma_B - \sigma_C. \quad (2.22)$$

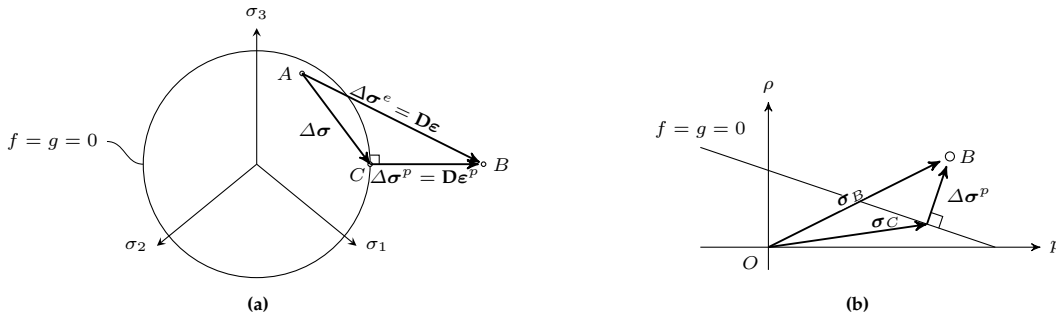


Figure 2.6: Geometrical illustration of return mapping in principal stress space, associated plasticity assumed. (a) deviatoric plane and (b) meridian plane $\nu = 0$.

The expression in Equation (2.22) can be evaluated directly if the gradient at point C is known, that is, the gradient at point C is the same as in point B. This is the case for some criteria, for instance Mohr Coulomb and Drucker Prager. The approximation of taking the gradient at point C for the updated stress is referred to as a fully implicit scheme, as the updated stress depends solely on information from the "next step". It has proven to be robust and is a common approach [de Borst et al., 2012]. Some further considerations of the return map scheme are made with multi-surface plasticity, for stress returns to yield surface discontinuities, see Appendix C for elaboration.

2.5.1 Accuracy of return mapping

In Equation (2.21) the potential gradient is assumed constant over the stress path. An approach to avoid this assumption is to adopt the infinitesimal elasto-plastic stress strain relation of Equation (2.17). The updated stress state can be obtained directly by integration as

$$\sigma_{j+1} = \sigma_j + \Delta\sigma = \sigma_j + \int_{\epsilon_j}^{\epsilon_j + \Delta\epsilon} \mathbf{D}^{ep} d\epsilon.$$

As the elasto-plastic constitutive matrix depends on the current stress state, a numerical integration scheme is called for. An explicit Euler integration with sub incrementation of the strain increment is applied as

$$\sigma_{j+1} = \sigma_j + \sum_{i=1}^N \delta\sigma_i, \quad \delta\sigma_{i+1} = \mathbf{D}^{ep} \left(\sigma_j + \sum_{k=1}^i \delta\sigma_k \right) \delta\epsilon, \quad \epsilon = \delta \frac{\epsilon}{N}. \quad (2.23)$$

The outcome of stress integration with the explicit integration scheme in Equation (2.23) is compared to the implicit return mapping in Figure 2.7. A yield surface of no hydrostatic stress dependency is utilized here, to visualize in the deviatoric plane. A surface with some curvature reveals the differences as the gradient clearly influences the outcome, whereas the linear surface has constant gradient, and the methods yields the same updated stress. A different outcome of the updated stress state is obtained

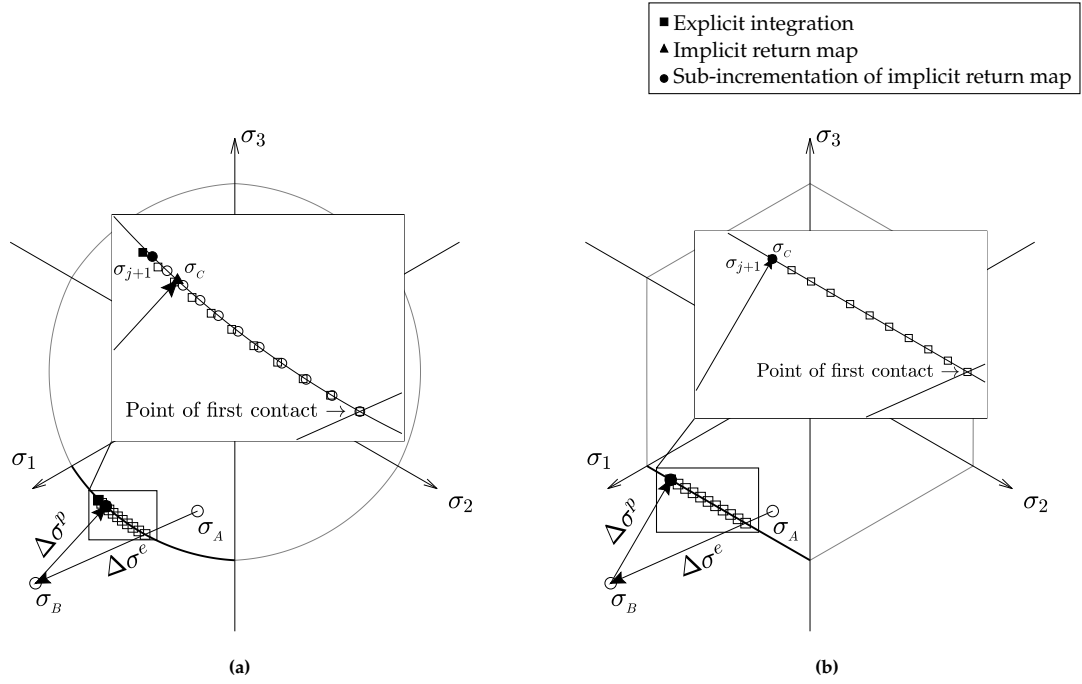


Figure 2.7: Stress update by explicit integration with a sub-incrementation of the strain increment, $N = 10$, implicit return mapping and successive implicit return mapping with sub-incrementation (a) von Mises plasticity (b) Tresca plasticity.

by sub-incrementation of the strain increment, and successively applying the implicit return mapping scheme, as illustrated in Figure 2.7a.

The true stress path is evidently better described by an explicit integration, however, with the obvious downfall that the yield criterion is not necessarily fulfilled, and the updated stress state drifts away from the yield surface as seen in Figure 2.7a. Return algorithms, which are not fully implicit, operating on average gradients has been used, see for instance [Ottosen and Ristinmaa, 2005], as these are considered a more accurate of the stress increment. However, the fully implicit return map is by far the most widely used method and is generally efficient and robust. The size of the strain increment has influence on the accuracy. The point of first contact with the yield surface needs to be calculated both with explicit integration and average gradient return mapping schemes, which is unnecessary in the implicit return map.

2.5.2 General solution algorithm for the implicit return map

The system of equations in (2.21) can readily be solved by Newtons method. The equations are stacked in a solution vector as

$$\mathbf{q} = \begin{Bmatrix} \sigma_C - \sigma_B + \Delta\lambda \mathbf{D} \nabla g_C \\ f(\sigma_C) \end{Bmatrix} = \mathbf{0}, \quad (2.24)$$

which is solved by Newton's method, where the solution in iteration $j + 1$ is calculated by,

$$\begin{Bmatrix} \sigma_C \\ \Delta\lambda \end{Bmatrix}_{j+1} = \begin{Bmatrix} \sigma_C \\ \Delta\lambda \end{Bmatrix}_j - \mathbf{J}_j^{-1} \mathbf{q}_j,$$

where, \mathbf{J} , is the Jacobian matrix given as

$$\mathbf{J} = \begin{bmatrix} \partial q_1 / \partial \sigma_{xx} & \partial q_1 / \partial \sigma_{yy} & \dots & \partial q_1 / \partial \Delta\lambda \\ \partial q_2 / \partial \sigma_{xx} & \partial q_2 / \partial \sigma_{yy} & \dots & \partial q_2 / \partial \Delta\lambda \\ \vdots & \vdots & \ddots & \vdots \\ \partial q_7 / \partial \sigma_{xx} & \partial q_7 / \partial \sigma_{yy} & \dots & \partial q_7 / \partial \Delta\lambda \end{bmatrix} = \begin{bmatrix} \mathbf{I} + \Delta\lambda \mathbf{D} \nabla^2 g & \mathbf{D} \nabla g \\ (\nabla f)^T & 0 \end{bmatrix},$$

for the general 6D stress space. A typical initial guess to initiate the Newton iterations is

$$\sigma_0 = [\sigma_B^T \quad 0]^T.$$

The Newton iterations are terminated when the incrementation is sufficiently low, that is

$$\| \mathbf{J}_j^{-1} \mathbf{q}_j \| < \varepsilon,$$

where, ε , is a prescribed tolerance of which the numeric value should depend on the units. The system of equations in Equation (2.24), can be reduced from seven equations in general stress space, to four if the calculations are carried out in principal stress space.

3 | Constitutive Models in Geomechanics

In this section, some widely used yield criteria in geomechanics are introduced for an overview. The yield criterion is the sole extraction from the constitutive models referenced in this chapter, as flow rule and hardening law are beyond the scope of the following discussion. Yield criteria of various characteristics for different purposes are available, some derived on an empirical basis and some with offset in a mathematical formulation. In the following, the yield surfaces are categorised on their hydrostatic stress dependency, either with none, linear or nonlinear. Some of the more advanced criteria is of a higher-order deviatoric trace and is formulated to accommodate results of true triaxial tests. To be further noted in the yield surface models in this chapter, is whether the ρ_t/ρ_c -ratio, or meridional eccentricity, is adjustable or fixed. Another characteristic of yield surfaces, with importance in numerical calculations, is the continuity of the deviatoric trace. All the criteria in this section are lastly presented in a complete schematic overview.

3.1 No Hydrostatic Stress Dependency

Yield surfaces without hydrostatic stress dependency are few, and not for modelling of frictional materials. Within geomechanics, however, the Tresca criterion can be highlighted.

3.1.1 The Tresca Criterion

The Tresca yield criterion was proposed by Tresca in 1864, and described in fore instance [Ottosen and Ristinmaa, 2005, sec. 8.7]. The criterion was proposed in relation to his works with metal plasticity, however, in geotechnical context used extensively in constitutive modelling of undrained clay. The yield criterion can be expressed as

$$f = \sigma_1 - \sigma_3 - m, \quad \sigma_1 \geq \sigma_2 \geq \sigma_3, \quad (3.1)$$

where, m , is a material parameter. For metals it is related to the yield strength, σ_Y , and for undrained clay it is related to the undrained shear strength (or cohesion), c_u . The physical interpretation of this criterion is that the elastic extend of the material is limited by a certain maximum shear stress, $(\sigma_1 - \sigma_3)/2$, independent of the hydrostatic stress. The yield surface is sketched in deviatoric and meridian planes in Figure 3.1. The deviatoric radius is smallest at the shear meridian, $\theta = \pi/3$, as seen clearly in the deviatoric plane, and constituted by the mathematical expression in Figure 3.1b.

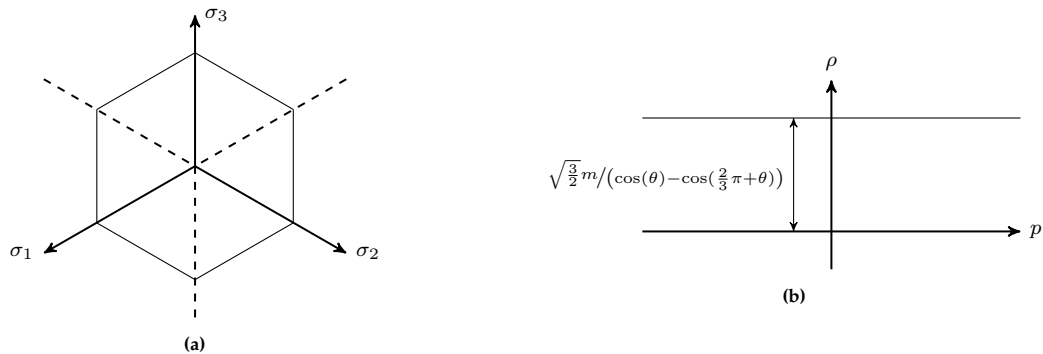


Figure 3.1: The Tresca yield surface sketched in (a) deviatoric plane and (b) meridian plane.

3.2 Yield Surfaces with Linear Generators

In the analysis of frictional materials, a dependency on the hydrostatic pressure is inherent. The Mohr-Coulomb and Drucker-Prager yield surfaces are examples with linear generators, and are described in

some detail in this section. These are amongst the oldest yield criteria and are used extensively in soil mechanics to this date.

Some more advanced models with linear generators is for instance the surface of Matsuoka-Nakai, as proposed in [Matsuoka and Nakai, 1974], developed for frictional materials. An efficient implementation of this criterion has been proposed by for instance [Panteghini and Lagioia, 2014]. An example of a yield surface with a more parametrically controlled deviatoric trace is the Modified Drucker-Prager model, which is a built-in plasticity model in the commercial software, Abaqus [Simulia, 2014, Sec. 23.3.2]. It is a modification of the Drucker-Prager criterion, with a continuous deviatoric trace, and an additional parameter to adjust the ρ_t/ρ_c -ratio. A yield surface model with quite some coverage in the deviatoric plane is the Reuleaux plasticity model [Coombs, 2010]. This surface is composed of three cone segments, and has a deviatoric discontinuity under triaxial compression. It is mentioned here, as it bears some resemblance, and is a special case of the yield surface proposed in this thesis. As a concept, the Paul-Mohr-Coulomb criterion [Paul, 1968] was proposed as a surface, composed of any number of linear segments. The amount of discontinuities is a disadvantage and the Paul-Mohr-Coulomb model has not gained commercial use, however, adopted in some researches as for instance [Meyer and Labuz, 2013]. Another yield surface which is similarly composed of linear segments in the deviatoric trace, is the Unified Strength theory [Yu, 2018]. This has been applied to a wider extend, at least within the academic community, for instance in studies of the intermediate principle stress effects [Ma et al., 2011] and [Zhou et al., 2013].

3.2.1 The Mohr-Coulomb criterion

The Mohr-Coulomb criterion is described in some detail in this section. This criterion dates back to [Coulomb, 1773] and is described in much literature since, fore instance [Ottosen and Ristinmaa, 2005, Sec. 8.5]. It is still used extensively in analysing soil, along with other frictional materials, for instance concretes. The yield criterion can be expressed in principle stresses as

$$\begin{aligned} f(\sigma_1, \sigma_3) &= \sigma_1 - \sigma_3 + (\sigma_1 + \sigma_3) - 2c \cos \varphi, & \sigma_1 \geq \sigma_2 \geq \sigma_3, \\ f(\sigma_1, \sigma_3) &= k\sigma_1 - \sigma_3 - \sigma_c \end{aligned} \quad (3.2)$$

where, k and σ_c , is the friction parameter and the uniaxial compression strength, respectively. Note the explicit absence of the intermediate principal stress, σ_2 , in Equation (3.2), which motivates the studies in Chapter 5. The Mohr Coulomb criterion is a restriction of the maximum shear as the Tresca criterion, however, the maximum shear capacity depends on the hydrostatic stress as well. The friction parameter, given through the internal angle of friction, and the uniaxial compression strength are given as

$$k = \frac{1 + \sin \varphi}{1 - \sin \varphi} \quad \wedge \quad \sigma_c = 2c\sqrt{k}, \quad (3.3)$$

The Mohr Coulomb criterion can be visualized in principle stress space as an irregular hexagonal pyramid. It is delineated in the deviatoric and meridian plane in Figure 3.2. The Mohr-Coulomb yield surface resembles the Tresca surface in the deviatoric trace for $\varphi = 0$, and the trace resembles a triangle for $\varphi = \pi/2$. The Mohr-Coulomb yield surface is of constant ρ_t/ρ_c -ratio given as

$$\frac{\rho_t}{\rho_c} = \frac{3 - \sin \varphi}{3 + \sin \varphi},$$

unlike for instance the Paul-Mohr-Coulomb model.

3.2.2 The Drucker-Prager criterion

The Drucker Prager criterion was suggested by [Drucker and Prager, 1951], and the surface forms a cone around the hydrostatic axis in principal stress space. The shape of the yield surface renders it more robust in numerical analysis than Mohr-Coulomb, as the only discontinuity is the apex. The yield criterion can be expressed though the first invariant, I_1 , and the second deviatoric stress invariant, J_2 , as

$$f(I_1, J_2) = \sqrt{3J_2} + \alpha I_1 - \beta, \quad (3.4)$$

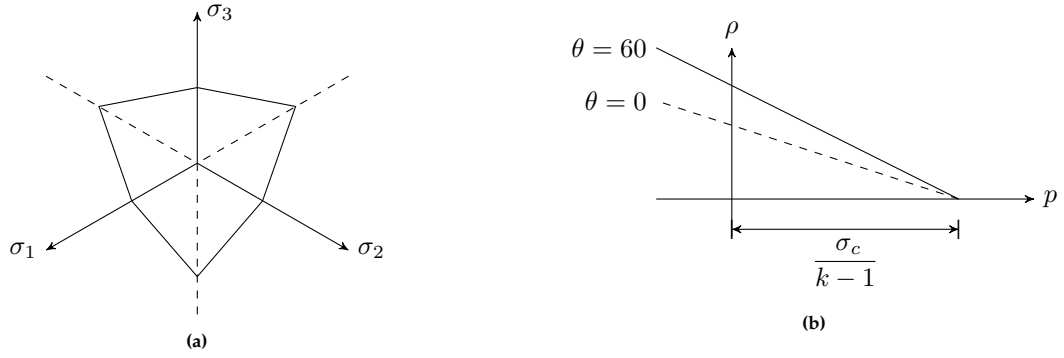


Figure 3.2: The Mohr-Coulomb yield surface in (a) deviatoric plane and (b) meridian plane.

where, α and β , are material parameters. These could for instance be expressed by the angle of friction and the cohesion, to fit the Mohr-Coulomb pyramid in some manner. The same limit load can be obtained with a Drucker-Prager model in plane strain conditions, see for instance [Drucker and Prager, 1951], however, the displacement response is rather different than with the Mohr-Coulomb model. A three-dimensional problem is, however, poorly described by the Drucker-Prager model, as discussed by for instance [Bishop, 1966] and [Alejano and Bobet, 2012]. The Drucker-Prager criterion equals Mohr-Coulomb in plane strain and circumscribes the Mohr-Coulomb pyramid, in the following settings of the parameters,

$$\left. \begin{aligned} \alpha &= \frac{\sin \varphi}{\sqrt{3 + \sin^2 \varphi}} \\ \beta &= \frac{3c \cos \varphi}{\sqrt{3 + \sin^2 \varphi}} \end{aligned} \right\} \quad \text{Drucker-Prager equals Mohr-Coulomb in plane strain,} \quad (3.5)$$

$$\left. \begin{aligned} \alpha &= \frac{2 \sin \varphi}{3 - \sin \varphi} \\ \beta &= \frac{6c \cos \varphi}{3 - \sin \varphi} \end{aligned} \right\} \quad \text{Drucker-Prager circumscribes Mohr-Coulomb.} \quad (3.6)$$

The failure surface is depicted in the deviatoric and meridian plane in Figure 3.3. The Drucker-Prager criterion is independent on the Lode angle, θ , as opposed to the Mohr-Coulomb criterion, seen clearly in the deviatoric plane in Figure 3.3a. The ρ_t/ρ_c -ratio is fixed and equal to one, opposed to the Modified Drucker-Prager criterion.

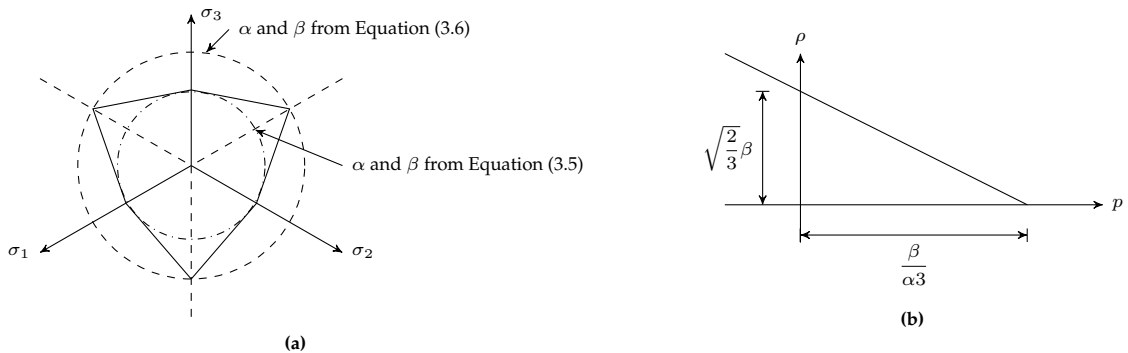


Figure 3.3: The Drucker-Prager surface in (a) deviatoric plane inscribing and circumscribing the Mohr-Coulomb surface and (b) meridian plane.

3.3 Yield Surfaces with Nonlinear Generators

Frictional soil materials often exhibits a decrease in the angle of friction, as the hydrostatic stress level increases. It is therefore more appropriate to operate with yield criteria of nonlinear hydrostatic stress dependency. Some famous yield criteria with nonlinear generators are briefly described in this section.

The surface of Lade [Lade, 1977], the Hoek-Brown criterion [Hoek and Brown, 1980] and the Bolton criterion [Bolton, 1986], are explored in some further detail in the following.

3.3.1 The Lade criterion

Lade's plasticity model is used to model purely frictional soil materials [Helwany, 2007, Sec. 2.10], and was presented by [Lade, 1977]. The mathematical expression of the failure criterion is given as

$$f(I_1, I_3) = \left(\frac{I_1^3}{I_3} - 27 \right) \left(\frac{I_1}{p_a} \right)^m - \eta_1 = 0, \quad (3.7)$$

where, η_1 and m determines the shape of the surface, and is determined through laboratory tests and p_a is the atmospheric pressure. The deviatoric trace is continuous with fixed ρ_t/ρ_c -ration, and a yield surface with linear generators is rendered with $m = 0$. The failure surface is plotted in the deviatoric plane, with η_1 such that it circumscribes the Mohr Coulomb pyramid, in Figure 3.4. Lade's yield criterion

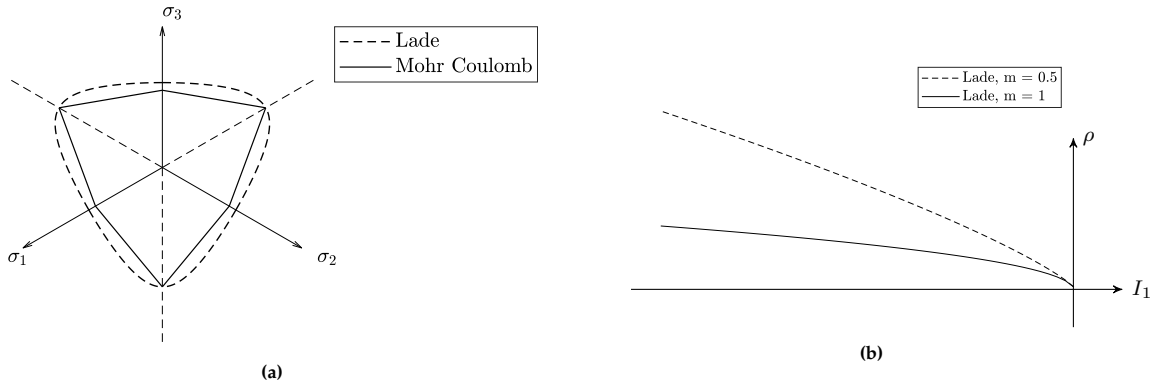


Figure 3.4: (a) The Lade yield surface made to circumscribe the Mohr-Coulomb surface with $m = 0$ and (b) Nonlinear generators of the Lade yield surface, $m \neq 0$

is found to describe purely frictional soil material quite well, and may obtain further popularity being of a particularly elegant mathematical formulation, with merely two parameters. The deviatoric trace seen in Figure 3.4a is a fairly good representation of the more dense sand types, as seen in true triaxial experiments [Lade and M. Duncan, 1973].

3.3.2 The Bolton criterion

This failure criterion is based on the works of [Bolton, 1986], where he examined experimental results from plane strain and triaxial compressions tests of 17 different types of sand. An empirical expression for the secant angle of friction as function of the hydrostatic stress level was proposed, however, no actual failure criterion is stated in his paper. This expression is then adopted in a Mohr-Coulomb model as the application of Bolton's formula. See for instance [Choo, 2018] for implementation in a computational framework, and the Bolton model is available in for instance the "Optum" software, see [Krabbenhof et al., 2016b]. The failure criterion reads

$$f = \sigma_1 - \sigma_3 + (\sigma_1 + \sigma_3) \sin(\varphi(p)), \quad \sigma_1 \geq \sigma_2 \geq \sigma_3, \quad (3.8)$$

where Bolton's formula for the secant angle of friction is

$$\varphi(p) = \varphi_{cv} + 0.8\psi_{max}(p). \quad (3.9)$$

Here, φ_{cv} , is the constant volume, or critical state, angle of friction, which is measured when shear failure occurs, and the volume is constant i.e. zero dilatation. This model is often referred to as a critical state model, as it operates on φ_{cv} . The maximum observed angle of dilatation reads

$$0.8\psi_{max}(p) = bI_r,$$

where

$$b = \begin{cases} 5, & \text{Plane strain} \\ 3, & \text{Triaxial strain} \end{cases},$$

and the relative dilatancy index, I_r , reads

$$I_r = I_d(Q - \ln(p) - R), \quad 0 \leq I_r \leq 4.$$

Here, I_d , is the relative density, Q , is a parameter related to particle crushing and, R , is a model parameter often set equal to 1. A value of 10 for the parameter, Q , fits well to quartz and feldspar grains, see for instance [Bolton, 1986] for the Q -parameter for some common soils. Bolton's formula (3.9) yields the angle of friction in degrees as a function of the hydrostatic pressure in kPa.

As the relative density enters these expressions directly, density effects may be incorporated in numerical analysis of sands without any further parameter calibration, as proposed by [Choo, 2018]. The yield surface is depicted in deviatoric and meridian plane in Figure 3.5. The ρ_t/ρ_c -ratio is fixed as in Mohr-Coulomb, however, varies with the hydrostatic pressure as the angle of friction.

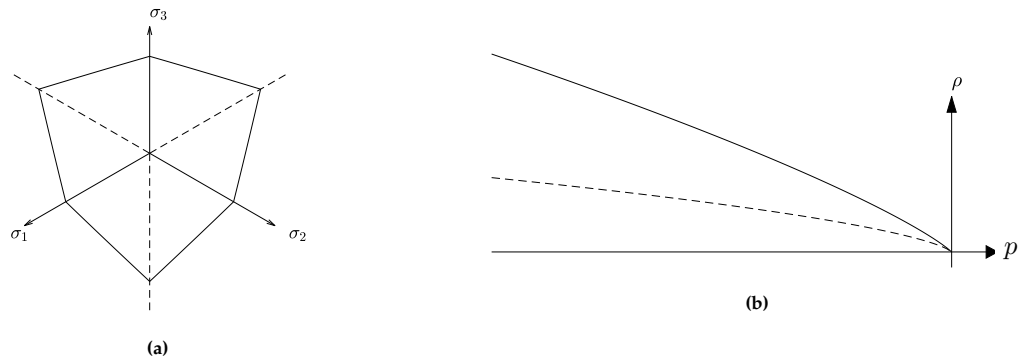


Figure 3.5: The Bolton surface depicted in (a) deviatoric plane and (b) meridian plane with different values of φ_{cv} .

3.3.3 The Hoek-Brown criterion

This criterion was proposed by [Hoek and Brown, 1980] and is formulated on an empirical basis. It has been modified since its original form in 1980, see for instance [Hoek et al., 2002] for a more recent version. It is a model for rock masses, and its applications are for instance underground excavations, slope stability calculations etc. It is one of few yield surfaces with non-linear generators, which has gained widespread use amongst practitioners. This popularity may stem from the so called GSI system, for determination of the parameters from in-situ observations.

The yield criterion is given as

$$f = \sigma_3 - \sigma_1 - \sigma_{ci} \left(s + m_b \frac{\sigma_1}{\sigma_{ci}} \right)^a, \quad \sigma_1 \leq \sigma_2 \leq \sigma_3, \quad (3.10)$$

where, σ_{ci} , is a scaling of the intact uniaxial compressive strength of the intact rock, σ_c , reading

$$\sigma_{ci} = \frac{\sigma_c}{(s)^a}.$$

Here, s , m_b , and a , are empirically defined parameters which are related to the in-situ conditions on the rock material. These are calculated from

$$\begin{aligned} m_b &= m_i \exp \left(\frac{GSI - 100}{28 - 14D} \right), \\ s &= \exp \left(\frac{GSI - 100}{9 - 3D} \right), \\ a &= \frac{1}{2} + \frac{1}{6} \left(\exp \left(-\frac{GSI}{15} \right) - \exp \left(-\frac{20}{3} \right) \right), \end{aligned}$$

where, GSI , is the geological strength index, D , accounts for blast damage and stress relaxation and, m_i , is a material constant which ideally is determined from laboratory tests. The geological strength

index and the factor, D , is determined through classifications of the visual conditions of the in-situ soil material found in fore instance [Hoek et al., 2002]. It is, however, necessary to conduct laboratory tests for the uniaxial compressive strength. The yield criterion is absent of σ_2 and resembles Mohr-Coulomb in the deviatoric trace, see Figure 3.6 for a sketch of the surface in deviatoric and meridian plane. The ρ_t/ρ_c -ratio is fixed, however, varies with the hydrostatic stress.

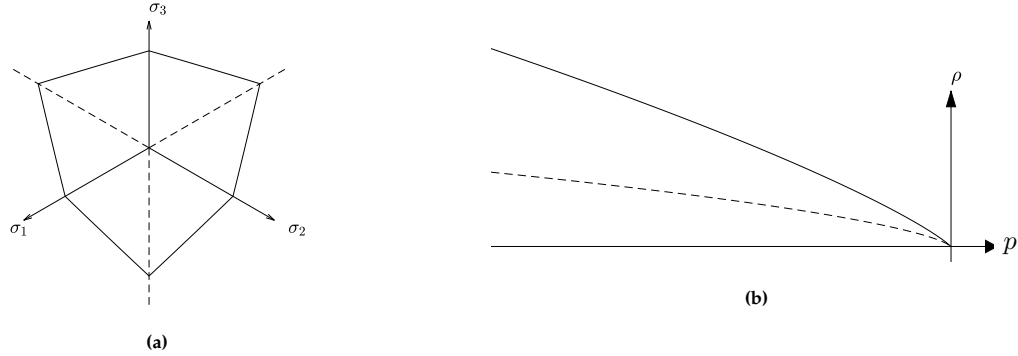


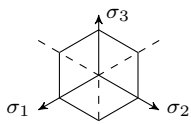
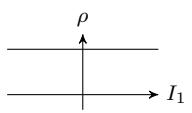
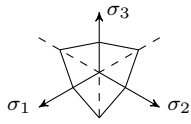
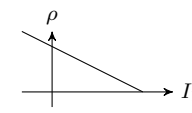
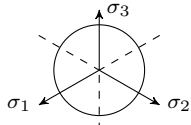
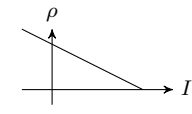
Figure 3.6: The Hoek Brown yield surface depicted in (a) deviatoric plane and (b) meridian plane with different values of a .

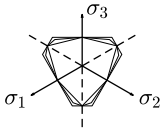
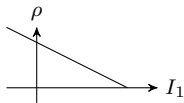
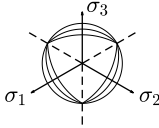
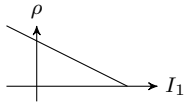
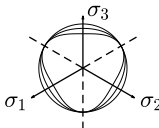
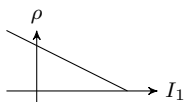
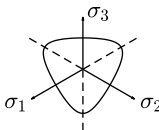
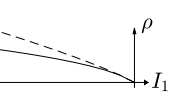
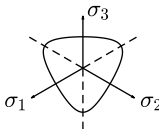
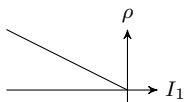
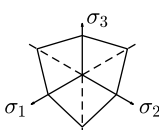
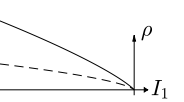
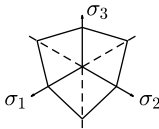
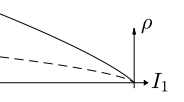
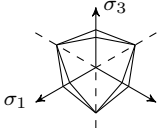
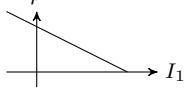
3.4 A Schematic Overview

Several yield criteria have been proposed throughout history, were some widely used have been described in this chapter. These are summarized along with their primary characteristics in Table 3.1.

Hydrostatic stress dependency is inherent in frictional materials. This dependency is often simplified as linear, for instance Mohr-Coulomb or Drucker-Prager, although, more sophisticated models have been proposed, for instance Lade, Hoek-Brown, or Bolton. The Mohr-Coulomb criterion is without influence of the intermediate principle stress, opposed to Drucker-Prager, where all the stresses are equally weighted. The Matsuoka-Nakai and the Lade surfaces are of elegant mathematical formulations and are widely accepted as describing some frictional soil materials, however, quite material specific. The modified Drucker-Prager, Reuleaux and Paul-Mohr-Coulomb surfaces are parametrically controlled in the deviatoric trace to some degree, and may therefore be used to model a wider range of materials.

Table 3.1: Primary characteristics of several yield surfaces used in geomechanics.

Tresca	$f = \sigma_1 - \sigma_3 - m$	 	<p>Modelling purpose examples: Metals and undrained clay</p> <p>Material parameters: m.</p> <p>Description: Discontinuous yield surface, independent of hydrostatic stress and σ_2, with fixed deviatoric trace. Failure due to maximum shear stress. See for instance [Ottosen and Ristinmaa, 2005].</p>
Mohr-Coulomb	$f = k\sigma_1 - \sigma_3 - 2c\sqrt{k}$	 	<p>Modelling purpose examples: Frictional and cohesive materials</p> <p>Material parameters: φ and c.</p> <p>Description: Discontinuous yield surface, linear dependency of hydrostatic stress and no influence from σ_2, with fixed deviatoric trace. Failure due to maximum shear stress. Originally proposed by [Coulomb, 1773], see for instance [Ottosen and Ristinmaa, 2005] for elaboration.</p>
Drucker-Prager	$f = \sqrt{3}J_2 + \alpha I_1 - \beta$	 	<p>Modelling purpose examples: Frictional and cohesive materials</p> <p>Material parameters: α and β.</p> <p>Description: Smooth continuous yield surface, linear dependency of hydrostatic stress and equal influence from all principle stresses, with fixed deviatoric trace. Failure is related to the change in shape. Proposed by [Drucker and Prager, 1951].</p>

Unified Strength Theory	$f = \begin{cases} (b\sigma_2 + \sigma_3)/(k(1+b)) - \sigma_1 + 2c/\sqrt{k}, & \sigma_2 \leq \sigma_1(1 + \sin \varphi)/2 + \sigma_3(1 - \sin \varphi)/2 \\ \sigma_3/k - (b\sigma_2 + \sigma_1)/(1+b) + 2c/\sqrt{k}, & \sigma_2 > \sigma_1(1 + \sin \varphi)/2 + \sigma_3(1 - \sin \varphi)/2 \end{cases}$	
		Modelling purpose examples: Frictional materials Material parameters: φ , c , and b . Description: Discontinuous yield surface, linear dependency of hydrostatic stress (in the version presented here) and influence from all principle stresses, with flexible deviatoric trace. Proposed by [Yu, 2018].
Modified Reuleaux	$f = \rho - \alpha \rho(\theta)$	
		Modelling purpose examples: Frictional and cohesive materials Material parameters: φ and $\bar{\rho}^e = \rho_t/\rho_c$. Description: Surface with linear generators with a sharp apex point and a discontinuity in the triaxial compression corner. Parametrically controlled ρ_c/ρ_t -ratio. Proposed by [Coombs, 2010].
Modified Drucker-Prager	$f = \sqrt{3}J_2/2 \left(1 + 1/K - (1 - 1/K) \left((27/2 J_3)^{1/3} / \sqrt{3} J_2 \right)^3 \right) - I_1/3 \tan \beta - d$	
		Modelling purpose examples: Frictional and cohesive materials Material parameters: d , β and K . Description: Smooth continuous yield surface, linear dependency of hydrostatic stress and influence from all principle stresses, with adjustable deviatoric trace. Failure is some combination of the change in shape and maximum shear stress. See for instance [Simulia, 2014].
Lade	$f = (I_1^3/I_3 - 27) (I_1/p_a)^m - \eta_1$	
		Modelling purpose examples: Frictional materials Material parameters: m and η_1 . Description: Smooth continuous yield surface, nonlinear dependency of hydrostatic stress and influence from all principle stresses, with fixed deviatoric trace. Proposed by [Lade, 1977].
Matsuoka-Nakai	$f = -9I_3 - \kappa I_3 + I_1 I_2$	
		Modelling purpose examples: Frictional materials Material parameters: κ . Description: Smooth continuous yield surface, linear dependency of hydrostatic stress (in the version presented here) and influence from all principle stresses, with fixed deviatoric trace. Proposed by [Matsuoka and Nakai, 1974].
Hoek Brown	$f = \sigma_3 - \sigma_1 - \sigma_{ci} \left(s + m_b \frac{\sigma_1}{\sigma_{ci}} \right)^a$	
		Modelling purpose examples: Developed for rock masses. Material parameters: σ_{ci} , m_i , D and GSi . Description: Criterion based on empiric. Discontinuous yield surface, nonlinear dependency of hydrostatic stress and no influence from σ_2 , with fixed deviatoric trace. A Maximum shear stress criterion. Proposed by [Hoek and Brown, 1980].
Bolton	$f = \sigma_1 - \sigma_3 + (\sigma_1 + \sigma_3) \sin(\varphi_{cv} + b(I_d(Q - \ln(p)) - R))$	
		Modelling purpose examples: Frictional soil Material parameters: φ_{cv} , b , I_d , Q and R . Description: Criterion based on plain strain and triaxial tests of 17 sands. Discontinuous yield surface with nonlinear generators and no influence from σ_2 , with fixed deviatoric trace. A Maximum shear stress criterion. Proposed by [Bolton, 1986].
Paul-Mohr-Coulomb	$f = A\sigma_1 + B\sigma_2 + C\sigma_3$ (simplest version)	
		Modelling purpose examples: Frictional and cohesive materials. Material parameters: A , B and C in this formulation. Description: Yield surface composed of $n \times 6$ planes with n as a positive integer. Discontinuous yield surface, linear dependency of hydrostatic stress and influence from all principle stresses, with adjustable deviatoric trace. Proposed by [Paul, 1968].

4 | The General Parametric Yield Surface Format

In this chapter, a concept of parametric yield surfaces is introduced, as proposed by professor Lars Damkilde [Damkilde, 2019]. A similar yield surface formulation has not been found in the existing literature by the authors. This concept of yield surfaces is herein referred to as the General Parametric Yield Surface Format. The scope is to formulate a multi-surface yield criterion, which can be used as model for a wide range of materials. This is previously attempted by some of the models described in chapter 3, for instance the Paul-Mohr-Coulomb model [Paul, 1968], Reuleaux Plasticity [Coombs, 2010] or the Unified Strength Theory [Yu, 2018], However, none of these are as versatile as the herein proposed. The works on some of the yield surface models in this chapter has resulted in two papers, which can be found in Appendix C and D. An overall description of these surfaces and the derivation of the yield criteria is given in this chapter, see the aforementioned appendices for a thorough mathematical description and finite element implementation. The third yield surface model proposed in this chapter is with nonlinear generators, and the implementation is analogous to the implementation in Appendix D.

The concept of the proposed yield surface is to formulate a deviatoric trace, composed of circular segments, as illustrated in Figure 4.1. A key element is to define the deviatoric trace, and the meridional variation separately. It is advantageous to assume the conventional ordering of the principal stresses as, $\sigma_1 \geq \sigma_2 \geq \sigma_3$, and isotropic behaviour, so the six-fold symmetry of the yield surface can be exploited. These assumptions is applied in Figure 4.1a, where the deviatoric trace is composed of one circular segment, defined by a centre, c , and radius, r . The entire trace rendered by the six-fold symmetry is shown in Figure 4.1b. Any number of circular segments can in principle be used to define the deviatoric trace. The factorization of the deviatoric and hydrostatic variation results in a highly adjustable surface formulation. With linear generators, the yield surface is composed of conical segments from an oblique cone. Any appropriate non-linear hydrostatic stress dependency is easily adopted, by replacing the aforementioned meridional function.

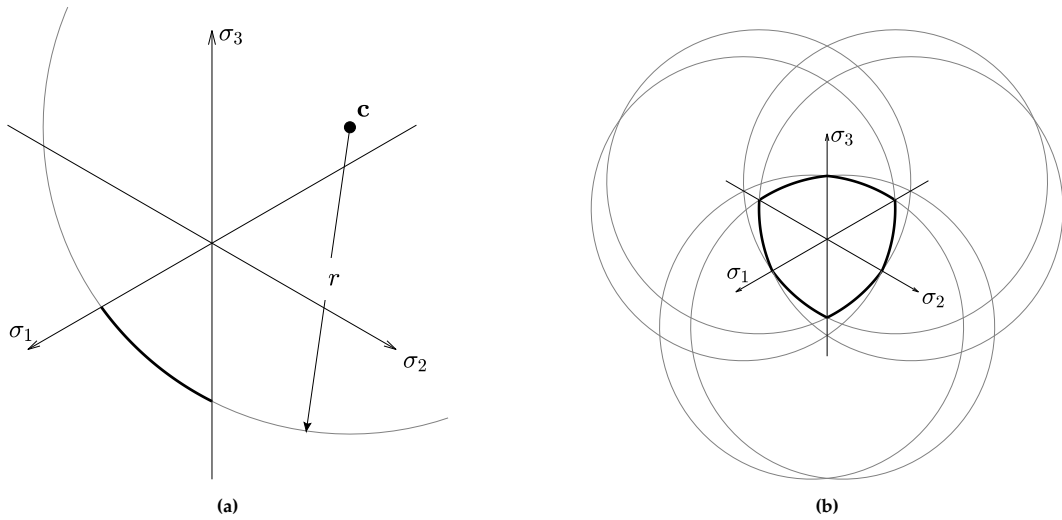


Figure 4.1: Conceptual sketch of the proposed yield surface model (a) circular segment in deviatoric plane sextant, $\sigma_1 \geq \sigma_2 \geq \sigma_3$, and (b) the entire trace.

In Section 4.2 a deviatoric trace of six circular segments is defined, which corresponds with the one illustrated in Figure 4.1. This is a discontinuous trace, which motivates the formulation of a continuous trace as in Section 4.3. In Sections 4.4 and 4.5 yield surfaces are rendered by linear and nonlinear generators respectively. The surface of linear generators arises from the Mohr-Coulomb surface, and covers a wide range of convex shapes between the Mohr-Coulomb and Drucker-Prager surfaces. The surface of nonlinear generators arises from the Bolton criterion, and can be considered an extension of the Bolton surface, with the option of adjusting the ρ_t/ρ_c -ratio and side curvature. On top of this, it furnishes

a numerically robust implementation as a smooth continuous approximation of the Bolton model.

4.1 Transformation to Reference Coordinates

As a preliminary consideration to formulating the yield surface, it is found convenient to define the deviatoric geometry in the cartesian σ^* -coordinate system illustrated in Figure 4.2.

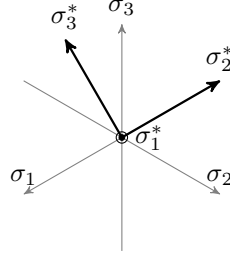


Figure 4.2: Illustration of the σ^* -coordinate system superimposed on the original principal stress axis, seen in the deviatoric plane.

The transformation from principal stresses to σ^* coordinates is performed by three plane rotations, as sketched in Figure 4.3. The first two rotations makes the σ_1^* -axis coincide with the hydrostatic axis, and the latter rotation of 30 degrees, makes the σ_2^* -axis coincide with the deviatoric projection of the first principal axis.

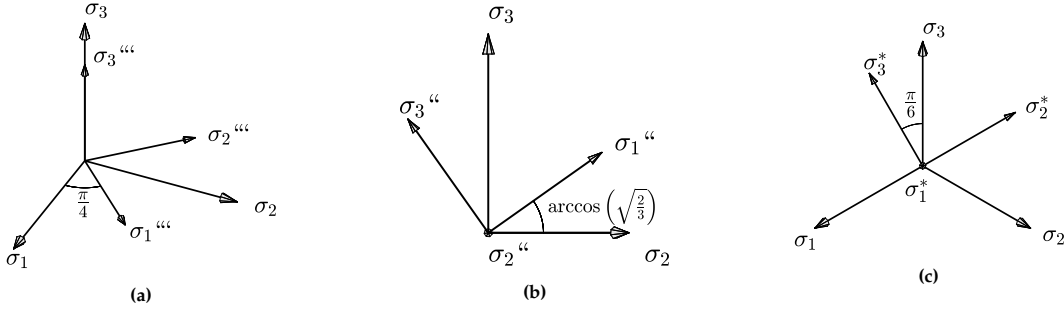


Figure 4.3: Transformation from principal stress to σ^* -coordinates in three steps (a) 45 degrees rotation about σ_3 (b) $\arccos \sqrt{2/3}$ radians rotation about σ_2'' and (c) 30 degrees rotation about σ_1^* .

The three transformations sketched in Figure 4.3 reads

$$\begin{aligned} \sigma^* = \mathbf{T}\sigma &= \begin{Bmatrix} \sigma_1^* \\ \sigma_2^* \\ \sigma_3^* \end{Bmatrix} = \begin{bmatrix} 1 & 0 & 0 \\ 0 & \sqrt{3}/2 & 1/2 \\ 0 & -1/2 & \sqrt{3}/2 \end{bmatrix} \begin{bmatrix} \sqrt{2/3} & 0 & 1/\sqrt{3} \\ 0 & 1 & 0 \\ -1/\sqrt{3} & 0 & 1/\sqrt{3} \end{bmatrix} \begin{bmatrix} \sqrt{2}/2 & \sqrt{2}/2 & 0 \\ -\sqrt{2}/2 & \sqrt{2}/2 & 0 \\ 0 & 0 & 1 \end{bmatrix} \begin{Bmatrix} \sigma_1 \\ \sigma_2 \\ \sigma_3 \end{Bmatrix} \\ &= \begin{bmatrix} 1/\sqrt{3} & 1/\sqrt{3} & 1/\sqrt{3} \\ -\sqrt{2/3} & 1/\sqrt{6} & 1/\sqrt{6} \\ 0 & -1/\sqrt{2} & 1/\sqrt{2} \end{bmatrix} \begin{Bmatrix} \sigma_1 \\ \sigma_2 \\ \sigma_3 \end{Bmatrix}. \quad (4.1) \end{aligned}$$

The inverse of, \mathbf{T} , equals the transpose, as exploited in the inverse transformation to principal stresses

$$\sigma = \mathbf{T}^{-1}\sigma^* = \mathbf{T}^T\sigma^* = \begin{bmatrix} 1/\sqrt{3} & -\sqrt{2/3} & 0 \\ 1/\sqrt{3} & 1/\sqrt{6} & -1/\sqrt{2} \\ 1/\sqrt{3} & 1/\sqrt{6} & 1/\sqrt{2} \end{bmatrix} \sigma^*. \quad (4.2)$$

Note the relations with the stress invariants

$$p = \frac{\sigma_1^*}{\sqrt{3}} \quad \wedge \quad \rho = \sqrt{(\sigma_2^*)^2 + (\sigma_3^*)^2}.$$

4.2 Discontinuous Deviatoric Trace

A deviatoric trace composed of six circular segments is described in general terms in this section. Isotropic material behaviour is assumed in order to utilize the six-fold symmetry of the trace, to merely operate on one of these circular segments. Two parameters denoted α and β_1 , are introduced, which adjust the meridional eccentricity and curvature, respectively. These parameters are solely related to the deviatoric trace, and meridional parameters are introduced in later sections to complete the surface formulation.

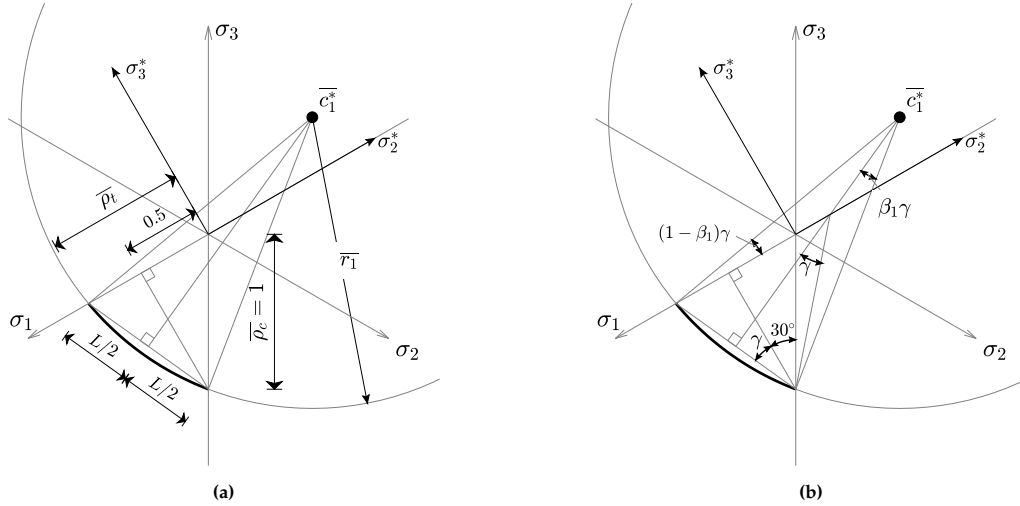


Figure 4.4: Sketch with relevant measures in the ρ_c -normalized deviatoric plane for derivation of the GPYS criterion, measures of (a) length and (b) angle.

The radius and centre of curvature are conveniently, with respect to later derivations, calculated in a ρ_c -normalized deviatoric plane with

$$\overline{\rho}_c = 1 \quad \wedge \quad \overline{\rho}_t = \alpha + \frac{3 - \sin \varphi}{3 + \sin \varphi} (1 - \alpha), \quad (4.3)$$

where, α and φ , is the meridional eccentricity and internal angle of friction, respectively. In this manner, the ρ_t/ρ_c -ratio is in coherence with the Mohr-Coulomb criterion for $\alpha = 0$ and gives $\rho_t = \rho_c$ for $\alpha = 1$. The secant length, L , and the angle, γ , of Figure 4.4, are calculated by the Pythagorean theorem and the tangent relation as

$$L = \sqrt{\left(\frac{\sqrt{3}}{2}\right)^2 + \left(\overline{\rho}_t - \frac{1}{2}\right)^2} \quad \wedge \quad \gamma = \arctan \left(\frac{\overline{\rho}_t - \frac{1}{2}}{\frac{\sqrt{3}}{2}} \right). \quad (4.4)$$

The normalized centre in σ^* -coordinates and radius is found by straightforward geometrical relations and reads

$$\overline{c}_1^* = \left\{ \begin{array}{l} \overline{r}_1 \cos((1 - \beta_1)\gamma) - \overline{\rho}_t \\ \overline{r}_1 \sin((1 - \beta_1)\gamma) \end{array} \right\} \quad \wedge \quad \overline{r}_1 = \frac{L}{2 \sin(\beta_1\gamma)}, \quad (4.5)$$

where, β , is introduced to adjust the curvature by scaling the angle γ . It is obvious from Equation (4.5), that β_1 cannot equal zero, however, approximates a straight line as it goes towards it, say 10^{-4} . The deviatoric trace is visualized in Figure 4.5 for an approximated Mohr-Coulomb hexagon, perfect circle and a Reuleaux triangle, to demonstrate the possibilities with the parametric circle in Equation (4.5).

4.3 Continuous Deviatoric Trace

Yield surfaces of discontinuous deviatoric traces can lead to poor convergence in numerical analysis, which is the main motivation for the deviatoric trace presented in this section. The fundamental issue is, that the gradient at the singularities of discontinuous yield surface is not uniquely defined. This

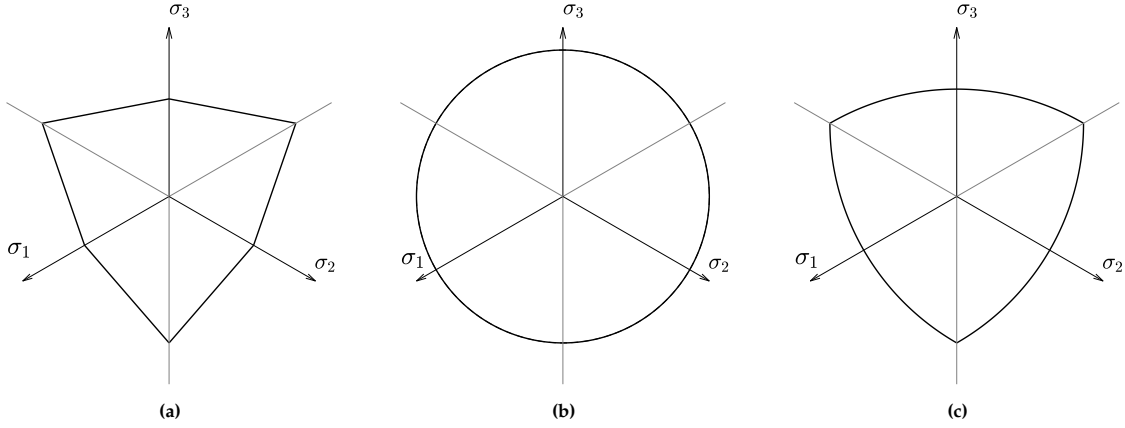


Figure 4.5: The deviatoric trace derived in the present section in different settings (a) Mohr-Coulomb hexagon $\alpha = \beta_1 = 0$ (b) perfect circle $\alpha = \beta_1 = 1$ and (c) Reuleaux triangle $\beta_1 = 1$.

constitutes a general issue in defining the consistent tangent matrix of Equation (2.18), which for instance can be addressed by formulating a continuous approximation of the original criterion. This is often referred to as a corner rounding, and the motivation for deviatoric trace in this section is to formulate a corner rounded version of the trace in Section 4.2. The concept is to introduce tangent circles at the deviatoric corners as illustrated in Figure 4.6. As in the preceding section, isotropic material behaviour is assumed in order to utilize the six-fold symmetry of the trace, to merely operate on three circular segments. Two additional parameters, β_2 and β_3 , are introduced to adjust the curvature of these circles. See Figure 4.6 for a sketch of the deviatoric geometry, which defines the trace.

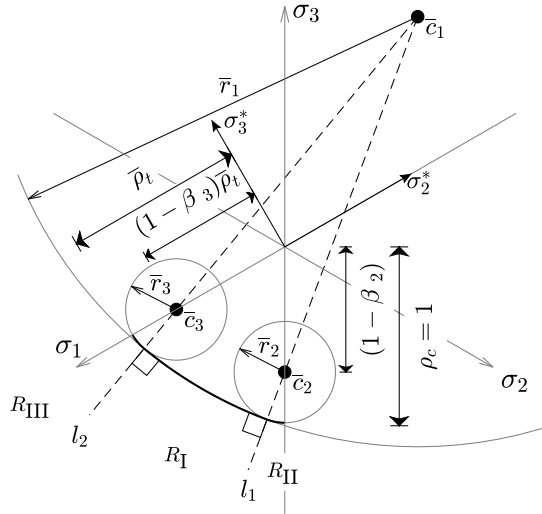


Figure 4.6: Geometrical relations of the present deviatoric trace.

The intention later on is to formulate a yield criterion as a multifunction expression, therefore, the regions denoted R_I , R_{II} and R_{III} , bounded by the lines l_1 and l_2 , are introduced. The intersection between l_1 and the deviatoric projection of the σ_3 -axis defines the second centre of curvature, c_2 , and the intersection between l_2 and the deviatoric projection of the σ_1 -axis defines the third centre of curvature, c_3 , as depicted in Figure 4.6. In this manner, the trace is inherently continuous and convex. The deviatoric measures, ρ_c and ρ_t , of Equation (4.3) is adopted, and the circular geometries defining the deviatoric

trace is expressed as

$$\begin{aligned}\bar{\mathbf{c}}_1^* &= \left\{ \frac{\bar{r}_1 \cos((1 - \beta_1)\gamma) - \bar{\rho}_t}{\bar{r}_1 \sin((1 - \beta_1)\gamma)} \right\} \wedge \quad \bar{r}_1 = \frac{L}{2 \sin(\beta_1 \gamma)}, \\ \bar{\mathbf{c}}_2^* &= (1 - \beta_2) \left\{ \frac{-1/2}{-\sqrt{3}/2} \right\} \wedge \quad \bar{r}_2 = \bar{r}_1 - \|\bar{\mathbf{c}}_1^* - \bar{\mathbf{c}}_2^*\|, \\ \bar{\mathbf{c}}_3^* &= (1 - \beta_3) \left\{ \frac{-\bar{\rho}_t}{0} \right\} \wedge \quad \bar{r}_3 = \bar{r}_1 - \|\bar{\mathbf{c}}_1^* - \bar{\mathbf{c}}_3^*\|. \end{aligned} \quad (4.6)$$

The region for a stress state is determined by the inequalities in Table 4.1, which uses the tangent vectors at the intersection point between l_n and the yield surface.

Table 4.1: Condition statements for determination of deviatoric region.

Condition	Region
$t_2^T (\sigma_d^* - \bar{\mathbf{c}}_1^* \rho_c) \leq 0 \quad \wedge \quad t_3^T (\sigma_d^* - \bar{\mathbf{c}}_1^* \rho_c) \geq 0$	R_I
$t_2^T (\sigma_d^* - \bar{\mathbf{c}}_1^* \rho_c) > 0$	R_{II}
$t_3^T (\sigma_d^* - \bar{\mathbf{c}}_1^* \rho_c) < 0$	R_{III}

$$t_2 = \left\{ \frac{-\bar{c}_{22}^* + \bar{c}_{12}^*}{\bar{c}_{21}^* - \bar{c}_{11}^*} \right\} \wedge \quad t_3 = \left\{ \frac{-\bar{c}_{32}^* + \bar{c}_{12}^*}{\bar{c}_{31}^* - \bar{c}_{11}^*} \right\}.$$

The parameters, β_1 , β_2 , and β_3 , are all dimensionless parameters in the interval $]0; 1]$. The capabilities of this geometry is illustrated in Figure 4.7 for different corner roundings of a Mohr-Coulomb hexagon, Reuleaux triangle and perfect hexagon (Tresca).

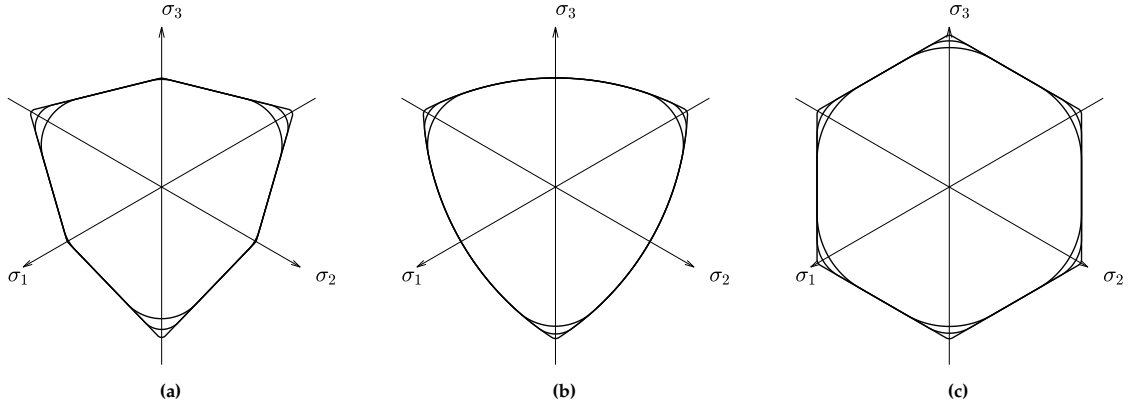


Figure 4.7: The deviatoric trace derived in the present section used in corner rounding, with different values of β_2 and β_3 , of (a) Mohr-Coulomb hexagon (b) Reuleaux triangle and (c) perfect hexagon.

4.4 Formulation with Mohr-Coulomb Generators

The yield surfaces generated by the deviatoric traces in sections 4.2 and 4.3 with linear hydrostatic stress dependency is presented in this section. The concept is to formulate a meridional function, ρ_c , as function of the hydrostatic stress, p , which is simply multiplied on the centres and radii of Equations (4.5) and (4.6), to obtain the deviatoric geometry for any hydrostatic stress. The meridional function is adopted as the compressive generator of the Mohr-Coulomb surface, defined by the internal angle of friction, φ , and cohesion, c , which establishes immediate familiarity in the parameters. Linear generators with circular segments in the deviatoric plane renders a surface composed of segments from oblique cones as sketched in Figure 4.8, along with the compressive generator of the yield surface.

The expression for ρ_c is found by formulating the Mohr-Coulomb criterion in Haigh-Westergaard space with $\theta = \pi/3$, and reads

$$\rho_c = \mu \left(p - \frac{2c\sqrt{k}}{k-1} \right), \quad \mu = \frac{1-k}{\sqrt{2/3}(k/2+1)}, \quad k = \frac{1+\sin \varphi}{1-\sin \varphi}. \quad (4.7)$$

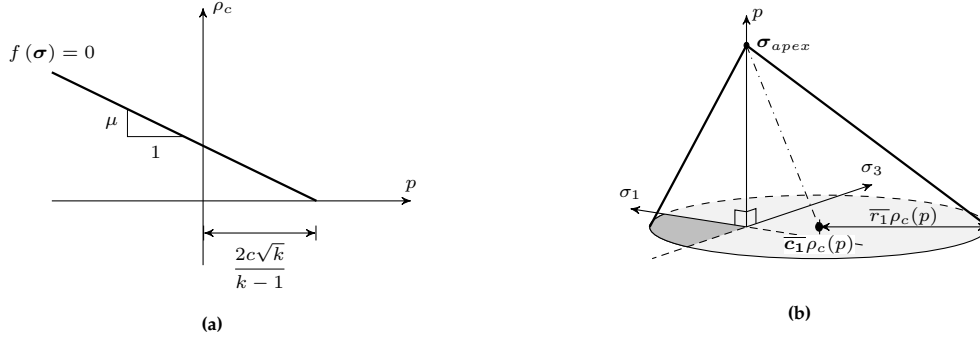


Figure 4.8: (a) Linear compressive generator and (b) oblique cone generated by a circular deviatoric trace with linear hydrostatic stress dependency.

The apex singularity leads to poor convergence in numerical analysis. Therefore, a smooth local rounding of the apex is proposed in the following, by introducing a circular segment in the meridian plane as sketched in Figure 4.9.

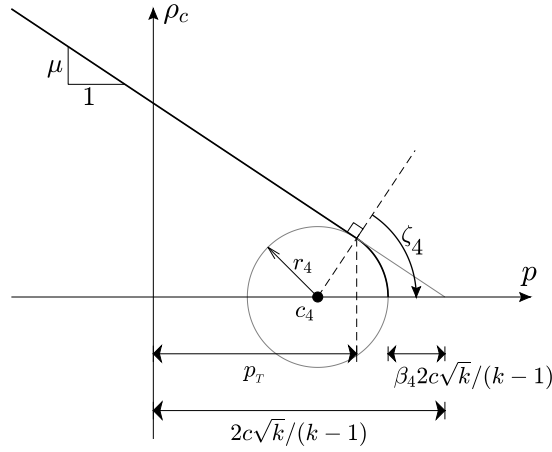


Figure 4.9: Geometrical relations for local rounding of apex singularity by circular segment.

The circular geometry for the rounded apex are calculated by straightforward geometrical relations as

$$c_4 = \left((1 - \beta_4) \frac{2c\sqrt{k}}{k-1} - r_4 \right) \begin{Bmatrix} 1 \\ 0 \end{Bmatrix} \quad \wedge \quad r_4 = \beta_4 \frac{2c\sqrt{k}}{k-1} \cot(\zeta_4) \cot\left(\frac{\zeta_4}{2}\right), \quad \zeta_4 = \arctan \frac{-1}{\mu},$$

where β_4 is a user-defined parameter in the interval $]0; 1]$. It approaches a sharp apex for $\beta_4 \rightarrow 0$ and renders a smooth tension cut-off for $\beta_4 = 1$. The multifunction expression for the ρ_c -meridional function of Figure 4.9 reads

$$\rho_c = \begin{cases} \mu \left(p - \frac{2c\sqrt{k}}{k-1} \right) & , p \leq p_T, \\ \left((r_4)^2 - (p - c_{41})^2 \right)^{0.5} & , p_T < p \leq p_{apex}, \end{cases} \quad (4.8)$$

where the limits, as illustrated in Figure 4.9, are expressed as

$$p_T = c_{41} + r_4 \cos \zeta_4 \quad \wedge \quad p_{apex} = (1 - \beta_4) \frac{2c\sqrt{k}}{k-1} = c_{41} + r_4.$$

The yield criterion is formulated as the difference between the current radius and the deviatoric distance from the considered stress state to the centre of curvature as

$$f_n = \|\sigma_d^* - \bar{c}_n^* \rho_c\| - \bar{r}_n \rho_c, \quad \sigma_d^* = [\sigma_2^* \quad \sigma_3^*]^T, \quad \sigma_1 \geq \sigma_2 \geq \sigma_3, \quad (4.9)$$

where subscript, n , refers to the deviatoric region. This yield function is applicable with both the deviatoric geometries defined by Equations (4.5) and (4.6). A yield surface with the deviatoric trace of Equations (4.5) and the meridional function of Equation (4.7) is presented in Appendix C. A completely continuous yield surface is obtained with the deviatoric trace of Equation (4.6) and the meridional function of Equation (4.8) as presented in Appendix D. These appendices gives thorough description of the yield surfaces and the numerical implementation. The discontinuous surface is implemented with methods for multi-surface plasticity from [Clausen et al., 2007]. The continuous yield surface rests mainly on well-known theoretical premises, except an amelioration of C^2 discontinuous transitions.

4.5 Formulation with Bolton Generators

A formulation of the novel yield surface format with nonlinear generators, which in following referenced as the GPYS-NC model, is presented in this section. The form of the generator is naturally depending on the material under consideration, and the yield function of Equation (4.9) is easily combined with any appropriate nonlinear function of hydrostatic stress. In Section 3, some existing models of nonlinear generators were explored, and either one of these models could constitute the generators. The Bolton model is selected for this purpose, as this is a widely accepted model for sands, and well known in the geotechnical community. It is efficiently implemented in the GPYS format, as it defines the secant angle of friction as a function of the hydrostatic stress directly. Surfaces, such as the modern Hoek-Brown [Hoek et al., 2002] or the GSK model [Krabbenhoft et al., 2016b], which are inseparable with respect to ρ_c , are conveniently approximated with the GPYS format, which is demonstrated lastly in this section. As a further note, a simple hardening model can be established without further parameter calibration, by operating on the void ratio, as proposed by [Choo, 2018].

The secant angle of friction of Bolton's formula, Section 3.3.2, is modified to accommodate the GPYS implementation in the following manner

$$\varphi(p) = \varphi_{cv} + bI_R = \varphi_{cv} + b \left(I_d \left(Q - \ln \left(\frac{p - p_{apex}}{-1 \text{ kPa}} \right) \right) - R \right), \quad 0 \leq I_R \leq 4 \quad \wedge \quad p < p_{apex}. \quad (4.10)$$

The Bolton generator goes to zero at the origin, and a cohesion parameter to include a small hydrostatic tensile strength is included in the model presented here, for the purpose of a circular apex. If this is an undesired property, an exact implementation as in Appendix C can be established as well, however, the present formulation is more robust in numerical analysis. Adopting the yield criterion of Equation (3.8) in terms of the Haigh Westergaard coordinates for $\theta = \pi/3$, the expression for ρ_c is found as

$$\rho_c(p) = -2 (p - p_{apex}) \sin(\varphi(p)) \left(\sqrt{3/2} - 1/\sqrt{6} \sin(\varphi(p)) \right)^{-1}. \quad (4.11)$$

As the angle of friction depends on the hydrostatic pressure, a slight difference from the previous models as the ρ_t/ρ_c -ratio, becomes dependent on this as well

$$\rho_t(p) = \rho_c(p) \left(\alpha + \frac{3 - \sin(\varphi(p))}{3 + \sin(\varphi(p))} (1 - \alpha) \right).$$

Once ρ_t and ρ_c are calculated for a certain level of hydrostatic stress, the remainder of the deviatoric geometry are calculated as described in Sections 4.2 and 4.3. The hydrostatic stress is divided by negative 1kPa in Equation (4.10), as a slight modification to Bolton's formula from [Bolton, 1986], to accommodate dimensionality and the sign convention in this thesis. The function in Equation (4.11) is combined with an apex rounding analogously to Section 4.4, and the multifunction for the generators reads

$$\rho_c(p) = \begin{cases} -2 (p - p_{apex}) \sin(\varphi(p)) \left(\sqrt{3/2} - 1/\sqrt{6} \sin(\varphi(p)) \right)^{-1}, & p \leq p_t \\ (r_4^2 - (p - c_{41})^2)^{0.5}, & p_t < p < (1 - \beta_4)p_{apex} \end{cases}, \quad (4.12)$$

where

$$p_{apex} = \frac{2c\sqrt{k_b}}{k_b - 1}, \quad k_b = \frac{1 + \sin(\phi_{cv} + b_4)}{1 - \sin(\phi_{cv} + b_4)}.$$

The transition pressure, p_T , and the centre of the apex circle, \mathbf{c}_4 , are calculated to accommodate the relations in Figure 4.9. However, for this model these are calculated by an iterative procedure, as the meridian is nonlinear, and done once for each material type. To obtain a continuous yield surface, the deviatoric geometry from Equation (4.6) is adopted, and the yield function reads

$$f_n = \|\boldsymbol{\sigma}_d^* - \mathbf{c}_n^*(p)\| - r_n(p), \quad \boldsymbol{\sigma}_d^* = [\sigma_2^* \quad \sigma_3^*]^T, \quad \sigma_1 \geq \sigma_2 \geq \sigma_3. \quad (4.13)$$

Here, subscript n denotes the deviatoric region according to Table 4.1. This yield surface is implemented in a MATLAB source code, and used in numerical applications in Section 5.2. The implementation in a numerical framework is straight forward as the yield surface is continuous, see for instance Appendix D. The fundamental mathematics behind the implementation is given by the return mapping procedure and consistent tangent operator in Section 2.5 and 2.4, respectively. However, the consistent tangent is modified according to the method described in Appendix D, to overcome the lack of C^2 continuity.

In Section 5.2, this yield surface model is used as an optimised material fit, demonstrating its versatile shape. The surface is exemplified in a spatial illustration in Figure 4.10, as a smooth continuous approximation of the Bolton surface, with parameter settings as in Table 4.2.

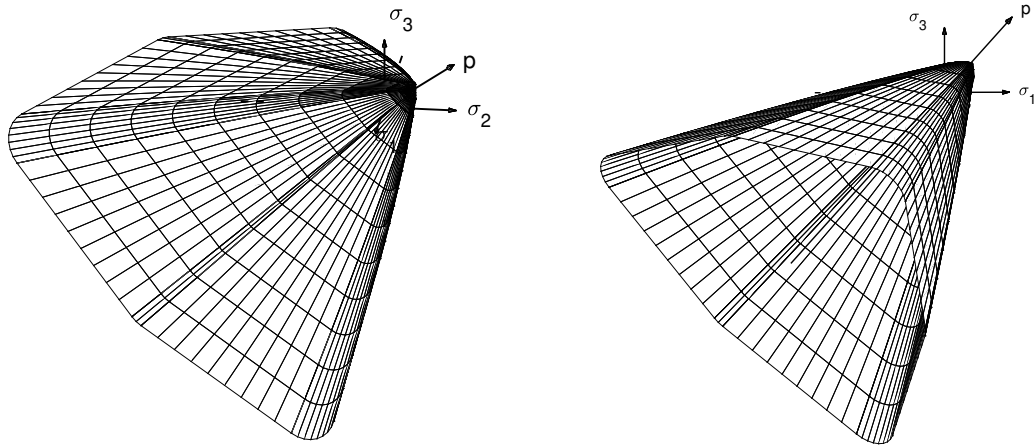


Figure 4.10: 3D visualization of a continuous approximation of the Bolton criterion with a positive apex. Parameters are set as, $\varphi_{cv} = 25$ deg, $c = 10$ kPa, $\alpha = 0.0$, $\beta_1 = 0.00$, $\beta_2 = \beta_3 = \beta_4 = 0.2$, $Q = 10$, $R = 1$, $b = 5$, which corresponds to a plane strain Bolton model for sands of quartz grains. Corner roundings are exaggerated for illustrative purposes

Table 4.2: Description of the surface parameters and approximation of some existing yield surfaces.

Description Symbol Range	Parameters									
	Angle of Friction	Cohesion	ρ_t/ρ_c -ratio	Curvature parameters				Mineralogy		
	φ_{cv}]0; $\pi/2$ [$c^{\dagger\dagger\dagger}$ > 0	α [0; 1]	β_1 [0; 1]	β_2 [0; 1]	β_3 [0; 1]	$\beta_4^{\dagger\dagger}$ [0; 1]	Q ≥ 0	R ≥ 0	b ≥ 0
Special cases of existing plasticity models										
Bolton	as is	as is	0.00	0.00 [†]	0.01	0.01	0.01	as is	as is	as is
Mohr Coulomb	as is	as is	0.00	0.00 [†]	0.01	0.01	0.01	0.00	0.00	0.00
Extended Tresca	as is	as is	1.00	0.00 [†]	0.01	0.01	0.01	0.00	0.00	0.00
Drucker-Prager	as is	as is	1.00	1.00	0.01	0.01	0.01	0.00	0.00	0.00
Reuleaux	as is	as is	as is	1.00	0.01	0.01	0.01	0.00	0.00	0.00

[†] An appropriately small value is 10^{-4} .

^{††} Set to 1.00 for a tension cut-off

^{†††} Units of pressure

Nonlinear criteria, which are inseparable with respect to ρ_c and p , are not conveniently adopted in the GPYS format. However, the model formulated in this section is fully capable of approximating other nonlinear models. A brief demonstration of such an approximation is presented here, where a series of stress states on the Compressive generator of the Hoek-Brown model are calculated by

$$\boldsymbol{\sigma} = \left[\sigma_1; \quad \sigma_1; \quad \sigma_1 - \sigma_{ci} \left(s - m_b \frac{\sigma_1}{\sigma_{ci}} \right)^a \right]^T,$$

and the deviator norm, ρ , is then calculated. The least squared error with respect to the compressive generator of Equation (4.12) is then minimized for the corresponding values of p . The parameters used in the optimization is φ_{cv} , Q , R , and b , and the compressive generators are juxtaposed in Figure 4.11, for an arbitrarily chosen set of Hoek-Brown parameters. The cohesion of the proposed model is set to render the apex of Hoek-Brown, which reads

$$c = \frac{s\sigma_{ci} k_b - 1}{m_b 2\sqrt{k_b}},$$

as the apex of the Hoek-Brown model is located at $s\sigma_{ci}/m_b$ of hydrostatic stress. One thousand equispaced stress states on the Hoek-Brown compressive generator are calculated and the parameters of the GPYS-NC model is calibrated to these data by the least squares method. The parameter settings of the Hoek-brown approximation in Figure 4.11 is listed in Table 4.3. Judging from Figure 4.11 and the standard deviation

$$\text{standard deviation} = \sqrt{\frac{\sum_{i=1}^{1000} (f(\sigma_i))^2}{1000}} = 0.057 \text{ MPa},$$

the present formulation of the GPYS format is capable of emulating the Hoek-Brown model.

Table 4.3: The present formulation of GPYS as an approximation of the Hoek-Brown model.

Hoek-Brown	s	m_b	a	σ_{ci} [MPa]						
	0.30	1.70	0.50	210.00						
GPYS-NC	φ_{cv}	c [MPa]	α	β_1	β_2	β_3	β_4	Q	R	b
	37.26	1431.86	0.00	0.00	0.01	0.01	0.01	11.24	0.00	13.55

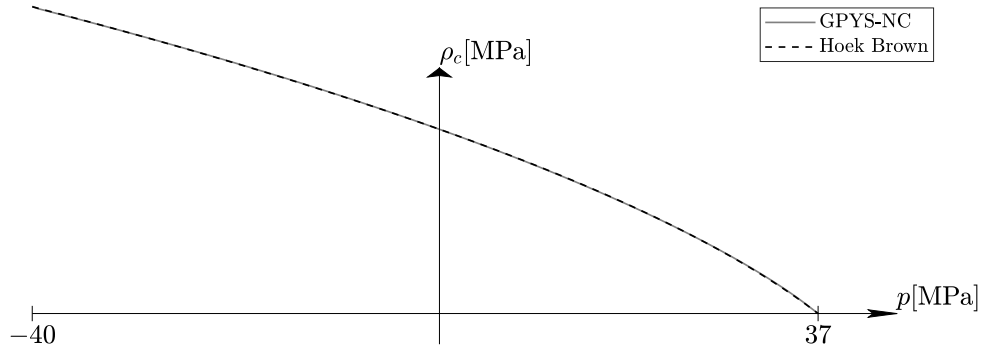


Figure 4.11: The present formulation of GPYS as an approximation of the Hoek-Brown model seen in the compressive meridian with parameters from Table 4.3.

4.6 Overview of the New Models

An overview of the yield surface models described in the preceding is given in this section. Three different models are represented: a formulation with linear generators and a discontinuous deviatoric trace, denoted GPYS-LD, a formulation with linear generators and a rounded apex and continuous deviatoric trace, denoted GPYS-LC, and finally, a formulation with nonlinear Bolton generators, a rounded apex and continuous deviatoric trace, denoted GPYS-NC. The GPYS-LD model is described in thorough detail in Appendix C and the GPYS-LC model in Appendix D. A schematic overview of the models is given in Table 4.4, in the form of the yield criterion along with the mathematical expressions to evaluate this, and a description of the input parameters. As a general note, the ρ_t/ρ_c -ratio changes with the stresses in the GPYS-NC model, which means that all the mathematical expressions for the deviatoric trace are calculated for each stress state. While this aspect of the nonlinear formulation makes it less efficient, it is a more accurate model.

As a general note on the yield criteria derived in this chapter, these are intended for numerical applications. The centre and radii may be awkward in hand calculations, however, elegantly implemented in a numerical framework.

Table 4.4: The three novel yield surfaces based on the GPYS format. All expressions assumes $\sigma_1 \geq \sigma_2 \geq \sigma_3$.

GPYS-LD	$f(\sigma) = \ \sigma_d^* - \bar{c}_1^* \rho_c\ - \bar{r}_1 \rho_c$										
Parameters	Angle of Friction φ] $0; \pi/2$ [Cohesion c^\dagger > 0	ρ_t/ρ_c -ratio α [0; 1]	Curvature parameter β_1 [0; 1]							
Deviatoric	$\bar{c}_1^* = \begin{cases} \bar{r}_1 \cos((1 - \beta_1) \gamma) - \bar{\rho}_t \\ \bar{r}_1 \sin((1 - \beta_1) \gamma) \end{cases}$ $\bar{\rho}_t = \alpha + (3 - \sin \varphi)/(3 + \sin \varphi) (1 - \alpha)$			$\bar{r}_1 = \sqrt{(\sqrt{3}/2)^2 + (\bar{\rho}_t - 0.5)^2}/(2 \sin(\beta_1 \gamma))$ $\gamma = \arctan((\bar{\rho}_t - 0.5)/(\sqrt{3}/2))$							
Meridian	$\rho_c = \frac{1 - k}{\sqrt{2/3}(k/2 + 1)} \left(p - \frac{2c\sqrt{k}}{k - 1} \right)$			$k = (1 + \sin \varphi)/(1 - \sin \varphi)$							
GPYS-LC	$f_n(\sigma) = \ \sigma_d^* - \bar{c}_n^* \rho_c\ - \bar{r}_n \rho_c$										
Parameters	Angle of Friction φ] $0; \pi/2$ [Cohesion c^\dagger > 0	ρ_t/ρ_c -ratio α [0; 1]	Curvature parameters β_1 β_2 β_3 β_4 [0; 1] [0; 1] [0; 1] [0; 1]							
Deviatoric	$(\bar{c}_n^*, \bar{r}_n) = \begin{cases} \left(\begin{cases} \bar{r}_1 \cos((1 - \beta_1) \gamma) - \bar{\rho}_t \\ \bar{r}_1 \sin((1 - \beta_1) \gamma) \end{cases}, \sqrt{(\sqrt{3}/2)^2 + (\bar{\rho}_t - 0.5)^2}/(2 \sin(\beta_1 \gamma)) \right), & \sigma \in R_I \text{ Tab. 4.1} \\ \left((1 - \beta_2) \begin{cases} -1/2 \\ -\sqrt{3}/2 \end{cases}, \bar{r}_1 - \ \bar{c}_1^* - \bar{c}_2^*\ \right), & \sigma \in R_{II} \text{ Tab. 4.1} \\ \left((1 - \beta_3) \begin{cases} -\bar{\rho}_t \\ 0 \end{cases}, \bar{r}_1 - \ \bar{c}_1^* - \bar{c}_3^*\ \right), & \sigma \in R_{III} \text{ Tab. 4.1} \end{cases}$ $\bar{\rho}_t = \alpha + (3 - \sin \varphi)/(3 + \sin \varphi) (1 - \alpha)$ $\gamma = \arctan((\bar{\rho}_t - 0.5)/(\sqrt{3}/2))$										
Meridian	$\rho_c = \begin{cases} \frac{1 - k}{\sqrt{2/3}(k/2 + 1)} \left(p - \frac{2c\sqrt{k}}{k - 1} \right), & p \leq c_{41} + r_4 \cos \zeta_4 \\ \left((r_4)^2, -(p - c_{41})^2 \right)^{0.5}, & c_{41} + r_4 \cos \zeta_4 < p \leq (1 - \beta_4) 2c\sqrt{k}/(k - 1) \end{cases}$ $c_4 = \left((1 - \beta_4) \frac{2c\sqrt{k}}{k - 1} - r_4 \right) \begin{cases} 1 \\ 0 \end{cases}, \quad r_4 = \beta_4 \frac{2c\sqrt{k}}{k - 1} \cot(\zeta_4) \cot\left(\frac{\zeta_4}{2}\right), \quad \zeta_4 = \arctan \frac{-1}{\mu}$										
GPYS-NC	$f_n(\sigma) = \ \sigma_d^* - c_n^*(p)\ - r_n(p)$										
Parameters	Angle of Friction φ_{cv}] $0; \pi/2$ [Cohesion c^\dagger > 0	ρ_t/ρ_c -ratio α [0; 1]	Curvature parameters β_1 β_2 β_3 $\beta_4^{\dagger\dagger}$ [0; 1] [0; 1] [0; 1] [0; 1]				Mineralogy Q R b ≥ 0 ≥ 0 ≥ 0			
Deviatoric	$(c_n^*, r_n) = \begin{cases} \left(\begin{cases} r_1 \cos((1 - \beta_1) \gamma) - \rho_t \\ r_1 \sin((1 - \beta_1) \gamma) \end{cases}, \rho_c \sqrt{(\sqrt{3}/2)^2 + (\rho_t - 0.5)^2}/(2 \sin(\beta_1 \gamma)) \right), & \sigma \in R_I \text{ Tab. 4.1} \\ \left((1 - \beta_2) \begin{cases} -1/2 \\ -\sqrt{3}/2 \end{cases}, r_1 - \ c_1^* - c_2^*\ \right), & \sigma \in R_{II} \text{ Tab. 4.1} \\ \left((1 - \beta_3) \begin{cases} -\rho_t \\ 0 \end{cases}, r_1 - \ c_1^* - c_3^*\ \right), & \sigma \in R_{III} \text{ Tab. 4.1} \end{cases}$ $\rho_t = \rho_c (\alpha + (3 - \sin \varphi(p))/(3 + \sin \varphi(p)) (1 - \alpha))$ $\gamma = \arctan((\rho_t - 0.5\rho_c)/(\rho_c \sqrt{3}/2))$ $\varphi(p) = \varphi_{cv} + bI_R = \varphi_{cv} + b(I_d(Q - \ln((p - p_{apex})/-1 \text{ kPa})) - R), \quad 0 \leq I_R \leq 4 \quad \wedge \quad p < p_{apex}.$										
Meridian	$\rho_c = \begin{cases} -2(p - p_{apex}) \sin(\varphi) \left(\sqrt{3}/2 - 1/\sqrt{6} \sin(\varphi) \right)^{-1}, & p \leq p_t \\ (r_4^2 - (p - c_{41})^2)^{0.5}, & p_t < p < p_a \end{cases}$ where, r_4 and c_4 , are calculated by an iterative procedure to ensure the geometry in Figure 4.9 and $p_{apex} = 2c\sqrt{k_b}/(k_b - 1)$								$k_b = \frac{1 + \sin(\varphi_{cv} + 4b)}{1 - \sin(\varphi_{cv} + 4b)}$ $p_a = (1 - \beta_4) p_{apex}$		

$\sigma^* = \mathbf{T}\sigma$, with \mathbf{T} from Equation (4.1), and $\sigma_d^* = [\sigma_2^* \ \sigma_3^*]^T$.

5 | Finite Element Analysis of Geomechanical Systems

In this chapter, the General Parametric Yield Surface Format is applied in finite element analysis of typical geotechnical problems. Most of the studies are conducted to investigate the intermediate principle stress influence, where an optimized material fit with the GPYS-LD model is compared to conventional Mohr-Coulomb models. Secondly, the advanced 10-parameter surface of GPYS-NC is calibrated for a more optimized fit than with the GPYS-LD model. This analysis are conducted to investigate whether essential discrepancies are found and to demonstrate the use of the GPYS-NC model. The GPYS-LC model is used in analysis of a square spread footing in Appendix D, where the computational performance is the subject of study, and in Section 5.1.4 with a tension cut-off. Sands of different strength properties are considered as this evidently influences the yield surface shape as mentioned in the thesis introduction, see Figure 1.2.

This chapter is accompanied by Appendix A, where the finite elements used in the analysis, and the test data used for material calibration is found. Furthermore, the GPYS-LD model as an approximation of the Mohr-Coulomb model is documented in Appendix A.2, based on the analysis in this chapter. Isotropic and linearly elastic perfectly plastic material behaviour along with associated flow is assumed, and the calculations are based on small strain theory, in all the analysis.

5.1 Influence of The Intermediate Principle Stress

In this section, strip footing, spread footing and slope stability problems are analysed, in elasto-plastic finite element analysis. The material properties used in the analysis are obtained by calibrating the parameters to experimental data from true triaxial tests, rendering realistic properties. The results obtained with the GPYS-LD model are compared to a conventional Mohr-Coulomb model, to investigate the intermediate principle stress influence and elucidate its prospects as an optimized material model.

5.1.1 Calibration of surface parameters

The parameters of the GPYS-LD model is calibrated with experimental data from true triaxial tests performed and published by [Bønding, 1977], which are presented and described in Appendix A.1. The GPYS-LD model is fitted by means of the least squares method to the individual batches of test data. The Mohr-Coulomb model is taken directly with φ and c from the GPYS-LD model, which corresponds well with a conventional fit to the test data in triaxial compression. The experimental results has been normalized by a scale factor to the nearest whole multiple of 50 of hydrostatic pressure and is depicted in Figure 5.1 along with the calibrated yield surface deviatoric trace.

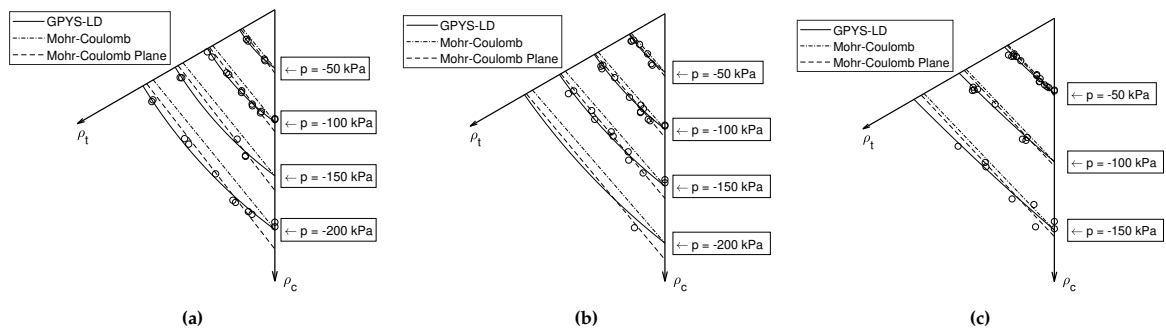


Figure 5.1: A sextant of the deviatoric trace, $\sigma_1 \geq \sigma_2 \geq \sigma_3$, of the model settings along with data from true triaxial tests normalised with respect to the nearest fifty'th value of the hydrostatic pressure by a scale factor (a) Dense (b) Medium dense and (c) Loose sand.

A second Mohr-Coulomb model is included in the analysis as well, given by the plane strain adjustment of the angle of friction suggested by the Danish National Annex to Eurocode 7 [Distribute, 2015]

$$\varphi_{pl} = (1 + 0.1I_d)\varphi_{tr},$$

where, I_d and φ_{tr} , are the relative density and the internal friction angle determined from triaxial tests. The fits are accepted based on the residual plots of Figure 5.2, where the yield function, $f(\sigma)$ is plotted over the hydrostatic pressure. It is, however, noted that the best fit of the new criteria, suggest a small cohesion in all batches, although the test material supposedly should be cohesionless. In practical application, the limited tensile strength of the material should be modelled with a tension cut-off, as with the GPYS-LC model.

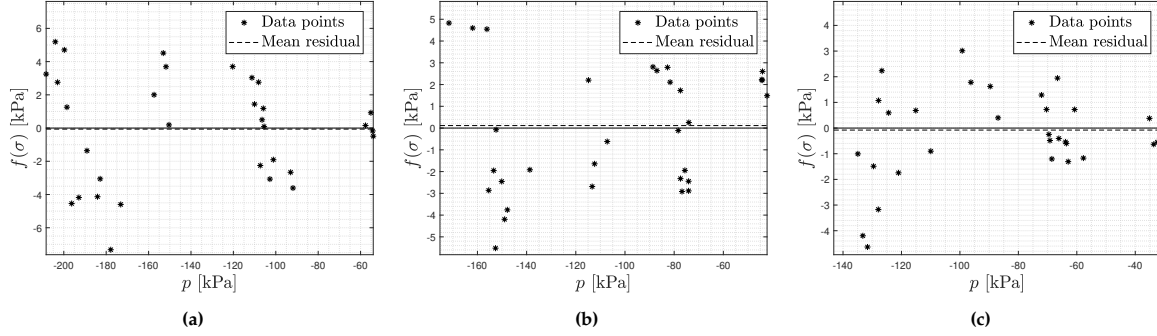


Figure 5.2: Residual plot over the hydrostatic pressure of the test data (a) Dense (b) Medium dense and (c) Loose sand.

The calibrated parameters of the plasticity models are listed in Table 5.1, along with relevant material properties. The Mohr-Coulomb setting of the GPYS-LD model, $\alpha = \beta = 0$, is simply referred to as Mohr-Coulomb. The full deviatoric traces of the models and the compression meridians are illustrated in Figure 5.3 and 5.4.

Table 5.1: Yield criteria parameters based on true triaxial tests performed by Danish Geotechnical Institute and published in [Bønding, 1977].

	Dense sand				Medium dense sand				Loose sand			
	$e = 0.55$	$\gamma = 1.71$			$e = 0.62$	$\gamma = 1.64$			$e = 0.75$	$\gamma = 1.51$		
	φ [deg]	c [kPa]	α	β_1	φ [deg]	c [kPa]	α	β_1	φ [deg]	c [kPa]	α	β_1
GPYS-LD	41.40	3.92	0.15	0.88	36.90	0.91	0.12	0.62	30.50	2.94	0.19	0.13
Mohr-Coulomb	41.40	3.92	0.00	0.00	36.90	0.91	0.00	0.00	30.50	2.94	0.00	0.00
Mohr-Coulomb Plane	45.05	3.92	0.00	0.00	39.40	0.91	0.00	0.00	31.40	2.94	0.00	0.00
Paul-Mohr-Coulomb	41.40	3.92	0.15	0.00	36.90	0.91	0.12	0.00	30.50	2.94	0.19	0.00

e Void ratio $e_{min} = 0.51$ $e_{max} = 0.85$
 γ Sample density [t/m³] Grain density, $\gamma_s = 2.65$ [t/m³]

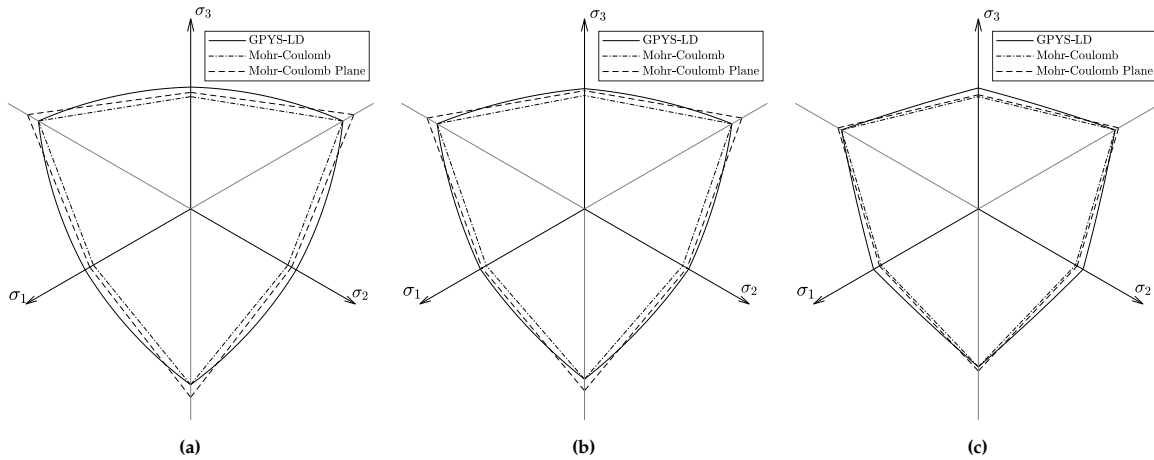


Figure 5.3: Deviatoric trace, at $p = -25$ kPa, of the GPYS-LD and Mohr-Coulomb models (a) Dense (b) Medium dense and (c) Loose sand.

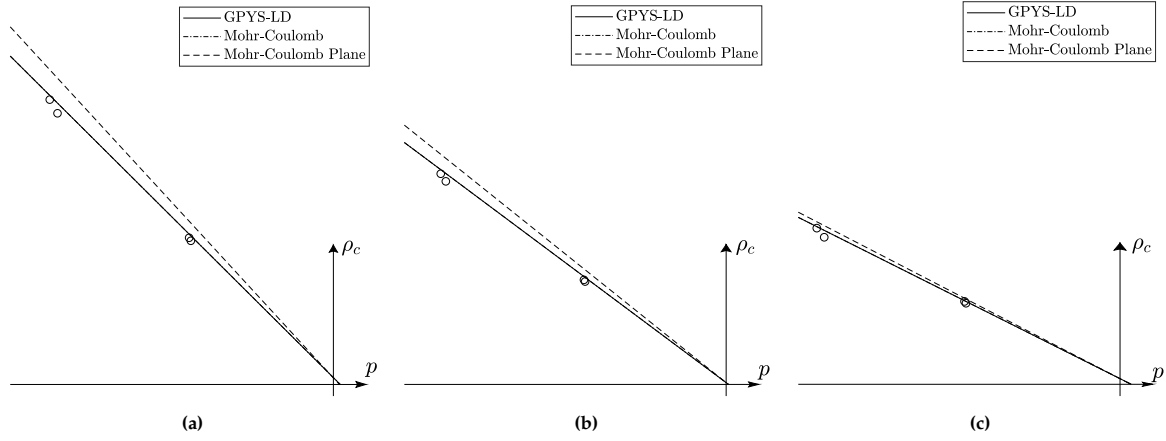


Figure 5.4: Meridian plane of the GPYS-LD and Mohr-Coulomb models, with the data points in triaxial compression from Appendix A.1 (a) Dense (b) Medium dense and (c) Loose sand.

5.1.2 Vertical concentric loading of strip footing

A vertically loaded strip footing is analysed in this section. This is a typical plane strain problem in geotechnical engineering, as the strip footing can be approximated of infinite extend in the out of plane direction. The in plane results such as the ultimate limit load or the vertical displacement are then found pr. unit length. For assessment of the numerical solution, the well known formula of the bearing capacity is used, as suggested by [Terzaghi, 1951, ch. 7],

$$R' = \gamma \frac{1}{2} B^2 N_\gamma + c B N_c + q' B N_q. \quad (5.1)$$

Here, γ , B and q' , are specific gravity, footing width and effective surcharge, respectively, and N_γ , N_c and N_q are dimensionless factors, which depends on the soil strength. Equation (5.1) is adequate in this analysis, however, a more versatile form of was proposed by Brinck Hansen in 1970, to account for load eccentricity and 3D footings. In this analysis, $q' = 0$, as the footing is placed directly on the soil surface. The dimensionless factors are given by the expressions

$$N_\gamma = \frac{1}{4} ((N_q - 1) \cos \varphi)^{3/2} \quad \vee \quad N_c = \frac{N_q - 1}{\tan \varphi} \quad \vee \quad N_q = \frac{1 + \sin \varphi}{1 - \sin \varphi} \exp(\pi \tan \varphi). \quad (5.2)$$

The N_c and N_q factors yields the exact collapse load when neglecting the soil weight, $\gamma = 0$, as found by Prandtl in 1920. This under assumption of a perfectly plastic linearly elastic material which obeys Mohr-Coulombs yield criterion with associated plasticity. However, that is a highly theoretical situation, and an exact analytical solution have not yet been formulated for the N_γ -problem. The N_γ factor has been proposed in various formulations, however, the most accepted solution for N_γ was established numerically in a finite difference framework by [Martin, 2003]. Equation (5.1) is in general found to yield conservative values for the bearing capacity, in comparison with results from numerical analysis.

Model description

A sketch of the model with geometry, boundary conditions and soil material properties along with the mesh grid used in the analysis is presented in Figure 5.5. No formal mesh refinement studies have been conducted, but the mesh density is increased in the zone where the shear slip failure occurs, and severely increased around the stress singularity at the outer corner of the foundation. The results are compared to the bearing capacity formula (5.1) and the commercial finite element software, OptumG2, and the finite element model presented in Figure 5.5 is found to perform quite well. The system is discretized, using the LST elements, as described in Appendix A.3 with a three point Gauss integration scheme. The line of symmetry is exploited to model merely one half of the system. An analysis with three of the material models from Table 5.1 are conducted. The foundation is assumed to behave linearly elastic and the soil material as linearly elastic perfectly plastic. The initial stresses in the soil domain varies linearly over the depth, using the depth coordinate from Figure 5.5

$$\sigma_{yy} = -d\gamma \quad \wedge \quad \sigma_{xx} = \sigma_{zz} = K_0 \sigma_{yy}.$$

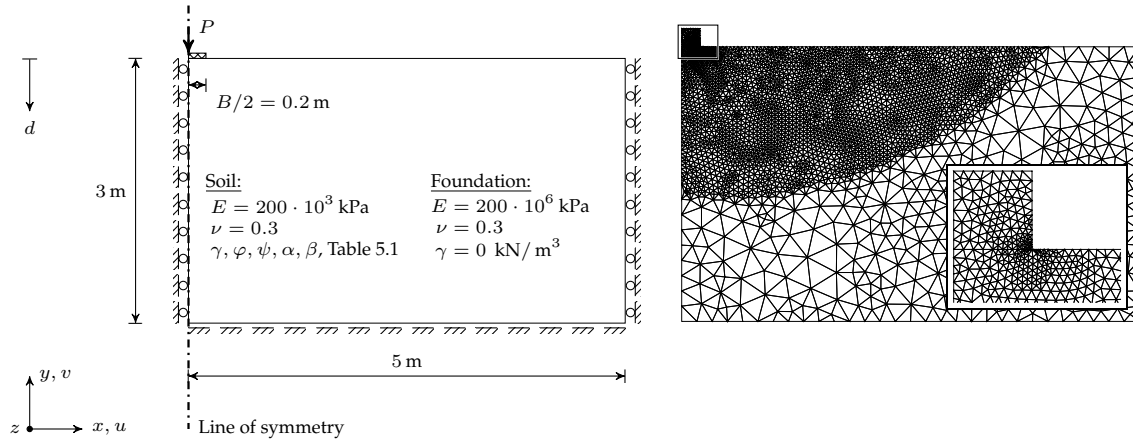


Figure 5.5: Model of strip footing with physical properties of soil material and the mesh grid of the finite element model.

The at rest earth pressure coefficient, K_0 , is set equal to one in the analysis, and the gravitational pull is 9.81 m/s^2 . The initial stresses are introduced at the Gauss integration points in the finite element mesh, prior to the nonlinear analysis. The analysis is performed by incrementing a downwards forced displacement on the topside nodes of the footing. The internal forces calculated with Equation (2.12) then yields the nodal reactions resulting from the forced displacement. The reaction force is evaluated as the twice the sum of the nodal forces at the topside nodes. The forced displacement is applied over 200 equal increments in all the analysis, however, the final displacement is varied with the type of sand.

Failure mode assessment

To assess the model, the failure mode is visualized in contour plots in Figure 5.8 from six of the analysis. The right hand side shows the results obtained with the GPYS-LD model and the left hand side, the Mohr-Coulomb model. The contours show the rate of maximum plastic shear strain, $(\varepsilon_1 - \varepsilon_3)/2$, at the final load step. The GPYS-LD model reveals a smaller angle of the shear slip line with the horizontal than the Mohr-Coulomb model, resulting in a larger plastic zone. The decrease in this angle, corresponds to an increase in the angle of friction, which is more pronounced for the stronger sand types. It is further noted, that the failure mode corresponds with the well-known pattern, which has been argued by for instance [Terzaghi, 1951, ch. 7], in formulation of the bearing capacity equation (5.1). The domain is deemed wide and deep enough to avoid interference from the far plane boundary.

Bearing capacity

The load bearing capacity from the Analysis, taken as the force reaction at failure, is presented in Table 5.2. These are compared to the corresponding values calculated with the bearing capacity formula (5.1), which in all cases gives a lower value. This outcome is expected as $\gamma \neq 0$, and with the displacement based LST elements, which often gives an upper bound value on the collapse load, however, not rigorously [Krabbenhoft et al., 2016c]. The Load displacement curves of the analysis are presented in

Table 5.2: Comparison of bearing capacity for the different material models and formula (5.1).

	Dense sand		Medium dense sand		Loose sand	
	Capacity [kN/m]	Ratio [-]	Capacity [kN/m]	Ratio [-]	Capacity [kN/m]	Ratio [-]
Formula (5.1)	285.52	0.80	82.69	0.81	55.81	0.81
MC	356.83	1.00	102.64	1.00	69.05	1.00
MC Plane	653.98	1.83	152.28	1.48	76.40	1.11
GPYS-LD	1256.38	3.52	199.23	1.94	106.26	1.54

Figure 5.11, along with the corresponding yield surface depicted in deviatoric plane. It is obvious, by inspection of Figure 5.11, that the influence of the intermediate principal stress becomes increasingly pronounced with decreasing void ratio. The load-displacement-curves exhibits a distinct kink in the Mohr-Coulomb models as the load bearing capacity is reached, opposed to the GPYS-LD models. In

Appendix C a similar strip footing system is analysed with different material models, including the Paul-Mohr-Coulomb model from Table 5.1, where the ρ_t/ρ_c -ratio is found as the governing impact on the limit load.

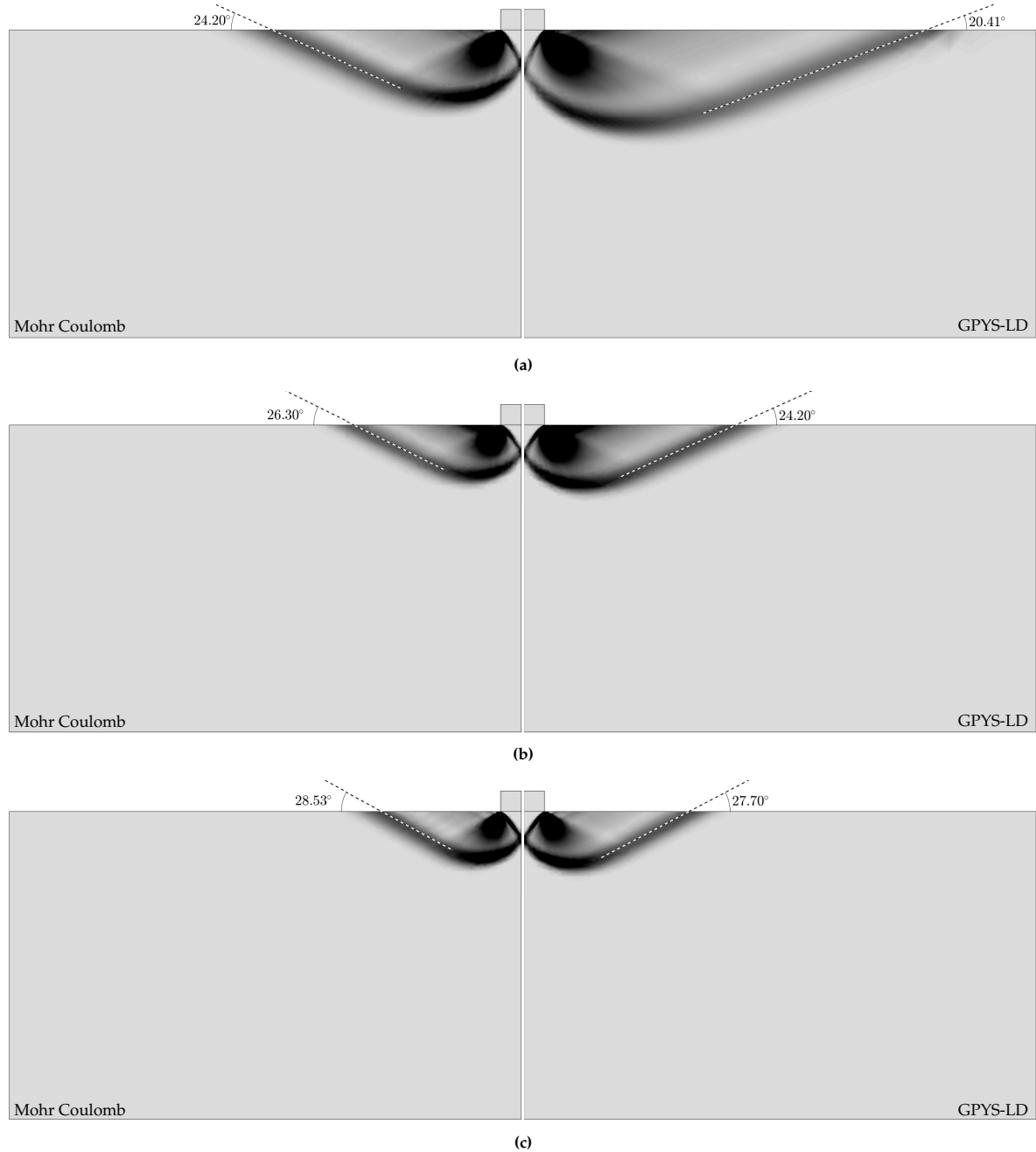


Figure 5.8: Rate of maximum plastic shear strain at failure of the analysis with Mohr-Coulomb and the GPYS-LD model. (a) Dense sand, (b) Medium dense sand and (c) Loose sand.

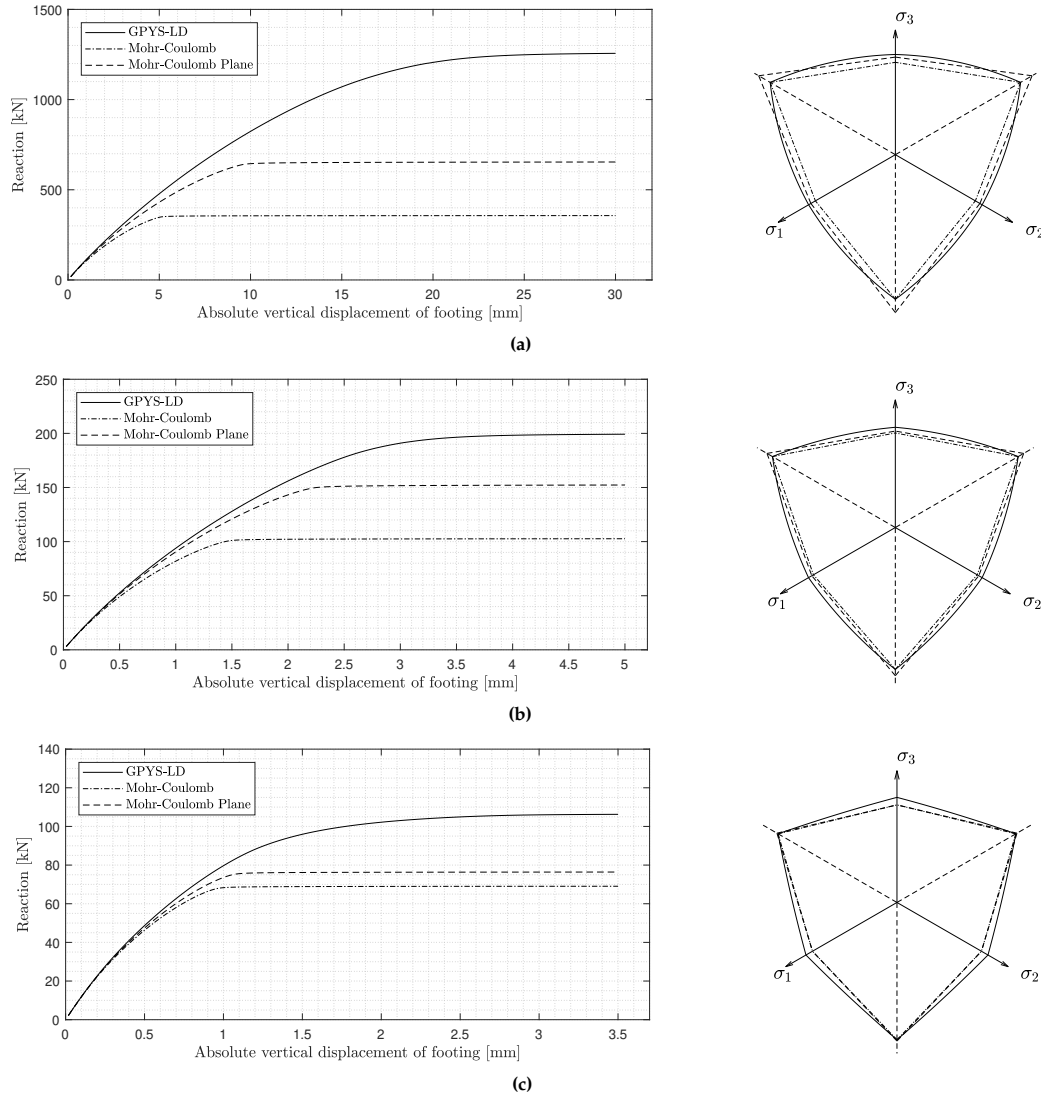


Figure 5.11: Load displacement curves from strip footing analysis with Material model fits from Table 5.1, seen in deviatoric plane at -25 kPa (a) Dense sand, (b) Medium dense sand and (c) Loose sand.

5.1.3 Vertical concentric loading of spread footing

In this section, vertical concentric loading of a rectangular spread footing system, is considered. This analysis is included herein, as it is a typical 3-Dimensional geotechnical problem. Three different width to length ratios of the footing is considered with the material models of Table 5.1, including the Paul-Mohr-Coulomb setting. The simulations are conducted in the commercial software, Abaqus, with the GPYS-LD model included as a user-defined subroutine. Once again, linearly elastic perfectly plastic material behaviour and associated flow, are assumed.

Model Description

The system is discretized with standard 10-node tetrahedral elements, with quadratic displacement interpolation and a 4 point Gauss integration scheme. A top view of the system is sketched and the mesh grid is visualized in Figure 5.24. The system is a $10 \times 10 \times 3$ m³ soil domain, with a shallow spread footing of 0.4×0.4 m², 0.4×0.8 m² and 0.4×1.6 m², respectively. Two symmetry planes are exploited to model merely one quarter of the system. The bottom surface is constrained in all directions and the vertical sides are constrained in their respective normal directions. The load is emulated with a uniform downwards displacement of the nodes in the footing footprint. Three of the plasticity models from Table 5.1 are analysed for the three different gradings of sand. Namely the GPYS-LD least square fit, the Paul-Mohr-Coulomb model where only the ρ_t/ρ_c -ratio are adjusted to the data and the Mohr-Coulomb

compression fit. The Paul-Mohr-Coulomb model is included here, as the ρ_t/ρ_c -ratio may be determined from standard cylindrical triaxial tests, and it may serve an affordable material optimisation, given that some noteworthy increase in bearing capacity can be observed. The at rest earth pressure coefficient and the gravitational pull are set as $K_0 = 1$ and $g = 9.81 \text{ m/s}^2$, respectively.

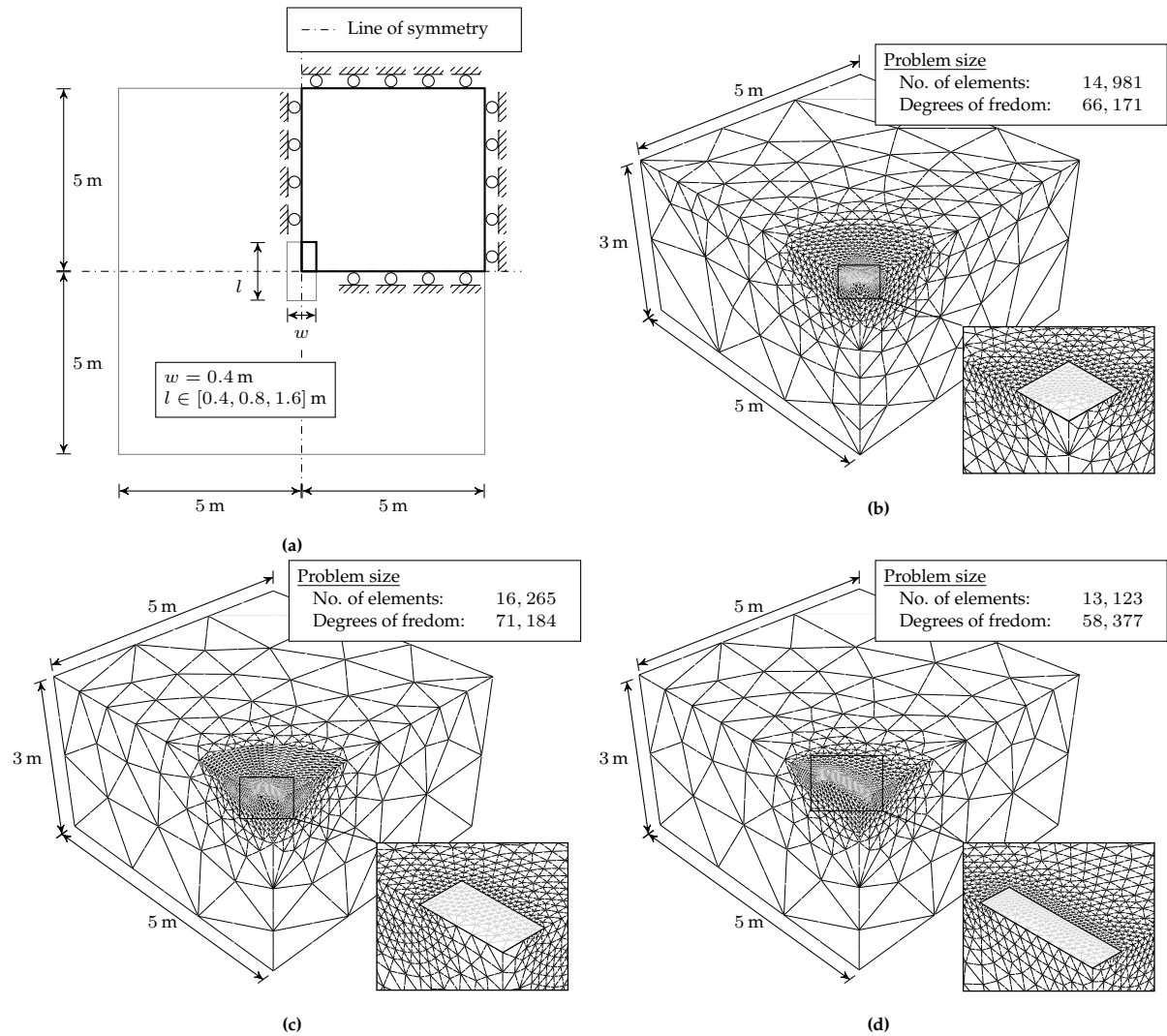


Figure 5.12: Mechanical system for spread footing (a) Top view with geometry and boundary conditions, the bottom surface is restrained in all directions as well. Width to length ratios (b) 1:1 (c) 1:2 and (d) 1:4.

Failure mode assessment

The simulation integrity are qualitatively assessed based on the failure mode, which is revealed in contours of the rate of plastic shear strain over the domain. This contour is depicted for the square and the rectangular 1:4 footing systems in Figure 5.13 for the GPYS-LD material model for dense sand. The failure modes are in good agreement with expected results, as the strip footing failure mode is recognised at the domain side. It is further noted, that the failure mode is unaffected by the far plane boundary conditions, validating the size of the domain.

Comparison of limit load

The force displacement history from the conducted analysis are plotted in Figure 5.14, 5.15, 5.16, and the collapse load along with the communal ratios between the models are presented in Table 5.3. Again, the increase in limit load is more pronounced in the more dense sand types. A more moderate increase in load bearing capacity is found, opposed to the plane strain problem from Section 5.1.2. The load bearing ratio increases severely with the width to length ratio, which corresponds to increasing the zone

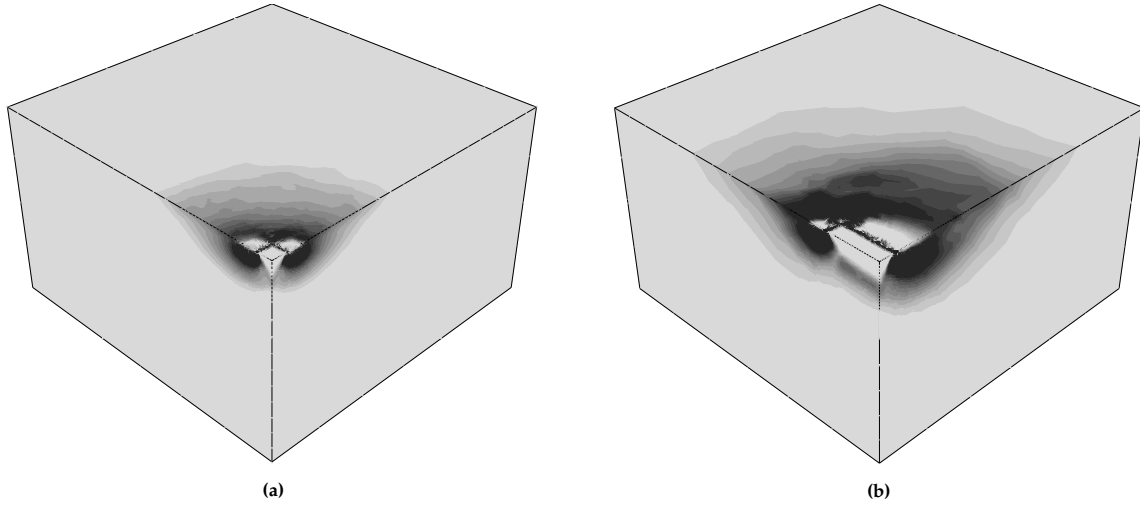


Figure 5.13: Contours of maximum plastic shear strain rate with the dense sand GPYS-LD model **a)** 1:1 footing and **b)** 1:4 footing.

of approximate plane strain conditions. The Paul-Mohr-Coulomb models does not provide nearly as much bearing capacity as the optimised least square fit. However, these can be obtained with standard cylindrical triaxial tests, and still bring a decent increase in bearing capacity.

Table 5.3: Simulation results and increase ratio in load bearing capacity, for the three different spread footing systems.

System	Model	Dense sand		Medium dense sand		Loose sand	
		Capacity [kN]	Ratio [-]	Capacity [kN]	Ratio [-]	Capacity [kN]	Ratio [-]
1:1	Mohr-Coulomb	343.18	1.00	70.62	1.00	46.21	1.00
	Paul-Mohr-Coulomb	376.23	1.10	73.87	1.05	48.12	1.04
	GPYS-LD	479.58	1.40	84.18	1.19	48.98	1.06
1:2	Mohr-Coulomb	572.79	1.00	126.69	1.00	81.48	1.00
	Paul-Mohr-Coulomb	699.53	1.22	141.36	1.12	89.67	1.10
	GPYS-LD	1,008.18	1.76	176.38	1.39	92.47	1.13
1:4	Mohr-Coulomb	993.65	1.00	231.85	1.00	147.16	1.00
	Paul-Mohr-Coulomb	1,388.35	1.40	280.72	1.21	174.06	1.18
	GPYS-LD	2,194.35	2.21	374.99	1.62	180.22	1.22

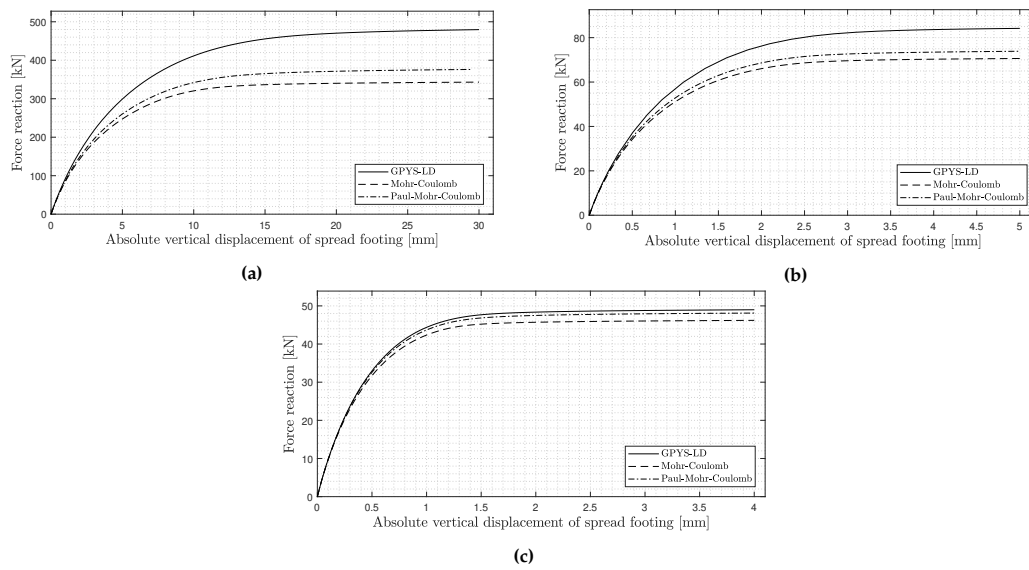


Figure 5.14: Load displacement curves from simulations for fully rough spread footing of width to length ratio = 1:1, for **(a)** Dense sand, **(b)** Medium dense sand, and **(c)** Loose sand.

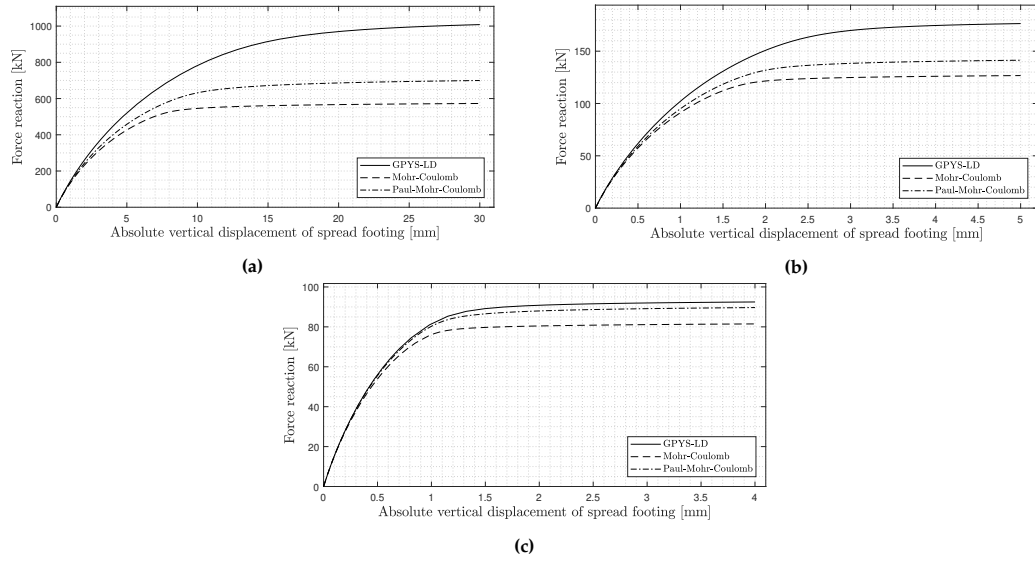


Figure 5.15: Load displacement curves from simulations for fully rough spread footing of width to length ratio = 1:2, for (a) Dense sand, (b) Medium dense sand, and (c) Loose sand.

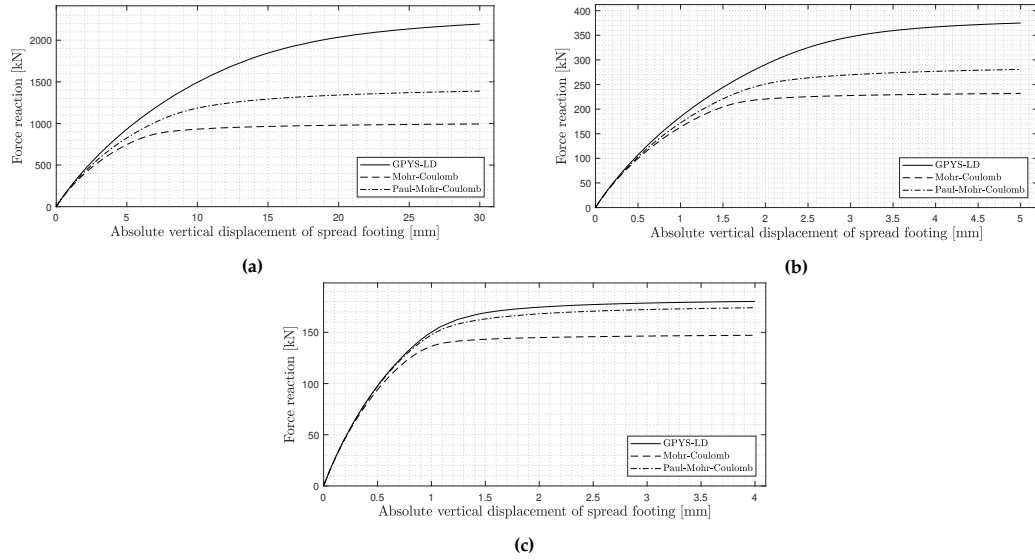


Figure 5.16: Load displacement curves from simulations for fully rough spread footing of width to length ratio = 1:4, for (a) Dense sand, (b) Medium dense sand, and (c) Loose sand.

5.1.4 Slope safety factor

In this section, the stability of a freestanding slope is considered. This is a typical stability problem in geomechanics, which have been dealt with by analytical mathematics in simplistic conditions. The finite element method is an attractive tool for this analysis, as more complicated conditions are easily modelled, such as different soil layers, a surcharge or influence of the ground water table. The stability is often evaluated by estimating the factor of safety, of which two common definitions are the gravity multiplier and the strength reduction factor. In this study, the latter is adopted, which in general yields more conservative safety factors [Krabbenhoft et al., 2016a]. For yield surfaces with linear generators, the Mohr-Coulomb failure criterion is typically used to define the shear strength of the material as

$$S = c + \sigma \mu = c + \sigma \tan \varphi.$$

The shear strength at failure is defined as

$$S_F = \frac{c + \sigma \tan \varphi}{F},$$

where, F , is the safety factor. The shear strength parameters are directly reduced as

$$c_F = \frac{c}{F}, \quad \varphi_F = \arctan\left(\frac{\tan \varphi}{F}\right).$$

The safety or strength reduction factor can be estimated in a finite element analysis by running a series of independent analysis with different values of F . When equilibrium cannot be established, the current value of the safety factor is too high and visa versa, which is sometimes referred to as the non-convergence method. By running independent analysis, with different values of, F , an interval can progressively be decreased. A predefined tolerance on the number of significant digits in F is used to terminate the analysis.

Model Description

A slope within a rectangular domain of 60×20 meters, with an inclination of 1:2, as illustrated in Figure 5.17, is considered. The three different types of sand and the models from Table 5.1 is considered in the studies. As the slope stability problem is governed by “small” stresses, a model with a tension cut-off is investigated as well. The Finite element discretization of the model consists of 1,947 triangular elements, as described in Appendix A.3, and 8,016 displacement degrees of freedom. The mesh density is increased in the area where the slip failure develops. No formal mesh refinement is performed, however, the results are compared to an analysis in OptumG2, which is conducted with adaptive mesh refinement and the results coincide quite well.

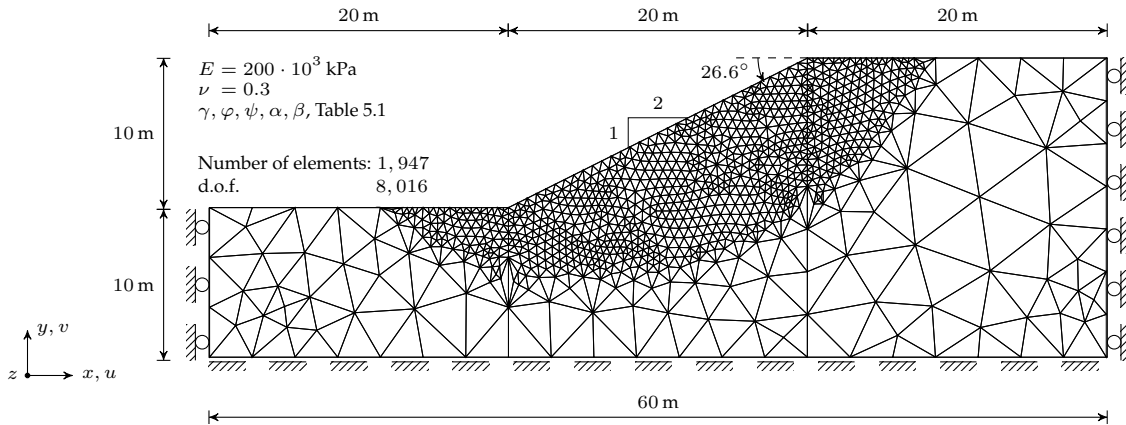


Figure 5.17: Illustration of slope model (a) Geometry and material properties and (b) Mesh grid.

The in situ stresses are simply obtained by equilibrium with the body forces in a linear analysis, such that the soil domain does not deform under the gravitational load, and the at rest earth pressure coefficient are thereby without influence on the result in this analysis. The analysis are initiated with a guess on the safety factor, and the corresponding reduced parameters are then calculated. If equilibrium is obtained, the safety factor is incremented, the initial stress field is reset and the next set of reduced material parameters are calculated. If equilibrium cannot be achieved, a smaller increment on the safety factor is attempted. The field of body forces are uniformly incremented over eight equal increments, and the convergence tolerance for the residual norm is set as one thousandth of the body force norm, $TOL = 10^{-3} \| \mathbf{f}_{body} \|$. Associated plasticity and linear elastic perfectly plastic material behaviour is assumed in all the analysis.

Failure mode assessment

The shear slip failure mode is studied by visual inspection of the rate of maximum plastic shear strain. Almost identical slip lines are observed for the different yield criteria, however, not for the different types of sand. Therefore, the slip lines of the different types of sands are visualized in Figure 5.18. The slip lines are drawn by locating nodal values of the plastic shear strain rate above a certain value, and a smooth line is obtained by calculating a moving average of the coordinates of these points. The pattern is in good agreement with the failure mode assumed in hand calculations, which shapes a logarithmic spiral. The

slip lines are juxtaposed in a graph in Figure 5.18d, where the medium dense sand is quite different from the others. No effect of the intermediate principal stress inclusion has been found in the failure modes, which on the other hand are quite affected by the cohesive properties of the material.

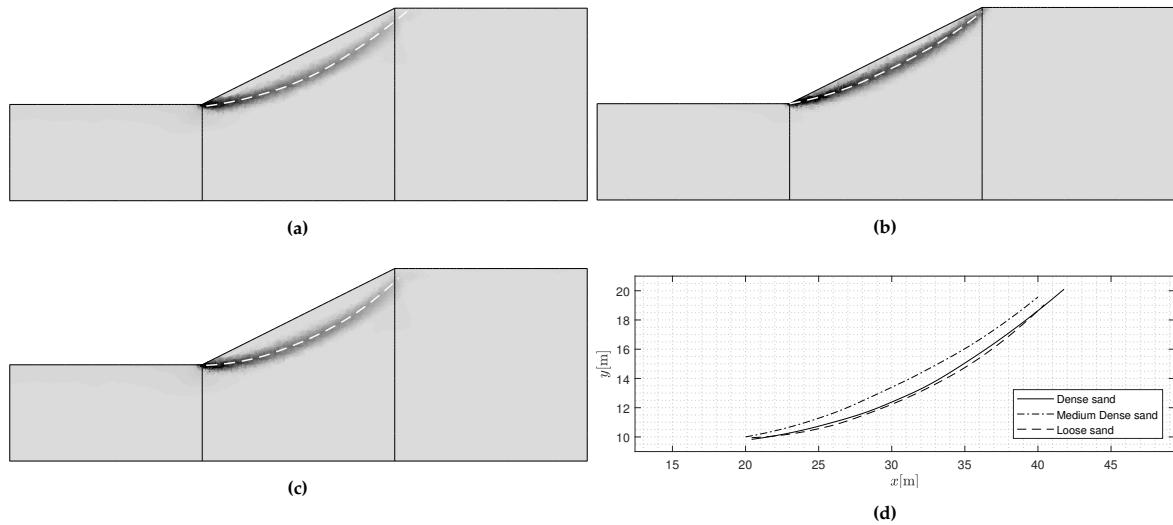


Figure 5.18: Contours of maximum plastic shear strain rate in slope stability analysis for (a) Dense sand (b) Medium dense sand (c) Loose sand and (d) comparison of slip lines.

Safety factor

The best estimates of the safety factor and the corresponding reduced shear strength parameters are shown in Table 5.4. All models in this chapter has a small value for the cohesion, which is found without notable influence on the result, considering the models with tension cut-off. In fact both the result on medium dense and dense sand is found unaffected by the tension cut-off, at least to the number of significant digits in the table. This lack of difference demonstrates one downfall of the non-convergence method, as the tension cut-off models definitively are weaker, but shows the same strength as the GPYS-IC models may have been terminated too soon. In any case, the tension cut-off does not affect the strength of this slope system notably.

Table 5.4: Slope safety factors and the corresponding reduced shear strength parameters from the twelve analysis.

	Dense sand			Medium dense sand			Loose sand		
	F [-]	φ_F [deg]	c_F [kPa]	F [-]	φ_F [deg]	c_F [kPa]	F [-]	φ_F [deg]	c_F [kPa]
Mohr-Coulomb	2.288	21.077	1.715	1.719	23.598	0.571	1.581	20.431	1.861
Mohr-Coulomb Plane	2.525	21.640	1.554	1.850	23.941	0.530	1.613	20.734	1.825
GPYS-LC	2.594	18.773	1.513	1.887	21.692	0.520	1.680	19.322	1.752
GPYS-LC Tension cut-off	2.594	18.773	1.513	1.887	21.692	0.520	1.675	19.375	1.757

5.2 Spread Footing Analysis with the GPYS-NC model

The nonlinear continuous formulation, GPYS-NC, is in this section applied in analysis of a geomechanical system. The model is used to obtain an even more accurate material calibration than with the Linear discontinuous GPYS model from Section 5.1.1. A three-dimensional mechanical system is considered, as the calibration is based on the true triaxial stress states from Appendix A.1. A square spread footing is once again the system of choice however with a slightly lower mesh density than in Section 5.1.3, as the present analysis are conducted in MATLAB code.

5.2.1 Calibration of surface parameters

The nonlinear continuous formulation of the proposed yield surface model, GPYS-NC, see Section 4.5, is in this section calibrated to the Experimental data from true triaxial tests, see Appendix A.1. The surface

parameters of the GPYS-NC and GPYS-LD models are calibrated by means of the least squares method. The calibrated models along with the data points are visualised in the deviatoric plane in Figure 5.19. The points are normalised with respect to the nearest whole multiple of 50 with a scale factor for illustrative purposes. The residuals to the data points with respect to the hydrostatic stress and the Lode angle are shown in Figure 5.21, and the standard deviations are listed in Table 5.5. The GPYS-NC model is found to make a decent fit with the data, especially pronounced for the dense sand, where the loose sand is more inconclusive as to which model is the best fit.

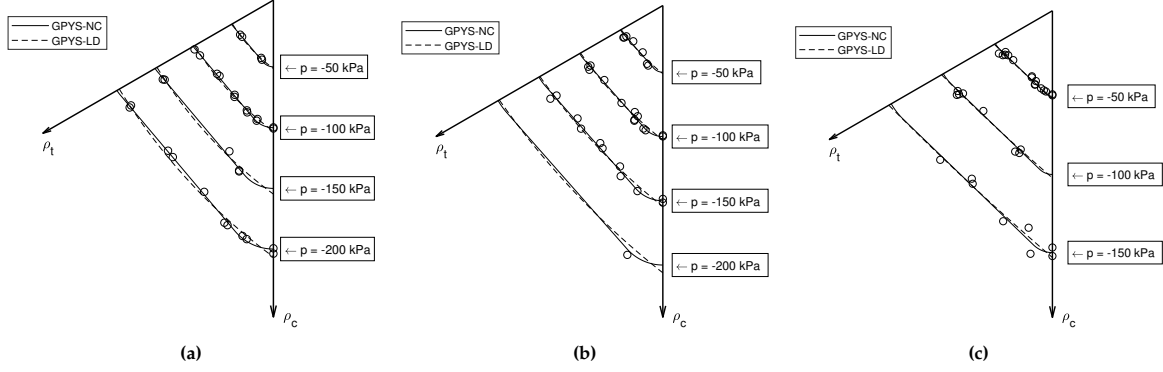


Figure 5.19: A sextant of the deviatoric trace, $\sigma_1 \geq \sigma_2 \geq \sigma_3$, of the calibrated models along with data from true triaxial tests normalised with respect to the nearest whole multiple of 50 of the hydrostatic pressure by a scale factor (a) Dense (b) Medium dense and (c) Loose sand.

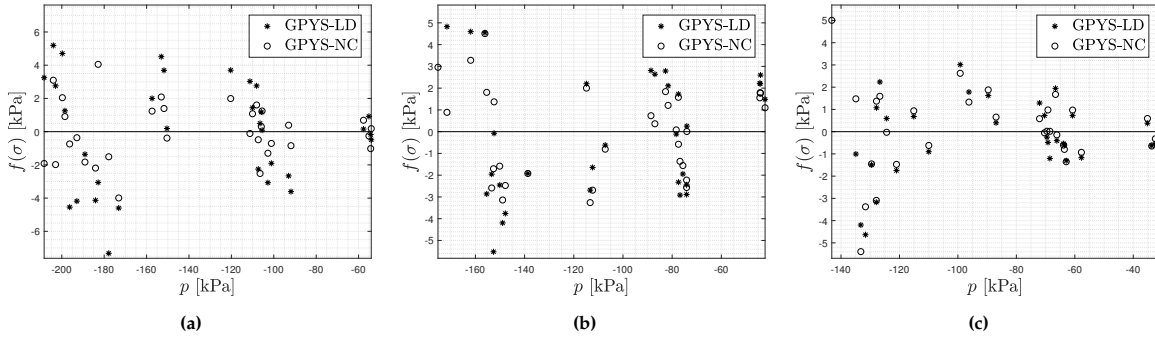


Figure 5.20: Scatter plot of the residual with the two different yield surfaces with respect to the hydrostatic stress (a) Dense (b) Medium dense and (c) Loose sand.

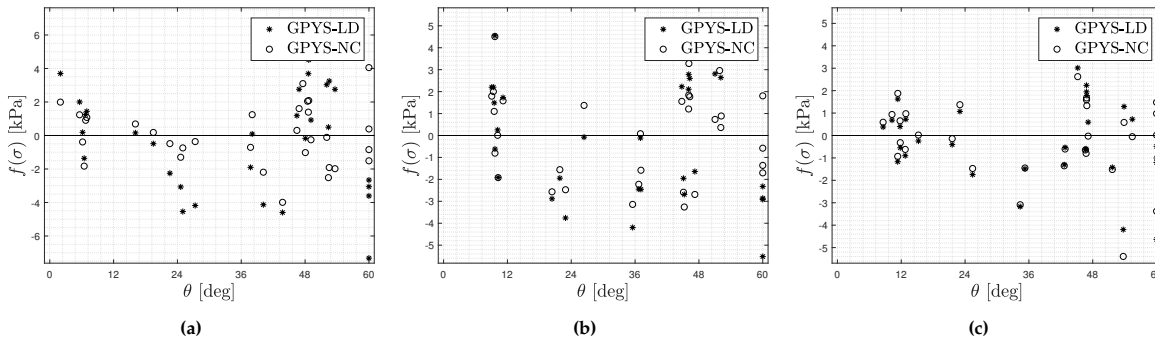


Figure 5.21: Scatter plot of the residual with the two different yield surfaces with respect to the Lode angle (a) Dense (b) Medium dense and (c) Loose sand.

The surface parameters of the calibration is presented in Table 5.6, and the corresponding yield surfaces are illustrated in the deviatoric plane and meridian in Figure 5.22 and 5.23, respectively. In general, the compressive corner is prone to take on a larger circular shape than the tension corner, and the trace in-between is linear. This trace is in general reported from true triaxial experiments, see for

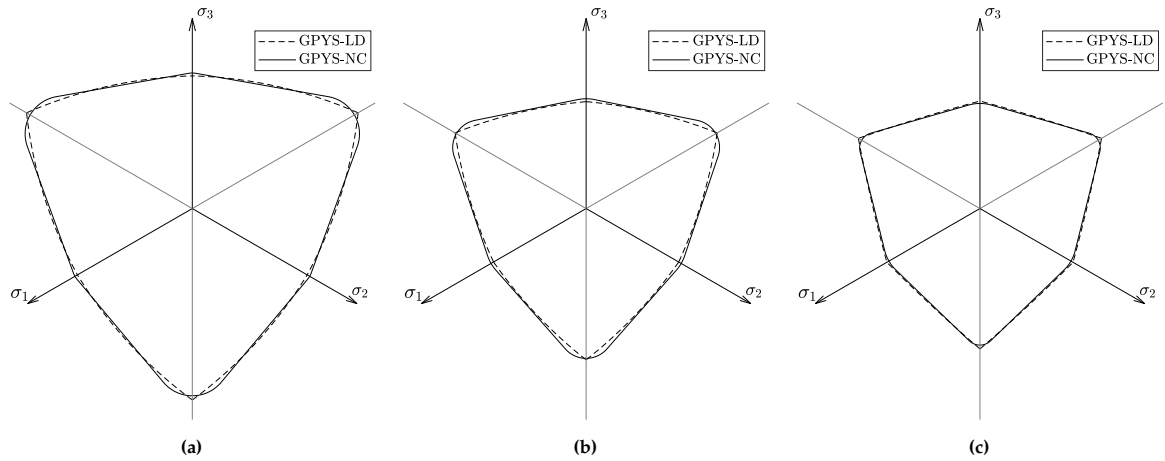
Table 5.5: Standard deviation from the calibration of the GPYS-LD and -NC models with data from true triaxial experiments performed by [Bønding, 1977], see Appendix A.1.

Model	Standard deviation $\sqrt{\frac{\sum_{i=1}^N (f(\sigma_i))^2}{N}}$ [kPa]		
GPYS-NC	9.71	11.58	10.57
GPYS-LD	17.93	17.14	11.77

instance [Bønding, 1977], [Praastrup, 2000] and [Wang and Lade, 2001]. The non-linearity in hydrostatic stress is almost absent for the dense and medium dense sand, $b \approx 0$, and somewhat pronounced for the loose sand, $b = 2.83$.

Table 5.6: Calibrated parameters of the GPYS-NL model, with data from true triaxial experiments performed by [Bønding, 1977], see Appendix A.1.

	φ	c [kPa]	α	β_1	β_2	β_3	β_4	Q	R	b
Dense sand	43.99	4.47	0.09	0.00	0.28	0.16	0.10	10.08	2.14	0.23
Medium dense sand	38.94	1.91	0.06	0.00	0.25	0.40	0.10	8.36	0.66	0.00
Loose sand	31.20	4.71	0.15	0.00	0.15	0.39	0.10	5.91	2.35	2.83

**Figure 5.22:** Deviatoric trace, at $p = -25$ kPa, of the GPYS-LD and -NC model fits (a) Dense (b) Medium dense and (c) Loose sand.

5.2.2 Analysis of square spread footing

An elasto-plastic finite element analysis of a square spread footing loaded to failure is conducted in section. The GPYS-NC model with parameters from Table 5.6 are compared with the GPYS-LD model with parameters of Table 5.1. The analysis are conducted to see if the “advanced” material calibration with the nonlinear model, GPYS-NC, yields a notable difference. The square spread footing system with boundary conditions, geometry and mesh grid of Figure 5.24, is considered. It is similar to that of Section 5.1.3, but with a less dense mesh, as the analysis is conducted by a MATLAB code opposed to the Abaqus software. Standard 10-node tetrahedral elements with second order interpolation and a 4-point Gauss integration scheme are used in the mesh discretization. The initial stresses are calculated with an at rest earth pressure coefficient of $K_0 = 1.0$ and a gravitational pull of $g = 9.81 \text{ m/s}^2$. A vertical downwards force is emulated by a uniform displacement of the nodes in the footing footprint.

The Load-displacement curves from the analysis are shown in Figure 5.25. The model differences for the dense and loose sands are small in this analysis, however, a quite notable difference is found for the Medium dense sand. The model for this sand stands out with apex in a larger value of hydrostatic stress, considering the meridian plots from the model calibration of Figure 5.23b. It furthermore encapsulates the GPYS-LD fit in the whole deviatoric trace, at least near the apex as seen in Figure 5.22b. This indicates a notable influence on the bearing capacity of the small hydrostatic stress levels near the apex.

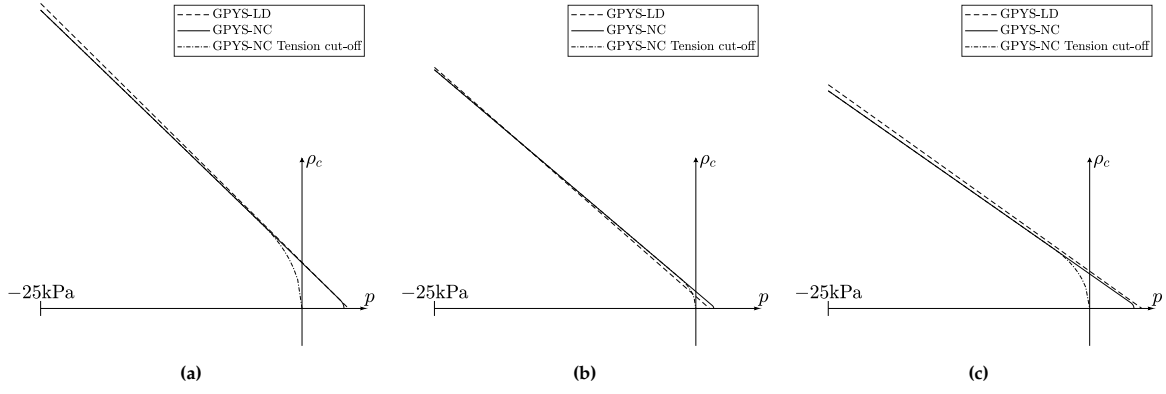


Figure 5.23: Meridian plane, from $p = -25\text{kPa}$ to the apex, of the GPYS-LD and -NC model fits (a) Dense (b) Medium dense and (c) Loose sand.

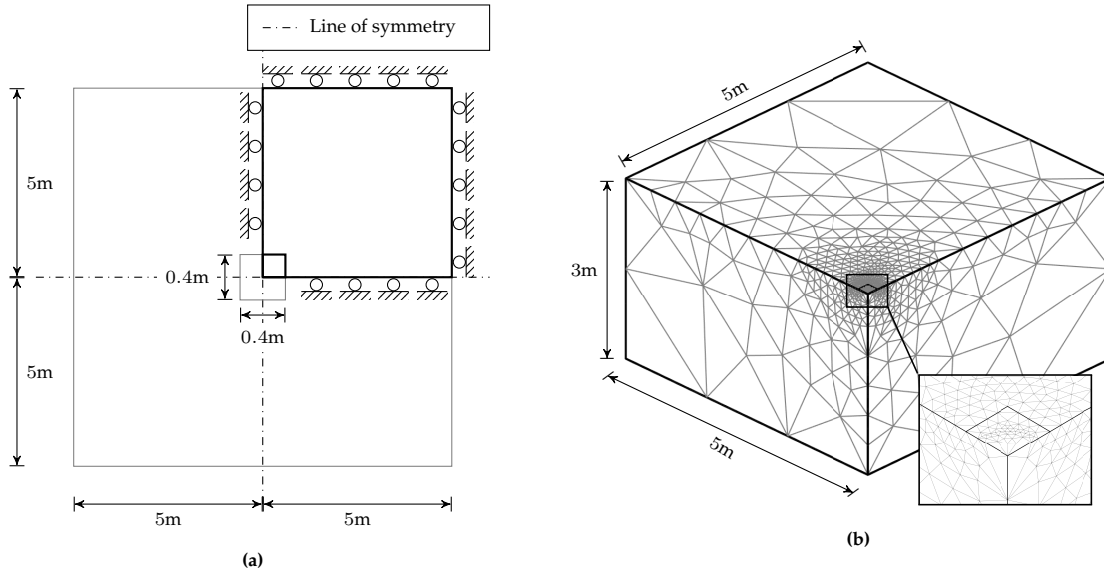


Figure 5.24: Mechanical system of spread footing (a) Top view with geometry and boundary conditions and (b) Discretized model with 5,042 tetrahedral elements and 23,166 d.o.f. and zoom on mesh at foundation footprint.

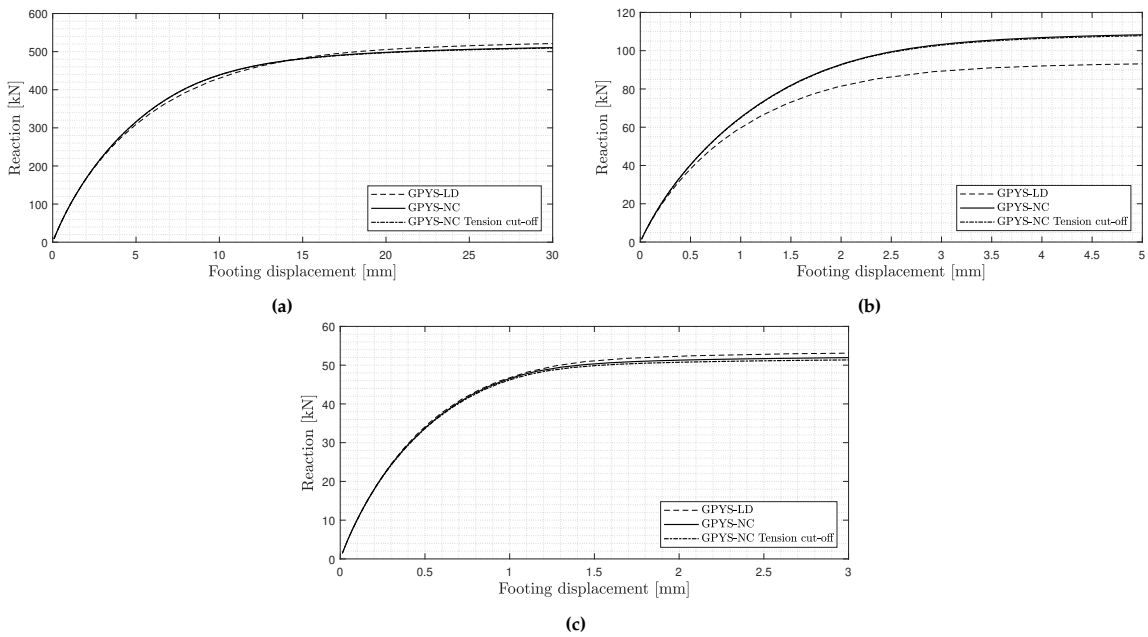


Figure 5.25: Load displacement graphs from the spread footing analysis (a) Dense (b) Medium dense and (c) Loose sand.

6 | Conclusion

In the field of constitutive modelling, an extensive amount of plasticity models for granular materials exists, where Mohr-Coulomb and Drucker-Prager are widely used in geomechanics. Here, the popularity of the latter might stem from its robustness in numerical analysis opposed to its ability to describe actual material behaviour. The Mohr-Coulomb model is in general a better representation of the material, however, excludes the intermediate principle stress, which is not in coherence with experimental evidence. The majority of the existing models to describe the actual three-dimensional stress state at failure of frictional soil, applies solely to a narrow range of materials, although, some attempts has been made to encompass several models in one. Most of the more advanced models, however, have yet to gain a widespread commercial use. This might stem from a lack of familiarity in the parameters, computational performance and implementation in commercial analysis software. Outside the world of academia, the Mohr-Coulomb model has to some extent become the assumption of true material behaviour. It is a well-known model with a minimal number of tests to be performed for calibration, however, there may be a vast unused potential in the material to be obtained with more accurate models.

A novel concept of versatile yield surfaces, based on geometrical relations in principal stress space, is explored in this thesis. The objective is not to simply add yet another model, however, to encompass several of the existing models in one, at least their overall characteristics. The first of three proposed yield surfaces operates on four parameters of which two are the well-known internal angle of friction and cohesion. The two additional parameters adjusts the side curvature and the ρ_t/ρ_c -ratio, which are fixed in the Mohr-Coulomb model. It is a multi-surface plasticity model, for which an exact implementation in numerical analysis is performed, where the discontinuities are handled explicitly. The implicit return mapping scheme can for this model be solved in closed form, which renders a robust stress return algorithm, especially in the vicinity of the apex. However, the global newton scheme is in general not as robust as desired with this model, which inspires the second proposed yield surface, as a corner rounded version of the first, for improved robustness. A new and versatile concept of local corner rounding is introduced, which mainly operates on simple vector calculus, opposed to trigonometric functions, as the existing methods in the literature. The third proposed yield surface is a continuous and with with nonlinear generators, based on Bolton's formula, introduced to investigate further material optimisation and to demonstrate the generality of the novel yield surface format. It is more complex than the first two models, however, easily used as for instance a smooth continuous approximation of the Mohr-Coulomb, Bolton, or Hoek-Brown models. The constitutive models are implemented in MATLAB and the first and second model in Fortran source code as well, for use in the Abaqus software, to demonstrate its potential and provide a complete tool for practical use.

The novel yield surfaces are embedded in an elasto-plastic finite element framework and applied in standard geotechnical problems, where the model parameters are calibrated to true triaxial experiments. Linearly elastic perfectly plastic material behaviour and associated flow are assumed for simplicity, which are common assumptions in geotechnical analysis. The plane strain simulations reveals a vast unused potential in comparison to the standard triaxial compression fit of Mohr-Coulomb, even with the correction of the triaxial angle of friction, proposed by the Danish code of practices. Three-dimensional spread footing systems are analysed as well, where the increase in load bearing capacity is less pronounced. However, increasing with the footing length to width ratio, as the zone of approximate plane strain conditions of the system are enlarged. Regarding the performance in numerical analysis, the corner rounded yield surface is compared to the first yield surface model in the analysis of a spread footing. It is found less efficient in computation time, however, highly robust and with minimal discrepancy in the limit load. The final proposed model with the Bolton generator, is calibrated with the previously mentioned data. The standard deviation is here severely reduced in comparison with the first model, especially for the more dense sand, however, the simulation result reveals no consistent tendencies. A increase in limit load is though expected in a design case with incorporated statistical safety, as the lower standard deviation yields a narrower confidence interval. Results from the simulations are not directly transferable to a design case, however, a basis to investigate the intermediate principle stress influence and the impact of a more optimised material calibration.

In selection of the constitutive model for a given geotechnical system, the accuracy, efficiency and robustness are of importance. The main advantage of the Drucker-Prager model is its efficiency and robustness in numerical simulations, however, its use in three-dimensional analysis is not recommended, as it poorly describes the stress state at failure for frictional soil. With substantial material uncertainties, as in geomechanics, a conservative and efficient constitutive model, as a triaxial compression fit of Mohr-Coulomb, can be appealing. However, this sample of studies indicates a substantial unused potential in the material in comparison with more optimized fits. The true deviatoric trace of the yield surface is determined from true triaxial tests, which are rarely conducted in practice as these are time consuming and expensive. A potential use of the new plasticity models are to determine the ρ_t/ρ_c -ratio from standard triaxial tests in both compression and extension, for a notable increase in bearing capacity. In relation to the performance of the yield surfaces proposed in this thesis, the corner rounded continuous models, are recommended. While these comes with a cost in computation time, they are superior in robustness and no parameter adjustment has been necessary to achieve simulation completion. These encompass several exiting models, for instance Mohr-Coulomb and the Bolton model, and are robust in numerical analysis, with a new method of local corner rounding, not found elsewhere in the existing literature.

Bibliography

- Leandro R. Alejano and Antonio Bobet. *Drucker-Prager Criterion*. Springer, 1 edition, 2012.
- A. W. Bishop. The strength of soils as engineering materials. *Géotechnique*, 16(2):91–130, 1966. URL <https://doi.org/10.1680/geot.1966.16.2.91>.
- Niels Bønding. *Bulletin No. 30 - Triaxial State of Failure in sand*. Danish Geotechnical Institute, 1977. <http://www.geo.dk/bibliotek/197x/trixial-state-of-failure-in-sand/>.
- Malcolm Bolton. Strength and dilatancy of sands. *Geotechnique*, 36:65–78, 01 1986. doi: 10.1680/geot.1986.36.1.65.
- Jinhyun Choo. Mohr–coulomb plasticity for sands incorporating density effects without parameter calibration. *International Journal for Numerical and Analytical Methods in Geomechanics*, 42(18):2193–2206, 2018. doi: 10.1002/nag.2851. URL <https://onlinelibrary.wiley.com/doi/abs/10.1002/nag.2851>.
- Johan Clausen, Lars Damkilde, and Lars Andersen. *Efficient return algorithms for associated plasticity with multiple yield planes*. John Wiley and Sons Ltd., 2005. Aalborg University Denmark.
- Johan Clausen, Lars Damkilde, and Lars Andersen. *An efficient return algorithm for non-associated plasticity with linear yield criteria in principal stress space*. Elsevier Ltd., 2007. Aalborg University Denmark.
- Robert D. Cook, David S. Malkus, Michael E. Plesha, and Robert J. Witt. *Concepts and applications of Finite Element Analysis*. John Wiley and Sons, inc., 4. edition, 2002.
- William M. Coombs. Reuleaux plasticity: Analytical backward euler stress integration and consistent tangent. 199:1733–, 2010. ISSN 0045-7825.
- C. A. Coulomb. Sur une application des regles de maximis & minimis á quelques problemes de statique, relatifs á l’architecture. 1773.
- Lars Damkilde. A general parametric yield surface model unifying several classical models. *International Journal of Solids and Structures*, 2019. Submitted 2019.
- E. H. Davis, A. M. I. C. E., and M. I. E. *Theories of Plasticity and the Failure of Soil Masses*. Butterworth & Co. Ltd., 1968. In: Soil Mechanics - Selected Topics by I. K. Lee.
- René de Borst, Mike A. Crisfield, Joris J.C. Remmers, and Clemens V. Verhoosel. *Non-Linear Finite Element Analysis of Solids and Structures*. John Wiley and Sons, inc., 2 edition, 2012.
- Standard Distribute. National annex for eurocode 7: Geotechnical design – part 1: General rules, 02 2015.
- Daniel Charles Drucker and William Prager. *Soil Mechanics and Plastic Analysis or Limit Design*. Brown University, 1 edition, 1951.
- Sam Helwany. *Applied Soil Mechanics with Abaqus Applications*. John Wiley and Sons, 1 edition, 2007. ISBN 978-0-471-79107-2.
- Evert Hoek and Edwin T. Brown. *Empirical Strength Criterion for Rock Masses*. Journal of the Geotechnical Engineering Division, 1980.
- Evert Hoek, Carlos Carranza-Torres, and Brent Corkum. *Hoek-Brown failure criterion – 2002 Edition*. NARMS-TAC Conference, Toronto, 2002.
- Kenneth Sixhøj Jepsen, Johan Nielsen, and Lars Damkilde. A concept of local rounding applied to a multi-surface plasticity model with sharp edges. *International Journal for Numerical Methods in Engineering*, 2019. Submitted for possible publish.
- K. Krabbenhoft, M.R. Karim, A. V. Lyamin, and S. W. Sloan. *Associated computational plasticity schemes for nonassociated frictional materials*. International Journal for Numerical Methods in Engineering, 2012.

- K. Krabbenhoft, A. V. Lyamin, and J. Krabbenhoft. Optumg2 - analysis, 2016a. www.optumce.com.
- K. Krabbenhoft, A. V. Lyamin, and J. Krabbenhoft. Optumg2 - materials, 2016b. www.optumce.com.
- K. Krabbenhoft, A. V. Lyamin, and J. Krabbenhoft. Optumg2 - theory, 2016c. www.optumce.com.
- Michael Kupferschmid. *Classical Fortran - Programming for Engineering and Scientific Applications*. Taylor and Francis Group, 2. edition, 2009. ISBN-13 nr. 978-1-4200-5907-6.
- Poul Lade and James M. Duncan. Cubical triaxial tests on cohesionless soil. *ASCE J Soil Mech Found Div*, 99:793–781, 10 1973. doi: 10.1016/0148-9062(74)91579-4.
- Poul V. Lade. *Elasto-plastic Stress-Strain Theory for Cohesionless Soil with Curved Yield Surfaces*. Mechanics and Structures Department, School of Engineering and Applied Science, University of California, 3 edition, 1977.
- Poul V. Lade. Assessment of test data for selection of 3-d failure criterion for sand. *International Journal for Numerical and Analytical Methods in Geomechanics*, 30(4):307–333, 2006. doi: 10.1002/nag.471. URL <https://onlinelibrary.wiley.com/doi/abs/10.1002/nag.471>.
- Zong Y. Ma, Hong J. Liao, and Mao H. Yu. Slope stability analysis using unified strength theory. *Applied Mechanics and Materials*, 137:59, 10 2011. Copyright - Copyright Trans Tech Publications Ltd. Oct 2011; Last updated - 2018-10-09.
- C. M. Martin. *ABC - Analysis of Bearing Capacity*. University of Oxford Department of Engineering Sciences, 2003. <http://www-civil.eng.ox.ac.uk/people/cmm/software/abc>.
- Hajime Matsuoka and Terou Nakai. *Stress-Deformation and Strength Characteristics of Soil Under Three Different Principal Stresses*. Proceedings of the Japan Society of Civil Engineers, 1 edition, 1974.
- James P. Meyer and Joseph F. Labuz. *Linear Failure Criteria with Three Principal Stresses*. International Journal of Rock Mechanics and Mining Sciences, 2013.
- Johan Nielsen, Kenneth Sixhøj Jepsen, and Lars Damkilde. Parametric transition from mohr-coulomb to drucker-prager by implementation of a general parametric yield surface format. *International Journal for Numerical and Analytical Methods in Geomechanics*, 2019. Submitted for possible publish.
- S. Valliappan O. C. Zienkiewicz and I. P. King. *Elasto-Plastic Solutions of Engineering Problems 'Initial Stress', Finite Element Approach*. International Journal for Numerical Methods in Engineering, 1 edition, 1969.
- Niels Ottosen and Matti Ristinmaa. *Material Science and Engineering*. The Mechanics of Constitutive Modeling, 1 edition, 2005. ISBN-13 9780080446066.
- Andrea Panteghini and Rocco Lagioia. A fully convex reformulation of the original matsuoka-nakai failure criterion and its implicit numerically efficient integration algorithm. *International Journal for Numerical and Analytical Methods in Geomechanics*, 38(6):593–614, 4 2014. ISSN 1096-9853. doi: 10.1002/nag.2228. URL <https://doi.org/10.1002/nag.2228>.
- B. Paul. *Generalized Pyramidal Fracture and Yield Criteria*. International Journal of Solids and Structures, 1 edition, 1968.
- Ulrik Praastrup. *Three Dimensional Stress-Strain Behavior of Soils Tested in the Danish Rigid Boundary True Triaxial Apparatus*. PhD thesis, Aalborg University Denmark, July 2000.
- William H. Press, Saul A. Teukolsky, William T. Vetterling, and Brian P. Flannery. *Numerical Recipes in Fortran 77 - The Art of Scientific Computing*. Press Syndicate of the University of Cambridge, 1992.
- Krishna R. Reddy and Surenda K. Saxena. Effects of cementation on stress-strain and strength characteristics of sands. *SOILS AND FOUNDATIONS*, 33(4):121–134, 1993.
- J. C. Simo and R. L. Taylor. Consistent tangent operators for rate-independent elastoplasticity. *Computer methods in applied mechanics an engineering*, (48):101–118, May 1984.

- Dassault Systems Simulia. Abaqus 6.14 analysis user's guide volume 3: Materials, 2014.
- Karl Terzaghi. *Theoretical Soil Mechanics*. John Wiley and Sons Inc., 6 edition, 1951.
- Qiong Wang and Poul V. Lade. Shear banding in true triaxial tests and its effect on failure in sand. 127: 754–761, 2001. ISSN 0733-9399. doi: 10.1061/(ASCE)0733-9399(2001)127:8(754).
- Mao-Hong Yu. *Unified Strength Theory and its Applications*. Xi'an Jiatong University Press, 2 edition, 2018. ISBN: 978-981-10-6246-9.
- Xue Zhang. *Particle Finite Element Method in Geomechanics*. PhD thesis, The University of Newcastle, september 2014.
- Xuan Zhou, Guo J. Shao, and Feng Hu. Ultimate bearing capacity based on unified strength theory. *Applied Mechanics and Materials*, 368-370:1838, 08 2013. Copyright - Copyright Trans Tech Publications Ltd. Aug 2013; Last updated - 2018-10-09.

A | Finite Element Analysis of Geomechanical Systems

This appendix is in reference to Chapter 5, and contains a description of the finite elements used in the analysis, test data for model calibrations and a note on the GPYS-LD model approximating the Mohr-Coulomb model.

A.1 Data from True Triaxial Experiments

The experimental data used in model calibrations in this thesis, is presented in Table A.1. The data are from true triaxial tests performed by [Bønding, 1977], and reads the three principal stresses at failure. The author conducted a thorough work to describe the three dimensional stress state of granular material at fracture, and fit a yield criterion combined of the Mohr-Coulomb and the Lade criteria. In order to do so, the author constructs and tests a new triaxial apparatus, which tests on a $0.2 \times 0.2 \times 0.2 \text{ m}^3$ cubical test element. The test material is composed of approximately cohesionless marine sand with a mean diameter $D_{50} = 0.24 \text{ mm}$ and a uniformity ratio $D_{60}/D_{10} = 1.67$. Thirty-two experiments were performed for each of three batches, composed of identical test material but with different void ratios, e , Dense sand $e = 0.55$, Medium dense sand $e = 0.62$ and Loose sand $e = 0.75$. Their tests are considered as thorough, and the results to be an acceptable premise for material model calibration.

Table A.1: Principal stresses at failure from true triaxial experiments performed by [Bønding, 1977].

Loose Sand			Medium Dense Sand			Dense Sand		
σ_1	σ_2	σ_3	σ_1	σ_2	σ_3	σ_1	σ_2	σ_3
-43.16	-130.28	-156.47	-43.16	-171.48	-201.40	-39.24	-249.27	-278.70
-43.16	-139.79	-162.36	-32.37	-144.31	-167.85	-39.24	-261.83	-294.50
-32.37	-104.38	-124.10	-21.58	-95.84	-114.97	-29.43	-210.52	-232.30
-32.37	-108.30	-128.22	-21.58	-92.12	-108.40	-29.43	-199.54	-222.20
-21.58	-69.55	-82.11	-10.79	-53.37	-62.49	-19.62	-145.68	-164.81
-21.58	-72.59	-88.09	-43.16	-196.00	-229.26	-19.62	-167.65	-173.74
-10.79	-44.15	-50.52	-32.37	-133.61	-155.68	-9.81	-62.59	-89.66
-10.79	-39.34	-47.19	-10.79	-56.31	-65.53	-9.81	-69.65	-93.59
-52.97	-137.73	-192.86	-51.01	-159.51	-246.72	-49.05	-210.42	-329.42
-52.97	-127.04	-183.05	-51.01	-160.79	-231.71	-49.05	-200.42	-329.22
-26.49	-72.40	-99.57	-25.51	-83.29	-118.11	-24.53	-118.90	-178.54
-26.49	-80.93	-101.24	-25.51	-82.80	-114.09	-24.53	-110.85	-172.95
-60.82	-121.84	-206.01	-56.90	-138.03	-251.92	-54.94	-134.20	-330.30
-30.41	-53.27	-105.16	-56.90	-135.67	-257.81	-54.94	-154.31	-343.06
-30.41	-53.76	-107.42	-28.45	-67.49	-126.45	-27.47	-91.63	-197.48
-60.82	-121.74	-201.20	-28.45	-70.73	-135.87	-27.47	-88.58	-187.37
-62.78	-99.67	-217.68	-62.78	-122.23	-300.77	-62.78	-134.30	-402.11
-62.78	-97.71	-212.68	-62.78	-119.98	-277.43	-62.78	-140.77	-408.49
-47.09	-79.85	-170.69	-47.09	-88.58	-204.34	-47.09	-101.24	-307.05
-47.09	-75.34	-166.28	-47.09	-83.88	-206.11	-47.09	-101.63	-310.49
-31.39	-51.70	-116.74	-31.39	-62.20	-154.51	-31.39	-75.54	-217.39
-31.39	-50.03	-109.28	-31.39	-61.61	-151.96	-31.39	-75.24	-211.01
-15.70	-21.97	-56.02	-15.70	-32.57	-83.97	-15.70	-36.40	-110.75
-15.70	-26.19	-59.15	-15.70	-34.04	-83.29	-15.70	-35.41	-114.29
-74.56	-93.10	-261.83	-72.59	-110.56	-331.58	-72.59	-114.88	-421.34
-74.56	-93.29	-231.81	-36.30	-58.76	-170.79	-72.59	-122.82	-429.58
-37.28	-45.32	-128.51	-36.30	-55.92	-168.83	-36.30	-62.69	-220.43
-37.28	-48.17	-130.77	-72.59	-113.21	-339.92	-36.30	-65.43	-232.01
-78.48	-78.48	-237.89	-78.48	-78.48	-309.31	-78.48	-78.48	-391.62
-78.48	-78.48	-247.80	-78.48	-78.48	-300.97	-78.48	-78.48	-376.61
-39.24	-39.24	-127.14	-39.24	-39.24	-153.82	-39.24	-39.24	-197.18
-39.24	-39.24	-129.10	-39.24	-39.24	-151.96	-39.24	-39.24	-200.52

A.2 The GPYS-LD model as approximation of Mohr-Coulomb

Preliminarily to applying the GPYS-LD model in analysis, its use as an approximation of Mohr-Coulomb is considered, to set a lower bound value for the curvature parameter β . The benchmark values of Mohr-Coulomb are conducted with an exact implementation of the Mohr-Coulomb plasticity model as given in [Clausen et al., 2005]. It is found a good approximation with, $\beta = 0.005$, as seen in the comparison in Table A.2.

Table A.2: Comparison of limit load from finite element analysis with an Exact Mohr-Coulomb model and the GPYS-LD model with $\beta = 0.005$ and $\alpha = 0$.

System	Section	Dense Sand			Medium Dense Sand			Loose Sand		
		MC	GPYS-LD	Ratio	MC	GPYS-LD	Ratio	MC	GPYS-LD	Ratio
Strip Footing	5.1.2	356.83	356.07	1.0021	102.64	102.45	1.0019	69.051	68.984	1.0010

A.3 Finite Elements

Parts of the finite element analysis performed in this thesis are conducted in a MATLAB program written by the authors. The element types used are described in this section.

A.3.1 Linear Strain Triangle

A linear strain triangle (LST), which is a plane element with six nodes, each with two d.o.f, is considered. The displacements are interpolated quadratically, which gives linear interpolation of strains, hence the name of the element. Literature on this element can be found in for instance [Cook et al., 2002, sec 7.2-7.3]. The element is depicted in area coordinates in Figure A.1.

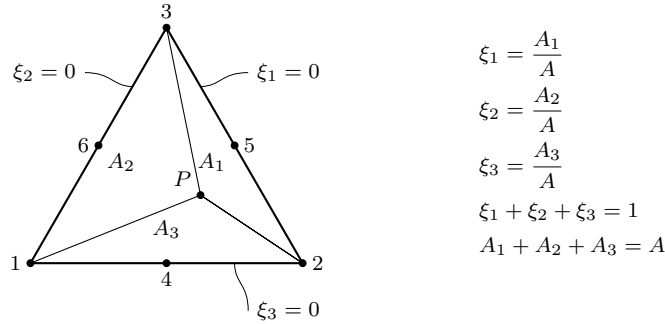


Figure A.1: Illustration of the LST element and the principle of area coordinates.

The shape function for each node is easily obtained as products of functions which gives zero in the other nodes, scaled to equal one in the node under consideration. The shape functions in area coordinates reads

$$\begin{aligned}N_1 &= \xi_1(2\xi_1 - 1) & N_2 &= \xi_2(2\xi_2 - 1) & N_3 &= \xi_3(2\xi_3 - 1), \\ N_4 &= 4\xi_1\xi_2 & N_5 &= 4\xi_2\xi_3 & N_6 &= 4\xi_3\xi_1.\end{aligned}\tag{A.1}$$

If the midside coordinates are positioned in the middle of the element edges and the edges are straight, the point P in Figure A.1 can be interpolated via the coordinates of the corner nodes (1, 2 and 3) as

$$\begin{Bmatrix} 1 \\ x \\ y \end{Bmatrix} = \begin{bmatrix} 1 & 1 & 1 \\ x_1 & x_2 & x_3 \\ y_1 & y_2 & y_3 \end{bmatrix} \begin{Bmatrix} \xi_1 \\ \xi_2 \\ \xi_3 \end{Bmatrix}.$$

The inverse relation gives the area coordinates as functions of x and y as

$$\begin{Bmatrix} \xi_1 \\ \xi_2 \\ \xi_3 \end{Bmatrix} = \frac{1}{2A} \begin{bmatrix} x_2y_3 - x_3y_2 & y_{23} & x_{32} \\ x_3y_1 - x_1y_3 & y_{31} & x_{13} \\ x_1y_2 - x_2y_1 & y_{12} & x_{21} \end{bmatrix} \begin{Bmatrix} 1 \\ x \\ y \end{Bmatrix}, \quad A = \frac{1}{2}(x_{21}y_{31} - x_{31}y_{21}), \quad \begin{matrix} x_{ij} = x_i - x_j \\ y_{ij} = y_i - y_j \end{matrix}, \quad (\text{A.2})$$

where A denotes the element area. In the plain strain calculations, all three normal stresses are considered, and the strain interpolation matrix is given as

$$\begin{Bmatrix} \varepsilon_{xx} \\ \varepsilon_{yy} \\ \varepsilon_{zz} \\ \gamma_{xy} \end{Bmatrix} = \begin{bmatrix} \frac{\partial N_1}{\partial x} & 0 & \frac{\partial N_2}{\partial x} & 0 & \dots & \frac{\partial N_6}{\partial x} & 0 \\ 0 & \frac{\partial N_1}{\partial y} & 0 & \frac{\partial N_2}{\partial y} & \dots & 0 & \frac{\partial N_6}{\partial y} \\ 0 & 0 & 0 & 0 & \dots & 0 & 0 \\ \frac{\partial N_1}{\partial y} & \frac{\partial N_1}{\partial x} & \frac{\partial N_2}{\partial y} & \frac{\partial N_2}{\partial x} & \dots & \frac{\partial N_6}{\partial y} & \frac{\partial N_6}{\partial x} \end{bmatrix} \begin{Bmatrix} u_1 \\ v_1 \\ u_2 \\ v_2 \\ \vdots \\ v_6 \end{Bmatrix},$$

which naturally ensures the out of plane strain to be equal to zero. The shape function derivatives with respect to the global coordinates is simply calculated with Equations (A.1) and (A.2). For instance the first entry of the strain interpolation matrix is calculated as

$$\frac{\partial N_1}{\partial x} = \frac{\partial N_1}{\partial \xi_1} \frac{\partial \xi_1}{\partial x} = (4\xi_1 - 1) \frac{y_{23}}{2A},$$

and the rest in the same manner. With the strain interpolation matrix, the usual integral for the stiffness matrix is performed via Gauss quadrature

$$\mathbf{K} = \int_{\Omega} \mathbf{B}^T \mathbf{D} \mathbf{B} \, d\Omega \approx \sum_{i=1}^n \mathbf{B}^T \mathbf{D} \mathbf{B} \, w_i \, t \, A,$$

where n , w_i and t is the order of the Gauss integration, the weight of integration point i , and the element thickness, respectively. The constitutive matrix is reduced to accommodate plane strain conditions, and for isotropic elasticity it reads

$$\mathbf{D} = \frac{E}{(1+\nu)(1-2\nu)} \begin{bmatrix} 1-\nu & \nu & \nu & 0 \\ \nu & 1-\nu & \nu & 0 \\ \nu & \nu & 1-\nu & 0 \\ 0 & 0 & 0 & \frac{1}{2}(1-2\nu) \end{bmatrix}.$$

The locations and weights of the Gauss integration points is listed for different orders in Table A.3.

Table A.3: Gauss integration points and weights for some orders of integration in a triangular element, see for instance [Cook et al., 2002, tab. 7.4-1].

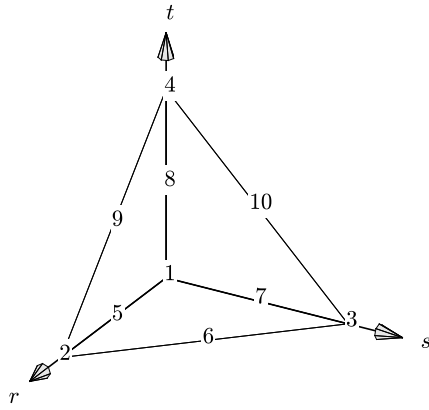
Integration order	ξ_1	ξ_2	ξ_3	w_i
2	2/3, 1/6, 1/6	1/6, 2/3, 1/6	1/6, 1/6, 2/3	1/3, 1/3, 1/3

A.3.2 Linear Strain Tetrahedron

A linear strain tetrahedral element is used for the three-dimensional analysis in this thesis, which is a straight forward extension of the LST element. The element has 10-nodes, 4 corner nodes and 6 mid-side nodes, and quadratic field interpolation functions. The element is sketched in isoparametric coordinates in Figure A.2. The isoparametric coordinates may be directly converted to volume coordinates, which are the three-dimensional parallel to the area coordinates.

The element shape functions reads

$$\begin{aligned} N1 &= (1-r-s-t)(1-2r-2s-2t) & N6 &= 4rs \\ N2 &= r(2r-1) & N7 &= 4s(1-r-s-t) \\ N3 &= s(2s-1) & N8 &= 4t(1-r-s-t) \\ N4 &= t(2t-1) & N9 &= 4tr \\ N5 &= 4r(1-r-s-t) & N10 &= 4st \end{aligned}$$



Node coordinates

1	(0, 0, 0)	6	(0, 0.5, 0.5)
2	(1, 0, 0)	7	(0, 0.5, 0)
3	(0, 1, 0)	8	(0, 0, 0.8)
4	(0, 0, 1)	9	(0.5, 0, 0.5)
5	(0.5, 0, 0)	10	(0, 0.5, 0.5)

Figure A.2: 10-node tetrahedron in isoparametric space.

A second order Gauss integration scheme is adopted, with weights and quadrature stations as in Table A.4

Table A.4: Gauss integration points and weights for second order integration in a tetrahedral element, see fore instance [Cook et al., 2002, tab. 7.4-2].

Integration order	r_i	s_i	t_i	w_i
2	(a, b, b, b)	(b, b, b, a)	(b, b, a, b)	$1/4$
$a = (5+3\sqrt{5})/20$				
$b = (5-\sqrt{5})/20$				

B | Implementation in Abaqus software

This appendix contains the procedure for implementation of a constitutive model in the commercial finite element program ABAQUS by Simulia Dassault Systems. Preliminary requirements:

- Abaqus on a research licence
- A Fortran compiler - Preferably “Intel Fortran”
- A code editor - “Notepad++” or “Visual studio”

The following introduction is conducted on Abaqus 2017 and a Intel Fortran 2013 compiler on Windows10 64bit platform. Code editing is performed in Microsoft Visual Studio 2010 and Notepad++, but any editor would do.

B.1 Writing UMAT in Fortran Fixed form

A user-defined subroutine for material behaviour is in Abaqus called, UMAT, for more information on this subject, see the Abaqus help manual section, Abaqus User Subroutines Reference Guide 1.1.41 UMAT. This section contains elaboration and recommendations by the authors. See Listing B.1 for a code snippet of an Abaqus UMAT file without any user-defined lines of code.

UMAT code for Abaqus is performed in Classical Fortran (Fixed form), where each line of code consists of 72 columns, of which the first 6 is reserved for special operands, any sign in column 6 will continue the previous line. A “C” in first column will comment out the hole line, whereas an “!” will do in-line comments. It is encouraged to do some pre-study on the subject of Classical Fortran see for instance [Kupferschmid, 2009].

Fortran operates in general with subroutines and functions, of which the latter assigns a value to it self, and can be used in an expression, in the same fashion as intrinsic functions. Subroutines are in general longer, and can assign values to multiple variables and is executed via the CALL statement. Be aware, that variables passing through a subroutine are updated.

Fortran bares some resemblance to Matlab, but with some key differences. Fortran is not case-sensitive and it is needed to allocate variable type and size at the beginning of any subroutine, as it is recommended to use the IMPLICIT NONE option, although this disables guarantee for transferability of the UMAT. In general, variables with initial letter I to N is regarded as integers. In MATLAB, the default assignment of a value to a variable is in floating points double precision, where it is Fortran code is specified for every value assignment. Inconsistency of precision affects the final result, and it is compiler and editor dependent whether any warning will appear. Double precision real values are assigned as $x.0D0$ or x_8 , where $D0$ is equivalent to 10^0 as it would for single precision be $x.0E0$.

Listing B.1: Abaqus standard UMAT code, Abaqus 2017.

```
1  SUBROUTINE UMAT(STRESS,STATEV,DDSDDE,SSE,SPD,SCD,  
2  1 RPL,DDSDDT,DRPLDE,DRPLDT,  
3  2 STRAN,DSTRAN,TIME,DTIME,TEMP,DTEMP,PRED,DPRED,CMNAME,  
4  3 NDI,NSHR,NTENS,NSTATV,PROPS,NPROPS,COORDS,DROT,PNEWDT,  
5  4 CELENT,DFGRD0,DFGRD1,NOEL,NPT,LAYER,KSPT,JSTEP,KINC)  
6  IMPLICIT NONE  
7  REAL*8 STRESS,STATEV,DDSDDE,SSE,SPD,SCD,  
8  1 RPL,DDSDDT,DRPLDE,DRPLDT,  
9  2 STRAN,DSTRAN,TIME,DTIME,TEMP,DTEMP,PRED,DPRED,  
10 3 PROPS,COORDS,DROT,PNEWDT,  
11 4 CELENT,DFGRD0,DFGRD1  
12 CHARACTER*80 CMNAME  
13 INTEGER*8 NSTATV,NTENS,NPROPS,NDI,NSHR,NOEL,NPT,KSPT,JSTEP,  
14 1 KINC,LAYER  
15 DIMENSION STRESS(NTENS),STATEV(NSTATV),  
16 1 DDSDDE(NTENS,NTENS),DDSDDT(NTENS),DRPLDE(NTENS),  
17 2 STRAN(NTENS),DSTRAN(NTENS),TIME(2),PRED(1),DPRED(1),  
18 3 PROPS(NPROPS),COORDS(3),DROT(3,3),DFGRD0(3,3),DFGRD1(3,3),  
19 4 JSTEP(4)  
20  
21 C      User defined code string  
22  
23 RETURN  
24 END SUBROUTINE UMAT
```

Full elaboration on the input variables is found in the Abaqus users guide. The variables of interest for the GPYS yield surface are given in Table B.1.

Table B.1: Main variables of focus

Input variables	
NPROPS	Number of material properties
NTENS	Dimension of stress vector
NSTATV	Number of state variables
PROPS	Real array containing material properties
DSTRAN	Real array containing strain increment in load step
Updated variables	
STRESS	Stress state in global coordinate system
STATEV	State variables passes information from previous load step and is stored in the results
Output variables	
DDSDDE	Consistent tangent in global coordinate system of size (NTENS×NTENS)

It is noted, that Abaqus arranges stress as $[\sigma_{xx}; \sigma_{yy}; \sigma_{zz}; \sigma_{xy}; \sigma_{xz}; \sigma_{yz}]^T$ which obviously affects construction of the stress tensor, as well as the transformation matrix to original stress space. After the obligated variables any variables used in the current subroutine is defined. As exemplified in the YIELD subroutine in Listing B.2.

Listing B.2: Subroutine example for yield function.

```

1  SUBROUTINE YIELD(F,SIG,PROPS,NPROPS)
2      IMPLICIT NONE
3      INTEGER*8,INTENT(IN)::NPROPS
4      REAL*8,INTENT(IN)::SIG(3),PROPS(NPROPS)
5      REAL*8,INTENT(OUT)::F
6      REAL*8 RHOC,PAPEX,SIGDEV(3),C(2),R,T(3,3)
7
8  C      User defined code string,
9  C      for calculating RHOC, Radius and Centre of curvature
10
11     SIGDEV(1:3) = MATMUL(T,SIG)
12     IF ( SIGDEV(1)/DSQRT(3.0D0)>PAPEX )THEN
13         F = NORM2( SIG-PAPEX )
14     ELSE
15         F = NORM2( SIGDEV(2:3)-C(1:2)*RHOC )-R*RHOC
16     ENDIF
17
18     RETURN
19 END SUBROUTINE YIELD

```

The intention statement for the input variables are not mandatory, but helps the compiler as well as code clarification for later use. Code should in general be written as thread-safe, for enabling parallel computing. Thread-safety is ensured via simple rules, as avoid writing to global variables and use of common blocks. Additionally pure subroutines and explicit interfaces can be utilized. Further, must the Fortran compiler be set up for single thread compiling, as illustrated in Listing B.5, as Fortran by default will optimize the code to use all accessible kernels. A declared Pure subroutine is unable to interfere with any global accessible variables or use print and write statements. Such a routine is exemplified in Listing B.3, along with different ways of constructing identity matrices.

Listing B.3: Pure subroutine example for double precision Identity matrix, size (n,n).

```

1  PURE SUBROUTINE DEYEM(EYE,n)
2      IMPLICIT NONE
3      INTEGER,INTENT(IN)::n
4      REAL*8,INTENT(OUT)::EYE(n,n)
5      INTEGER i
6
7      EYE(1:n,1:n) = 0.0D0
8      FORALL(i=1:n) EYE(i,i)=1.0D0
9  C or as follows
10     EYE(1:n,1:n) = 0.0D0
11     DO i=1,n
12         EYE(i,i) = 1.0D0
13     ENDDO
14  C or as but not recommended
15     EYE(1:n,1:n) = 0.0D0

```

```

16 | EYE(1,1) = 1.0D0
17 | EYE(2,2) = 1.0D0
18 | ! ...
19 | EYE(n,n) = 1.0D0
20 |
21 | RETURN
22 | END SUBROUTINE DEYEM

```

Transferability is in general of high priority, use of locally stored toolboxes and packages should therefore be avoided. Code snippets of necessary commands are highly available on-line and found in much literature see for instance [Press et al., 1992]. Fortran intrinsic functions are though highly recommended, as they are thread safe and accurate.

When generating multiple subroutines and thousand lines of code, a subdivision in to multiple files can be beneficial. The `INCLUDE` statement followed by the name of the file containing other subroutines, shall be placed outside any other subroutine as in Listing B.4.

Listing B.4: Example of subroutine with interface for a pure subroutine placed in another file named “UtilityRoutines.for”.

```

1 | SUBROUTINE Name(VAL1,VAL2)
2 |   IMPLICIT NONE
3 |   REAL*8,INTENT(IN)::VAL1
4 |   REAL*8,INTENT(OUT)::VAL2
5 |   REAL*8 EYE3(3,3)
6 |
7 |   INTERFACE
8 |     PURE SUBROUTINE DEYEM(EYE,n)
9 |       INTEGER,INTENT(IN)::n
10 |       REAL*8,INTENT(OUT)::EYE(n,n)
11 |     END SUBROUTINE DEYEM
12 |   END INTERFACE
13 |
14 |   CALL DEYEM(EYE3,3)
15 |
16 |   RETURN
17 | END SUBROUTINE Name
18 |
19 | INCLUDE 'UtilityRoutines.for'

```

B.2 Linking Abaqus and Fortran compiler

First of all, all programs are installed in correspondence with any given guidelines, probably in the following order “Intel Fortran”, “Microsoft Visual Studio” and lastly “Abaqus”. Visual Studio is optional, however, used for code editing and pre-compiling generated code. In the following we will create an environment file for Abaqus and consider two methods of linking Abaqus and the Fortran compiler, or in fact pre-launch the compiler.

An environment file called “`abaqus_v6.env`” is created, to alternate the Abaqus licence and the Fortran compiler directives, and placed in the Windows Temp folder, case-sensitive. The environment file is created in the text editor, and saved with the `.env` extension. The first line of the environment file of Listing B.5 will chance to a research licence, provided that Abaqus is installed as academic and a research licence is available. The later content alternates the standard Fortran compiler directives to accommodate parallel computing.

Listing B.5: Content of “`abaqus_v6.env`” file, case-sensitive Intel Fortran 2013 and Abaqus 2017.

```

academic=RESEARCH

compile_fortran=[ 'ifort',
                  '/c', '/DABQ_WIN86_64', '/extend-source', '/fpp',
                  '/iface:cref', '/recursive', '/Qauto-scalar',
                  '/QxSSE3', '/QxAVX',
                  '/heap-arrays:1',
                  '/thread', '/Qopenmp', '/libs:static', # <--- Added for parallel computing
                  '/Od', '/Ob0', # <--- Optimization Debugging
                  '/Zi', # <--- Debugging
                  '/include:%I' ]

```

The methods of pre-launching the compiler are, either to modify the short-cut target or to create a new short-cut as a batch file. The advantage of the latter approach is to have separate short-cuts for standard Abaqus usage and one for usage with UMAT where Fortran compiler is launched simultaneously with Abaqus. In both cases, locate the “ifortvars.bat” file, probably located in the following directory “C:\Program Files (x86)\Intel\Composer XE 2013\bin\ifortvars.bat”. The full path to this file (store it in a .txt document) is needed. Subsequently we will locate the short-cut for “Abaqus CEA” and “Abaqus Command”, and modify or copy their target to the aforementioned batch-file.

To modify the short-cut target, the previous found path is pasted, followed by “ intel64 vs2010 & ” prior to the current target, as shown in the tree of Figure B.1. The “intel64” refers to Intel Fortran 64 bit, and “vs2010” to Visual Studio 2010, this is of course software dependent. The Fortran Compiler is then set up to launch prior to the “Abaqus CEA” and “Abaqus Command” when using the start menu short-cut, provided, that the entered path is correct.

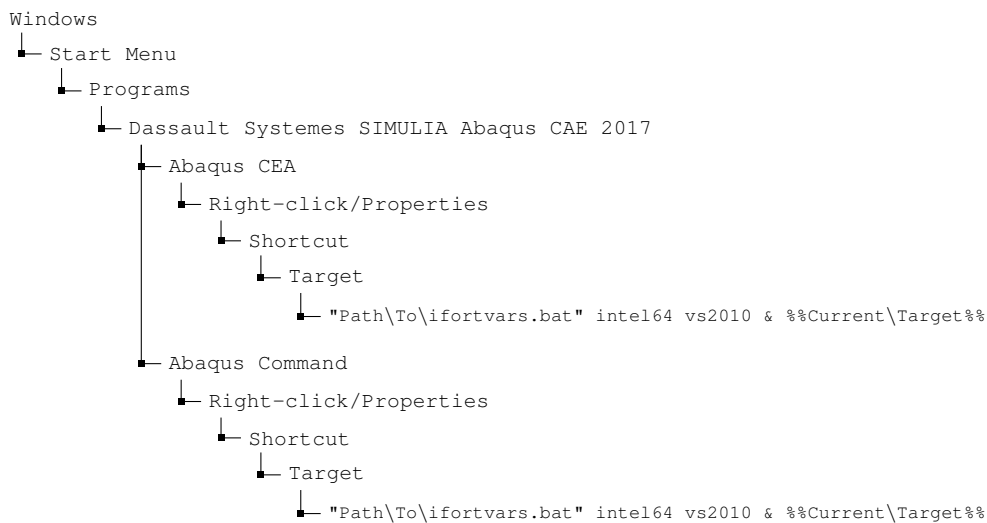


Figure B.1: Tree for locating Abaqus shortcut target and modification.

The other method rests on creating batch files, which will execute commands, in the same fashion as previously described. A batch file is created in a editor such as Notepad or Notepad++, and saved with the “.bat” extension. The batch files shall, in this case, be placed in the same folder as the “abaqus_v6.env” file of Listing B.5 (Make a new folder in \Temp). Firstly, the “IfortAbaqusCEA.bat” file of Listing B.6, is created, which initially deletes the abaqus.rpy file then launches the Fortran compiler followed by “Abaqus CEA”. In the preferred editor, copy/paste the previously found path to the “ifortvars.bat” file, followed by “ intel64 vs2010 & ” depending on your software. Locate the short-cut target for Abaqus CEA as in Figure B.1, copy the entire target and paste it to the .bat file. The result should look something like Listing B.6, where the ^ is used to continue the line. Double quotation, “”, is mandatory when a path contain spaces.

Listing B.6: Example of content in IfortAbaqusCEA.bat file.

```

1 del abaqus.rpy
2
3 "C:\Program Files (x86)\Intel\Composer XE 2013\bin\ifortvars.bat" intel64^
4 vs2010 & C:\SIMULIA\CAE\2017\win_b64\resources\install\cae\launcher.bat cae || pause

```

The second .bat file, “IfortCMD.bat”, of Listing B.7 will launch the Fortran compiler followed by the Windows Command Prompt, and is used to run Abaqus system check and verification. The file is constructed in the same fashion as Listing B.6, but with the target of short-cut “Abaqus Command” instead. The third line will run the Abaqus system check, which is optional and can be typed directly in the launched command prompt. Once again, the ^ is used to continue the line.

Listing B.7: Example of content of IfortCMD.bat file.

```

1 "C:\Program Files (x86)\Intel\Composer XE 2013\bin\ifortvars.bat" intel64^
2 vs2010 & C:\Windows\system32\cmd.exe /k^
3 abaqus info=system

```

When running the `IfortCMD.bat` file, Windows command window will launch a system check, where it is checked, that the correct Fortran compiler is linked. The result should look something like Listing B.8.

Listing B.8: Command snippet of result from the `IfortCMD.bat` file.

Virtual Memory:	14367 Available / 18726 Total Mbytes	
OS Version:	Windows 10 Education (Build 17134)	
C++ Compiler:	Unable to locate or determine the version of a C++ compiler on this system. If a C++ compiler is installed on this system, please load <code>vcvars64.bat</code> file before running Abaqus	
Linker Version:	Microsoft (R) Incremental Linker Version 10.00.30319.01	
Fortran Compiler:	Intel Fortran Compiler 13.0	<— OK
MPI:	MS-MPI 5.0.12435.6	
Browser:	Internet Explorer 11.0.17134.1	
Graphics Details:		

Alternative commands would be “`abaqus verify -user_std`”, to verify user defined subroutines are admissible (NOTE: Just type it in the launched command window). Provided that the Fortran compiler is correct and user defined subroutines are admissible, we are ready to set up the Abaqus CEA analyses for use of UMAT.

B.3 Preparing Abaqus CEA for UMAT analysis

The use of UMAT in Abaqus CEA requires some initiation. The model is generated as usual, but with alternation of the “Material model”, “Field output request” and initiation of the current job.

In the UMAT for GPYS-LD model, as described in Appendix C, 19 state variables and 9 input material parameters are defined, as listed in Table B.2. The later affects merely the convergence rate, and not the final result.

Table B.2: Input and output in the GPYS-UMAT.

User material		
1	ν	Poisson's Ratio
2	E	Youngs modulus
3	c	Cohesion
4	ϕ	Internal angle of friction
5	ψ	Internal angle of dilatation
6	α	Meridional eccentricity
7	β	Deviatoric curvature
8	χ_{apex}	Apex stiffness corrector
9	χ_{line}	Line stiffness corrector
Solution-dependent state variables		
1-6	Accumulated elastic strain	
7-12	Accumulated plastic strain	
13-18	Rate of plastic strain	
19	Rate of max plastic shear strain	

The set-up for use of UMAT in Abaqus is outlined in the tree of Figure B.2, which is a reduced version of the “Abaqus CEA” model tree. Obviously the material of the current model, has to be set-up for the desired material model, which in the case of a GPYS material is stated in Table B.2. In order to store and visualize the analysis results of the desired state variables, SDV has to be checked on under “Field Output Request.” The analysis job is created as usual, however, the path to the “.for” file containing the UMAT subroutine has to be defined. It is noted, that the GPYS-UMAT is thread safe and parallel computing is possible, with compiler settings as in Listing B.5.

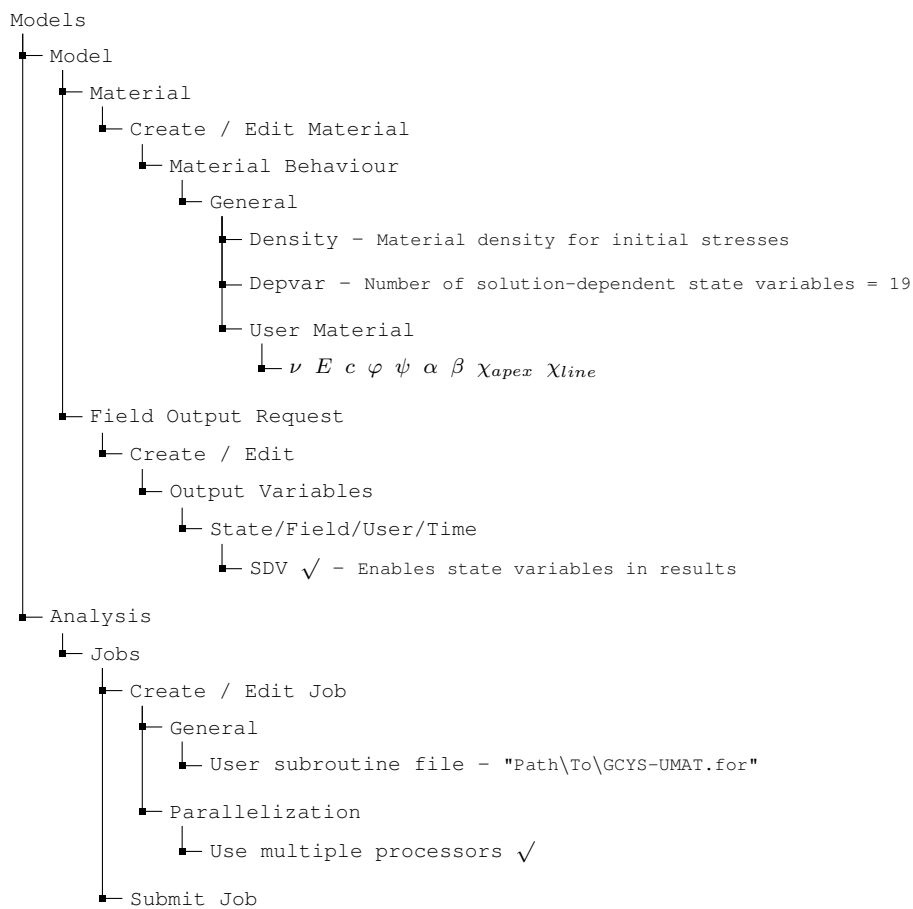


Figure B.2: Abaqus Model tree for UMAT analysis, bare minimum.

C | Parametric Transition from Mohr-Coulomb to Drucker Prager by Implementation of the General Parametric Yield Surface Format

The article in this appendix is submitted for peer review in “*International Journal for Numerical and Analytical Methods in Geomechanics*” June 2019 [Nielsen et al., 2019].

Summary:

The Mohr-Coulomb and Drucker-Prager yield criteria are often used as plasticity models in the analysis of frictional materials. Mohr-Coulomb is in better coherence with the actual behaviour of soil materials than the Drucker-Prager criterion, however, true material behaviour is evidently somewhere in-between these two extrema. This paper introduces a novel conical multi-surface plasticity model, which covers a wide range of convex shapes from Mohr-Coulomb to the Drucker-Prager surface. It operates on the well-known internal angle of friction and cohesion, plus two additional parameters to further adjust the shape. The surface is formulated with linear generators for simplicity, although, a nonlinear hydrostatic stress dependency is a straight forward extension of the model. The formulation with linear generators enables a closed form solution to the implicit return mapping scheme, furnishing a robust algorithm. The complete mathematical description and implementation in elasto-plastic finite element analysis is described, and the plasticity model is implemented in a commercial finite element software, to demonstrate its potential. The proposed yield surface is calibrated to true triaxial test data and used to analyse a strip footing in plane strain, which yields a noteworthy increase in load bearing capacity, as compared to a conventional Mohr-Coulomb model.

ARTICLE TYPE

Parametric Transition from Mohr-Coulomb to Drucker-Prager by Implementation of the General Parametric Yield Surface Format

Johan Nielsen | Kenneth Sixhøj Jepsen | Lars Damkilde*

¹Department of Civil Engineering, Aalborg University Esbjerg, 6700 Esbjerg, Denmark

Correspondence

*L. Damkilde, Aalborg University Esbjerg.
Email: lda@civil.aau.dk

Present Address

Niels Bohrs vej 8, 6700 Esbjerg, Denmark

Summary

The Mohr-Coulomb and Drucker-Prager yield criteria are often used as plasticity models in the analysis of frictional materials. Mohr-Coulomb is in better coherence with the actual behaviour of soil materials than the Drucker-Prager criterion, however, true material behaviour is evidently somewhere in-between these two extrema. This paper introduces a novel conical multi-surface plasticity model, which covers a wide range of convex shapes from Mohr-Coulomb to the Drucker-Prager surface. It operates on the well-known internal angle of friction and cohesion, plus two additional parameters to further adjust the shape. The surface is formulated with linear generators for simplicity, although, a nonlinear hydrostatic stress dependency is a straight forward extension of the model. The formulation with linear generators enables a closed form solution to the implicit return mapping scheme, furnishing a robust algorithm. The complete mathematical description and implementation in elasto-plastic finite element analysis is described, and the plasticity model is implemented in a commercial finite element software, to demonstrate its potential. The proposed yield surface is calibrated to true triaxial test data and used to analyse a strip footing in plane strain, which yields a noteworthy increase in load bearing capacity, as compared to a conventional Mohr-Coulomb model.

KEYWORDS:

Multi-surface plasticity, Intermediate principle stress, Elasto-plastic finite element analysis, Mohr-Coulomb, General Parametric Yield Surface, Return mapping in principle stress space.

1 | INTRODUCTION

In the analysis of geotechnical problems, the Mohr-Coulomb and the Drucker-Prager yield criterion is often used as the plasticity model for frictional materials. However, contradictions arises as the intermediate principal stress is neglected by the Mohr-Coulomb criterion, opposed to the Drucker-Prager model, where all stresses are of equal importance. The true material behaviour is somewhere between these two extrema, as supported by experimental researches as for instance Lade and Duncan,¹ Krishna and Surenda² or Bønding,³ to mention a few. In general terms, the Mohr-Coulomb criterion better represents the actual behaviour of frictional soil than the Drucker-Prager criterion, as discussed by for instance Bishop in 1966⁴ and more recently Alejano and Bobet in 2012.⁵ It is therefore of interest to formulate a yield surface, which can include the intermediate principal stress to some extent, to better represent the actual behaviour of a wide range of materials.

This paper offers the complete mathematical description and implementation in elasto-plastic finite element analysis of a novel yield surface, proposed by Damkilde.⁶ The surface is composed of conical sections, and covers a wide range of convex shapes from Mohr-Coulomb to the Drucker-Prager surface. Similar models are to the authors knowledge not present in the literature, although, other multi-surface models to cover a wide range of materials have been proposed, see for instance Yu 1961,⁷ Paul 1968⁸ or Coombs et al. 2010.⁹

The proposed yield surface is formulated as a composition of geometrical shapes in principle stresses, and makes use of advances in multi-surface plasticity made by Clausen et al.¹⁰ The concept is to define circles in the deviatoric plane, and through manipulation of the centre and radius, several convex shapes are covered, as illustrated in Figure 1. Isotropic material behaviour is assumed and the conventional ordering of the principal stresses, $\sigma_1 \geq \sigma_2 \geq \sigma_3$, is adopted, to exploit the six-fold symmetry of the yield surface and merely define one circular geometry. The Mohr-Coulomb deviatoric trace is approximated by defining the radius as a numerically large number and the Drucker-Prager with the centre at the hydrostatic axis. Considering more advanced models, the Reuleaux plasticity model, see Coombs et al.⁹ occurs as a special case of this yield surface. The surface is proposed with linear hydrostatic stress dependency for simplification, although, employment of nonlinear generators is a straight-forward extension of the mathematical formulation. Linear hydrostatic stress dependency further enables an analytical solution to the classical fully implicit return mapping scheme. The deviatoric trace could in general be composed of any number of circular segments, where convexity is ensured by limits on the surface parameters derived by geometrical arguments. See Jepsen et al.¹¹ for a formulation of this yield surface with multiple circular segments.

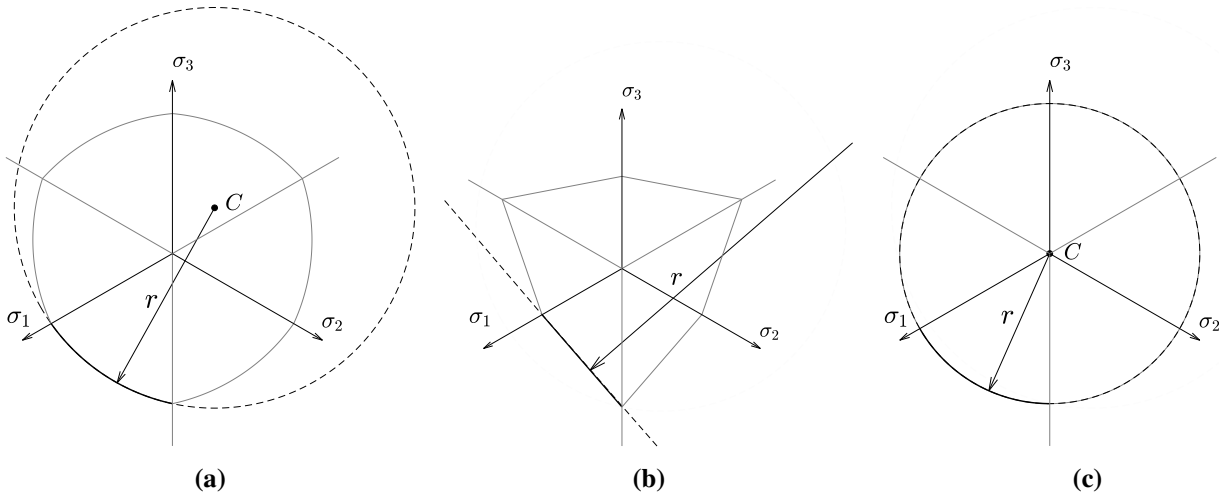


FIGURE 1 The concept of GPYS illustrated in deviatoric traces (a) intermediate setting (b) Mohr-Coulomb setting and (c) Drucker-Prager setting.

Yield surfaces can in general be grouped as discontinuous or continuous in the deviatoric trace, of which the latter is superior regarding global convergence rate in elasto-plastic finite element analysis. Some famous continuous yield surfaces in geomechanics is for instance, Drucker-Prager, 1951,¹² Matsuoka-Nakai, 1974,¹³ Lade, 1977,¹⁴ or the modified Drucker-Prager model,¹⁵ to mention a few. Yield surfaces, which are not continuously differentiable, such as, Mohr-Coulomb dating back to 1773,¹⁶ Unified Strength Theory, 1961,⁷ Hoek-Brown, 1980,¹⁷ or Reuleaux plasticity, 2010,⁹ are in general troublesome in numerical analysis, as discontinuities leads to poor convergence rate, or no convergence at all. To remedy this shortcoming, several approaches are available, such as corner rounding, see for instance Abbo et al. 2011,¹⁸ or by modifying the consistent tangent as proposed by Clausen et al. 2007.¹⁹ The latter is adopted in this paper, although, a corner rounded formulation of the proposed yield surface has been developed by the authors as well, see Jepsen et al.¹¹

The remainder of this paper is organized as follows: the mathematical description of the General Parametric Yield Surface (GPYS) is given in Section 2, followed by the return mapping scheme and calculation of the consistent elasto-plastic constitutive matrix in Section 3, and its use in numerical analysis is exemplified in Section 4. Throughout this paper, linearly elastic, perfectly plastic material behaviour and associated flow is assumed. Stresses are assumed as effective and the conventional apostrophe is omitted in the notations. Compressive stresses are given as negative quantities.

2 | MATHEMATICAL DESCRIPTION OF THE YIELD SURFACE

The mathematical description of the proposed yield surface is presented in this section. Principal stress representation is utilized to formulate the surface based on spatial geometry, see for instance Clausen et al.¹⁰ for an elaboration on the transformation between the general six-dimensional and principal stress space. Under the previously mentioned assumptions, the yield surface is defined by one circular segment in the deviatoric plane, by its centre and radius, as sketched in Figure 2a. The deviatoric geometry is then scaled by the deviatoric measure, ρ_c , which is defined as a function of hydrostatic stress. Here, the linear compression generator of Mohr-Coulomb is adopted, as sketched in Figure 2b. Considering the three-dimensional shape, the full yield surface is composed of six sections from an oblique cone, as illustrated in Figure 2c. A convex surface is ensured by simple limits on the surface parameters through geometrical considerations.

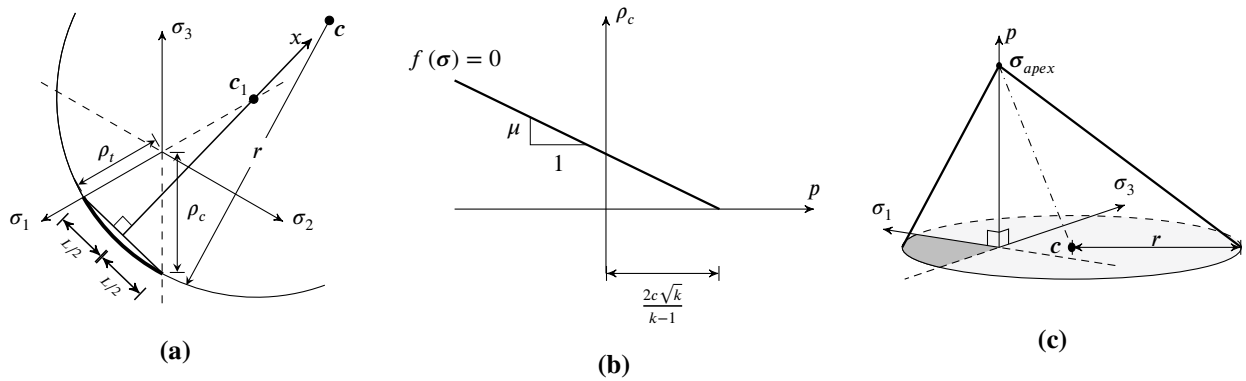


FIGURE 2 Geometrical illustration of the General Parametric Yield Surface (a) deviatoric plane (b) compressive meridian and (c) oblique cone generated by a circular deviatoric trace and linear generators.

The surface shape is governed by four parameters, the internal angle of friction and cohesion, plus two parameters denoted α and β , which controls the meridional eccentricity and the deviatoric curvature, respectively. The internal angle of friction and cohesion are well-known in geotechnical engineering, and the additional parameters are defined such that $\alpha = \beta = 0$ yields Mohr-Coulomb and $\alpha = \beta = 1$ the Drucker-Prager surface. The ρ_t/ρ_c -ratio is governed by the α -parameter, as the positioning of intersection point, c_1 , of the x -axis and the projected σ_1 -axis, see Figure 2a. The side curvature, is adjusted by the β -parameter, as the positioning of the centre of curvature, c , on the x -axis. A description of the surface parameters are given in Table 1 along with settings to emulate some existing yield criteria. The lower bound on the β -parameter prevents a zero-division, and a straight deviatoric trace is approximated for a value of 10^{-4} , as found through numerous numerical analysis. The limits on α and β in Table 1 ensures a convex deviatoric trace, and their impact on the shape is visualized in Figure 3.

TABLE 1 Parameter description, range of validity and approximation of some existing yield surfaces.

Description Symbol Range	Parameters			
	Angle of Friction φ Range	Cohesion $c^{\dagger\dagger}$ ≥ 0	Meridional eccentricity α [0; 1]	Curvature β [0; 1]
Special cases of existing plasticity models				
Mohr Coulomb ¹⁶	as is	as is	0.00	0.00 [†]
Extended Tresca ⁴	as is	as is	1.00	0.00 [†]
Drucker-Prager ¹²	as is	as is	1.00	1.00
Reuleaux ⁹	as is	as is	as is	1.00

[†] An appropriately small value is 10^{-4} .

^{††} Units of pressure

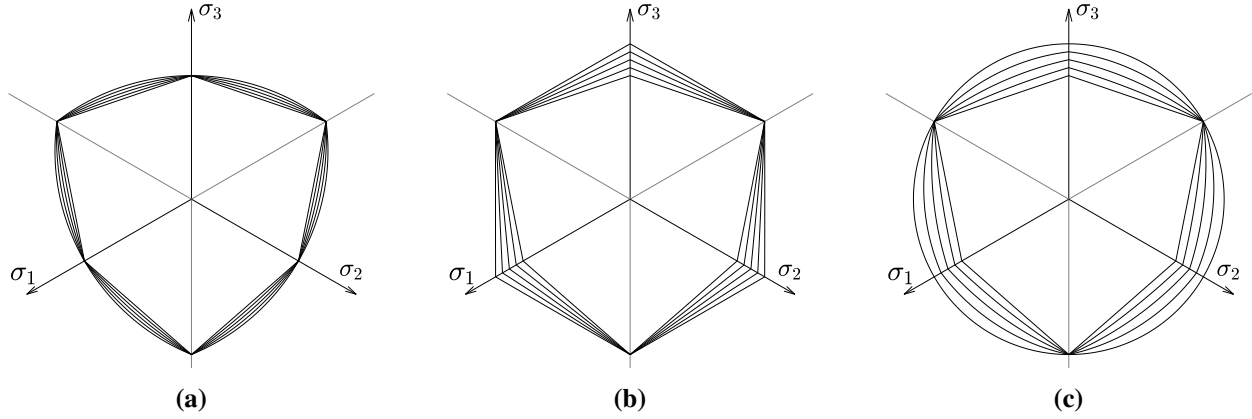
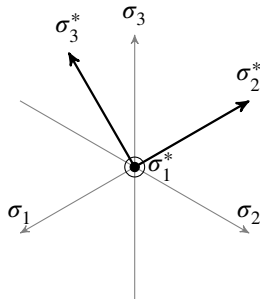


FIGURE 3 GPYS Deviatoric trace with various configurations of α and β from 0 to 1 with increments of 0.25. **(a)** Variation of β with fixed $\alpha = 0$ **(b)** variation of α with fixed $\beta = 0$ and **(c)** variation of α and β .

The surface is formulated with the apex at the origin, and stress states are parallel shifted with the apex hydrostatic stress, in the implementation in numerical analysis. The apex of Mohr-Coulomb is adopted as

$$p_{\text{apex}} = \frac{2c\sqrt{k}}{k-1}.$$

A key element in the formulation of the novel yield surface is to operate with a deviatoric geometry, which is scaled with a function of the hydrostatic stress. The typical decomposition of stresses in deviatoric and hydrostatic components is exploited, and it is found convenient to define the deviatoric geometry in the cartesian σ^* -coordinate system as illustrated in Figure 4. For an elaboration on this transformation, see Appendix A.



$$\sigma^* = \mathbf{T}\sigma = \begin{bmatrix} 1/\sqrt{3} & 1/\sqrt{3} & 1/\sqrt{3} \\ -\sqrt{2}/3 & 1/\sqrt{6} & 1/\sqrt{6} \\ 0 & -1/\sqrt{2} & 1/\sqrt{2} \end{bmatrix} \begin{Bmatrix} \sigma_1 \\ \sigma_2 \\ \sigma_3 \end{Bmatrix} = \begin{Bmatrix} \sigma_1^* \\ \sigma_2^* \\ \sigma_3^* \end{Bmatrix} = \begin{Bmatrix} p\sqrt{3} \\ \sigma_2^* \\ \sigma_3^* \end{Bmatrix}$$

FIGURE 4 Transformation from principal stresses to the σ^* coordinates, seen in the deviatoric plane.

A sketch with relevant measures in the deviatoric plane to derive the mathematical expression for the yield surface is presented in Figure 5.

The parameters are calculated in the ρ_c -normalized deviatoric plane with

$$\bar{\rho}_c = 1 \quad \wedge \quad \bar{\rho}_t = \alpha + \frac{3 - \sin \varphi}{3 + \sin \varphi} (1 - \alpha),$$

where, α , is introduced as the meridional eccentricity. The tension meridian equals Mohr-Coulomb with $\alpha = 0$ and yields $\rho_t = \rho_c$ for $\alpha = 1$. The secant length, L , of Figure 5a, and the angle, γ , of Figure 5b, are calculated by the Pythagorean theorem and the tangent relation as

$$L = \sqrt{\left(\frac{\sqrt{3}}{2}\right)^2 + \left(\bar{\rho}_t - \frac{1}{2}\right)^2} \quad \wedge \quad \gamma = \arctan\left(\frac{\bar{\rho}_t - \frac{1}{2}}{\frac{\sqrt{3}}{2}}\right).$$

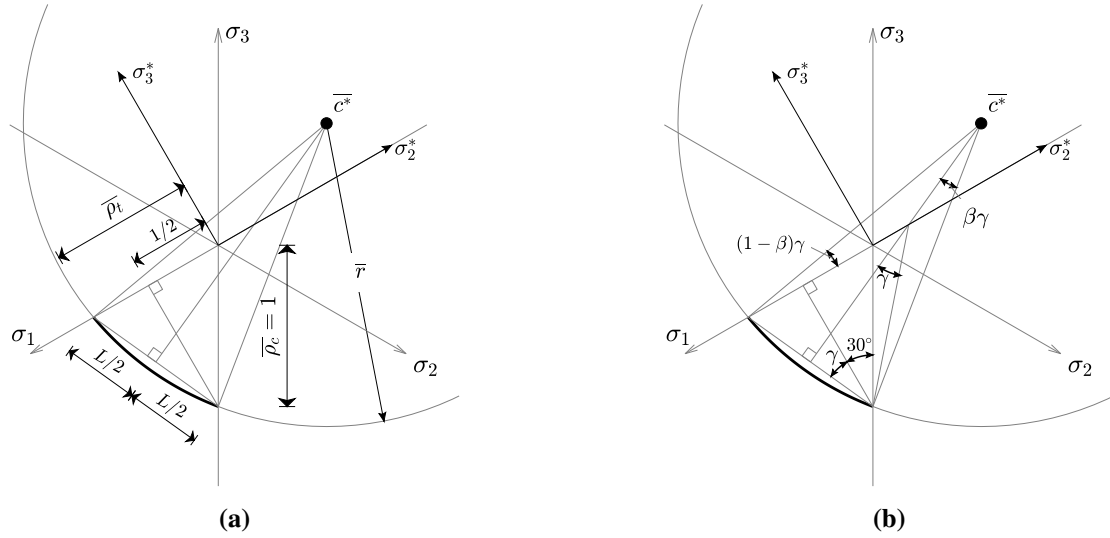


FIGURE 5 Sketch with relevant measures in the ρ_c -normalized deviatoric plane for derivation of the GPYS criterion (a) measures of length and (b) angular relations.

The normalized centre in σ^* -coordinates and radius is found by straightforward geometrical relations and reads

$$\bar{c}^* = \left\{ \begin{array}{c} \sqrt{3}/\mu \\ \bar{r} \cos((1-\beta)\gamma) - \bar{\rho}_t \\ \bar{r} \sin((1-\beta)\gamma) \end{array} \right\} \quad \wedge \quad \bar{r} = \frac{L}{2 \sin(\beta\gamma)},$$

where, β , is introduced to adjust the curvature by scaling the angle γ . The expression for ρ_c is adopted as the compressive meridian of Mohr-Coulomb, which along with its first and second partial derivatives, used in the finite element implementation, with respect to the stresses becomes

$$\rho_c = \mu p \quad \wedge \quad \frac{\partial \rho_c}{\partial \sigma_i} = \frac{\mu}{3} \quad \wedge \quad \frac{\partial^2 \rho_c}{\partial \sigma_i \partial \sigma_j} = 0,$$

where, μ , is the slope of the Mohr-Coulomb compressive generator, see Figure 2b, given as

$$\mu = \frac{1-k}{\sqrt{2/3}(k/2+1)}, \quad k = \frac{1+\sin \varphi}{1-\sin \varphi}.$$

The yield criterion is formulated as the difference between the radius and the deviatoric distance from the current stress state to the centre of curvature. The yield criterion and its first and second partial derivatives with respect to the principal stresses, used in the finite element implementation, are given as

$$f = \|\sigma^* - \bar{c}^*\rho_c\| - \bar{r}\rho_c, \quad (1)$$

$$\frac{\partial f}{\partial \sigma_i} = \|\sigma^* - \bar{c}^*\rho_c\|^{-1} h_i - \bar{r} \frac{\partial \rho_c}{\partial \sigma_i}, \quad (2)$$

$$\frac{\partial^2 f}{\partial \sigma_i \partial \sigma_j} = \|\sigma^* - \bar{c}^*\rho_c\|^{-1} \frac{\partial h_i}{\partial \sigma_j} - \|\sigma^* - \bar{c}^*\rho_c\|^{-3} h_i h_j - \bar{r} \frac{\partial^2 \rho_c}{\partial \sigma_i \partial \sigma_j}, \quad (3)$$

where,

$$h_i = (\sigma_2^* - \bar{c}_2^*\rho_c) \left(T_{2i} - \bar{c}_2^* \frac{\partial \rho_c}{\partial \sigma_i} \right) + (\sigma_3^* - \bar{c}_3^*\rho_c) \left(T_{3i} - \bar{c}_3^* \frac{\partial \rho_c}{\partial \sigma_i} \right),$$

$$\frac{\partial h_i}{\partial \sigma_j} = \left(T_{2j} - \bar{c}_2^* \frac{\partial \rho_c}{\partial \sigma_j} \right) \left(T_{2i} - \bar{c}_2^* \frac{\partial \rho_c}{\partial \sigma_i} \right) + \left(T_{3j} - \bar{c}_3^* \frac{\partial \rho_c}{\partial \sigma_j} \right) \left(T_{3i} - \bar{c}_3^* \frac{\partial \rho_c}{\partial \sigma_i} \right) - \left((\sigma_2^* - \bar{c}_2^*\rho_c) \bar{c}_2^* + (\sigma_3^* - \bar{c}_3^*\rho_c) \bar{c}_3^* \right) \frac{\partial^2 \rho_c}{\partial \sigma_i \partial \sigma_j}.$$

The expressions are kept in terms of ρ_c and its derivatives for the sake of generality, i.e. any function of the hydrostatic stress could be formulated for, ρ_c , differentiated twice and used in Equations (1) to (3). The transformation matrix, \mathbf{T} , of Figure 4 enters the expressions as result of differentiating the σ^* -coordinates with respect to the principal stresses. The normalized centre, \bar{c}^* , and radius, \bar{r} , are conveniently calculated prior to an analysis, to avoid calculation at every stress point for each global iteration. The generality of the surface is well established at this point, as the circular geometry in the deviatoric plane covers a wide range of convex shapes, and the generators simply needs to be a function of hydrostatic stress, and could have any appropriate non-linear variation.

3 | IMPLEMENTATION IN ELASTO-PLASTIC FINITE ELEMENT ANALYSIS

The implementation in elasto-plastic finite element analysis of the proposed plasticity model is described in this section. A general introduction is given here, and a thorough mathematical description is given in Appendices B, C and D. Appendix B describes the determination of the stress return type, and the expressions for the return mapping algorithm is derived in Appendix C. The consistent tangent operator for the different return types are derived in Appendix D. The implicit return mapping scheme, see for instance de Borst et al.²⁰ is here explained from the geometrical illustration in Figure 6.

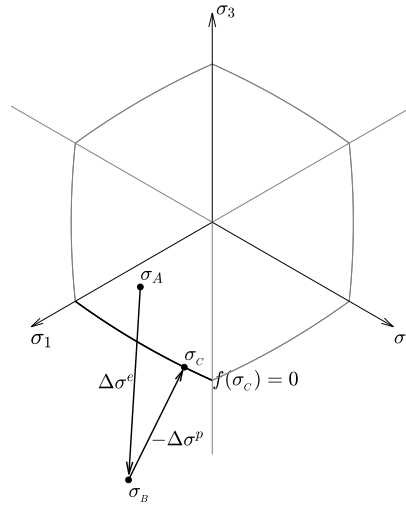


FIGURE 6 Geometrical illustration of return mapping seen in a deviatoric plane.

A nonlinear finite element procedure is assumed, where a strain increment, $\Delta \epsilon$, results in an elastic predictor stress state, σ_B , see Figure 6, as

$$\sigma_B = \sigma_A + \Delta \sigma^e = \sigma_A + \mathbf{D} \Delta \epsilon,$$

where, σ_A , is the stress state prior to the strain increment and, \mathbf{D} , is the isotropic elasticity matrix. If $f(\sigma_B) > 0$, the stress state is inadmissible, and the fully implicit return mapping scheme is adopted to calculate the stress state as consequence of $\Delta \epsilon$. The conventional decomposition of a strain increment into an elastic and a plastic part is assumed, and the plastic strain increment is described via the flow rule

$$d\epsilon = d\epsilon^e + d\epsilon^p \quad \wedge \quad d\epsilon^p = d\lambda \nabla g, \quad (4)$$

where superscripts, e and p , denotes a purely elastic and plastic quantity, respectively, $d\lambda$ is the plastic multiplier, and g is the potential function. Associated flow $g = f$ is assumed in this implementation of the GPYS model, however, g is maintained in the notations for generality. An infinitesimal stress increment is found by isolating the elastic strain increment in Equation (4) and applying the elastic stress strain relation as

$$d\sigma = \mathbf{D} d\epsilon^e = \mathbf{D} (d\epsilon - d\epsilon^p) = \mathbf{D} (d\epsilon - d\lambda \nabla g). \quad (5)$$

Integration over a finite increment is assumed with constant plastic strain direction, evaluated for the updated stress state, i.e. a fully implicit numerical integration scheme. This yields the following relation for the updated stress state

$$\sigma_C = \sigma_A + \mathbf{D}\Delta\epsilon - \int_{\lambda}^{\lambda+\Delta\lambda} \mathbf{D}\nabla g \, d\lambda = \sigma_A + \Delta\sigma^e - \Delta\sigma^p \simeq \sigma_A + \mathbf{D}\Delta\epsilon - \Delta\lambda \mathbf{D}\nabla g(\sigma_C),$$

where subscript, C , denotes the updated stress state, and $\Delta\sigma^e$ and $\Delta\sigma^p$ are the elastic predictor and plastic corrector, respectively. Employing the yield criterion as a constrained equation, the following system is obtained for the stress update

$$\begin{aligned} \sigma_C &= \sigma_B - \Delta\lambda \mathbf{D}\nabla g(\sigma_C), \\ f(\sigma_C) &= 0, \end{aligned} \quad (6)$$

where the prior stress state, σ_A , is omitted as it merely is needed to calculate the elastic predictor, σ_B .

For the proposed plasticity model, three return types are encountered, namely to the surface, an intersection line or the apex point, as illustrated in Figure 7a. A systematic approach is to introduce four regions in principal stress space, as proposed by for instance Clausen et al.^{10,19} for return to the surface, the compressive and tensile meridians and the apex, respectively. The return region is determined from the derivations in Appendix B and can be illustrated by the surfaces depicted in Figure 7b.

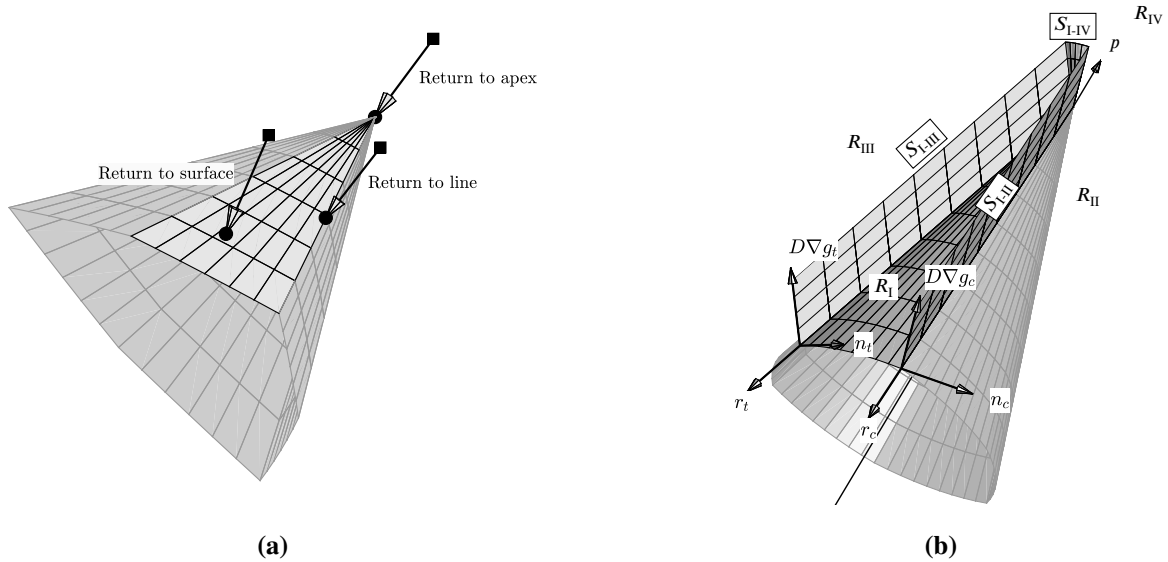


FIGURE 7 (a) Encountered stress return types and (b) three-dimensional illustration of border surfaces, S_{I-II} , S_{I-III} and S_{I-IV} .

When an elastic predictor stress state is situated in region IV, it is simply returned to the apex. In regions, II and III, the stress state is returned to the intersections lines via a geometrical approach presented by Clausen et al.¹⁹ the details of which are given in Appendix C.2. A predictor stress state situated in region I is returned to the surface as the solution to the system of Equation (6), which can be solved with a numerical procedure or in closed form as thoroughly described in Appendix C.1. The closed form solution, inspired by the works of Coombs et al.⁹ and Crouch et al.²¹ consists of rather long expressions, however, it is superior in robustness, especially for stress returns in the vicinity of the apex.

When a material point is subjected to plastic straining, the stress and strain increments are related by the consistent elasto-plastic constitutive matrix, or simply referred to as the consistent tangent, as elaborated in Appendix D. The consistent tangent relates changes in finite increments of stress and strain as

$$d(\Delta\sigma) = \mathbf{D}^{epc} d(\Delta\epsilon),$$

where superscript, epc , denotes a consistent elasto-plastic quantity. It provides stiffness tangential to the yield surface and is singular in direction of the plastic strain increment, as

$$\Delta\sigma = \mathbf{D}^{epc} (\Delta\epsilon^e + \Delta\epsilon^p) = \mathbf{D}^{epc} \Delta\epsilon^e + 0.$$

The consistent tangent operator is determined posterior to updating the stress state, and different expressions are needed for the respective return regions. At the surface, region I, it is determined via the well known expression as first derived by Simo and Taylor²², see Appendix D.1. For stress return to a singularity, region II, III and IV, formulations by Clausen et al.²³ are used to calculate the consistent tangent. Here, the Koiter method²⁴ are modified for improved convergence rate, see Appendices D.2 and D.3 for further elaboration.

4 | NUMERICAL EXAMPLE

An application of the GPYS model is illustrated by its use as the well known Mohr-Coulomb plasticity model, and as a more refined material model, fitted to data from true triaxial experiments. The system of choice is a 0.4m wide, fully rough, vertically loaded, shallow strip footing on frictional soil, analysed in plane strain conditions. The vertical line of symmetry is exploited to model one half of the system, and linearly elastic perfectly plastic behaviour and associated flow is assumed for the material. The geometrical and mechanical properties of the system along with the mesh grid of the model is presented in Figure 8. A highly refined mesh grid is in general needed near the footing corner to obtain representative results, which here is obtained manually, without any adaptivity studies. The finite element model consists of 11,398 six-node triangular elements and 46,010 displacement degrees of freedom. The vertical force is simulated by a uniform downwards displacement of the nodes in the foundation footprint, and the reaction force is calculated as twice the sum of the vertical forces in these nodes. The field of initial stresses is calculated with an at rest earth pressure coefficient, $K_0 = 1$. The analysis are conducted in the commercial finite element software, Abaqus, with the proposed plasticity model implemented as a user-defined subroutine. The elements of choice are the standard displacement based plane continuum elements, CPE6 of the Abaqus library, with second order interpolation and a three point Gauss integration scheme.

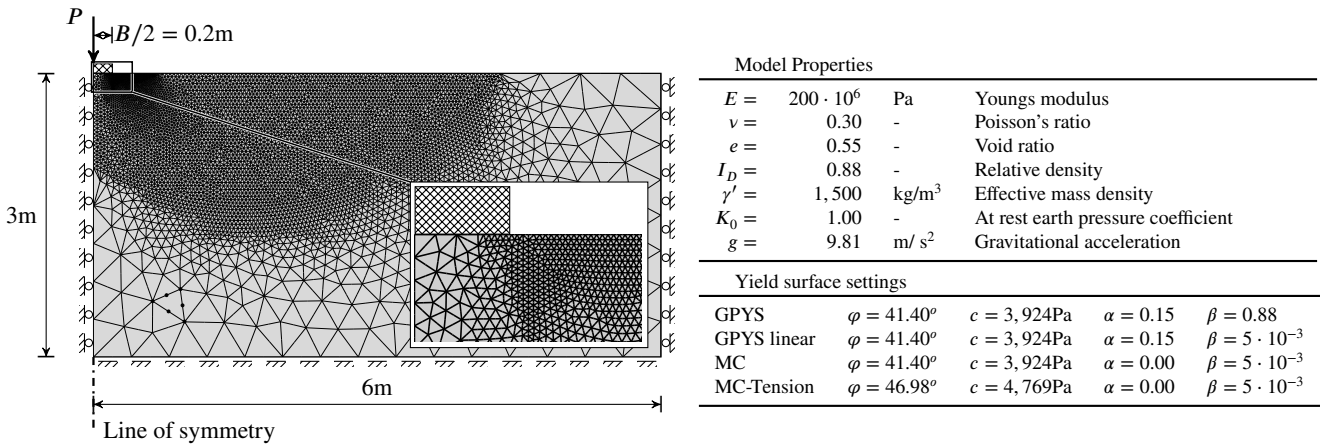


FIGURE 8 Finite element model of strip footing with visual mesh grid and model properties.

The constitutive models are calibrated to data from true triaxial experiments on a dense sand, $I_D = 0.88$, performed by Bønding,³ whom measured the principal stresses at failure. No safety factors or correction for non-associated flow are imposed on the angle of friction, which will therefore seldom occur of this magnitude in geotechnical design. The differences between the models are severely pronounced in this example, both due to the large angle of friction and plane strain conditions.

Four analysis are conducted with different settings of the novel yield surface model, to elucidate the impact of yield surface curvature and the ρ_t/ρ_c -ratio, which is fixed in Mohr-Coulomb plasticity. One model is calibrated by means of the least squares method to the aforementioned data, and one as a corresponding linear model with minimal side curvature, $\beta \approx 0$, is considered. These are compared to two Mohr-Coulomb models, which intersects the GPYS fit in the compression and tensile meridian, respectively. The former is a conservative Mohr-Coulomb fit and the latter is unsafe in general three-dimensional problems, however, a basis for comparison in this study. The models are visualized in the deviatoric plane in Figure 9a and the plane of the

compression meridian in Figure 9b along with data points in a select range of hydrostatic stress and Lode angle, respectively. It is noted, that the curvature of the GPYS model exceeds the Mohr-Coulomb tension fit in the deviatoric plane.

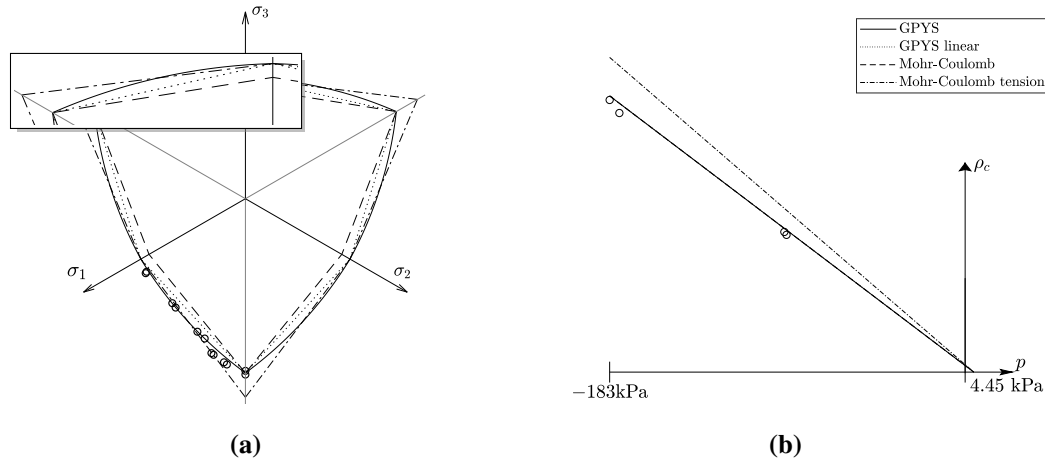
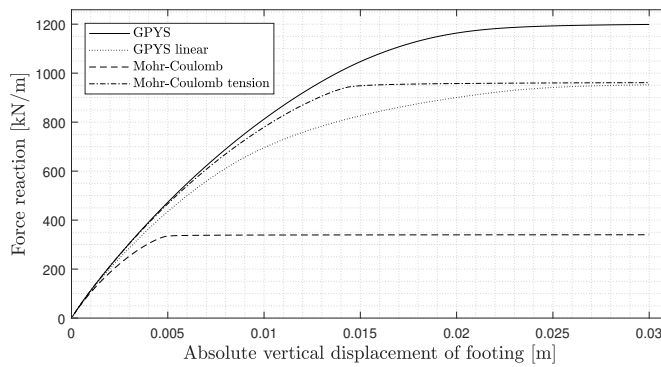


FIGURE 9 Illustration of the four yield surface models along with some of the data points from the parameter calibration, seen in (a) deviatoric plane at -200kPa and (b) plane of the compressive meridian.

The analysis results are visualised as force-displacement curves in Figure 10, revealing failure in all cases. The rate of maximum plastic shear strain at failure from the four analysis is visualised in Figure 11, and the well-known failure mode is recognized, verifying the domain width.



	Capacity [kN/m]	Ratio [-]
Mohr-Coulomb	340.2	1.00
Mohr-Coulomb tension	961.2	2.83
GPYS linear	952.4	2.80
GPYS	1,198.9	3.52

FIGURE 10 Force-displacement curves for the simulations, with results as load bearing capacity and ratio.

A noteworthy increase in load bearing capacity is found in comparison with the Mohr-Coulomb compressive fit. This is severely pronounced as it is a dense sand in an N_γ analysis, and the limit load is exponentially related to the angle of friction, see for instance Terzaghi.²⁵ A factor of 3.52 is not a general factor for increasing the compression calibrated Mohr-Coulomb, but definitely an indication of unused potential. As a further note to this, the angle of friction is often increased in plane strain analysis, however, such an increase cannot be argued in general 3D considerations, where a material model, such as GPYS, is necessary for material optimisation. See Jepsen et al.¹¹ for a 3D application of the GPYS model on a sand of similar properties as in the present analysis.

The linear compression-tension fit of GPYS yields almost the same limit load as the tension fit of Mohr-Coulomb, however, the displacement response under load is quite different. How the Mohr-Coulomb parameters in associated plasticity are fitted by practitioners is beyond the scope of this paper, however, a tensile fit is unsafe in general considerations. As the ρ_t/ρ_c -ratio is

rather influential on the model strength, a simple use of the GPYS model, is to calibrate with standard cylindrical triaxial tests, in both compression and extension.

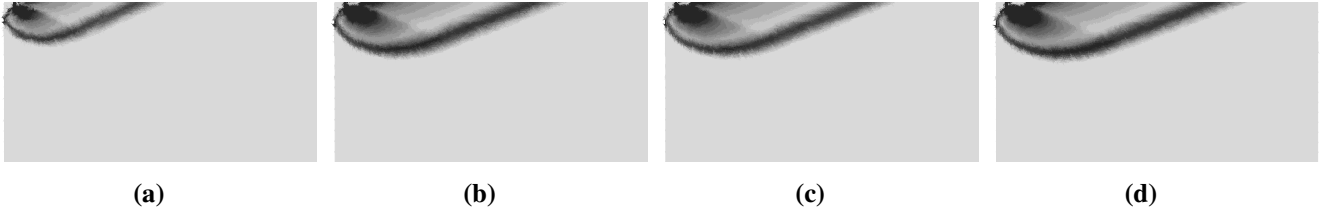


FIGURE 11 Rate of maximum plastic shear strain at failure (a) Mohr-Coulomb criterion, compression fit. (b) Mohr-Coulomb criterion, tension fit. (c) GPYS, linear compression-tension fit. (d) GPYS, least square fit.

5 | CONCLUSION

A novel yield surface, which encompasses several classical models and describes a wide range of frictional materials, has been introduced. It operates on the well-known shear strength parameters of Mohr-Coulomb, to establish familiarity, and two additional parameters to adjust the ρ_t/ρ_c -ratio and deviatoric curvature. The complete mathematical description and implementation in a computational elasto-plastic finite element framework is given, and the model is implemented in a commercial finite element software to demonstrate its potential. The surface is introduced with linear generators for simplicity, although, extension to a nonlinear hydrostatic stress dependency is straightforward. The formulation with linear generator, perfect plasticity and associated flow enables a closed form solution to the implicit return mapping scheme, which renders a robust return algorithm.

The novel yield surface model is applied in analysis of a shallow strip footing under plain strain conditions, where a noteworthy increase in load bearing capacity is found in comparison to a Mohr-Coulomb compressive fit. The ρ_t/ρ_c -ratio is found rather influential on the load bearing capacity, and a simple and prosperous use of the GPYS model, is to calibrate with standard cylindrical triaxial compression and extension tests. The conventional triaxial compression fit of Mohr-Coulomb is in general conservative, rendering a more optimized material model, such as the herein presented, an attractive tool in constitutive modelling of frictional soil.

The presented plasticity model is FORTRAN source code, for use in the Abaqus software, and in MATLAB as well, which can be obtained from the corresponding author.



APPENDIX

A TRANSFORMATION BETWEEN REFERENCE COORDINATE SYSTEMS

The transformation between the principal stress and the σ^* -coordinate systems, which are used in formulation of the proposed yield surface, is described in this Appendix. The transformation from principal stresses to σ^* -coordinates is performed by three plane rotations, as sketched in Figure A1. The first two rotations makes the σ_1^* -axis coincide with the hydrostatic axis, and the latter rotation of 30 degrees, makes the σ_2^* -axis coincide with the deviatoric projection of the first principal axis.

The three transformations sketched in Figure A1 reads

$$\sigma^* = \mathbf{T}\sigma = \begin{Bmatrix} \sigma_1^* \\ \sigma_2^* \\ \sigma_3^* \end{Bmatrix} = \begin{bmatrix} 1 & 0 & 0 \\ 0 & \sqrt{3}/2 & 1/2 \\ 0 & -1/2 & \sqrt{3}/2 \end{bmatrix} \begin{bmatrix} \sqrt{2/3} & 0 & 1/\sqrt{3} \\ 0 & 1 & 0 \\ -1/\sqrt{3} & 0 & 1/\sqrt{3} \end{bmatrix} \begin{bmatrix} \sqrt{2}/2 & \sqrt{2}/2 & 0 \\ -\sqrt{2}/2 & \sqrt{2}/2 & 0 \\ 0 & 0 & 1 \end{bmatrix} \begin{Bmatrix} \sigma_1 \\ \sigma_2 \\ \sigma_3 \end{Bmatrix} = \begin{bmatrix} 1/\sqrt{3} & 1/\sqrt{3} & 1/\sqrt{3} \\ -\sqrt{2/3} & 1/\sqrt{6} & 1/\sqrt{6} \\ 0 & -1/\sqrt{2} & 1/\sqrt{2} \end{bmatrix} \begin{Bmatrix} \sigma_1 \\ \sigma_2 \\ \sigma_3 \end{Bmatrix}. \quad (\text{A1})$$

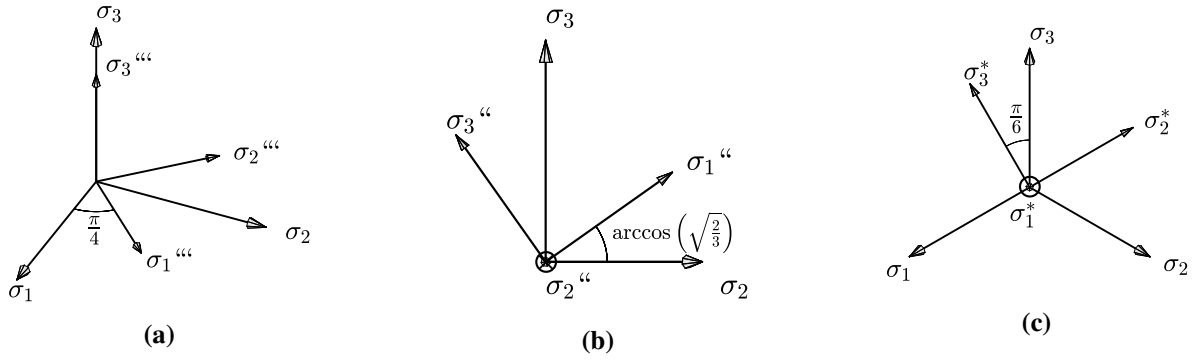


FIGURE A1 Transformation from principal stress to σ^* -coordinates in three steps (a) 45 degrees rotation about σ_3 (b) $\arccos \sqrt{2/3}$ radians rotation about σ_2'' and (c) 30 degrees rotation about σ_1^* .

The inverse of, \mathbf{T} , equals the transpose, as exploited in the inverse transformation to principal stresses

$$\boldsymbol{\sigma} = \mathbf{T}^{-1} \boldsymbol{\sigma}^* = \mathbf{T}^T \boldsymbol{\sigma}^* = \begin{bmatrix} 1/\sqrt{3} & -\sqrt{2/3} & 0 \\ 1/\sqrt{3} & 1/\sqrt{6} & -1/\sqrt{2} \\ 1/\sqrt{3} & 1/\sqrt{6} & 1/\sqrt{2} \end{bmatrix} \boldsymbol{\sigma}^*. \quad (\text{A2})$$

B DETERMINATION OF RETURN REGION

Correct stress return is crucial to achieve satisfactory convergence rate in the global iteration scheme. In this appendix, four regions denoted, R_I , R_{II} , R_{III} and R_{IV} , which determines whether a stress state is updated to the surface, the compression and tensile meridian or the apex, respectively, are described. For a similar approach in implementation of a multi-surface plasticity model, see for instance Clausen et al.¹⁹ Three surfaces are used to determine the return region as visualized in three-dimensional illustrations in Figure B2b. As a preliminary consideration, it is advantageous to formulate the potential normal, which is proportional to the potential gradient, ∇g . The surface normal is expressed in terms of hydrostatic stress and the angle, ζ , which is illustrated in Figure B2a. Considering the parametric construction of the potential surface in principal stresses as

$$\boldsymbol{\sigma}(p, \zeta) = [\sigma_1 \ \sigma_2 \ \sigma_3]^T = \rho_c(p) (\bar{\mathbf{c}} + \bar{r}(\mathbf{a} \cos \zeta + \mathbf{b} \sin \zeta)), \quad \mathbf{a} = 1/\sqrt{6} [2 \ -1 \ -1]^T \quad \wedge \quad \mathbf{b} = 1/\sqrt{2} [0 \ -1 \ 1]^T. \quad (\text{B3})$$

Reducing the vector cross product of the partial derivatives with respect to, p and ζ , the surface normal reduces to a particularly convenient form

$$\mathbf{n}(\zeta) = \frac{\frac{\partial \boldsymbol{\sigma}(p, \zeta)}{\partial p} \times \frac{\partial \boldsymbol{\sigma}(p, \zeta)}{\partial \zeta}}{\left\| \frac{\partial \boldsymbol{\sigma}(p, \zeta)}{\partial p} \times \frac{\partial \boldsymbol{\sigma}(p, \zeta)}{\partial \zeta} \right\|} = \frac{(\mathbf{b} \times \bar{\mathbf{c}}) \cos \zeta + (\bar{\mathbf{c}} \times \mathbf{a}) \sin \zeta + \bar{r}(\mathbf{b} \times \mathbf{a})}{\|(\mathbf{b} \times \bar{\mathbf{c}}) \cos \zeta + (\bar{\mathbf{c}} \times \mathbf{a}) \sin \zeta + \bar{r}(\mathbf{b} \times \mathbf{a})\|} \propto \nabla g. \quad (\text{B4})$$

It is noted from Equation (B4), that the surface normal is independent of the hydrostatic pressure.

The condition statements of the surfaces, S_{I-II} and S_{I-III} , is formulated as

$$S_{I-II} = \mathbf{n}_c^T (\boldsymbol{\sigma}_{apex} - \boldsymbol{\sigma}) \quad \wedge \quad S_{I-III} = \mathbf{n}_t^T (\boldsymbol{\sigma}_{apex} - \boldsymbol{\sigma}), \quad \boldsymbol{\sigma}_{apex} = \frac{2c\sqrt{k}}{k-1} [1 \ 1 \ 1]^T,$$

where, \mathbf{n}_c and \mathbf{n}_t , are the border surface orthogonal vectors at the compressive and tensile meridians, respectively, as illustrated in Figure B2b, given as

$$\mathbf{n}_c = (\mathbf{D} \mathbf{n}(\zeta_c)) \times \mathbf{r}_c \quad \wedge \quad \mathbf{n}_t = (\mathbf{D} \mathbf{n}(\zeta_t)) \times \mathbf{r}_t, \quad (\text{B5})$$

$$\mathbf{r}_c = [1 \ 1 \ k]^T \quad \wedge \quad \mathbf{r}_t = [1 \ 1 \ 1]^T - \left((1-\alpha) \frac{k-1}{k+1/2} + \alpha \frac{k-1}{k/2+1} \right) [1 \ -1/2 \ -1/2]^T, \quad (\text{B6})$$

$$\zeta_c = -(1+\beta)\gamma \quad \wedge \quad \zeta_t = -(1-\beta)\gamma. \quad (\text{B7})$$

Equation (B6) is the direction vectors of the compressive and tensile meridians, and the ζ -angles of Equation (B7) are shown in Figure B2a. Setting, S_{I-II} and S_{I-III} , equal to zero, renders the surfaces in Figure B2b.

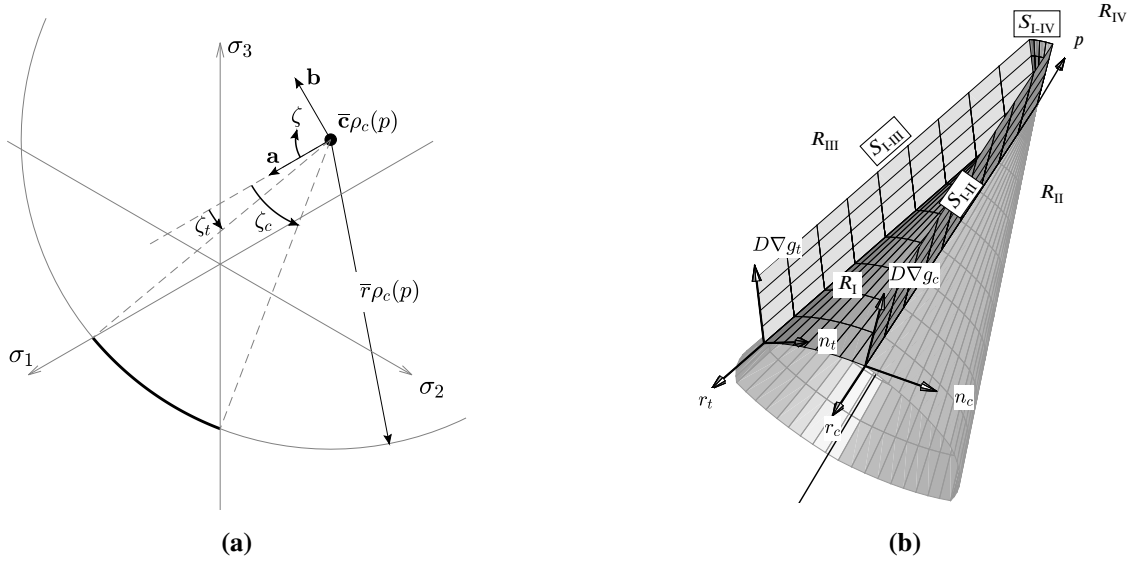


FIGURE B2 Sketches for determination of return region (a) deviatoric quantities for Equation (B3) and (b) three-dimensional illustration of border surfaces, S_{I-II} , S_{I-III} and S_{I-IV} .

The potential normal from Equation (B4), originating at the apex and premultiplied by \mathbf{D} defines the generators of the surface S_{I-IV} . The condition equation for this surface is established as

$$S_{I-IV} = \cos v_1 - \cos v_2 = \frac{(\mathbf{D} \mathbf{n}(\zeta_b))^T \mathbf{n}_p}{\| \mathbf{D} \mathbf{n}(\zeta_b) \| \| \mathbf{n}_p \|} - \frac{\mathbf{v}_1^T \mathbf{n}_p}{\| \mathbf{v}_1 \| \| \mathbf{n}_p \|}, \quad \mathbf{n}_p = [1 \ 1 \ 1]^T,$$

where the vectors, \mathbf{v}_1 and \mathbf{n}_p , are illustrated in Figure B3b. The angle, ζ_b , illustrated in Figure B3a, is calculated as

$$\zeta_b = \arccos \left(\frac{\mathbf{a}^T \mathbf{s}_B}{\| \mathbf{a} \| \| \mathbf{s}_B \|} \right), \quad \mathbf{s}_B = \boldsymbol{\sigma}_B - [p \ p \ p]^T,$$

where \mathbf{s}_B is the stress deviator of the predictor stress state. As the centre coincides with the hydrostatic axis at the apex, the angle, ζ_b , is simply the Lode angle of the predictor stress state.

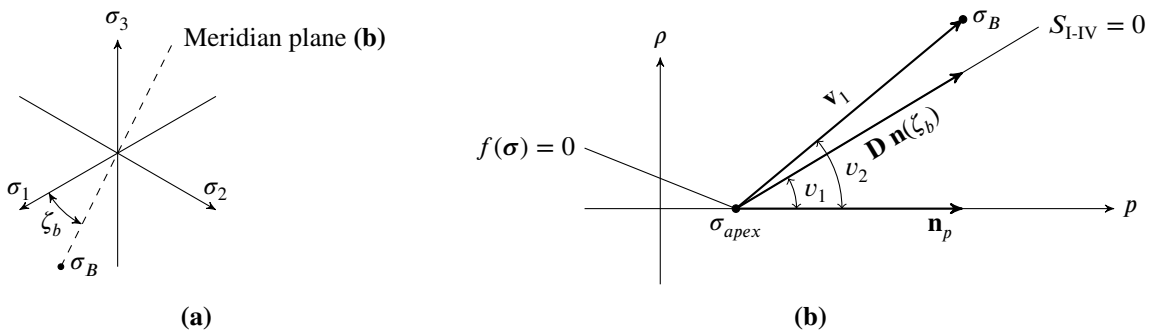


FIGURE B3 Geometrical illustration for determination of condition statements for the S_{I-IV} -surface (a) deviatoric plane and (b) meridian plane.

The conditions for determination of the correct return region for a stress state is listed in Table B1. The line parameters, t_c and t_t , in Table B1, are calculated in Equation (C18) and explained in the corresponding section. The components of the normal vector in Equation (B4) depends solely on the surface parameters, and can, for the purpose of optimization, be calculated prior to an elasto-plastic analysis.

TABLE B1 Condition statements for determination of return region for a GPYS material.

Condition			Return region
$S_{I-II} < 0$	\wedge	$S_{I-III} > 0$	R_I
$S_{I-II} \geq 0$	\wedge	$t_c > 0$	R_{II}
$S_{I-III} \leq 0$	\wedge	$t_t > 0$	R_{III}
$S_{I-IV} \leq 0$			R_{IV}
$S_{I-II} > 0$	\wedge	$t_c \leq 0$	R_{IV}
$S_{I-III} < 0$	\wedge	$t_t \leq 0$	R_{IV}

† t_c and t_t are calculated from Equation (C18)

C STRESS RETURN FOR A GPYS MATERIAL

The mathematical formulation for the stress update procedure of the proposed plasticity model is presented in this appendix. When the return region is determined from the conditions in Table B1, the stress is updated accordingly, either to the yield surface, compressive or tensile meridians or the apex.

C.1 Closed form stress return to the yield surface

When a predictor stress state is situated in region I by the conditions defined in Table B1, the stress state is returned to the surface. The objective in this section is to formulate a fourth order polynomial in the energy-mapped stress space, to obtain a closed form expression for the updated stress state. The coefficients of this polynomial are rather long expressions, and the overall computation time may not differ notably from the classical iterative newton's method. However, stress returns in the vicinity of the apex tends to be troublesome with an iterative approach, whereas the closed form solution is robust.

The problem in Equation (6) can be shown to correspond to a minimization of the complementary elastic energy, as explained in for instance Coombs et al.⁹

$$\begin{aligned} &\text{minimize} \quad (\sigma_B - \sigma_C)^T \mathbf{C} (\sigma_B - \sigma_C), \\ &\text{subject to} \quad f(\sigma_C) = 0, \end{aligned}$$

where, \mathbf{C} , is the elastic flexibility matrix. By mapping to a stress space normalized with respect to the elastic energy, and assuming associated flow, the problem can be solved as the closest point projection onto the yield surface. This has been exploited by for instance Coombs et al.⁹ or Crouch et al.²¹ and can be applied to the GPYS model as well to achieve a one-step calculation of the updated stress state. The energy mapped stresses, ζ , are defined as the quantities which satisfies

$$\frac{1}{E} \zeta^T \zeta = (\sigma_B - \sigma_C)^T \mathbf{C} (\sigma_B - \sigma_C).$$

The transformation to the energy normalized stress space depends solely on Poisson's ratio for isotropic elasticity and reads

$$\zeta = \mathbf{T}_\zeta \sigma, \quad (\text{C8})$$

where \mathbf{T}_ζ is a linear map given in principal stresses as⁹

$$\mathbf{T}_\zeta = \frac{\sqrt{1-2\nu}}{3} \begin{bmatrix} 1 & 1 & 1 \\ 1 & 1 & 1 \\ 1 & 1 & 1 \end{bmatrix} + \frac{\sqrt{1+\nu}}{3} \begin{bmatrix} 2 & -1 & -1 \\ -1 & 2 & -1 \\ -1 & -1 & 2 \end{bmatrix}.$$

The return mapping procedure in energy normalized stress space in contrast to the principal stress space is illustrated in Figure C4 for different values of Poisson's ratio to illustrate the impact of the energy mapping of Equation (C8).

The predictor stress state is transformed to the energy-mapped stress space by Equation (C8) and the axes are subsequently rotated by the transformation in Equation (A1)

$$\zeta_B^* = \mathbf{T} \mathbf{T}_\zeta \sigma_B.$$

The closest point projection to be solved hereby reads

$$\begin{aligned} \zeta_B^* - \zeta_C^* &= \lambda_\zeta \nabla g_{\zeta_C}^*, \\ f_\zeta^*(\zeta_C) &= 0. \end{aligned} \quad (\text{C9})$$

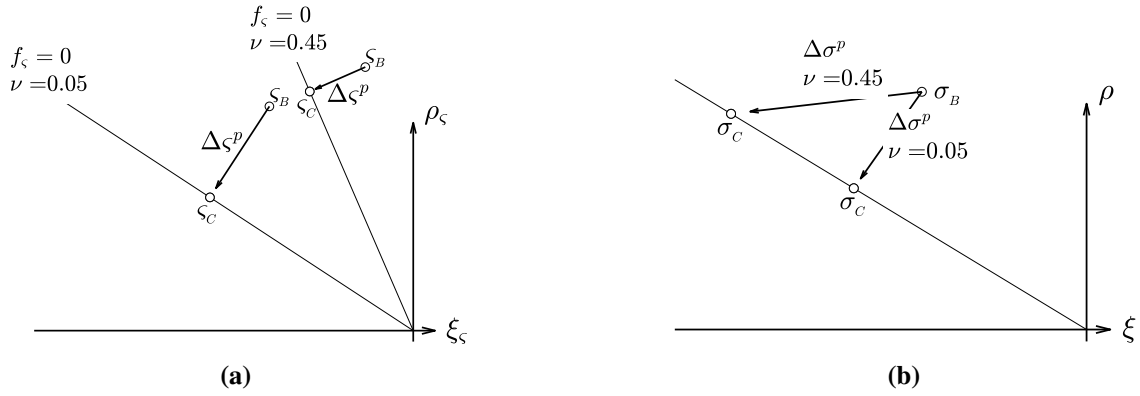


FIGURE C4 Stress return for the same trial stress, σ_B , for two different values of Poisson's ratio, seen in meridian plane in (a) energy mapped stress space and (b) principal stress space.

To arrive at an equation that can be solved directly, the following mathematical formulation of the energy mapped yield and potential functions are adopted

$$f_\epsilon^* = g_\epsilon^* = (\zeta_2^* - c_{\zeta_2}^* \zeta_1^*)^2 + (\zeta_3^* - c_{\zeta_3}^* \zeta_1^*)^2 - (r_\epsilon \zeta_1^*)^2, \quad (C10)$$

where, r_ϵ and \mathbf{c}_ϵ^* , is the energy mapped radius and transformed centre coordinates, obtained by

$$r_\epsilon = \frac{\sqrt{1+\nu}}{\sqrt{1-2\nu}} \frac{\mu}{\sqrt{3}} \bar{r} \quad \wedge \quad c_\epsilon^* = \frac{\sqrt{1+\nu}}{\sqrt{1-2\nu}} \frac{\mu}{\sqrt{3}} \bar{\mathbf{c}}^*.$$

The term with $1/\sqrt{3}$ is a map between hydrostatic pressure and the Haigh-Westergaard abscissa, ξ , and the prior fraction is the energy mapping. The apex is assumed at the origin in Equation (C10), and the stress state is simply translated hydrostatically with the mean pressure of the apex, prior to the operations in the following. Inserting the energy mapped yield surface of Equation (C10) and its derivative with respect to the energy mapped transformed stress components, ζ^* , into Equation (C9) yields the system of equations

$$\zeta_{B1}^* - \zeta_{C1}^* = \lambda_\epsilon \left(2\zeta_{C1}^* \left((c_{\zeta_2}^*)^2 + (c_{\zeta_3}^*)^2 \right) - 2c_{\zeta_2}^* \zeta_{C2}^* - 2c_{\zeta_3}^* \zeta_{C3}^* - 2r_\epsilon^2 \zeta_1^* \right), \quad (C11)$$

$$\zeta_{B2}^* - \zeta_{C2}^* = \lambda_\epsilon \left(2\zeta_{C2}^* - 2c_{\zeta_2}^* \zeta_1^* \right), \quad (C12)$$

$$\zeta_{B3}^* - \zeta_{C3}^* = \lambda_\epsilon \left(2\zeta_{C3}^* - 2c_{\zeta_3}^* \zeta_1^* \right), \quad (C13)$$

$$(\zeta_{C2}^* - c_{\zeta_2}^* \zeta_{C1}^*)^2 + (\zeta_{C3}^* - c_{\zeta_3}^* \zeta_{C1}^*)^2 - (r_\epsilon \zeta_{C1}^*)^2 = 0. \quad (C14)$$

This system of four equations with four unknowns can be solved directly by tedious but otherwise straightforward manipulation and substitution. By manipulation of the first three equations, the following expression for the components of the updated energy-mapped stress state, ζ_C^* , is obtained

$$\zeta_{C1}^* = \frac{-2\lambda_\epsilon \left(c_{\zeta_2}^* \zeta_{B2}^* + c_{\zeta_3}^* \zeta_{B3}^* \right) - \zeta_{B1}^* (1 + 2\lambda_\epsilon)}{4r_\epsilon^2 \lambda_\epsilon^2 + 2 \left(r_\epsilon^2 - \left((c_{\zeta_2}^*)^2 + (c_{\zeta_3}^*)^2 \right) - 2 \right) \lambda_\epsilon - 1} \quad \wedge \quad \zeta_{C2}^* = \frac{2\lambda_\epsilon c_{\zeta_2}^* \zeta_{C1}^* + \zeta_{B2}^*}{1 + 2\lambda_\epsilon} \quad \wedge \quad \zeta_{C3}^* = \frac{2\lambda_\epsilon c_{\zeta_3}^* \zeta_{C1}^* + \zeta_{B3}^*}{1 + 2\lambda_\epsilon}. \quad (C15)$$

Inserting these into Equation (C14) and rearranging, reduces to a fourth order polynomial with λ_ϵ as the independent variable as

$$A_1 \lambda_\epsilon^4 + A_2 \lambda_\epsilon^3 + A_3 \lambda_\epsilon^2 + A_4 \lambda_\epsilon + A_5 = 0. \quad (C16)$$

The coefficients of the polynomial reads

$$A_1 = -B_1 C_1 + C_1^2 \left((\zeta_{B2}^*)^2 + (\zeta_{B3}^*)^2 \right),$$

$$A_2 = C_1 \left(-8(\zeta_{B1}^*)^2 - 8\zeta_{B1}^* \left(\zeta_{B2}^* c_{\zeta_2}^* + \zeta_{B3}^* c_{\zeta_3}^* \right) + 2C_2 \left((\zeta_{B2}^*)^2 + (\zeta_{B3}^*)^2 \right) \right),$$

$$A_3 = B_1 C_3 - (\zeta_{B1}^*)^2 C_1 - B_2 C_1 + \left(\zeta_{B2}^* c_{\zeta_2}^* + \zeta_{B3}^* c_{\zeta_3}^* \right) \left(2\zeta_{B1}^* C_1 + 4C_2 \left(\zeta_{B2}^* c_{\zeta_2}^* + \zeta_{B3}^* c_{\zeta_3}^* \right) + 4C_2 \zeta_{B1}^* \right) + \left((\zeta_{B2}^*)^2 + (\zeta_{B3}^*)^2 \right) (C_2^2 - 2C_1),$$

$$A_4 = B_2 C_3 - (\zeta_{B1}^*)^2 C_1 + \left(\zeta_{B2}^* c_{\zeta 2}^* + \zeta_{B3}^* c_{\zeta 3}^* \right) \left(2 \zeta_{B1}^* C_2 - 4 \left(\zeta_{B2}^* c_{\zeta 2}^* + \zeta_{B3}^* c_{\zeta 3}^* \right) - 4 \zeta_{B1}^* \right) - 2 C_2 \left((\zeta_{B2}^*)^2 + (\zeta_{B3}^*)^2 \right),$$

$$A_5 = (\zeta_{B1}^*)^2 C_3 - 2 \zeta_{B1}^* \left(\zeta_{B2}^* c_{\zeta 2}^* + \zeta_{B3}^* c_{\zeta 3}^* \right) + ((\zeta_{B2}^*)^2 + (\zeta_{B3}^*)^2),$$

where

$$B_1 = 4 \left(\zeta_{B2}^* c_{\zeta 2}^* + \zeta_{B3}^* c_{\zeta 3}^* \right)^2 + 4 (\zeta_{B1}^*)^2 + 8 \zeta_{B1}^* \left(\zeta_{B2}^* c_{\zeta 2}^* + \zeta_{B3}^* c_{\zeta 3}^* \right),$$

$$B_2 = 4 (\zeta_{B1}^*)^2 + 4 \zeta_{B1}^* \left(\zeta_{B2}^* c_{\zeta 2}^* + \zeta_{B3}^* c_{\zeta 3}^* \right),$$

and

$$C_1 = 4 r_{\zeta}^2,$$

$$C_2 = 2 \left(r_{\zeta}^2 - \left((c_{\zeta 2}^*)^2 + (c_{\zeta 3}^*)^2 \right) - 2 \right),$$

$$C_3 = \left((c_{\zeta 2}^*)^2 + (c_{\zeta 3}^*)^2 \right) - r_{\zeta}^2.$$

It is noted, that the B -terms depend on the predictor stresses and the C -terms solely on the material properties. The roots of Equation (C16) can be obtained in closed form, see for instance Malhotra.²⁶ It is, however, found more efficiently solved by a numerical routine, as for instance the Laguerre method, see for instance Press et al.²⁷ The result is two complex roots, which obviously is of no interest, and two real roots corresponding to the stress return to the yield surface and the complementary cone defined by Equation (C10). The root corresponding to the correct stress return yields the smallest real value of $\zeta_{C1}^* = \xi_{\zeta}$, which is used to calculate the remaining components, ζ_{C2}^* and ζ_{C3}^* , from Equation (C15). The principal stresses of the updated stress state is simply recovered by inverse transformation as

$$\sigma_C = \mathbf{T}_{\zeta}^{-1} \mathbf{T}^{-1} \zeta_C^*,$$

and the plastic multiplier is calculated from Equation (6) as

$$\Delta \lambda = \frac{\| \sigma_C - \sigma_B \|}{\| \mathbf{D} \nabla g(\sigma_C) \|}.$$

Here, ∇g is evaluated for the updated stress state.

C.2 Return to a line

When a predictor stress state is situated in region II or III of Table B1, the stress update is performed by returning to either the compression or tensile meridian, respectively. The direction vectors for these lines can be seen in Figure B2 and are mathematically expressed in Equation (B6). The lines of intersection are formulated as parametric vector equations as

$$\sigma = \begin{cases} t_t \mathbf{r}_t + \sigma_{apex}, & \sigma_1 \geq \sigma_2 = \sigma_3 \quad (\text{triaxial extension}) \\ t_c \mathbf{r}_c + \sigma_{apex}, & \sigma_1 = \sigma_2 \geq \sigma_3 \quad (\text{triaxial compression}) \end{cases} \quad (\text{C17})$$

where, σ_{apex} , is the apex point. Indices, t and c , denotes the tensile and compressive lines respectively, and are omitted in the following, as the expressions adhere to both. Subscript, f and g , on the direction vectors are used to indicate yield and potential surfaces for generality. An incrementation in plastic strain is required to be orthogonal to the line of the potential surface, which can be stated as

$$(\Delta \epsilon^p)^T \mathbf{r}_g = (\mathbf{D}^{-1} \Delta \sigma^p)^T \mathbf{r}_g = 0.$$

Inserting the plastic corrector from Equation (6), the following expression is obtained

$$(\mathbf{D}^{-1} \Delta \sigma^p)^T \mathbf{r}_g = (\mathbf{D}^{-1} (\sigma_B - \sigma_c))^T \mathbf{r}_g = 0.$$

Substituting the expression for the updated stress, σ_C , with Equation (C17), the parameter, t , can be obtained in closed form as

$$(\mathbf{D}^{-1} (\sigma_B - (t \mathbf{r}_f + \sigma_{apex})))^T \mathbf{r}_g = 0 \quad \Leftrightarrow \quad t = \frac{\mathbf{r}_g^T \mathbf{D}^{-1} (\sigma_B - \sigma_{apex})}{\mathbf{r}_g^T \mathbf{D}^{-1} \mathbf{r}_f}. \quad (\text{C18})$$

The updated stress state is found by using the parameter, t , from Equation (C18) in the corresponding Equation in (C17).

C.3 Return to the apex

When a trial stress state is situated in region IV according to Table B1, the updated stress state is simply the apex point,

$$\sigma_C = \sigma_{apex} = \frac{2c\sqrt{k}}{k-1} [1 \ 1 \ 1]^T.$$

D THE CONSISTENT ELASTO-PLASTIC CONSTITUTIVE MATRIX

The consistent tangent operator for the GPYS model is described in this appendix. The consistent tangent relates changes in finite increments of stress and strain as

$$d(\Delta\sigma) = \mathbf{D}^{epc} d(\Delta\epsilon),$$

where superscript, *epc*, denotes a consistent elasto-plastic quantity. As the normal and shear components of the isotropic elasticity matrix, \mathbf{D} , are decoupled, it is advantageous to consider these separately, as follows

$$\mathbf{D} = \begin{bmatrix} \hat{\mathbf{D}} & \mathbf{0}_{3 \times 3} \\ \mathbf{0}_{3 \times 3} & \tilde{\mathbf{D}} \end{bmatrix} \quad \wedge \quad \mathbf{D}^{epc} = \begin{bmatrix} \hat{\mathbf{D}}^{epc} & \mathbf{0}_{3 \times 3} \\ \mathbf{0}_{3 \times 3} & \tilde{\mathbf{D}}^{epc} \end{bmatrix}.$$

This decomposition is convenient, as it is sufficient to merely calculate the first and second order gradients of the yield and potential surfaces, with respect to the normal stresses. The shear stress submatrix of the consistent tangent is shown by Clausen et al.¹⁹ to be given by

$$\tilde{\mathbf{D}}^{epc} = \begin{bmatrix} \frac{\sigma_{C1}-\sigma_{C2}}{\sigma_{B1}-\sigma_{B2}} & 0 & 0 \\ 0 & \frac{\sigma_{C1}-\sigma_{C3}}{\sigma_{B1}-\sigma_{B3}} & 0 \\ 0 & 0 & \frac{\sigma_{C2}-\sigma_{C3}}{\sigma_{B2}-\sigma_{B3}} \end{bmatrix} \tilde{\mathbf{D}},$$

where indexes, *C* and *B*, again denotes the updated stress and the predictor stress, respectively. The ordering of the stresses corresponds to

$$\sigma = [\sigma_{xx} \ \sigma_{yy} \ \sigma_{zz} \ \tau_{xy} \ \tau_{xz} \ \tau_{yz}]^T,$$

as adopted by the Abaqus software. The normal stress submatrix of the consistent tangent is presented in the following sections, and varies for the different return regions.

D.1 Consistent elasto-plastic constitutive matrix on the yield surface

The consistent tangent at the continuous part of the yield surface is considered in this section. The consistency condition requires infinitesimal stress increments to act tangential to the elastic domain, and reads

$$(\nabla f)^T d\sigma = 0.$$

Substituting Equation (5) into the consistency condition and isolating the plastic multiplier, $d\lambda$, yields

$$(\nabla f)^T (\mathbf{D}(d\epsilon - d\lambda \nabla g)) = 0 \quad \Leftrightarrow \quad d\lambda = \frac{(\nabla f)^T \mathbf{D} d\epsilon}{(\nabla f)^T \mathbf{D} \nabla g}.$$

The plastic multiplier inserted in (5) yields the elasto-plastic constitutive matrix for perfectly plastic material behaviour

$$d\sigma = \mathbf{D}^{ep} d\epsilon = \left(\mathbf{D} - \frac{\mathbf{D} \nabla g (\nabla f)^T \mathbf{D}}{(\nabla f)^T \mathbf{D} \nabla g} \right) d\epsilon, \quad (\text{D19})$$

as first derived by Zienkiewicz et al.²⁸ The matrix in Equation (D19) relates infinitesimal increments in stresses and strains, and leads to slow convergence rate, if used in numerical analysis. To obtain a relation which relates finite increments in stresses and strains during plastic loading, the decomposition of the stress increment in a predictor and a corrector term in Equation (5) is considered, to formulate an equation as

$$\mathbf{p} = -\Delta\sigma + \hat{\mathbf{D}}\Delta\epsilon - \Delta\lambda \hat{\mathbf{D}}\nabla g = 0.$$

Differentiating and rearranging yields the relation between changes in finite stress and strain increments as

$$d(\Delta\sigma) = \left(\mathbf{I} + \Delta\lambda \hat{\mathbf{D}} \nabla^2 g \right)^{-1} \hat{\mathbf{D}} (d(\Delta\epsilon) - d(\Delta\lambda) \nabla g) = \hat{\mathbf{D}}^c d(\Delta\epsilon^e).$$

Insertion in Equation (D19) gives the upper part of the consistent tangent as

$$\hat{\mathbf{D}}^{epc} = \hat{\mathbf{D}}^c - \frac{\hat{\mathbf{D}}^c \nabla g (\nabla f)^T \hat{\mathbf{D}}^c}{(\nabla f)^T \hat{\mathbf{D}}^c \nabla g}, \quad \hat{\mathbf{D}}^c = \left(\mathbf{I}_3 + \Delta \lambda \hat{\mathbf{D}} \nabla^2 g \right)^{-1} \hat{\mathbf{D}}, \quad (\text{D20})$$

which was first argued by Simo and Taylor.²²

D.2 Consistent elasto-plastic constitutive matrix on a line

The consistent elasto-plastic constitutive matrix for a stress state on a line of intersection is presented in the following. The first and second derivatives of the surface is not uniquely defined at the singularities, which was addressed by Koiter in 1953.²⁴ The approach presented here was proposed by Clausen et al. in 2007,¹⁹ and is a modification of the consistent tangent obtained by Koiter's assumption. The method is based on geometrical considerations, which results in particularly compact expression of the Koiter matrices. The consistent tangent on the line is calculated by a linear combination with the derivatives of the two active surfaces, as illustrated in Figure D5.

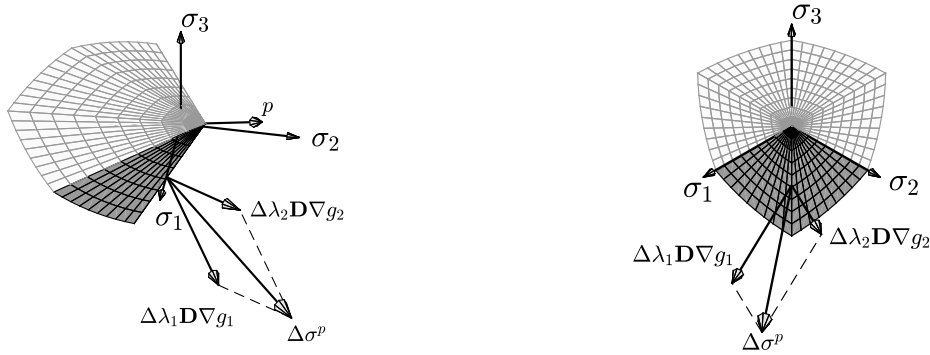


FIGURE D5 Illustration of stress update with two active yield surfaces.

Requiring the consistent tangent to contribute stiffness in the direction of the elastic strain increment and to be singular with respect to both active yield surfaces gives the systems of equations as

$$\hat{\mathbf{D}}_l^{ep} \hat{\mathbf{D}}^{-1} \mathbf{r}_f = \mathbf{r}_f, \quad (\text{D21})$$

$$\hat{\mathbf{D}}_l^{ep} \nabla g_1 = \mathbf{0}, \quad (\text{D22})$$

$$\hat{\mathbf{D}}_l^{ep} \nabla g_2 = \mathbf{0}, \quad (\text{D23})$$

where subscripts, 1 and 2, denotes the active surfaces. The direction vectors of the intersection lines \mathbf{r}_f and \mathbf{r}_g can be calculated from Equation (B6) or through the vector cross product of the return stress point gradients as

$$\mathbf{r}_f = \nabla f_1 \times \nabla f_2 \quad \wedge \quad \mathbf{r}_g = \nabla g_1 \times \nabla g_2.$$

Exploiting these relations, a solution to the Equations in (D21) reads

$$\hat{\mathbf{D}}_l^{ep} = \frac{\mathbf{r}_f (\mathbf{r}_g)^T}{(\mathbf{r}_g)^T \hat{\mathbf{D}}^{-1} \mathbf{r}_f} = \frac{(\nabla f_1 \times \nabla f_2)(\nabla g_1 \times \nabla g_2)^T}{(\nabla g_1 \times \nabla g_2)^T \hat{\mathbf{D}}^{-1} (\nabla f_1 \times \nabla f_2)}, \quad (\text{D24})$$

which corresponds to the Koiter assumption. The derivatives of the secondary surface, indexed 2, are simply obtained with index rotation of these quantities from the primary surface. The elasto-plastic constitutive matrix is modified to relate finite increments in stresses and strains as in the preceding Section. As illustrated in Figure D5, the plastic corrector can be expressed as a linear combination of contributions from the two active yield surfaces, which is utilized to formulate the following equation

$$\mathbf{p} = -\Delta \sigma + \hat{\mathbf{D}} \Delta \epsilon - \Delta \lambda_1 \hat{\mathbf{D}} \nabla g_1 - \Delta \lambda_2 \hat{\mathbf{D}} \nabla g_2 = \mathbf{0}.$$

Differentiation and rearranging yields

$$\begin{aligned} d(\Delta\sigma) &= \left(\mathbf{I} + \Delta\lambda_1 \hat{\mathbf{D}} \nabla^2 g_1 + \Delta\lambda_2 \hat{\mathbf{D}} \nabla^2 g_2 \right)^{-1} \hat{\mathbf{D}} (d(\Delta\epsilon) - d(\Delta\lambda_1) \nabla g_1 - d(\Delta\lambda_2) \nabla g_2) \\ &= \hat{\mathbf{D}}_l^c (\Delta\epsilon) - d(\Delta\lambda_1) \hat{\mathbf{D}}_l^c \nabla g_1 - d(\Delta\lambda_2) \hat{\mathbf{D}}_l^c \nabla g_2, \end{aligned}$$

Substituting into Equation (D24) yields the consistent tangent operator on the line as

$$\hat{\mathbf{D}}_l^{epc} = \frac{\mathbf{r}_f (\mathbf{r}_g)^T}{(\mathbf{r}_g)^T (\hat{\mathbf{D}}_l^c)^{-1} \mathbf{r}_f}, \quad \hat{\mathbf{D}}_l^c = \left(\mathbf{I}_3 + \Delta\lambda_1 \hat{\mathbf{D}} \nabla^2 g_1 + \Delta\lambda_2 \hat{\mathbf{D}} \nabla^2 g_2 \right)^{-1} \hat{\mathbf{D}}. \quad (\text{D25})$$

This quantity is further modified according to the Clausen method.²³ A contribution in the form of a symmetrical matrix is added to Equation (D25) as

$$\hat{\mathbf{D}}_{l,mod}^{epc} = \frac{\mathbf{r}_f (\mathbf{r}_g)^T}{(\mathbf{r}_g)^T (\hat{\mathbf{D}}_l^c)^{-1} \mathbf{r}_f} + \chi_{line} \frac{\mathbf{c}_{per} \mathbf{c}_{per}^T}{\mathbf{c}_{per}^T (\hat{\mathbf{D}}_l^c)^{-1} \mathbf{c}_{per}},$$

where, χ_{line} , is a user-defined parameter, and \mathbf{c}_{per} is an orthogonal vector to the plastic strain direction and the yield surface intersection line, calculated as

$$\mathbf{c}_{per} = \Delta\epsilon^p \times \mathbf{r}_g.$$

The χ_{line} parameter is system dependent, recommended in the interval [0; 1], and affects merely the global convergence rate.

D.3 Consistent elasto-plastic constitutive matrix at the apex

When a stress state is updated to the yield surface apex, the consistent elasto-plastic constitutive matrix is singular with respect to all directions i.e. the zero-matrix. To avoid issues with singular stiffness matrices, the Koiter assumption is applied, defining it only as singular with respect to the current direction of plastic strain incrementation,

$$\hat{\mathbf{D}}_p^{epc} = \hat{\mathbf{D}} - \frac{\hat{\mathbf{D}} \Delta\epsilon^p (\Delta\epsilon^p)^T \hat{\mathbf{D}}}{(\Delta\epsilon^p)^T \hat{\mathbf{D}} \Delta\epsilon^p}. \quad (\text{D26})$$

The matrix in Equation (D26) is often found to decrease the global convergence rate, if employed directly in numerical analysis, and is therefore modified by equal scaling of all entries, as proposed by Clausen et al.²³ as

$$\hat{\mathbf{D}}_{p,mod}^{epc} = \chi_{apex} \left(\hat{\mathbf{D}} - \frac{\hat{\mathbf{D}} \Delta\epsilon^p (\Delta\epsilon^p)^T \hat{\mathbf{D}}}{(\Delta\epsilon^p)^T \hat{\mathbf{D}} \Delta\epsilon^p} \right),$$

where, χ_{apex} , is a user-defined parameter. The χ_{apex} parameter is system dependent, recommended in the interval [0; 1], and affects merely the global convergence rate.

References

1. Lade P, M. Duncan J. Cubical triaxial tests on cohesionless soil. *ASCE J Soil Mech Found Div* 1973; 99: 793-781. doi: 10.1016/0148-9062(74)91579-4
2. Reddy KR, Saxena SK. Effects of Cementation on Stress-Strain and Strength Characteristics of Sands. *Soils and Foundations* 1993; 33(4): 121-134.
3. Bonding N. *Bulletin No. 30 - Triaxial State of Failure in sand*. Danish Geotechnical Institute . 1977. <http://www.geo.dk/bibliotek/197x/triaxial-state-of-failure-in-sand/>.
4. Bishop AW. The Strength of Soils as Engineering Materials. *Géotechnique* 1966; 16(2): 91-130.
5. Alejano LR, Bobet A. Drucker–Prager Criterion. *Rock Mechanics and Rock Engineering* 2012; 45(6): 995–999.
6. Damkilde L. A General Parametric Yield Surface model unifying several classical models. *International Journal of Solids and Structures*. Submitted 2019.
7. Yu MH. *Unified Strength Theory and its Applications*. Xi'an Jiatong University Press. 2 ed. 2018.

8. Paul B. Generalized Pyramidal Fracture and Yield Criteria. *International Journal of Solids and Structures* 1968(4): 175-196.
9. Coombs WM, Crouch RS, Augarde CE. Reuleaux plasticity: Analytical backward Euler stress integration and consistent tangent. *Computer Methods in Applied Mechanics and Engineering* 2010; 199(25): 1733 - 1743. doi: <https://doi.org/10.1016/j.cma.2010.01.017>
10. Clausen J, Damkilde L, Andersen L. Efficient return algorithms for associated plasticity with multiple yield planes. 2006; 66: 1036–1059. doi: 10.1002/nme.1595
11. Jepsen KS, Nielsen J, Damkilde L. A Concept of Local Rounding Applied to a Multi-Surface Plasticity Model with Sharp Edges. *International Journal for Numerical Methods in Engineering*. Submitted 2019.
12. Drucker DC, Prager W. *Soil Mechanics and Plastic Analysis or Limit Design*. Brown University. 1 ed. 1951.
13. Matsuoka H, Nakai T. Stress deformation and Strength characteristics of soil under three different principal stresses. *Proceedings of the Japan Society of Civil Engineers* 1974; 1974.
14. Lade PV. *Elasto-plastic Stress-Strain Theory for Cohesionless Soil with Curved Yield Surfaces*. Mechanics and Structures Department, School of Engineering and Applied Science, University of California. 3 ed. 1977.
15. Simulia DS. Abaqus 6.14 Analysis User's Guide Volume 3: Materials. http://130.149.89.49:2080/v6.14/pdf_books/ANALYSIS_3.pdf; 2014.
16. Coulomb CA. Sur une application des regles de Maximis & Minimis á quelques Problemes de Statique, relatifs á l'Architecture. 1773.
17. Hoek E, Brown ET. Empirical Strength Criterion for Rock Masses. *Journal of the Geotechnical Engineering Division* 1980(9): 1013-1035.
18. Abbo AJ, Lyamin AV, Sloan SW, Hambleton JP. A C2 continuous approximation to the Mohr Coulomb yield surface. 2011; 48: 3001–3010. doi: 10.1016/j.ijsolstr.2011.06.021
19. Clausen J, Damkilde L, Andersen L. An efficient return algorithm for non-associated plasticity with linear yield criteria in principal stress space. *Computers and structures* 2007(85): 1795-1807.
20. Borst dR, Crisfield MA, Remmers JJ, Verhoosel CV. *Non-Linear Finite Element Analysis of Solids and Structures*. John Wiley and Sons, inc. 2 ed. 2012.
21. Crouch RS, Askes H, Li T. Analytical CPP in energy-mapped stress space: Application to a modified Drucker-Prager yield surface. *Computer Methods in Applied Mechanics and Engineering* 2009; 198(5): 853 - 859. doi: <https://doi.org/10.1016/j.cma.2008.10.009>
22. Simo J, Taylor R. Consistent tangent operators for rate-independent elastoplasticity. *Computer Methods in Applied Mechanics and Engineering* 1985; 48(1): 101 - 118. doi: [https://doi.org/10.1016/0045-7825\(85\)90070-2](https://doi.org/10.1016/0045-7825(85)90070-2)
23. Clausen J, Damkilde L, Andersen LV. Robust and efficient handling of yield surface discontinuities in elasto-plastic finite element calculations. *Engineering Computations* 2015; 32(6): 1722-1752. doi: 10.1108/EC-01-2014-0008
24. Koiter WT. Stress-Strain Relations, Uniqueness and Variational Theorems for Elastic-Plastic Materials with a Singular Yield Surface. *Quarterly of Applied Mathematics* 1953; 11(3): 350–354.
25. Terzaghi K. *Theoretical Soil Mechanics*. John Wiley and Sons Inc. 6 ed. 1951.
26. Malhotra PK. A New Method of Solving a Quartic. 1958; 65: 280–282. doi: 10.2307/2310252
27. Press WH, Teukolsky SA, Vetterling WT, Flannery BP. *Numerical Recipes in Fortran 77 - The Art of Scientific Computing*. Press Syndicate of the University of Cambridge . 1992.
28. Zienkiewicz OC, Valliappa S, King IP. *Elasto-Plastic Solutions of Engineering Problems 'Initial Stress', Finite Element Approach*. International Journal for Numerical Methods in Engineering. 1 ed. 1969.

D | A Concept of Local Rounding Applied to a Multi-Surface Plasticity Model with Sharp Edges

The article in this appendix is intended for peer review in “*International Journal for Numerical Methods in Engineering*” June 2019 [Jepsen et al., 2019].

Summary:

Yield surfaces of discontinuous deviatoric trace are notoriously hard on global convergence in elasto-plastic finite element analysis. The methods to address the singularities and achieve a satisfactory convergence rate can be considered in two different groups. Either the original surface is implemented exactly, and the consistent tangent at the singularities are modified based on some physical arguments, or the original criterion is approximated with an expression for a continuous surface. This paper is in coherence with the latter, and offers a new concept of local rounding, which reshapes the surface at the deviatoric corners and at the apex singularity as well. Elegant mathematical expressions is obtained from geometrical considerations in principal stress space, opposed to the current corner rounding methods in the literature.

The concept is applied to the General Parametric Yield Surface Format, which is an all-encompassing constitutive model for frictional material. This paper offers the full mathematical description and implementation in a computational elasto-plastic framework. The baptism of fire of the novel yield surface is the analysis of a square spread footing on frictional soil. The new concept proves robust in numerical analysis in comparison with an exact implementation, with marginal discrepancy in bearing capacity.

ARTICLE TYPE

A Concept of Local Rounding Applied to a Multi-Surface Plasticity Model with Sharp Edges

Kenneth Sixhøj Jepsen | Johan Nielsen | Lars Damkilde*

¹Department of Civil Engineering, Aalborg University Esbjerg, 6700 Esbjerg, Denmark

Correspondence

*L. Damkilde, Aalborg University Esbjerg.
Email: lda@civil.aau.dk

Present Address

Niels Bohrs vej 8, 6700 Esbjerg, Denmark

Summary

Yield surfaces of discontinuous deviatoric trace are notoriously hard on global convergence in elasto-plastic finite element analysis. The methods to address the singularities and achieve a satisfactory convergence rate can be considered in two different groups. Either the original surface is implemented exactly, and the consistent tangent at the singularities are modified based on some physical arguments, or the original criterion is approximated with an expression for a continuous surface. This paper is in coherence with the latter, and offers a new concept of local rounding, which reshapes the surface at the deviatoric corners and at the apex singularity as well. Elegant mathematical expressions are obtained from geometrical considerations in principal stress space, opposed to the current corner rounding methods in the literature.

The concept is applied to the General Parametric Yield Surface Format, which is an all-encompassing constitutive model for frictional material. This paper offers the full mathematical description and implementation in a computational elasto-plastic framework. The baptism of fire of the novel yield surface is the analysis of a square spread footing on frictional soil. The new concept proves robust in numerical analysis in comparison with an exact implementation, with marginal discrepancy in bearing capacity.

KEYWORDS:

General Parametric Yield Surface, Corner Rounding, Multi-surface plasticity, Return Mapping, Spread footing analysis.

1 | INTRODUCTION

Discontinuous yield surfaces often occur as material models for granular materials, and the discontinuities, or so called “corners,” leads to poor convergence in numerical analysis. A widely accepted material model is the Mohr-Coulomb failure criterion, where quite some approaches to deal with the discontinuities have been proposed. Methods of exact implementation of the Mohr-Coulomb model with a modification of the consistent tangent operator at the corners is proposed by for instance Clausen et al.^{1,2,3} whom modifies the method of Koiter.⁴ Another approach is to approximate the mathematical formulation of the original yield surface with a smoothing in the vicinity of the discontinuities, often referred to as a corner rounding. A simple rounding of the corners was proposed by Owen and Hinton,⁵ whom preserved the original surface and used the gradient of a smooth geometry in the vicinity of the singularities, to ensure the flow direction as uniquely defined for all stress states. This method is

illustrated in Figure 1a, where the Drucker-Prager surface gradient is adopted near the corners of a Mohr-Coulomb surface. The simulations with such a method, however, tends to require an excessive amount of global iterations, see for instance Clausen et al. 2008.² A popular corner rounded approximation of the Mohr-Coulomb model, is the multifunction yield criterion proposed by Abbo and Sloan, 1995,⁶ which was later enhanced to the C^2 function class by Abbo et al. 2011,⁷ as depicted in Figure 1b. A similar approach was recently applied by Dai et al. 2018,⁸ to approximate the Hoek-Brown model. However, the method of Clausen is generally associated with some manual parameter adjustment to obtain convergence, and corner rounding generally involves an approximation. It is therefore of interest to eliminate surface discontinuities in a robust manner, without manual parameter adjustment, and with minimal discrepancies of the original criteria.

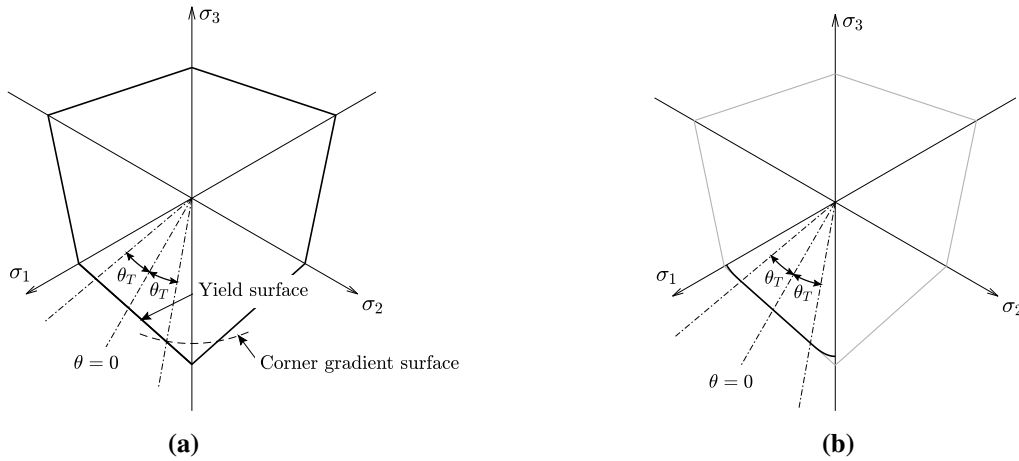


FIGURE 1 Sketches in the deviatoric plane of two corner rounding approaches (a) discontinuous yield surface with continuous gradient surface near singularities⁵ and (b) C^2 continuous approximation of the Mohr-Coulomb surface.⁷ The transition Lode angle, $\theta_T = 20^\circ$, is exaggerated for illustrative purposes.

This paper offers the mathematical formulation and implementation of a continuous convex version of the General Parametric Yield Surface (GPYS) formulated by Damkilde⁹ and implemented numerically by Nielsen et al.¹⁰ This model is adopted as it bears resemblance to the proposed corner rounding concept, and it covers a wide range of convex shapes from Mohr-Coulomb to the Drucker-Prager model. It operates on the well-known parameters of Mohr-Coulomb, which establishes a familiarity, plus two additional parameters to adjust the ρ_t/ρ_c -ratio and deviatoric curvature. The proposed concept rests on geometrical arguments, and all operations are therefore performed in principal stress space. As previously mentioned, discontinuous yield surfaces are inferior regarding global convergence rate, due to the lack of C^1 and C^2 continuity, meaning the first and second derivatives are not continuously differentiable. The method proposed in this paper is C^1 continuous and ensured convex through simple geometrical arguments. The lack of C^2 continuity presents an issue in the consistent tangent, to which a pragmatic but fruitful solution is proposed. The herein proposed concept rose from the works on the GPYS model,¹⁰ and similar methods are to the authors knowledge not presented before in the literature. However, Pietruszczak briefly visited the idea of a partly circular deviatoric trace in 1988.¹¹

The proposed concept is to introduce circles tangent to the original surface in the vicinity of the discontinuities, as illustrated in Figure 2a. A smooth continuous version of the Mohr-Coulomb yield surface with this concept of corner rounding, is visualized in the deviatoric plane in Figure 2b and meridian plane in Figure 2c, for different sizes of the rounding. The circle centres are positioned along the mirroring axis for the intersecting surfaces, which, in the case of an isotropic elasticity and hardening type model, is on the deviatoric projection of the principal stress axis. The rounding intensity is adjusted by manipulation of the centre of curvature.

The remainder of this paper is organized as follows: the mathematical description of the yield surface is given in Section 2, and the fully implicit return mapping scheme and calculation of the consistent elasto-plastic constitutive matrix is described in Section 3. Finally, the proposed corner rounded yield surface is juxtaposed an exact implementation in a numerical analysis in Section 4. Throughout the paper, linearly-elastic perfectly-plastic material behaviour and associated flow is assumed for simplicity. Compressive stresses are given as negative quantities.

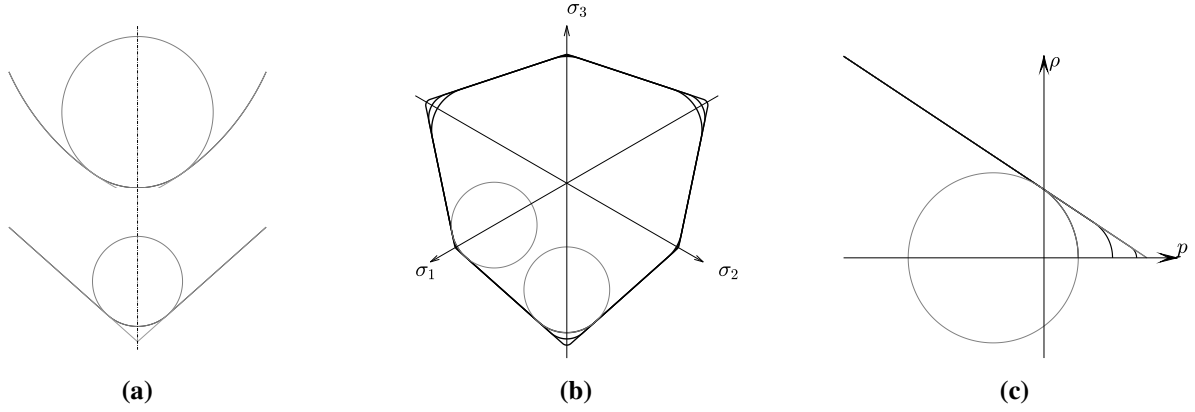


FIGURE 2 The concept of corner roundings by employment of circular segments **(a)** conceptual sketch, **(b)** rounded Mohr-Coulomb deviatoric trace, exaggerated for illustrative purposes, and **(c)** elimination of sharp apex point in meridian plane.

2 | MATHEMATICAL FORMULATION

In this section, the proposed corner rounding concept is applied to obtain a continuous version of the General Parametric Yield Surface Format. Firstly, the construction of the yield surface and the parameters are explained, followed by the mathematical derivation of the yield criterion. Principal stress representation is utilized to formulate the surface via spatial geometry, see for instance Clausen et al.¹ for the transformation between the general six-dimensional and principal stress space. The yield criterion is constructed as a multifunction expression, obtained by multiplication of a deviatoric and a meridional function. The deviatoric trace is described by circular segments, as sketched in Figure 3a, where the lines l_1 and l_2 defines the limits between function expressions. The curvature of the corner roundings are adjusted by manipulation of the centres c_2 and c_3 , which are positioned on the projected σ_3 - and σ_1 -axis, respectively. The meridional function is constructed of a linear segment and a tangential circular segment as depicted in Figure 3b, where the function expressions are limited by the hydrostatic stresses p_T and p_{apex} . A linear generator for, $p < p_T$, is used for simplicity, but could be replaced by any appropriate nonlinear expression if desired. Continuity and convexity of the surface is ensured by limits on the parameters derived from geometrical considerations.

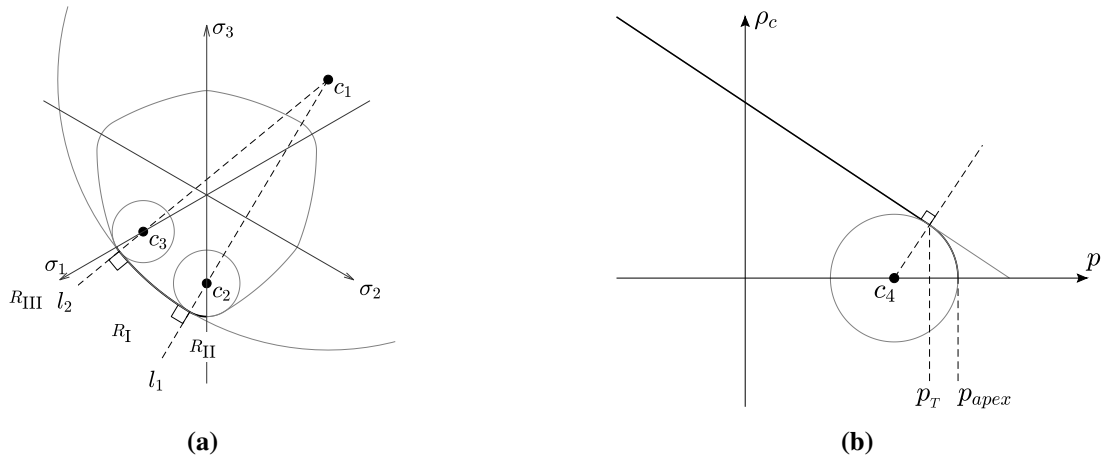


FIGURE 3 The concept of local corner rounding applied to the GPYS model by employment of circular segments **(a)** deviatoric trace and **(b)** elimination of sharp apex point in meridian plane.

The original GPYS model is described via four parameters, φ , c , α and β_1 , which is the internal angle of friction, cohesion, meridional eccentricity and side curvature, respectively. The rounding concept introduces three additional parameters β_2 , β_3 and

β_4 , which adjusts the curvature at the compression and tension corners and the apex singularity, respectively. The parameters are described along with settings to approximate some existing yield surfaces in Table 1. It is noted, that the top rounding acts as a smooth tension cut-off for $\beta_4 = 1$. The additional parameters β_2 , β_3 and β_4 , are set to, 0.01, as a general setting for everyday use, however, could be used as an advanced constitutive model for optimized material modelling as well.

TABLE 1 Description of the surface parameters and approximation of some existing models.

Description Symbol Range	Parameters						
	Angle of Friction	Cohesion	Meridional eccentricity	Curvature parameters			
	φ] $0; \pi/2$ [$c^{\dagger\dagger\dagger}$ > 0	α [0; 1]	β_1 [0; 1]	β_2 [0; 1]	β_3 [0; 1]	$\beta_4^{\dagger\dagger}$ [0; 1]
Special cases of existing plasticity models							
Mohr Coulomb	as is	as is	0.00	0.00 [†]	0.01	0.01	0.01
Extended Tresca	as is	as is	1.00	0.00 [†]	0.01	0.01	0.01
Drucker-Prager	as is	as is	1.00	1.00	0.01	0.01	0.01
Reuleaux ¹²	as is	as is	as is	1.00	0.01	0.01	0.01

[†] An appropriately small value is 10^{-4} .

^{††} Set to 1.00 for a tension cut-off

^{†††} Units of pressure

Due to the mathematical formulation, the β parameters cannot equal zero, and $\beta_1 = 10^{-4}$, is found to approximate a linear surface. The limits on α , β_1 , β_2 and β_3 , of Table 1 ensures a convex deviatoric trace. The impact of α and β_1 on the shape is visualized in Figure 4, with fixed $\beta_2 = \beta_3 = 0.20$.

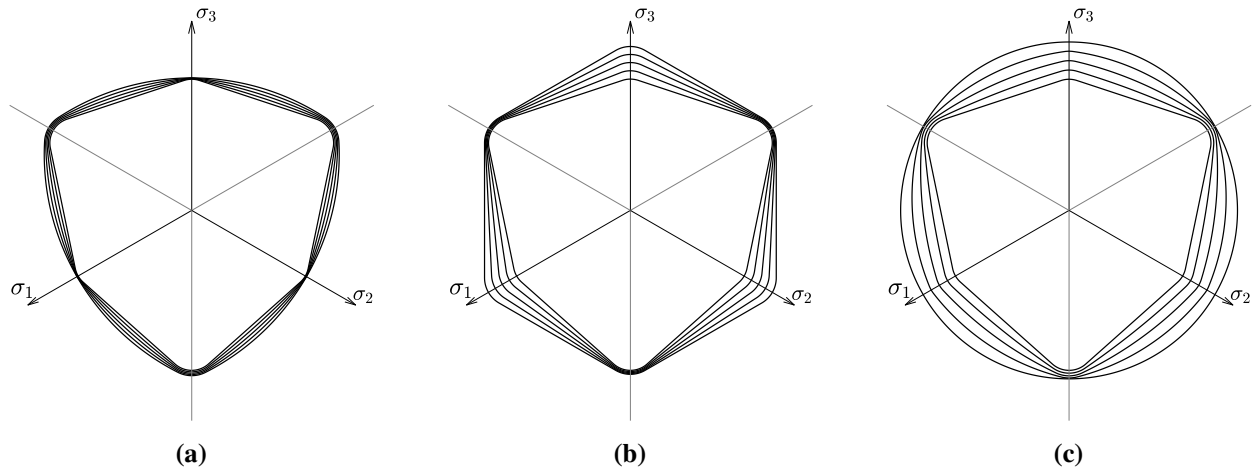


FIGURE 4 Deviatoric trace with various configurations of α and β_1 from 0 to 1 with increments of 0.25 and fixed $\beta_2 = \beta_3 = 0.20$. (a) Variation of β_1 with fixed $\alpha = 0$ (b) variation of α with fixed $\beta_1 = 0$ and (c) variation of α and β_1 .

The remainder of this section is devoted to derivation of the yield criterion, along with its first and second derivatives for the implementation in a numerical framework. A key element in the mathematical formulation is to operate with a deviatoric geometry, which is scaled with a function of the hydrostatic stress. The typical decomposition of stresses in deviatoric and hydrostatic components is exploited, and it is found convenient to define the deviatoric geometry in the cartesian σ^* -coordinate system illustrated in Figure 5. See Appendix A for an elaboration on this transformation.

A sketch for derivation of the yield criterion is given in Figure 6, where axis in the meridian plane of Figure 6b are the hydrostatic stress and the Euclidean norm of the stress deviator, given as

$$p = \frac{\sigma_1 + \sigma_2 + \sigma_3}{3} = \sqrt{3}\sigma_1^* \quad \wedge \quad \rho = \sqrt{(\sigma_2^*)^2 + (\sigma_3^*)^2}.$$

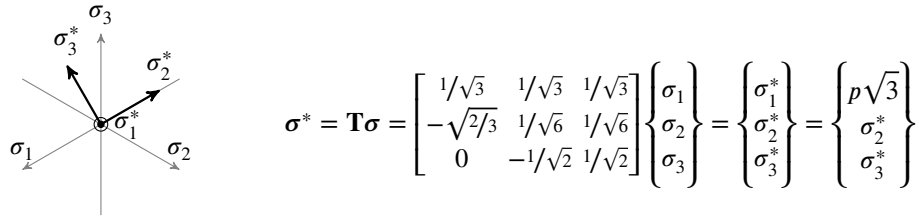


FIGURE 5 Transformation between principal stresses and the σ^* coordinates, seen in the deviatoric plane.

The deviatoric geometry is calculated in the ρ_c -normalized plane, with

$$\overline{\rho_c} = 1 \quad \wedge \quad \overline{\rho_t} = \alpha + \frac{3 - \sin(\varphi)}{3 + \sin(\varphi)} (1 - \alpha),$$

where the over-bar, $\overline{(\bullet)}$, denotes ρ_c -normalized parameters and the ρ_t/ρ_c -ratio of Mohr-Coulomb is obtained with $\alpha = 0$ and equals unity for $\alpha = 1$. The deviatoric corner roundings introduces two additional regions, denoted R_{II} and R_{III} , bounded by the lines l_1 and l_2 . The second centre of curvature c_2 defines the intersection between l_1 and the projected σ_3 -axis, and the third centre of curvature c_3 defines the intersection between l_2 and the projected σ_1 -axis, as depicted in Figure 6a. The three circular geometries defining the deviatoric trace are expressed as

$$\begin{aligned} \overline{c_1^*} &= \begin{Bmatrix} \overline{r_1} \cos \left((1 - \beta_1) \arctan \left(\frac{\overline{\rho_t} - 1/2}{\sqrt{3}/2} \right) \right) - \overline{\rho_t} \\ \overline{r_1} \sin \left((1 - \beta_1) \arctan \left(\frac{\overline{\rho_t} - 1/2}{\sqrt{3}/2} \right) \right) \end{Bmatrix} & \wedge & \quad \overline{r_1} = \frac{\sqrt{\left(\frac{\sqrt{3}}{2} \right)^2 + \left(\overline{\rho_t} - \frac{1}{2} \right)^2}}{2 \sin \left(\beta_1 \arctan \left(\frac{\overline{\rho_t} - 1/2}{\sqrt{3}/2} \right) \right)}, \\ \overline{c_2^*} &= (1 - \beta_2) \begin{Bmatrix} -\frac{1}{2} \\ -\frac{\sqrt{3}}{2} \end{Bmatrix} & \wedge & \quad \overline{r_2} = \overline{r_1} - \|\overline{c_1^*} - \overline{c_2^*}\|, \\ \overline{c_3^*} &= (1 - \beta_3) \begin{Bmatrix} -\overline{\rho_t} \\ 0 \end{Bmatrix} & \wedge & \quad \overline{r_3} = \overline{r_1} - \|\overline{c_1^*} - \overline{c_3^*}\|. \end{aligned}$$

The expressions for the first centre and radius, $\overline{c_1^*}$ and $\overline{r_1}$, is merely presented here, see Appendix B or Nielsen et al.¹⁰ for a thorough elaboration. The parameters, β_1 , β_2 and β_3 , are all dimensionless parameters in the interval $]0; 1[$.

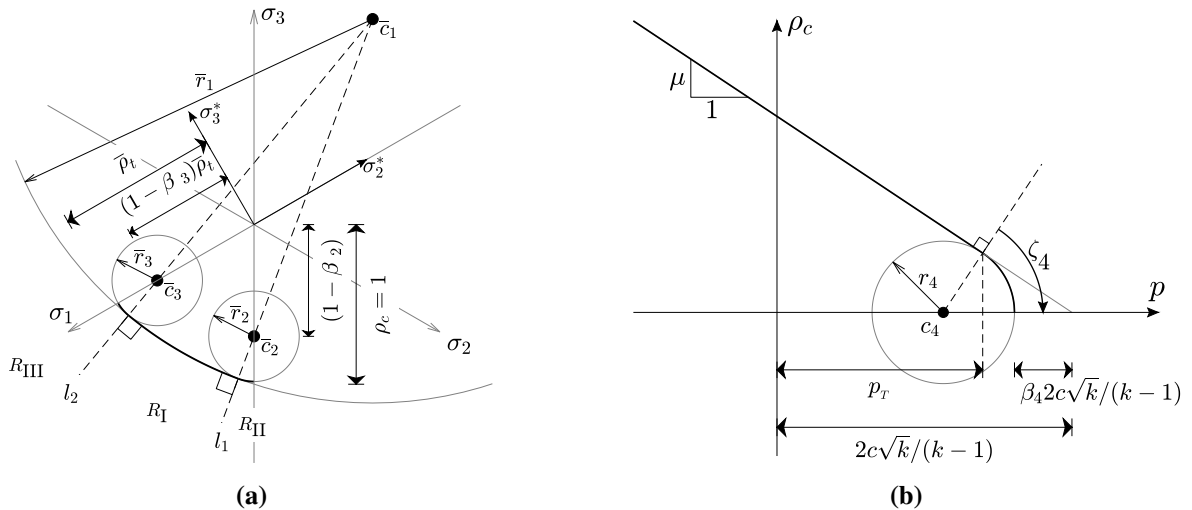


FIGURE 6 Geometrical relations for the novel yield surface seen in (a) ρ_c -normalised deviatoric plane and (b) plane of the compressive meridian.

The hydrostatic stress dependency is defined with the compressive meridian of Mohr-Coulomb, which has the slope

$$\mu = \frac{1-k}{\sqrt{2/3}(k/2+1)}, \quad k = \frac{1+\sin(\varphi)}{1-\sin(\varphi)},$$

and a circular segment at the top given as

$$c_4 = \left((1-\beta_4) \frac{2c\sqrt{k}}{k-1} - r_4 \right) \begin{Bmatrix} 1 \\ 0 \end{Bmatrix} \quad \wedge \quad r_4 = \beta_4 \frac{2c\sqrt{k}}{k-1} \cot(\zeta_4) \cot\left(\frac{\zeta_4}{2}\right), \quad \zeta_4 = \arctan\left(\frac{-1}{\mu}\right).$$

Here, $\beta_4 \in]0; 1]$ is the user-defined parameter to adjust the apex rounding, which renders a tension cut-off when set to one. The multifunction expression for the ρ_c -meridian of Figure 6b along with the first and second partial derivatives, used in the finite element implementation, reads

$$\rho_c = \begin{cases} \mu \left(p - \frac{2c\sqrt{k}}{k-1} \right) & , p \leq p_T \\ \left((r_4)^2 - (p - c_{41})^2 \right)^{0.5} + c_{42} & , p_T < p \leq p_{apex} \end{cases}, \quad (1)$$

$$\frac{\partial \rho_c}{\partial \sigma_i} = \begin{cases} \frac{\mu}{3} & , p \leq p_T \\ - \left((r_4)^2 - (p - c_{41})^2 \right)^{-0.5} \frac{p - c_{41}}{3} & , p_T < p \leq p_{apex} \end{cases}, \quad (2)$$

$$\frac{\partial^2 \rho_c}{\partial \sigma_i \partial \sigma_j} = \begin{cases} 0 & , p \leq p_T \\ - \left((r_4)^2 - (p - c_{41})^2 \right)^{-0.5} \frac{1}{9} - \left((r_4)^2 - (p - c_{41})^2 \right)^{-1.5} \left(\frac{p - c_{41}}{3} \right)^2 & , p_T < p \leq p_{apex} \end{cases}, \quad (3)$$

where the limits, as illustrated in Figure 6b, is expressed as

$$p_T = c_{41} + r_4 \cos(\zeta_4) \quad \wedge \quad p_{apex} = (1 - \beta_4) \frac{2c\sqrt{k}}{k-1} = c_{41} + r_4.$$

The top rounding, which is the second expression in Equation (1), yields complex values if evaluated for hydrostatic stresses above the apex. The formulation is treated as undefined for hydrostatic stress values above the apex, and temporary stress states above p_{apex} in the return map iterations, are replaced by an appropriate quantity below p_{apex} in hydrostatic stress. The yield function is formulated as the difference between the radius and the deviatoric distance from the stress state to the centre of curvature. The yield criterion along with its first and second partial derivatives with respect to the principal stresses are thereby given as

$$f_n = \|\sigma_d^* - \overline{c_n^*} \rho_c\| - \overline{r_n} \rho_c \quad (4)$$

$$\frac{\partial f_n}{\partial \sigma_i} = \|\sigma_d^* - \overline{c_n^*} \rho_c\|^{-1} h_{ni} - \overline{r_n} \frac{\partial \rho_c}{\partial \sigma_i}, \quad (5)$$

$$\frac{\partial^2 f_n}{\partial \sigma_i \partial \sigma_j} = \|\sigma_d^* - \overline{c_n^*} \rho_c\|^{-1} \frac{\partial h_{ni}}{\partial \sigma_j} - \|\sigma_d^* - \overline{c_n^*} \rho_c\|^{-3} h_{ni} h_{nj} - \overline{r_n} \frac{\partial^2 \rho_c}{\partial \sigma_i \partial \sigma_j}, \quad (6)$$

where subscript, n , denotes the deviatoric region, as illustrated in Figure 6a, and

$$\sigma_d^* = [\sigma_2^* \ \sigma_3^*]^T,$$

$$h_{ni} = \left(\sigma_2^* - \overline{c_{n1}^*} \rho_c \right) \left(T_{2i} - \overline{c_{n1}^*} \frac{\partial \rho_c}{\partial \sigma_i} \right) + \left(\sigma_3^* - \overline{c_{n2}^*} \rho_c \right) \left(T_{3i} - \overline{c_{n2}^*} \frac{\partial \rho_c}{\partial \sigma_i} \right),$$

$$\begin{aligned} \frac{\partial h_{ni}}{\partial \sigma_j} = & \left(T_{2j} - \overline{c_{n1}^*} \frac{\partial \rho_c}{\partial \sigma_j} \right) \left(T_{2i} - \overline{c_{n1}^*} \frac{\partial \rho_c}{\partial \sigma_i} \right) + \left(T_{3j} - \overline{c_{n2}^*} \frac{\partial \rho_c}{\partial \sigma_j} \right) \left(T_{3i} - \overline{c_{n2}^*} \frac{\partial \rho_c}{\partial \sigma_i} \right) \\ & - \left(\left(\sigma_2^* - \overline{c_{n1}^*} \rho_c \right) \overline{c_{n1}^*} + \left(\sigma_3^* - \overline{c_{n2}^*} \rho_c \right) \overline{c_{n2}^*} \right) \frac{\partial^2 \rho_c}{\partial \sigma_i \partial \sigma_j}. \end{aligned}$$

The deviatoric region for a stress state is determined by the inequalities in Table 2, which uses the tangent vectors at the intersection point between l_n and the yield surface.

TABLE 2 Condition statements for determination of deviatoric region.

Condition	Region
$t_2^T (\sigma_d^* - \overline{c_1^*} \rho_c) \leq 0 \quad \wedge \quad t_3^T (\sigma_d^* - \overline{c_1^*} \rho_c) \geq 0$	R_I
$t_2^T (\sigma_d^* - \overline{c_1^*} \rho_c) > 0$	R_{II}
$t_3^T (\sigma_d^* - \overline{c_1^*} \rho_c) < 0$	R_{III}

$$t_2 = \left\{ \begin{array}{c} -\overline{c_{22}^*} + \overline{c_{12}^*} \\ \overline{c_{21}^*} - \overline{c_{11}^*} \end{array} \right\} \quad \wedge \quad t_3 = \left\{ \begin{array}{c} -\overline{c_{32}^*} + \overline{c_{12}^*} \\ \overline{c_{31}^*} - \overline{c_{11}^*} \end{array} \right\}.$$

3 | IMPLEMENTATION IN ELASTO-PLASTIC FINITE ELEMENT ANALYSIS

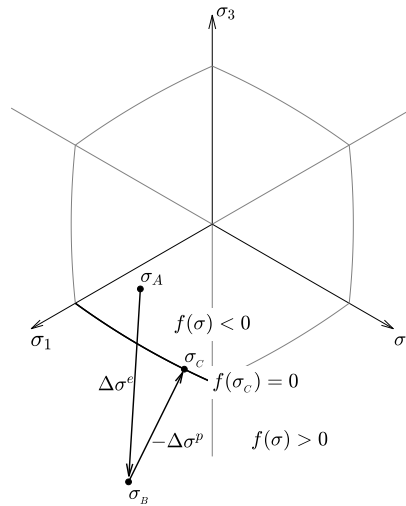
In this section, the implementation of the novel yield surface model in a computational elasto-plastic framework is described. A typical incremental global Newton-Raphson scheme is assumed, where an increment in forces gives a displacement increment, which updates the stresses in the element integration points. For a plastic stress state, the classical implicit return mapping scheme, or backward Euler stress integration, is adopted to update the stress state. All the operations are performed in principal stress space, both to accommodate the formulation of the yield surface, and to obtain an efficient return mapping and convenient expressions for the consistent tangent matrix. The implementation is schematically presented as pseudo-code in Appendix D.

3.1 | Stress Update by Return Mapping

A brief introduction to the implicit return mapping scheme for integration of the constitutive relation is described in this section, see for instance de Borst et al.¹³ for a thorough elaboration. The general equations and the iterative solution procedure is initially stated followed by some specifics towards the proposed yield surface. A non-linear finite element procedure is assumed, where a strain increment, $\Delta\epsilon$, results in an elastic predictor stress state, σ_B , see Figure 7, as

$$\sigma_B = \sigma_A + \Delta\sigma^e = \sigma_A + \mathbf{D}\Delta\epsilon,$$

where σ_A is the stress state prior to the strain increment and \mathbf{D} is the isotropic elasticity matrix.

**FIGURE 7** Geometrical illustration of the fully implicit return mapping scheme.

It is preliminarily assumed that a strain increment can be decomposed into an elastic and a plastic component and the plastic strain obey the flow rule as

$$d\epsilon = d\epsilon^e + d\epsilon^p \quad \wedge \quad d\epsilon^p = d\lambda \nabla g.$$

Here superscript e and p denotes elastic and plastic components respectively, $d\lambda$ and g are the plastic multiplier and potential function, respectively. In the analysis presented in this paper, associated flow is assumed, $f = g$, however, g is maintained in

the notations for the sake of generality. An infinitesimal stress increment is found by isolating the elastic strain increment and premultiplying by the elasticity matrix, \mathbf{D} , as

$$d\boldsymbol{\sigma} = \mathbf{D} d\boldsymbol{\varepsilon}^e = \mathbf{D} (d\boldsymbol{\varepsilon} - d\boldsymbol{\varepsilon}^p). \quad (7)$$

A finite stress increment is found by integration, as conducted with constant gradient over the stress path evaluated at the return point, i.e. a fully implicit integration scheme

$$\Delta\boldsymbol{\sigma} = \Delta\boldsymbol{\sigma}^e - \Delta\boldsymbol{\sigma}^p = \mathbf{D}\Delta\boldsymbol{\varepsilon} - \int_{\lambda}^{\lambda+\Delta\lambda} \mathbf{D}\nabla g d\lambda \simeq \mathbf{D}\Delta\boldsymbol{\varepsilon} - \Delta\lambda\mathbf{D}\nabla g(\boldsymbol{\sigma}_C), \quad (8)$$

where, $\Delta\boldsymbol{\sigma}^e$ and $\Delta\boldsymbol{\sigma}^p$, are the elastic predictor and plastic corrector, respectively. Combining Equation (8) with the proposed yield criterion of Equation (4), yields the following system of four equations with four unknowns

$$\mathbf{q} = \left\{ \begin{array}{c} \boldsymbol{\sigma}_C - \boldsymbol{\sigma}_B + \Delta\lambda \mathbf{D} \nabla g_n(\boldsymbol{\sigma}_C) \\ f_n(\boldsymbol{\sigma}_C) \end{array} \right\} = \mathbf{0}. \quad (9)$$

Here subscript, n , denotes the active deviatoric region, and the yield and potential functions are calculated for the updated stress state, $\boldsymbol{\sigma}_C$. It is noted that the previous stress state, $\boldsymbol{\sigma}_A$, does not enter Equation (9), as it merely is needed to calculate the elastic predictor, $\boldsymbol{\sigma}_B$. This system is for the sake of generality solved by Newton's method, although, a closed form solution can be obtained for the linear portion of the surface, see Nielsen et al.¹⁰ The solution in iteration, $j + 1$, is calculated by

$$\left\{ \begin{array}{c} \boldsymbol{\sigma}_C \\ \Delta\lambda \end{array} \right\}_{j+1} = \left\{ \begin{array}{c} \boldsymbol{\sigma}_C \\ \Delta\lambda \end{array} \right\}_j - \mathbf{J}_j^{-1} \mathbf{q}_j,$$

where, \mathbf{J} , is the Jacobian matrix, obtained in closed form by straight forward differentiation, yielding

$$\mathbf{J} = \begin{bmatrix} \mathbf{I} + \Delta\lambda \mathbf{D} \nabla^2 g_n(\boldsymbol{\sigma}_C) & \mathbf{D} \nabla g_n(\boldsymbol{\sigma}_C) \\ (\nabla f(\boldsymbol{\sigma}_C))^T & 0 \end{bmatrix}.$$

The iterative procedure is terminated when the Euclidean norm of \mathbf{q} is below an appropriate tolerance $\|\mathbf{q}_j\| \leq TOL$. The Newton algorithm is initiated with the following initial guesses

$$\boldsymbol{\sigma}_{C,0} = \begin{cases} \boldsymbol{\sigma}_B, & p_B < p_{apex} \\ \mathbf{T}^T \begin{bmatrix} (p_{apex} - 0.01r_4)\sqrt{3} & \sigma_{B2}^* r_4 \sqrt{(\sigma_{B2}^*)^2 + (\sigma_{B3}^*)^2}^{-1} & \sigma_{B3}^* r_4 \sqrt{(\sigma_{B2}^*)^2 + (\sigma_{B3}^*)^2}^{-1} \end{bmatrix}^T, & p_B \geq p_{apex} \end{cases},$$

as the yield criterion is undefined for hydrostatic stresses above p_{apex} , and the plastic multiplier is given as

$$\Delta\lambda = \frac{\|\boldsymbol{\sigma}_B - \boldsymbol{\sigma}_C\|}{\|\mathbf{D}\nabla g(\boldsymbol{\sigma}_C)\|}.$$

The initial guess for predictor stress states above the apex preserves the Lode angle of $\boldsymbol{\sigma}_B$ and is just below the apex in hydrostatic stress, and close to the surface in the deviatoric plane.

3.2 | Consistent Elasto-Plastic Constitutive Matrix

In this section the calculation of the consistent elasto-plastic constitutive matrix, or simply referred to as the consistent tangent, is briefly described. When plastic strains occur, Hooke's law no longer applies, and an additional stress strain relation is needed, as the material point only carries additional stresses tangential to the yield surface. As the normal and shear components of the isotropic elasticity matrix are decoupled, it is advantageous to consider these separately, as follows

$$\mathbf{D} = \begin{bmatrix} \hat{\mathbf{D}} & \mathbf{0}_{3 \times 3} \\ \mathbf{0}_{3 \times 3} & \tilde{\mathbf{D}} \end{bmatrix} \quad \wedge \quad \mathbf{D}^{epc} = \begin{bmatrix} \hat{\mathbf{D}}^{epc} & \mathbf{0}_{3 \times 3} \\ \mathbf{0}_{3 \times 3} & \tilde{\mathbf{D}}^{epc} \end{bmatrix},$$

where superscript, epc , denotes a consistent elasto-plastic quantity. This decomposition is convenient as the shear stress submatrix of the consistent tangent is given as

$$\tilde{\mathbf{D}}^{epc} = \begin{bmatrix} \frac{\sigma_{C1} - \sigma_{C2}}{\sigma_{B1} - \sigma_{B2}} & 0 & 0 \\ 0 & \frac{\sigma_{C1} - \sigma_{C3}}{\sigma_{B1} - \sigma_{B3}} & 0 \\ 0 & 0 & \frac{\sigma_{C2} - \sigma_{C3}}{\sigma_{B2} - \sigma_{B3}} \end{bmatrix} \tilde{\mathbf{D}},$$

as shown by Clausen et al.³ Indices, C and B , again denotes the updated and the predictor stress state, respectively, and the ordering of the stresses corresponds to, $\{\sigma_{xx} \sigma_{yy} \sigma_{zz} \tau_{xy} \tau_{xz} \tau_{yz}\}$. To calculate the normal stress submatrix, $\hat{\mathbf{D}}^{epc}$, the elasto-plastic constitutive matrix is used, which for perfect plasticity reads

$$\mathbf{D}^{ep} = \left(\mathbf{D} - \frac{\mathbf{D} \nabla g (\nabla f)^T \mathbf{D}}{(\nabla f)^T \mathbf{D} \nabla g} \right), \quad (10)$$

as first derived by Zienkiewicz et al.¹⁴ This matrix is singular with respect to the plastic strain component, and the stress incrementation is given by the elastic strain component as

$$\mathbf{D}^{ep} d\epsilon^p = \mathbf{D}^{ep} d\lambda \nabla g = \mathbf{0} \quad \wedge \quad d\sigma = \mathbf{D}^{ep} (d\epsilon^e - d\epsilon^p) = \mathbf{D}^{ep} d\epsilon^e.$$

The elasto-plastic constitutive matrix of Equation (10) relates infinitesimal stress and strain increments and does not conform with a finite increment procedure, resulting in slow convergence rate. To ameliorate this, a relation between changes in finite stress and strain increments is derived by considering Equation (8) as

$$\mathbf{p} = -\Delta\sigma + \hat{\mathbf{D}}\Delta\epsilon - \Delta\lambda \hat{\mathbf{D}}\nabla g = 0.$$

Differentiation gives,

$$d(\mathbf{p}) = \left(\frac{\partial \mathbf{p}}{\partial \Delta\epsilon} \right)^T d(\Delta\epsilon) + \left(\frac{\partial \mathbf{p}}{\partial \Delta\sigma} \right)^T d(\Delta\sigma) + \left(\frac{\partial \mathbf{p}}{\partial \Delta\lambda} \right)^T d(\Delta\lambda) = \hat{\mathbf{D}}d(\Delta\epsilon) - \left(\mathbf{I} + \Delta\lambda \hat{\mathbf{D}}\nabla^2 g \right) d(\Delta\sigma) - d(\Delta\lambda) \hat{\mathbf{D}}\nabla g = 0,$$

and rearranging yields the relation between changes in finite stress and strain increments as

$$d(\Delta\sigma) = \left(\mathbf{I} + \Delta\lambda \hat{\mathbf{D}}\nabla^2 g \right)^{-1} \hat{\mathbf{D}} (d(\Delta\epsilon) - d(\Delta\lambda) \nabla g) = \hat{\mathbf{D}}^c d(\Delta\epsilon^e).$$

Insertion in Equation (10) yields the normal stress submatrix of the consistent tangent as

$$\hat{\mathbf{D}}^{epc} = \hat{\mathbf{D}}^c - \frac{\hat{\mathbf{D}}^c \nabla g (\nabla f)^T \hat{\mathbf{D}}^c}{(\nabla f)^T \hat{\mathbf{D}}^c \nabla g}, \quad \hat{\mathbf{D}}^c = \left(\mathbf{I} + \Delta\lambda \hat{\mathbf{D}}\nabla^2 g \right)^{-1} \hat{\mathbf{D}}. \quad (11)$$

This expression was first derived by Simo and Taylor¹⁵ and is presented in most literature on the subject since.

3.3 | Improvement of Consistent Tangent for C^2 Discontinuities

The lack of C^2 continuity of the yield surface leads to poor global convergence rate in numerical analysis. This section presents a modification of the yield surface second derivative to increase the global convergence rate. The considered issue is the abrupt change in curvature at the transition between regions, which is handled in the following by defining a new radius and centre of curvature, to be used in Equations (3) and (6). A straight-forward approach is to interpolate the curvature over an arc segment, giving the interpolated ρ_c -normalized deviatoric radius and centre of curvature, see Figure 8a, as

$$\overline{r_{n,int}} = \overline{r_n} w_n + \overline{r_1} (1 - w_n) \quad \wedge \quad \overline{c_{n,int}}^* = \overline{c_n}^* + (\overline{r_n} - \overline{r_{int}}) \frac{\mathbf{v}_1}{\|\mathbf{v}_1\|}, \quad \sigma_C \in R_n.$$

Here, w_n , is a linear interpolation of the angle, ζ , in deviatoric region n , proposed as

$$w_n = \begin{cases} \frac{\zeta_C}{\zeta_n \chi}, & \zeta_C \leq \zeta_n \chi, \\ 1, & \text{else} \end{cases}, \quad (12)$$

where, $\chi \in]0; 1]$, is a parameter to interpolate over a portion of the arc, and the interpolation angles are calculated as

$$\zeta_C = \arccos \left(\frac{\mathbf{v}_1^T \mathbf{v}_2}{\|\mathbf{v}_1\| \|\mathbf{v}_2\|} \right) \quad \wedge \quad \zeta_n = \arccos \left(\frac{\mathbf{v}_2^T \overline{c_n}^*}{\|\mathbf{v}_2\| \|\overline{c_n}^*\|} \right). \quad (13)$$

The deviatoric direction vectors \mathbf{v}_1 and \mathbf{v}_2 are given as

$$\mathbf{v}_1 = \sigma_{Cd}^* - \rho_c \overline{c_n}^* \quad \wedge \quad \mathbf{v}_2 = \overline{c_n}^* - \overline{c_1}^*,$$

where subscript, d , indicates the 2nd and 3rd entry of the transformed stress state as described in Section 2, and ρ_c is calculated for the updated stress state via Equation (1). Subscript n , denotes the deviatoric region.

Considering the apex rounding in the ρ_c -meridian plane, the interpolation is performed analogously to the procedure for the deviatoric plane, with a weight quantity as in Equation (12) and the interpolation angles are calculated as in Equation 13. Here, the meridional direction vectors are given as

$$\mathbf{v}_1 = \left\{ \begin{matrix} p_C \\ \rho_c(p_C) \end{matrix} \right\} - \mathbf{c}_4 \quad \wedge \quad \mathbf{v}_2 = \left\{ \begin{matrix} 1 \\ -\mu \end{matrix} \right\},$$

where p_C is the hydrostatic stress of the updated stress state used to calculate ρ_c from Equation (1). The interpolated radius and centre of curvature, in the ρ_c -meridian plane, are hereby given as

$$r_{4,int} = r_4 w_n + r_{inf}(1 - w_n) \quad \wedge \quad \mathbf{c}_{4,int} = \mathbf{c}_{4,int} + (r_4 - r_{4,int}) \frac{\mathbf{v}_1}{\|\mathbf{v}_1\|}, \quad p_C > p_T,$$

where, r_{inf} , is a numerically large value in a relative sense, say $r_4 \cdot 10^3$, opposed to infinity for a linear generator. The interpolated centres forms traces as illustrated in Figure 8b and 8c, which depends on the χ -parameter.

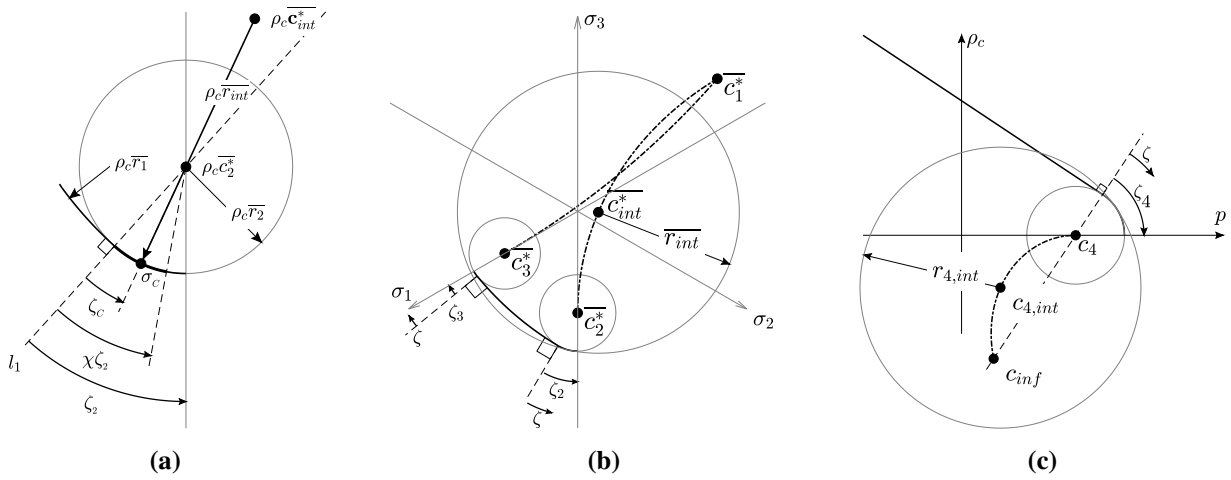


FIGURE 8 Illustration of the proposed interpolation method to modify the second derivative of the surface (a) zoom on the compressive corner (b) trace of interpolated centres in deviatoric plane and (c) trace of interpolated centre in meridian plane.

In the conducted analysis, $\chi = 0.01$, is found an appropriate setting. In general considerations, the higher value of χ leads to slower global convergence, however, may be more consistently monotonic and vice versa. The interpolation affects merely the global convergence rate, and not the final result.

4 | NUMERICAL ILLUSTRATION

The proposed smooth C^1 continuous yield surface is in this section applied in an elasto-plastic finite element analysis. The system under consideration is a shallow square spread footing, on frictional soil. This is a typical three-dimensional geotechnical problem, known as challenging in numerical analysis, as severe singularities requires highly refined meshes, and high stress gradients requires good estimates of the material consistent tangent. The analysis with the proposed yield surface are compared with an exact implementation of the GPYS model, see Nielsen et al.¹⁰ which modifies the consistent tangent at discontinuities as briefly described in Appendix C. Linearly elastic perfectly plastic material behaviour and associated flow, is assumed, and all analysis in this section are performed in a MATLAB code.

A top view sketch and the mesh discretization of the system is shown in Figure 9. The soil domain is of dimension $10 \times 10 \times 3 \text{ m}^3$ and the footing footprint measures $0.4 \times 0.4 \text{ m}^2$. Two symmetry planes are exploited to model a mere quarter of the system. The bottom surface is constrained in all directions and the vertical sides are constrained in their respective normal directions. A concentric vertical load is simulated as a uniform downwards displacement of the nodes in the footing footprint, which are restrained in the horizontal directions for fully rough conditions. An at rest earth pressure coefficient of $K_0 = 1$ and the

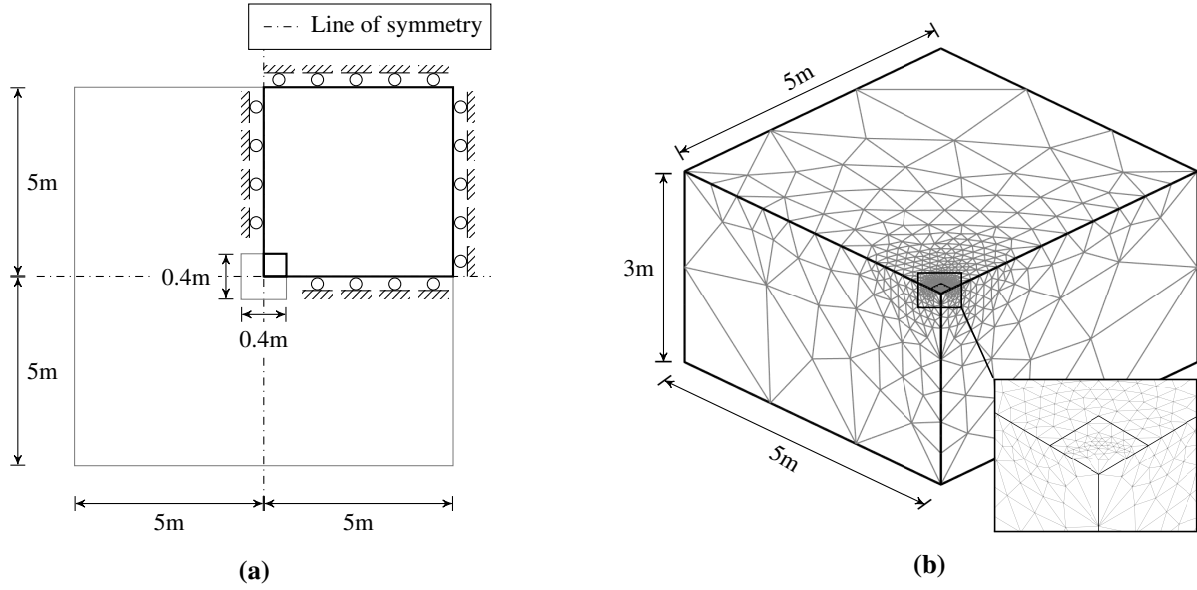


FIGURE 9 Mechanical system of square spread footing **(a)** Top view with geometry and boundary conditions and **(b)** Discretized model with 5,042 tetrahedral elements and 23,166 d.o.f. and zoom on mesh at footing footprint.

gravitational pull of $g = 9.81 \text{ m/s}^2$ is used to set the field of initial stresses and body forces. The system is discretized with standard 10-node tetrahedral elements, with quadratic displacement interpolation and a 4 point Gauss integration scheme, see for instance Cook et al.¹⁶ for an elaboration on the element type.

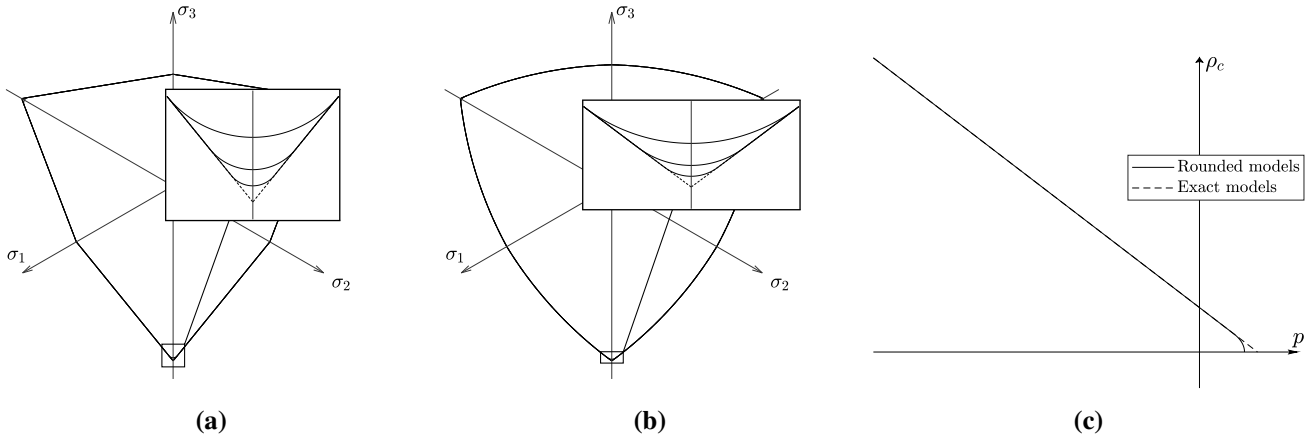


FIGURE 10 Sketch of yield surfaces for the material models **(a)** MC models with close-up on compressive corner for illustration of corner roundings, **(b)** GPYS models and **(c)** compressive meridian for all the material models.

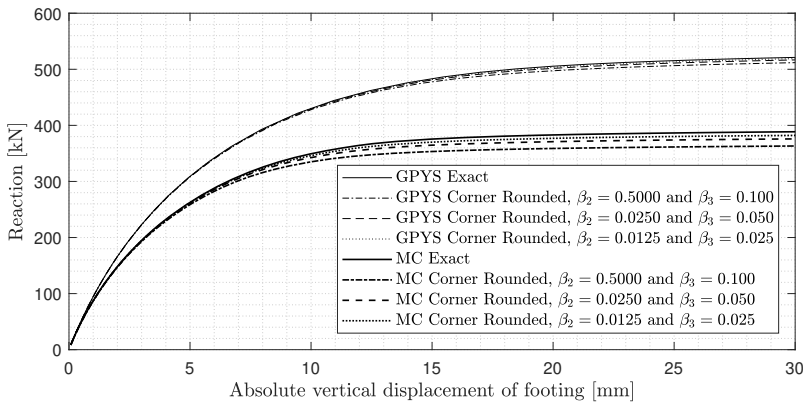
Two material models are considered, a Mohr-Coulomb setting and an optimized material calibrated to true triaxial experiments performed by Bønding.¹⁷ These are compared to their respective rounded approximations, with three different settings of the corner rounding parameters. The material parameters for the conducted analysis are listed in Table 3, and the deviatoric traces and meridians are visualized in Figure 10, with a close-up on the compressive corner.

The nonlinear finite element analysis are conducted with a standard Newton scheme for each load increment. If two consecutive load increments converge within three iterations, the load increment is increased with a factor of 1.5, with an upper bound on the incrementation of 0.05. The footing is indisputably forced to failure in all the analysis as seen in the load displacement

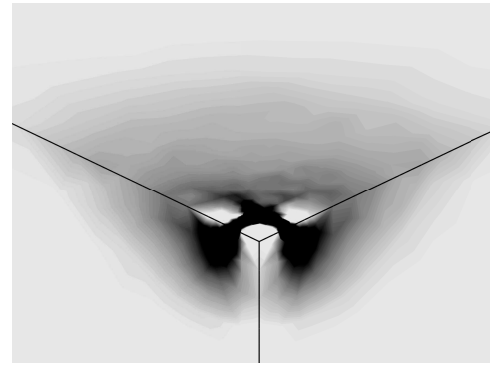
TABLE 3 Parameters of the six different corner rounded yield surface models, in the present analysis of a spread footing system.

Model	φ [deg]	c [kPa]	α [-]	β_1 [-]	β_2 [-]	β_3 [-]	β_4 [-]
MC	41.40	3.92	0.00	$5 \cdot 10^{-3}$	0.05/0.025/0.0125	0.1/0.05/0.025	0.145
GPYS	41.40	3.92	0.15	0.88	0.05/0.025/0.0125	0.1/0.05/0.025	0.145

curves in Figure 11a. The boundary conditions are verified by inspection of the failure mode, shown in a close-up of the contour of maximum shear strain rate at failure in Figure 11b.



(a)



(b)

FIGURE 11 Visualization of analysis results (a) load displacement curves and (b) rate of maximum plastic shear strain, $(\epsilon_1 - \epsilon_3)/2$, at failure in close-up at footing zone from analysis with the GPYS model.**TABLE 4** Comparison of analysis performance with the different material models.

		Exact implementation $\chi_{apex} = 0.0118$ and $\chi_{line} = 0.1600$	$\beta_2 = 0.05$ and $\beta_3 = 0.10$	$\beta_2 = 0.025$ and $\beta_3 = 0.05$	$\beta_2 = 0.0125$ and $\beta_3 = 0.025$
MC	Load steps	50	48	48	50
	Global Iterations	242	192	206	209
	Average iterations	4.84	4.00	4.29	4.18
	Run time ratio	1.00	1.41	1.70	1.72
	Limit load [kN]	389.07	363.57	375.90	382.53
	Ratio	1.0000	0.9344	0.9661	0.9832
GPYS	Load steps	36	35	36	36
	Global Iterations	108	105	111	111
	Average iterations	3.00	3.00	3.08	3.08
	Run time ratio	1.00	1.54	1.53	1.58
	Limit load [kN]	521.64	512.73	517.83	519.67
	Ratio	1.0000	0.9829	0.9927	0.9962

In evaluation of the performance of the novel plasticity model, limit load discrepancy, number of global iterations and run time, as seen in Table 4, are of interest. The performance of the corner rounded model is promising regarding the global convergence rate, especially in the Mohr-Coulomb settings, as sharp corners leads to low convergence rate. The analysis run time is, however, in all cases lower with the exact implementation. The analysis conducted with the exact implementation have required substantial adjustment of the convergence parameters to run the analysis to completion, as these only ensures convergence within a certain range.¹⁸ All simulations with the corner rounded model has completed with monotonic convergence, which emphasizes the

robustness of this method. The discrepancy on the limit load is notably affected by the corner roundings in this three-dimensional example. This indicates the importance of severely small roundings, which can be obtained with a model, such as the herein proposed. The effect of β_4 on the limit load is not investigated in these analysis.

5 | CONCLUSION

A concept for local rounding of multi-surface plasticity models has been introduced, and applied to formulate a continuous version of the General Parametric Yield Surface model. This model is intended for analysis of granular, frictional materials, however, the rounding concept could be applied in other fields as well. The full mathematical description and implementation of this model in elasto-plastic finite element analysis is given. The mathematical formulation of the surface is based on simple spatial geometry, operating on principal stresses, resulting in elegant expressions. The yield criterion is a multifunction of the C^1 class, where a pragmatic but fruitful solution is proposed for C^2 continuity for the consistent tangent operator. In analysing a square spread footing on frictional soil, the corner rounded model is compared in performance to an exact implementation of the original criterion. The novel yield surface model has proven robust and superior to the exact implementation regarding global convergence, with marginal discrepancy in limit load.

The return map and consistent tangent of the proposed model is written in MATLAB source code, which can be obtained from the corresponding author, and a Fortran code for use with the Abaqus software is available as well.



APPENDIX

A TRANSFORMATION BETWEEN REFERENCE COORDINATE SYSTEMS

The transformation between the principal stress and the σ^* -coordinate systems, which are used in formulation of the proposed yield surface, is described in this Appendix. The transformation from principal stresses to σ^* coordinates is performed by three plane rotations, as sketched in Figure A1. The first two rotations makes the σ_1^* -axis coincide with the hydrostatic axis, and the latter rotation of 30 degrees, makes the σ_2^* -axis coincide with the deviatoric projection of the first principal axis.

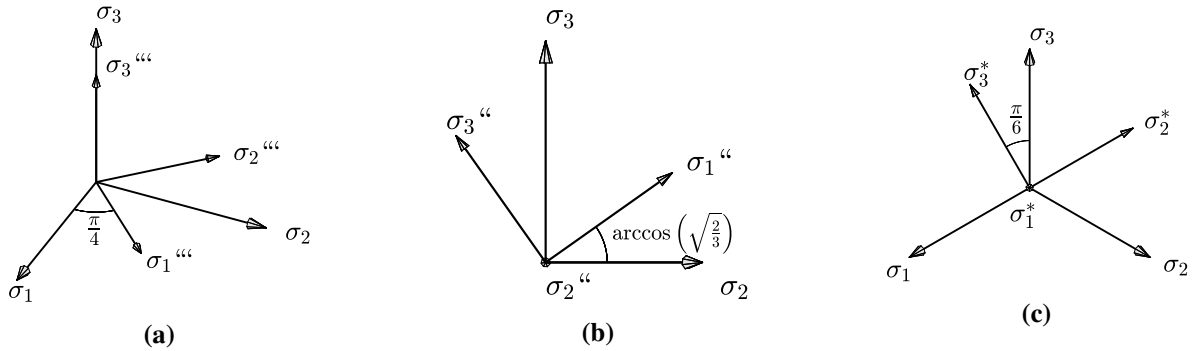


FIGURE A1 Transformation from principal stress to σ^* -coordinates in three steps (a) 45 degrees rotation about σ_3 (b) $\arccos \sqrt{2/3}$ radians rotation about σ_2'' and (c) 30 degrees rotation about σ_1^* .

The three transformations sketched in Figure A1 reads

$$\sigma^* = \mathbf{T}\sigma = \begin{Bmatrix} \sigma_1^* \\ \sigma_2^* \\ \sigma_3^* \end{Bmatrix} = \begin{bmatrix} 1 & 0 & 0 \\ 0 & \sqrt{3}/2 & 1/2 \\ 0 & -1/2 & \sqrt{3}/2 \end{bmatrix} \begin{bmatrix} \sqrt{2/3} & 0 & 1/\sqrt{3} \\ 0 & 1 & 0 \\ -1/\sqrt{3} & 0 & 1/\sqrt{3} \end{bmatrix} \begin{bmatrix} \sqrt{2}/2 & \sqrt{2}/2 & 0 \\ -\sqrt{2}/2 & \sqrt{2}/2 & 0 \\ 0 & 0 & 1 \end{bmatrix} \begin{Bmatrix} \sigma_1 \\ \sigma_2 \\ \sigma_3 \end{Bmatrix} = \begin{bmatrix} 1/\sqrt{3} & 1/\sqrt{3} & 1/\sqrt{3} \\ -\sqrt{6}/3 & \sqrt{6}/6 & \sqrt{6}/6 \\ 0 & -\sqrt{2}/2 & \sqrt{2}/2 \end{bmatrix} \begin{Bmatrix} \sigma_1 \\ \sigma_2 \\ \sigma_3 \end{Bmatrix}. \quad (\text{A1})$$

The inverse of, \mathbf{T} , equals the transpose, as exploited in the inverse transformation to principal stresses

$$\boldsymbol{\sigma} = \mathbf{T}^{-1} \boldsymbol{\sigma}^* = \mathbf{T}^T \boldsymbol{\sigma}^* = \begin{bmatrix} 1/\sqrt{3} & -\sqrt{6}/3 & 0 \\ 1/\sqrt{3} & \sqrt{6}/6 & -\sqrt{2}/2 \\ 1/\sqrt{3} & \sqrt{6}/6 & \sqrt{2}/2 \end{bmatrix} \boldsymbol{\sigma}^*. \quad (\text{A2})$$

B DEVIATORIC GEOMETRY OF THE GENERAL PARAMETRIC YIELD SURFACE

The deviatoric geometry of the General Parametric Yield Surface is derived in this section, with relevant measurements in Figure B2, see Nielsen et al.¹⁰ for a thorough elaboration. The geometry is calculated in a ρ_c -normalized system, giving the compressive and tensile meridian as

$$\bar{\rho}_c = 1 \quad \wedge \quad \bar{\rho}_t = \alpha + \frac{3 - \sin \varphi}{3 + \sin \varphi} (1 - \alpha),$$

where $\alpha \in [0; 1]$, is introduced as a scaling parameter of ρ_c yielding the Mohr-Coulomb meridian when $\alpha = 0$. The side secant length, L , and the angle, γ , as sketched in Figure B2, is evaluated by applying the Pythagorean theorem and the tangent relation

$$L = \sqrt{\left(\frac{\sqrt{3}}{2}\right)^2 + \left(\bar{\rho}_t - \frac{1}{2}\right)^2} \quad \wedge \quad \gamma = \arctan\left(\frac{\bar{\rho}_t - \frac{1}{2}}{\frac{\sqrt{3}}{2}}\right).$$

The deviatoric radius and centre of curvature is calculated using the right angle triangle in Figure B2b by straightforward geometrical operations

$$\bar{r}_1 = \frac{L}{2 \sin(\beta\gamma)} \quad \wedge \quad \bar{c}_1^* = \left\{ \begin{array}{l} \bar{r}_1 \cos((1 - \beta)\gamma) - \bar{\rho}_t \\ \bar{r}_1 \sin((1 - \beta)\gamma) \end{array} \right\}, \quad (\text{B3})$$

where the curvature parameter, $\beta \in]0; 1]$, is introduced as a scaling of the angle γ , as depicted in Figure B2.

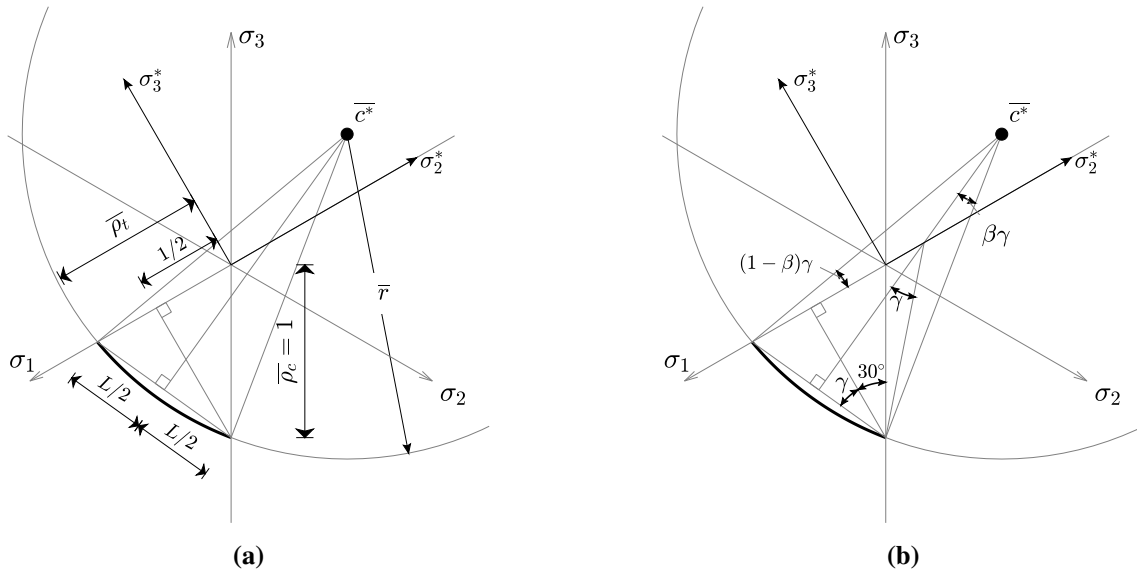


FIGURE B2 Sketch with relevant measures in the ρ_c -normalized deviatoric plane for derivation of the GPYS criterion (a) measures of length and (b) angular relations.

C MODIFIED CONSISTENT TANGENT IN EXACT IMPLEMENTATION OF GPYS

The consistent tangent at surface singularities, is in the implementation of the GPYS model, see Nielsen et al.¹⁰ modified according to the method proposed by Clausen et al.¹⁸ At the apex singularity, the elasto-plastic constitutive matrix is, in theory, singular with respect to all directions. To avoid ill-conditioning of the global stiffness matrix, the method of Koiter⁴ is adopted, which is further modified according to Clausen et al.¹⁸ for optimized convergence rate, where the upper part of the consistent tangent for an apex stress return is calculated as

$$\hat{\mathbf{D}}_{apex}^{epc} = \left(\hat{\mathbf{D}} - \frac{\hat{\mathbf{D}} \Delta \boldsymbol{\epsilon}^p (\boldsymbol{\epsilon}^p)^T \hat{\mathbf{D}}}{(\boldsymbol{\epsilon}^p)^T \hat{\mathbf{D}} \Delta \boldsymbol{\epsilon}^p} \right) \chi_{apex}, \quad (\text{C4})$$

where $\Delta \boldsymbol{\epsilon}^p$ is the plastic strain increment and χ_{apex} is a user defined parameter which in general is system dependent. When a stress state is returned to a line, the constitutive matrix is singular with respect to both active surfaces, in coherence with the Koiter assumption, which again is further adjusted as proposed by Clausen et al.¹⁸ where the upper part of the consistent tangent for a line return is calculated as

$$\hat{\mathbf{D}}_l^{epc} = \frac{\mathbf{r} \mathbf{r}_g^T}{\mathbf{r}^T (\hat{\mathbf{D}}_l^c)^{-1} \mathbf{r}_g} + \frac{(\Delta \boldsymbol{\epsilon}^p \times \mathbf{r}) (\Delta \boldsymbol{\epsilon}^p \times \mathbf{r})^T}{(\Delta \boldsymbol{\epsilon}^p \times \mathbf{r})^T (\hat{\mathbf{D}}_l^c)^{-1} (\Delta \boldsymbol{\epsilon}^p \times \mathbf{r})} \chi_{line}. \quad (\text{C5})$$

Here, \mathbf{r} and \mathbf{r}_g , are the intersection curve direction vector for yield and potential surface, respectively, and χ_{line} is a user defined parameter, which in general is system dependent. The consistent constitutive matrix on a line, is calculated as a linear combination with respect to both active yield surfaces as

$$\hat{\mathbf{D}}_l^c = \left(\mathbf{I} + \Delta \lambda_1 \hat{\mathbf{D}} \nabla^2 g_1 + \Delta \lambda_2 \hat{\mathbf{D}} \nabla^2 g_2 \right)^{-1} \hat{\mathbf{D}},$$

where subscripts, 1 and 2, refers to the respective yield and potential surfaces.

D SCHEMATIC OF STRESS UPDATE AND CONSISTENT TANGENT

The schematics of stress update and evaluation of the consistent tangent, with the proposed yield surface model is presented as pseudo-code in Algorithm 1.

Algorithm 1 Schematics of stress update and consistent tangent for the proposed yield surface model.

Input, $\boldsymbol{\sigma}_A$ and $\Delta \boldsymbol{\epsilon}$

Calculate elastic predictor $\boldsymbol{\sigma}_B = \boldsymbol{\sigma}_A + \mathbf{D} \Delta \boldsymbol{\epsilon}$

Calculate $\rho_c(\boldsymbol{\sigma}_B)$ by Equation (1)

Determine deviatoric region, n , for $\boldsymbol{\sigma}_B$ according to Table 2

if $f_n(\boldsymbol{\sigma}_B) \leq 0$ **then** (Purely elastic increment)

$\boldsymbol{\sigma}_C = \boldsymbol{\sigma}_B$

$\mathbf{D}^{epc} = \mathbf{D}$

else (Plastic stress state)

 Calculate $\boldsymbol{\sigma}_C$ by return mapping scheme, Section 3.1

if $p_C > p_T$ **then**

 Calculate ρ_c and its the derivatives of Equations, (1) to (3), with, $\mathbf{c}_{4,int}$ and $\mathbf{r}_{4,int}$, from Section 3.3

else

 Calculate ρ_c and its the derivatives by Equations, (1) to (3)

end if

 Determine deviatoric region, n , for $\boldsymbol{\sigma}_C$ according to Table 2

if $n = 2 \vee n = 3$ **then**

 Calculate surface derivatives of Equation, (5) and (6), with, $\overline{\mathbf{c}}_{n,int}^*$ and $\overline{\mathbf{r}}_{n,int}$, from Section 3.3

else

 Calculate surface derivatives of Equation, (5) and (6), with, $\overline{\mathbf{c}}_1^*$ and $\overline{\mathbf{r}}_1$

end if

 Calculate consistent tangent \mathbf{D}^{epc} by Equation (11)

end if

Transform $\boldsymbol{\sigma}_C$ and \mathbf{D}^{epc} back to global coordinate system

References

1. Clausen J, Damkilde L, Andersen L. Efficient return algorithms for associated plasticity with multiple yield planes. 2006; 66: 1036–1059. doi: 10.1002/nme.1595
2. Clausen J, Damkilde L. An exact implementation of the Hoek Brown criterion for elasto-plastic finite element calculations. 2008; 45: 831–847.
3. Clausen J, Damkilde L, Andersen L. An efficient return algorithm for non-associated plasticity with linear yield criteria in principal stress space. *Computers and structures* 2007(85): 1795-1807.
4. Koiter WT. Stress-Strain Relations, Uniqueness and Variational Theorems for Elastic-Plastic Materials with a Singular Yield Surface. *Quarterly of Applied Mathematics* 1953; 11(3): 350–354.
5. Owen DRJ, Hinton E. *Finite Elements in Plasticity: Theory and Practice*. 91 West Cross Lane, West Cross, Swansea U.K.: Pineridge Press Limited . 1980. ISBN 0-906674-05-2.
6. Abbo AJ, Sloan SW. A Smooth Hyperbolic Approximation to the Mohr-Coulomb Yield Criterion. *Computers and Structures* 1995(3): 427-441.
7. Abbo AJ, Lyamin AV, Sloan SW, Hambleton JP. A C2 continuous approximation to the Mohr-Coulomb yield surface. 2011; 48: 3001–3010. doi: 10.1016/j.ijsolstr.2011.06.021
8. Dai ZH, You T, Xu X, Zhu QC. Removal of Singularities in Hoek-Brown Criterion and Its Numerical Implementation and Applications. *International Journal of Geomechanics* 2018; 18(10): 04018127. doi: 10.1061/(ASCE)GM.1943-5622.0001201
9. Damkilde L. A General Parametric Yield Surface model unifying several classical models. *International Journal of Solids and Structures*. Submitted 2019.
10. Nielsen J, Jepsen KS, Damkilde L. Parametric Transition from Mohr-Coulomb to Drucker-Prager by Implementation of a General Parametric Yield Surface Format. *International Journal for Numerical and Analytical Methods in Geomechanics*. Submitted 2019.
11. Jiang J, Pietruszczak S. Convexity of yield loci for pressure sensitive materials. *Computers and Geotechnics* 1988; 5(1): 51 - 63. doi: [https://doi.org/10.1016/0266-352X\(88\)90016-X](https://doi.org/10.1016/0266-352X(88)90016-X)
12. Coombs WM, Crouch RS, Augarde CE. Reuleaux plasticity: Analytical backward Euler stress integration and consistent tangent. *Computer Methods in Applied Mechanics and Engineering* 2010; 199(25): 1733 - 1743. doi: <https://doi.org/10.1016/j.cma.2010.01.017>
13. De-Borst R, Crisfield MA, Remmers JJ, Verhoosel CV. *Non-Linear Finite Element Analysis of Solids and Structures*. John Wiley and Sons, inc. 2 ed. 2012.
14. Zienkiewicz OC, Valliappa S, King IP. *Elasto-Plastic Solutions of Engineering Problems 'Initial Stress', Finite Element Approach*. International Journal for Numerical Methods in Engineering. 1 ed. 1969.
15. Simo JC, Taylor RL. Consistent tangent operators for rate-independent elastoplasticity. *Computer methods in applied mechanics and engineering* 1984(48): 101-118.
16. Cook RD, Malkus DS, Plesha ME, Witt RJ. *Concepts and applications of Finite Element Analysis*. John Wiley and Sons, inc. 4. ed. 2002.
17. Bonding N. *Bulletin No. 30 - Triaxial State of Failure in sand*. Danish Geotechnical Institute . 1977. <http://www.geo.dk/bibliotek/197x/triaxial-state-of-failure-in-sand/>.
18. Clausen J, Damkilde L, Andersen LV. Robust and efficient handling of yield surface discontinuities in elasto-plastic finite element calculations. *Engineering Computations* 2015; 32(6): 1722-1752.